# Pulsed mm-Wave Electron Cyclotron Maser Experiments.

Stephen N. Spark

(B.Sc. University of Strathclyde).

Department of Physics and Applied Physics.

University of Strathclyde.

Thesis Submitted for the degree of Ph.D.

September 1988.

*I would like to dedicate this piece of work to my Mum and Dad, Dougie and John.*

**CONTENTS.**

ACKNOWLEDGMENTS.

I would like to thank my supervisors, Dr A.D.R. Phelps and Dr H.E.R. Preston for their constant help, encouragement and useful discussions throughout the period of this work.

I would also like to thank Mr J. Richmond for his technical help (particularly in the construction of the maser) and the S.E.R.C. for providing the personal financial support and funding for this research.

I would also like to thank the following people for their personal help and support over the last three years; Audrey and John Turnbull, Carol and John Collins, Janice and Nigel Mansell, Jim and Babs McFadyen, Nessie and Jimmy Bryans, Alex and Helen Doak, Eddie, John and Margaret McInally, Colin Brown, Elspeth Ritchie and last but certainly not least Donald, Muriel, Drew and Julie Munro.

## ABSTRACT.

A pulsed Electron Cyclotron Maser (E.C.M.) was developed and used to generate high power mm-waves in the W-band (75-110GHz) and the G-band (150-220GHz) frequency ranges. The relativistic electron beam (R.E.B.) was produced from a field-immersed, field-emission, cold cathode. A shaped anode cavity was designed for the optimum cavity Q, resonant frequencies, relative mode density, reflection coefficients and mode conversion in the output coupler.

Two pulsed conventional field coils were used; coil#1 (maximum B-field ≃9T) produced the uniform intra-cavity magnetic field and coil#2 (maximum B-field ≃1T) acted as a cathode field tuning coil. The addition of the cathode tuning coil increased the useful output energy in any pulse by a factor of ≃400.

Four diagnostics were used to determine the characteristics of the maser; 1) direct uncalibrated power monitoring, 2) calibrated frequency measurements (made using a quasi-optical diffraction grating spectrometer), 3) near field radiation pattern measurements and 4) calibrated absolute power measurements (made using a thermopile calorimeter).

The following characteristics of the maser oscillation were identified: in the W-band, single mode oscillation in the $TE_{03}$ mode was observed, centred at 95.2GHz, with an output power of ≃50kW. The cavity was crudely step-tunable with the excitation of the $TE_{13}$ mode at 81.4GHz and the $TE_{42}$ mode at 88.0GHz. In the G-band, multi-mode oscillation was observed at all values of the intra-cavity magnetic field. With the increased mode density at these frequencies, the maser was quasi-continuously tunable and 200GHz oscillation was observed.

These results proved to be self-consistent with the device-dependent calculations used to design the system and the general E.C.M. theory developed previously.

## SYMBOL LIST.

A = Area.

a = The cavity diameter.

$a_g$= Diffraction grating groove spacing.

B = Magnetic induction.

C = Capacitance.

c = Speed of light.

E = Electric field.

$E_l$= Energy stored in an inductor.

$E_C$= Energy stored in a capacitor.

-e = Charge on an electron.

$f_{ce}$= Cyclotron frequency of the electrons in the presence of an magnetic field

H = Magnetic field,

= $(1/\mu_0)B$

I, i = Current.

$J_p(x)$ = Bessel function of order p.

$J_p'(x)$ = $d/dx(J_p(x))$.

j = $\sqrt{(-1)}$

$k_{||}$= The parallel wave number of the guided electromagnetic wave.

$k_\perp$= The perpendicular wave number of the guided electromagnetic wave.

$k_0$= The free space wave number of the electromagnetic wave,

= $(k_{||}^2 + k_\perp^2)^{1/2}$.

L = Inductance.

l = The length of the magnetic field coil.

$l_C$= The length of the oscillating cavity.

m = Order of diffracted signal.

$m_0$= Rest mass of an electron.

N = Total number of turns.

n = Number of turns per unit length.

P = Power.

$P_f$= Magnetic field pressure.

$Q_\Omega$= The cavity ohmic quality factor.

$Q_D$= The cavity diffraction quality factor.

$Q_T$= The cavity quality factor,

$= (1/Q_\Omega + 1/Q_D)^{-1}$.

R, r = Resistance.

S = The Poynting vector.

V = Electric potential difference.

$v_\parallel$= Parallel component of electron velocity w.r.t. the magnetic field lines.

$v_\perp$= Perpendicular component of electron velocity w.r.t. the magnetic field lines.

v = Velocity,

$= (v_\parallel^2 + v_\perp^2)^{1/2}$.

$\alpha$ = Incident angle of collimated radiation on diffraction grating.

$\beta$ = Angle of diffracted signal from the spectrometer grating.

$\gamma$ = The Lorentz correction factor.

$= (1-v^2/c^2)^{-1}$

$\delta = \alpha + \beta$.

$\epsilon_0$= The permittivity of free space.

$\eta$ = Efficiency.

$\mu_0$= The permeability of free space.

$\sigma$ = Electrical conductivity.

$\chi_{pq}$= The $q^{th}$ root of $J_p(x)=0$.

$\chi_{pq}'$= The $q^{th}$ root of $J_p'(x)=0$.

$\omega$ = Angular frequency.

$\omega_b$= The modified electron plasma frequency.

$\omega_{ce}$= The cyclotron frequency of an electron in the presence of a magnetic field.

$\omega_g$= The frequency of oscillation of the guided radiation.

## FIGURE LIST.

## TABLE LIST.

# CHAPTER -1-

# THE ELECTRON CYCLOTRON MASER.

## 1.1 General Introduction.

Many authors have produced reviews of electron cyclotron maser (E.C.M.) development and current research, (1,2,3).

The astrophysicist R.Q. Twiss (4) is regarded as the first to recognise an amplifying mechanism for free electron gyroradiation in 1958. This work was followed independently by the theorists Schneider (5), using a quantum mechanical approach, and Gaponov (6) using a classical approach.

This theory was followed up in the early sixties by experimentalists such as Pantell (7), Chow and Pantell (8), Bott (9,10) and Feinstein (11). All of these devices used low voltage ($\simeq$10kV), low current ($\simeq$1mA) electron beams with total mm-wave output power $\ll$1W.

Later high power devices owe their success to the Russian development of the three electrode, thermionic cathode, magnetron injection gun (MIG) (12). This is capable of producing high currents and imparting large transverse energies to the electrons. Using the MIG, people such as Granatstein (13), Ginzburg (14), and Frank (15) demonstrated the feasibility of the device at conventional microwave frequencies. Workers such as Voronkov (16), who produced 23MW at 40GHz, and Gold (17), who produced 20MW at 35GHz, moved the gyrotron into an operating regime completely outwith the boundaries of conventional microwave devices, such as magnetrons and klystrons.

Subsequent experiments have moved to still higher frequencies, such as the results produced by Jory (18) at 60GHz, Gaponov (19) at 86GHz, Andronov (20) at 100GHz and Kreischer (21) at 140GHz, all of these devices producing in excess of 100kW.

The above experiments are all pulsed. Continuous wave (cw) gyrotrons have also been developed by Varian (18), who produced $>$200kW at both 28GHz and 60GHz, primarily developed for electron cyclotron resonance heating (E.C.R.H.), and Brand (22), who produced $<$10W between $\simeq$75GHz and 250GHz for plasma diagnostics.

Some typical results are shown graphically in fig.(1.1). This also demonstrates how the output power and frequency range of gyrotrons compares with conventional mm-wave sources (klystrons,

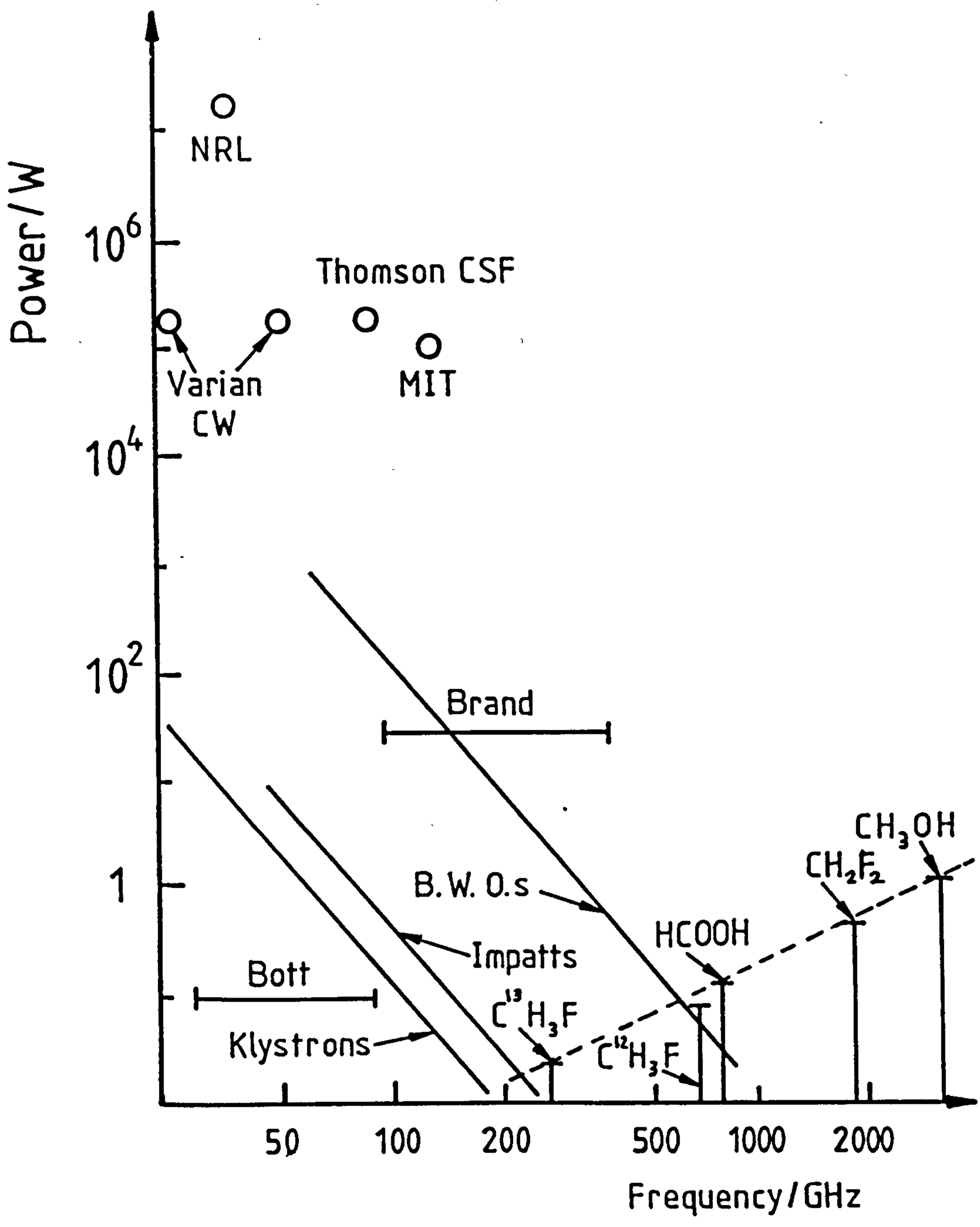


Fig.(1.1). Comparison of frequency and power capabilities of microwave, mm and sub-mm wave sources.

impatt diodes and backward wave oscillators (B.W.O.'s)), and low frequency lasers.

The gyrotron has many varied and important uses filling in a region of the electromagnetic spectrum where no high power devices have previously been available. They have been successfully used in E.C.R.H. (12,23) and for plasma diagnostics, utilising their high power and narrow line width ($\lesssim$1kHz).

## 1.2 E.C.M. Theory.

In the presence of a magnetic field an electron will gyrate at the Doppler shifted cyclotron frequency given by (24),

$$\omega_0 = \frac{e\,B}{\gamma\, m_0} + v_{\parallel}\, k_{\parallel} = \omega_{ce} + v_{\parallel}\, k_{\parallel}. \qquad (1.1)$$

Where,

$-e$ = charge on an electron,

$B$ = magnetic induction experienced by an electron,

$m_o$ = rest mass of an electron,

$\omega_{ce}$= cyclotron frequency of an electron in the presense of a magnetic field,

$v_{\parallel}$ = parallel component of electron velocity,

$k_{\parallel}$ = parallel wave number of generated wave,

$\gamma$ = the Lorentz correction factor,

$$= \frac{1}{\sqrt{(1-v^2/c^2)}},$$

$v$ = total electron velocity,

$c$ = speed of light.

If this interacts with a positive energy waveguide mode,

$$\omega_g^2 = c^2 k_0^2 = c^2\, k_{\perp}^2 + c^2\, k_{\parallel}^2, \qquad (1.2)$$

where $\omega_g$= the frequency of oscillation of the guided radiation,
and $k_{\perp}$= the perpendicular wave number of the guided wave,

then a net transfer of energy may occur, resulting in the wave

guide mode experiencing gain. The dispersion relation for this interaction is shown in fig.(1.2). Maximum gain occurs at grazing incidence of the waveguide mode and the Doppler shifted cyclotron frequency of the electrons. Substituting eqn.(1.1) into (1.2) and solving the quadratic in $k_{\parallel}$, assuming only one solution, yields.

$$k_{\parallel} = \frac{\omega_{ce} v_{\parallel}}{c^2 - v_{\parallel}^2} \quad \text{and} \quad k_{\perp}^2 = \frac{\omega_{ce}^2}{c^2 - v_{\parallel}^2} \qquad (1.3),(1.4)$$

Equation (1.3) provides first order information on the length of the cavity and eqn.(1.4) on the diameter of the cavity.

The coherence of the radiation is due to the natural phase bunching of the electrons as they spiral through the the B-field (2,25). This is a purely relativistic effect known as the cyclotron maser instability (26) which is a subset of the negative mass group of instabilities.

There are three mathematical models which have been used to describe the electron cyclotron maser mechanism (27).

1) The quantum mechanical approach. This was one of the first to describe the E.C.M. interaction, used by Schneider in 1959 (5,28). This theory predicted a possible gain mechanism and allowed the calculation of some necessary conditions, however like many problems the design and analysis of a practical E.C.M. does not lend itself well to a quantum mechanical approach due to the extreme complexity of the mathematical formalism required.
2) The ballistic approach. This is based on the self consistent solution of the relativistic Vlasov eqn. with the Lorentz force eqn. calculating the electron trajectories and their subsequent interaction with an existing waveguide mode. All generated eqns. must be solved via computational techniques.
3) The plasma physics approach. This is based on the self consistent solution of the relativistic Vlasov eqn. with the electromagnetic wave eqn. Using this formalism it has been possible to develop analytical expressions, thus providing a greater understanding of the E.C.M. mechanism. Subsequent

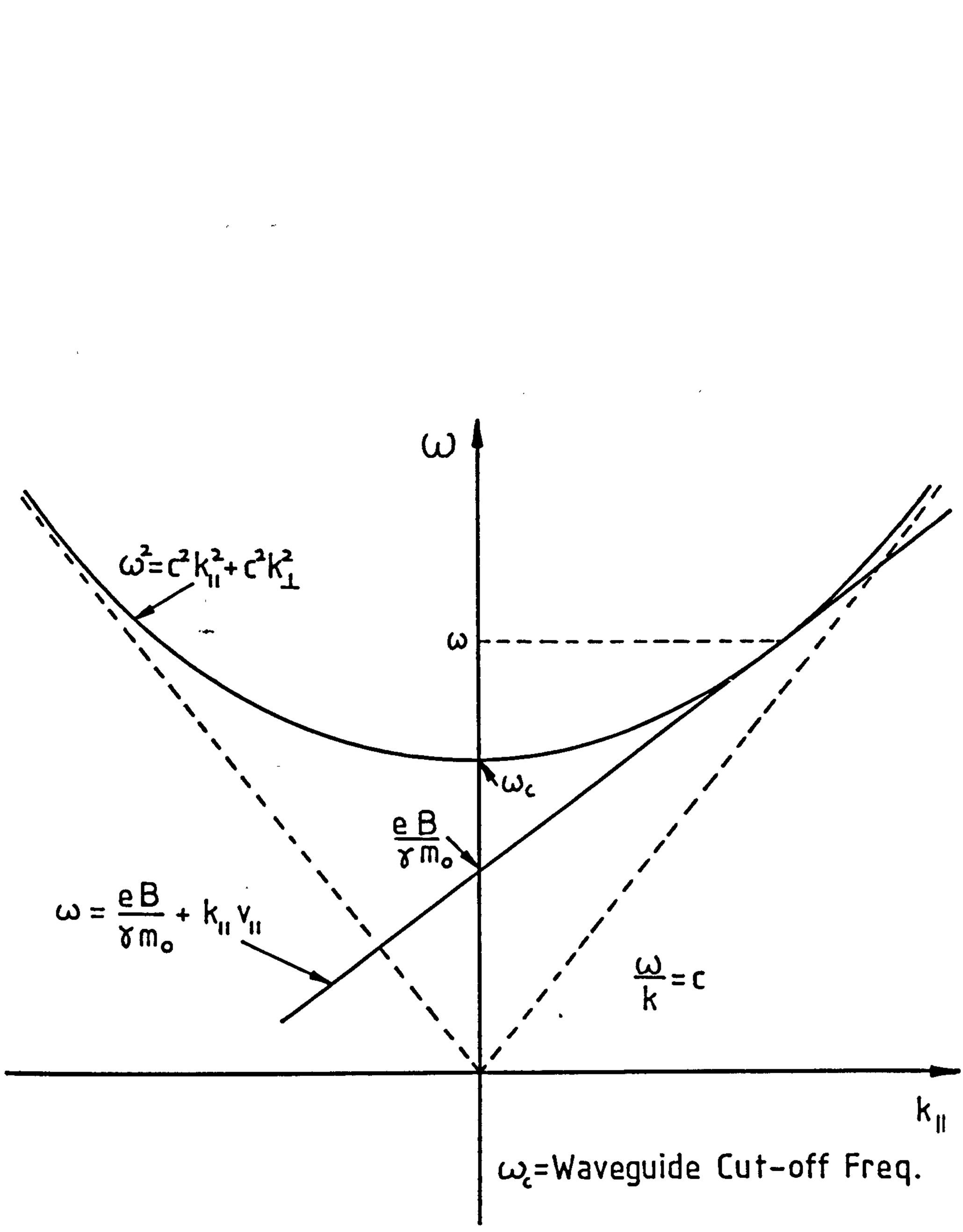


Fig.(1.2). The dispersion diagram of the Electron Cyclotron Maser interaction.

equations, however, haved to be solved using computational methods.

The linear dispersion relation was developed for an infinitely thin planar electron beam propagating mid-way between two semi-infinite conducting slabs immersed in a constant B-field parallel to both, by Ott and Manheimer (29). An almost identical expression was derived by Lau (30) for the more realistic case of a cylindrical beam propagating through a cylindrical waveguide. Sprangle and Drobot (31) also derived the dispersion relation with a geometry similar to that of Ott and Manheimer. In their paper they also developed non-linear expressions governing the E.C.M. interaction.

The plasma physics model also allows the inclusion of the temperature distribution within the initial electron beam and its subsequent evolution as the electrons interact with the intra-cavity radiation, the only model to do so.

The theory presented by Sprangle and Drobot (31) will be outlined briefly below.

Linear Plasma Theory.

The following theory is developed from the subsequent linearisation and solution of the highly non-linear Vlasov eqn.

$$\frac{\partial f}{\partial t} + v \cdot \nabla_r f + F \cdot \nabla_p f = 0 \qquad (1.5)$$

and the electromagnetic wave eqn.

$$\nabla \times \nabla \times E = -\frac{1}{c^2}\frac{\partial^2 E}{\partial t^2} - \mu_0 \frac{\partial J}{\partial t} \qquad (1.6)$$

For the case of an infinitely thin electron sheet placed in the middle plane of a parallel plate waveguide with a constant magnetic field parallel to both, the dispersion relation takes the form,

$$\omega^2 - c^2(k_\perp^2 + k_\parallel^2) = \frac{\omega_b^2}{\gamma}\,[1 + (-1)^{n+l}]\left[\frac{(\omega - k_\parallel v_\parallel)}{\omega - k_\parallel v_\parallel - \omega_{ce}}\,Q_n(x_n) - \frac{(v_\perp/c)^2(\omega^2 - k_\parallel^2 c^2)}{(\omega - k_\parallel v_\parallel - \omega_{ce})^2}\,W_n(x_n)\right]. \qquad (1.7)$$

Where,

2 a = the separation of the waveguide plates,

$$k = \frac{n\,\pi}{2\,a}\,, \qquad \omega_{ce} = \frac{l\,e\,B}{\gamma\,m_0}\,,$$

$l$ = the magnetic harmonic number

$v_\parallel$ and $v_\perp$ = the initial values of the longitudinal and transverse components of velocity.

$$\gamma = \left[1 - \frac{(v_\perp^2 + v_\parallel^2)}{c^2}\right]^{-\frac{1}{2}}$$

$\omega_b$ = the modified electron plasma frequency.

$$Q_n = x_n\left[\frac{l^2}{x_n^2} - 1\right]\frac{d}{dx}\left[J_l^2(x_n)\right]$$

$$W_n = \left[\frac{d}{dx}\left[J_l(x_n)\right]\right]^2$$

$$x_n = \frac{v_\perp k_\perp}{\omega_{ce}}$$

This expression is by no means straightforward, however it may be shown that the first term in the brackets on the R.H.S. of eqn.(1.7) is always stabilising and the second destabilising.

There must also exist a frequency shift as the relation is undefined for,

$$\omega = \omega_{ce} + k_\parallel v_\parallel = \omega_0.$$

Looking for solutions near $\omega_0$, and writing,

$$\omega = \omega_0 + \delta\omega \ , \quad \omega^2 = \omega_0{}^2 + 2\,\delta\omega\,\omega_0 \ , \text{ and } \quad \delta\omega \ll \omega_0$$

substituting into eqn.(1.7), yields.

$$\delta\omega^2 = \left[ \frac{\omega_b{}^2}{\gamma} \right] (1 - (-1)^{n+1}) \frac{(\omega_0 + \delta\omega - k_{\parallel} v_{\parallel})}{2\,\omega_0} \; Q_n(x_n).$$

$$\left[ 1 - \frac{(v_{\perp}/c)^2(\omega_0{}^2 + 2\,\delta\omega\,\omega_0 - k_{\parallel}{}^2 c^2)}{\delta\omega\,(\omega_0 + \delta\omega - k_{\parallel} v_{\parallel})} \; \frac{W_n(x_n)}{Q_n(x_n)} \right]. \quad (1.8)$$

$W_n(x_n)$ and $Q_n(x_n)$ are always positive for any given gyrotron and hence imaginary roots of this eqn. will exist only if $\delta\omega$ is positive. It may also be shown that a maximum growth rate occurs for frequencies where $\delta\omega$ is small. There is also a critical value of $v_{\perp}$, below which no unstable modes exist. This leads to one of the possible saturation mechanisms; as the electrons lose energy and $v_{\perp}$ drops below the critical value, energy transfer will cease. This is known as free energy depletion.

Non-linear Plasma Theory.

To gain any information from the complex and cumbersome analytic results from the non-linear theory, computational techniques must be employed.

One graphic result which may be extracted from the non-linear theory is a constant of motion. This may be used to qualitatively describe the phase bunching of the electron beam, the associated frequency up-shift of the resulting radiation and a second saturation mechanism. This states that each particle moves in a phase space $(u_{\perp},\lambda)$, where $u_{\perp}=\beta_{\perp}\gamma_{\perp}$ and $\lambda$ is the relative phase angle of the electrons w.r.t. the travelling wave, on C=constant curves shown in fig.(1.3). (Many different systems throughout physics demonstrate this bounded behaviour which arises from the solution of the forced pendulum equation). When a monoenergetic beam begins to interact with an electromagnetic wave, at a time $t=t_0$ fig(1.4), at a later time it will begin to demonstrate phase

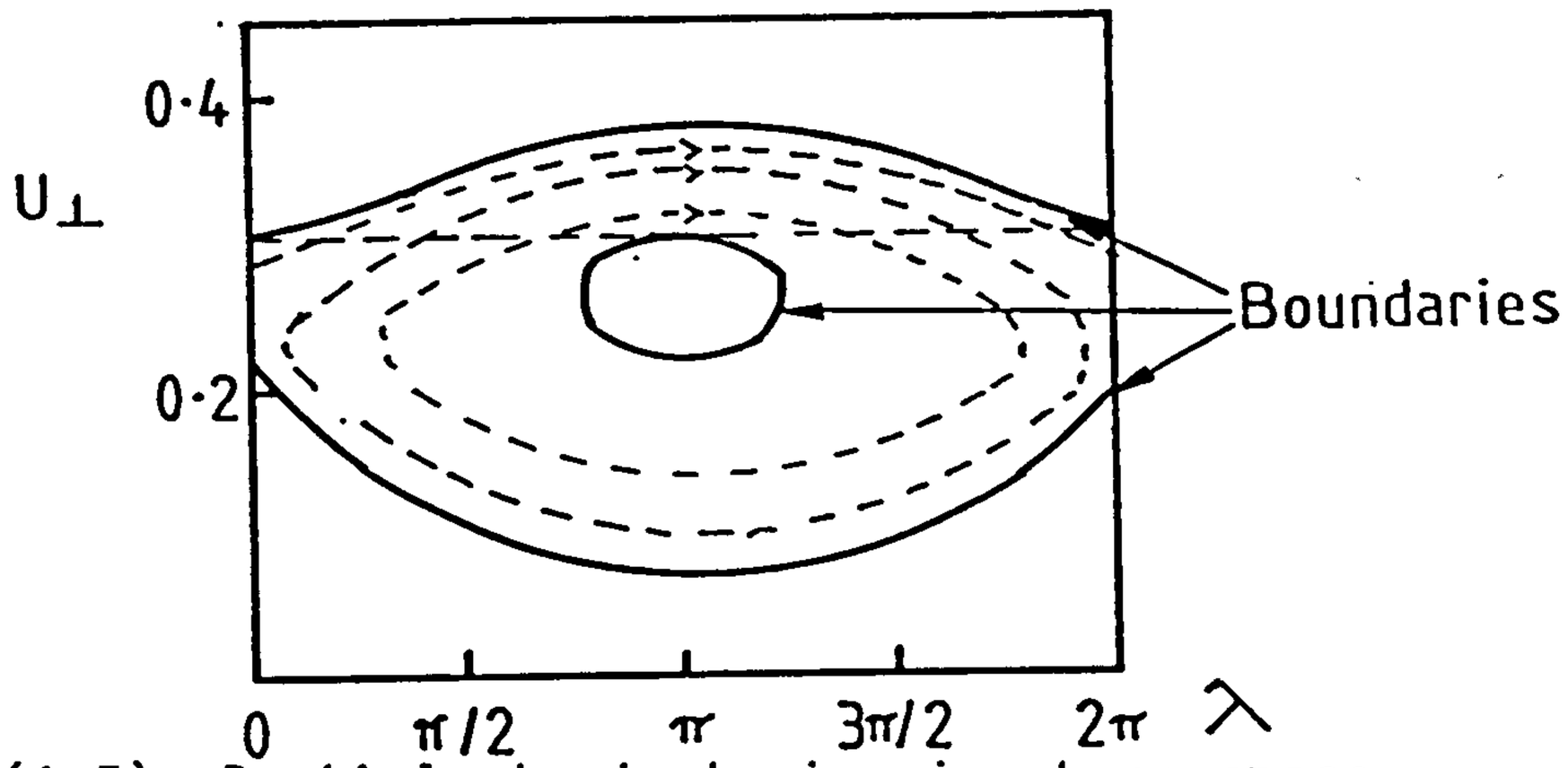


Fig.(1.3). Particle trajectories in phase space showing the boundaries of regions accessible to particles initially distributed between $0 \leq \lambda \leq 2\pi$ and with $U_\perp = U_{\perp o}$.

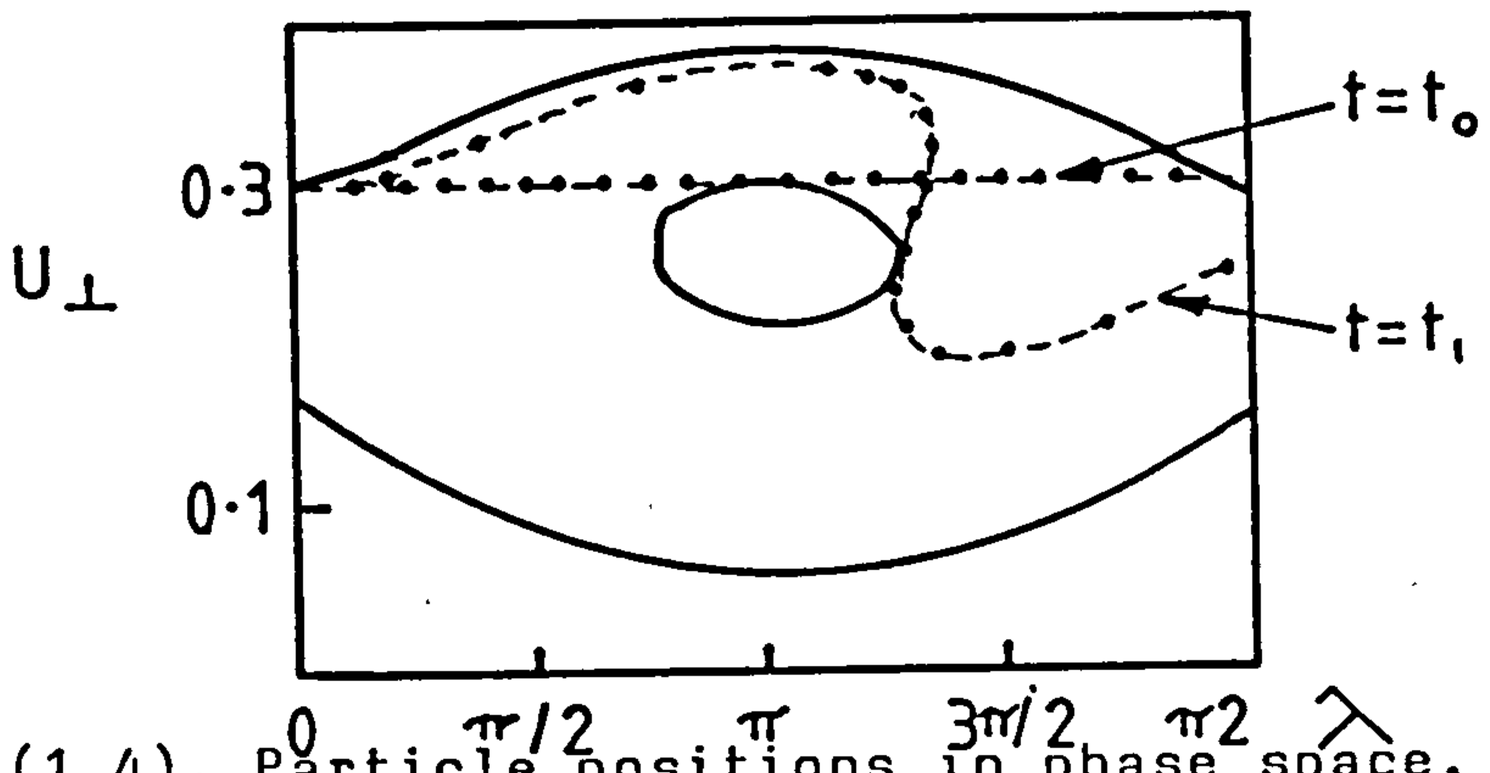


Fig.(1.4). Particle positions in phase space, t=to indicates initial conditions, $t=t_1$ indicates the onset of phase bunching.

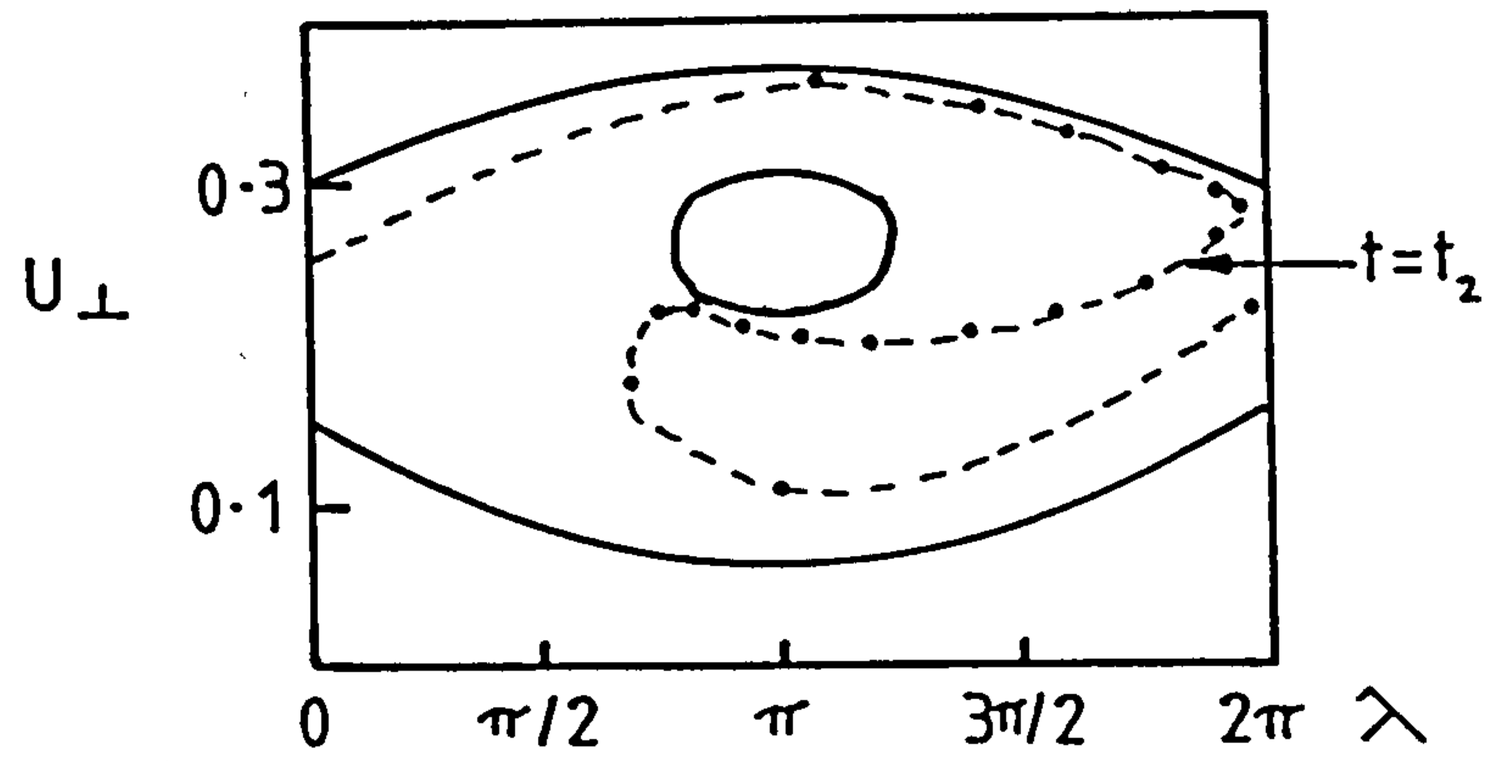


Fig.(1.5). $t=t_2$ corresponds to the particles when they have lost their maximum energy and are in a state corresponding to saturation.

bunching, $t=t_1$. This will continue until the electrons are in a position corresponding to a time $t=t_2$, fig.(1.5), and are in the lowest average energy state. This leads to the second possible saturation mechanism; phase trapping. If allowed to continue their motion in phase space the average energy of the electrons will increase at the expense of the electromagnetic wave.

Hence the non-linear theory, with the inclusion of some reasonable boundary conditions, allows the modelling of the subsequent evolution of the E.C.M. interaction.

The salient points from the above linear and non-linear theory are.

1) Only the perpendicular energy of the electrons is available to the E.C.M. interaction.
2) There also exists a critical value of $v_\perp$ below which no unstable modes exist.
3) The maser cannot oscillate at or below the cyclotron frequency.
4) From the non-linear theory the growth rate increases with $\delta\omega$ to some maximum, this will then reduce with further increase of $\delta\omega$. This is caused by the limitation of the efficiency of conversion of the beam energy into electromagnetic radiation and the limitation of the growth rate as $\delta\omega$ moves past its optimum value.
5) The above theory has provided a clear graphical description of the phase bunching of the electron beam which was hitherto assumed to be the physical mechanism of the interaction.
6) There are two completely different saturation mechanisms, free energy depletion and phase trapping.

## 1.3 Development of Strathclyde University E.C.M.

Most of the above mentioned gyrotrons have made use of the three electrode, thermionic cathode, magnetron injection gun (M.I.G.) to produce the high current relativistic electron beam, and a superconducting magnet to produce the intra-cavity magnetic

field. At Strathclyde University it has been possible to demonstrate the high power generation of mm-waves using various two electrode configurations with a field immersed, field-emission, cold cathode. The required magnetic field was generated from a pulsed, water cooled, mechanically reinforced, wound coil.

A gridded anode diode was used to generate 100kW of electromagnetic radiation in the X-band, 8.2-12.4GHz (32) (a full definition of all the μ-wave and mm-wave frequency bands, along with their designations and waveguide dimensions is given in appendix 1, table(A1.1)). With an improved field coil this was developed into the present two electrode diode configuration (33). This produced single mode oscillation in the Ka-band, 26.5-40GHz, generating a peak power of ≃1MW. This same anode-cathode configuration was subsequently operated in the W-band, 75-110GHz, with further improvements to the field coil (34,35). This resulted in the generation of .3MW at a frequency of 85GHz with the cavity oscillating in the overmoded regime.

A schematic diagram of the electrode system, cavity and field coil position is shown in fig.(1.6). Another novel aspect of the work at Strathclyde University has been the successive use of only one field coil to produce both the cavity and the cathode magnetic field. In the MIG system two coils are used, one to produce the large intra-cavity field, and a second used as a tuning coil to shape and enhance the cathode field for optimum beam position and current.

The maser was operated under the following typical conditions; the HT voltage, produced from a Marx bank generator, across the anode-cathode gap was ≃65kV resulting in explosive electron emission from the cold cathode, producing a 100A, 400ns electron beam. This interacted with a quasi-static magnetic field, continuously variable up to 4T, with a rise time of ≃120μs.

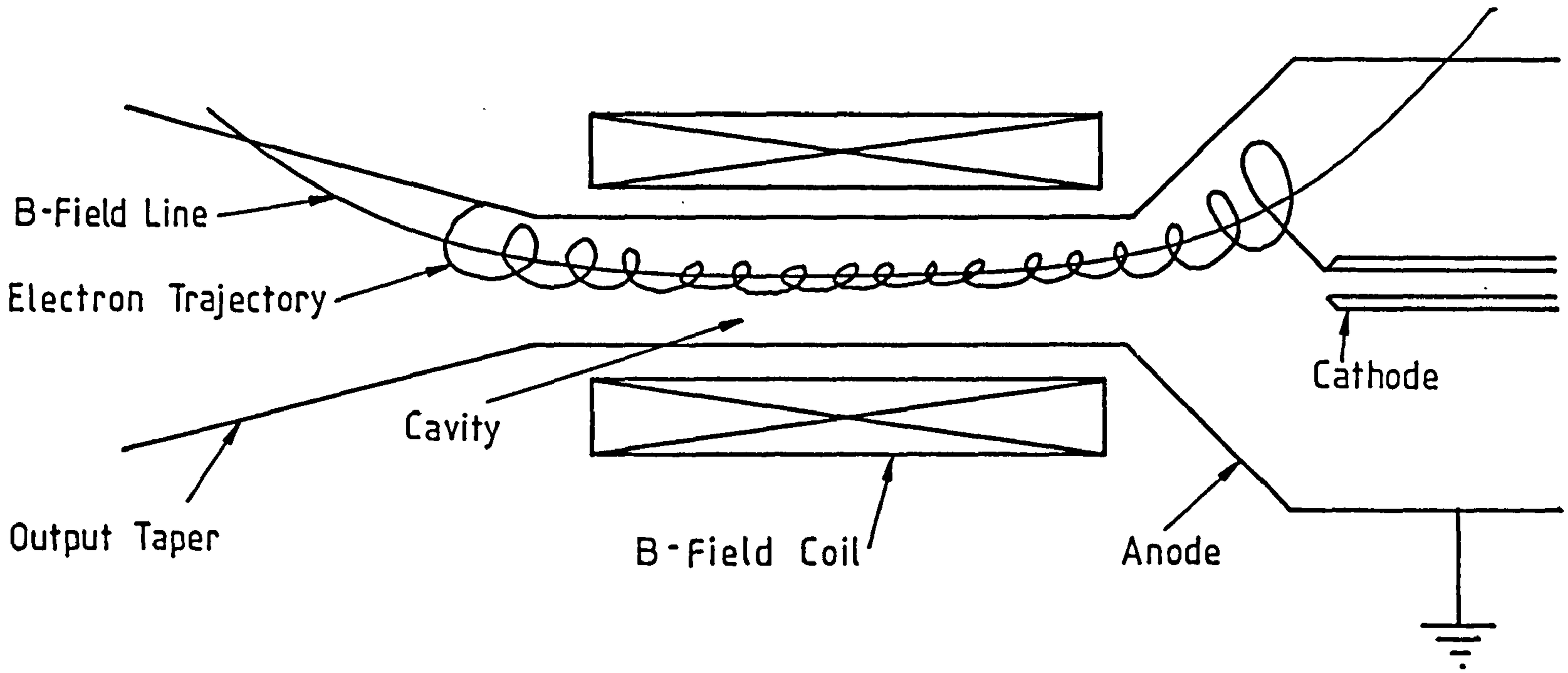


Fig.(1.6). Schematic diagram of Strathclyde University E.C.M.

## 1.4 New Developments Which form the Major Part of the Work Described in this Thesis.

For many applications, including E.C.R.H. at the fundamental plasma cyclotron frequency, high frequency, high power, gyrotron operation above 140GHz is required. It was therefore a fundamental aim of our experiments to produce radiation at 200GHz, corresponding to an intra-cavity B-field of 7.14T (for $\gamma$=1). At these frequencies the designed cavity oscillates in the over-moded regime. The cavity also operates in the W-band where single mode oscillation can be identified. The following major components of the maser were redesigned and constructed.

1) Cavity B-field production. A new cavity field coil was constructed which produced >8T and produced a uniform interaction region.
2) Cathode B-Field Production. A completely new cathode tuning coil was added to the system, this allows optimisation of the electron beam production, greatly enhancing the beam current.
3) The cavity. This was completely redesigned taking into account such features as: resonant frequencies, the relative mode density, the calculation of the ohmic and diffraction quality factors, the calculation of the output couplers' reflection coefficients, and the minimisation of mode conversion.
4) The cathode. A two electrode system was used with a cold, field-immersed, field-emission, cathode. This has been redesigned in conjunction with the cavity.
5) The output window. A completely novel output window has been developed, constructed from .15mm thickness Mylar. This results in no measurable attenuation of the mm-waves.

Along with the redesigned maser the following significant improvements have also been made in the control, operation and diagnostics used on the maser.

1) For the first time full control of the experiment, including monitoring, operation and data aquisition and manipulation,

were completely performed by an HP9816 personal computer via extensive use of peripherals.

2) A new diffraction grating optimised for 200GHz was designed for use in the present spectrometer.

3) A completely new method has been developed for measuring the radiation pattern from the output horn. This facilitates the identification of the mode oscillating in the cavity. This also incorporates a novel two detector system, the first used to measure the relative radiation intensity across the output window and the second producing a reference by which the fluctuating output power of the maser may be monitored.

4) A witness plate beam probe was also constructed, primarily to measure the relativistic electron beam current. This is also used to determine the position of the beam in the cavity and estimate the relative magnitude of the beam current while altering various parameters of the maser.

5) A successful attempt was then made to produce a completely self-consistent analysis of the cyclotron frequency of the electron beam and the measured frequency and mode of oscillation of the cavity. The first two parameters were linked via the measured cavity magnetic field and the predicted frequency up-shift. The mode of oscillation was determined from the mode dependent quality factor and the measured spatial coupling of the relativistic electron beam in conjunction with the calculated intra-cavity E-field maxima.

# CHAPTER -2-

## DESIGN AND CONSTRUCTION OF THE Mk-6 E.C.M.

## 2.1 Introduction

This chapter describes the design considerations, relevant theory, and the construction of the MK-6 E.C.M.

This includes the design and construction of the cavity magnetic field coil, coil#1. This produced more than 8T and had a flat spatial profile over a reasonable interaction region within the cavity, ≈10cm. A second tuning coil, coil#2, was also constructed and placed around the cathode. This was capable of producing 1.0T at the cathode tip, enhancing and optimising the cathode B-field. This played an important role in the production of the relativistic electron beam.

A cavity resonant at 200GHz was produced, this was capable of oscillating under single mode conditions at 100GHz, and overmoded operation at 200GHz. Due to the low conductivity of the cavity construction material there were large ohmic losses in the cavity walls. This minimises the B-field exclusion and discriminates towards the $TE_{0n}$ modes, because of the high losses of the whispering gallery modes. The cavity has a very low reflectance, low mode conversion output coupler.

The production of the mildly relativistic electron beam, from a field-immersed field-emission cold cathode, is also described. The HT voltage was produced from a Marx bank generator.

## 2.2 Design and Construction of Magnetic field coils.

Previous experiments at Strathclyde University have used one field coil to produce both the cavity magnetic field and the cathode electron beam focusing field. As with many gyrotron systems a two coil configuration was used on the Mk-6 E.C.M. This comprises an intracavity field coil#1 and a cathode tuning coil#2.

This configuration improves the system in three ways.

1) It increased the magnitude of the B-field at the cathode thus increasing the magnetic insulation of the diode. This ensured more electrons were trapped onto field lines, with fewer electrons striking the anode before they entered the cavity.

2) The magnetic field compression ratio, defined as the ratio of the cavity field to the cathode field, was reduced. This helped prevent electrons mirroring as they moved to regions of higher field.

3) The cathode coil resulted in enhanced focusing of the relativistic electron beam, producing a well collimated stream of electrons through the centre of the cavity.

Cavity Field Coil#1.

As previously described the electrons gyrate at a frequency given by,

$$\omega_{ce} = \frac{e\ B}{\gamma\ m_0} . \qquad (2.1)$$

To first order this may be used to relate a particular B-field to any output frequency of the E.C.M. Thus,

$$\frac{\omega}{2\pi} = \frac{28}{\gamma}\ \frac{B}{T}\ \text{GHz}. \qquad (2.2)$$

(N.B. $e/m_0$=176 GHz $T^{-1}$)

To achieve oscillation at 200GHz, for $\gamma$=1, a B-field of 7.14T was required. As the field coil was pulsed and placed around a conducting stainless steel cavity, there was approximately 10% field exclusion (34). Coil#1 was therefore designed to produce 10T to allow for this, and any other losses which may arise in the circuit.

Cathode Field Coil#2.

This coil was used in a purely empirical way. The coil was designed to produce 1.5T, which after field exclusion and resistive losses in the coil circuit, resulted in a field of 1.0T at the cathode tip.

Field Coil Theory.

The B-field produced by a solenoidal coil is given by the simple 'on-axis' expression,

$$B = \frac{\mu_0 \, n \, I}{2} \left( \cos \varphi_1 - \cos \varphi_2 \right). \qquad (2.3)$$

Where,

n = number of turns per unit length,

I = the current through the coil windings,

and $\varphi_1$, $\varphi_2$ are defined in fig.(2.1).

The constructed coils were placed in the simplified circuit shown in fig.(2.2). This circuit may be analysed using the following expression (36),

$$\frac{d\,I}{d\,t} + \frac{R\,I}{L} + \frac{Q}{L\,C} = 0, \qquad (2.4)$$

with the boundary conditions I=0 and $Q_0=CV_0$, at time t=0. L may be evaluated from (37),

$$L = a_1 \, N \, \chi \left[ a_1, \frac{2\,l}{a_1} \right]. \qquad (2.5)$$

Where,

$a_1$ = internal radius of the coil,

N = total number of turns,

l = length of the coil,

$\chi$ = geometric constant dependent on $a_1$ and l.

Using eqns.(2.3),(2.4) and (2.5) it was thus possible to gain a

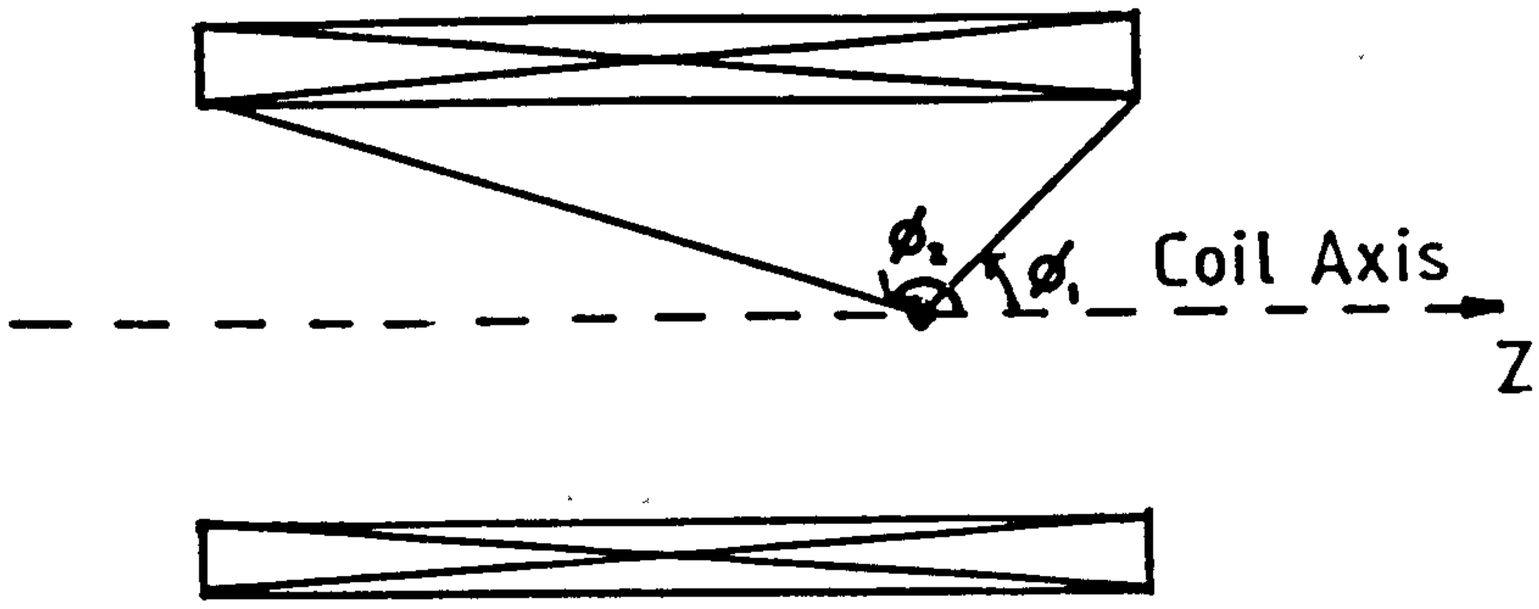


Fig.(2.1). B-field coil, defining parameters used in "on axis" field expression.

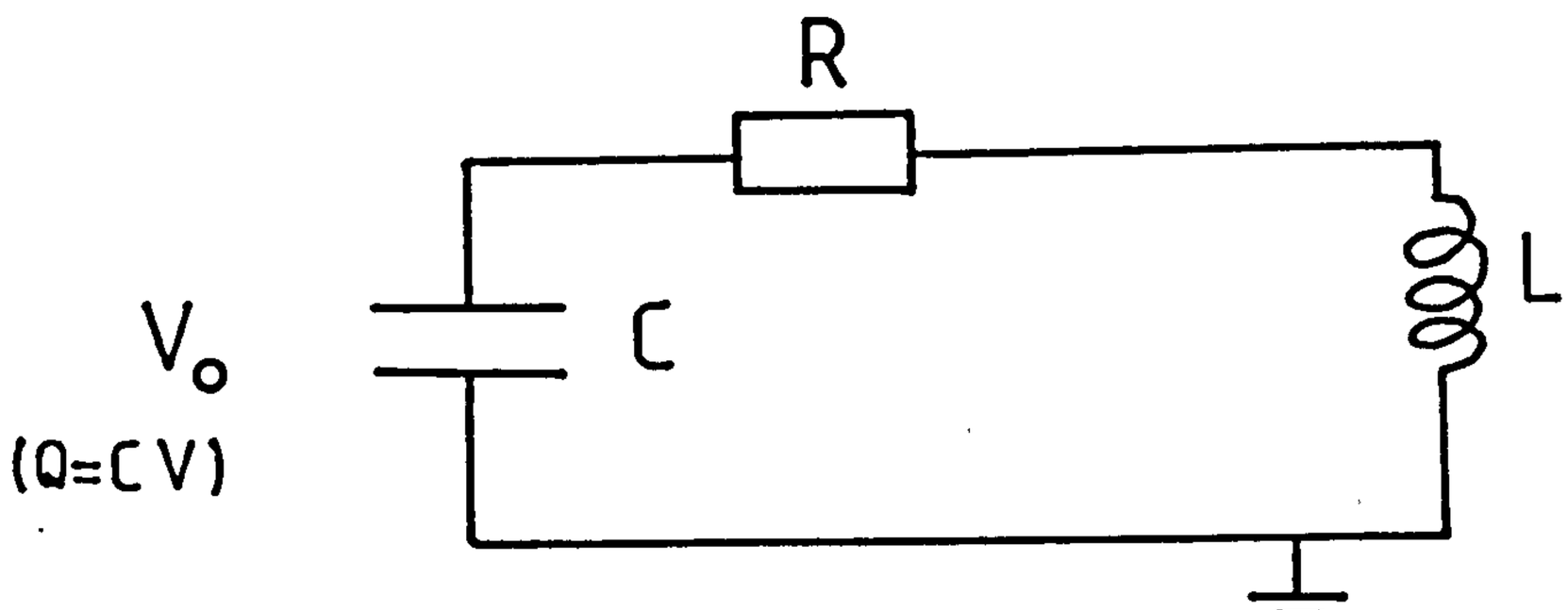


Fig.(2.2). Schematic diagram of coil circuit.

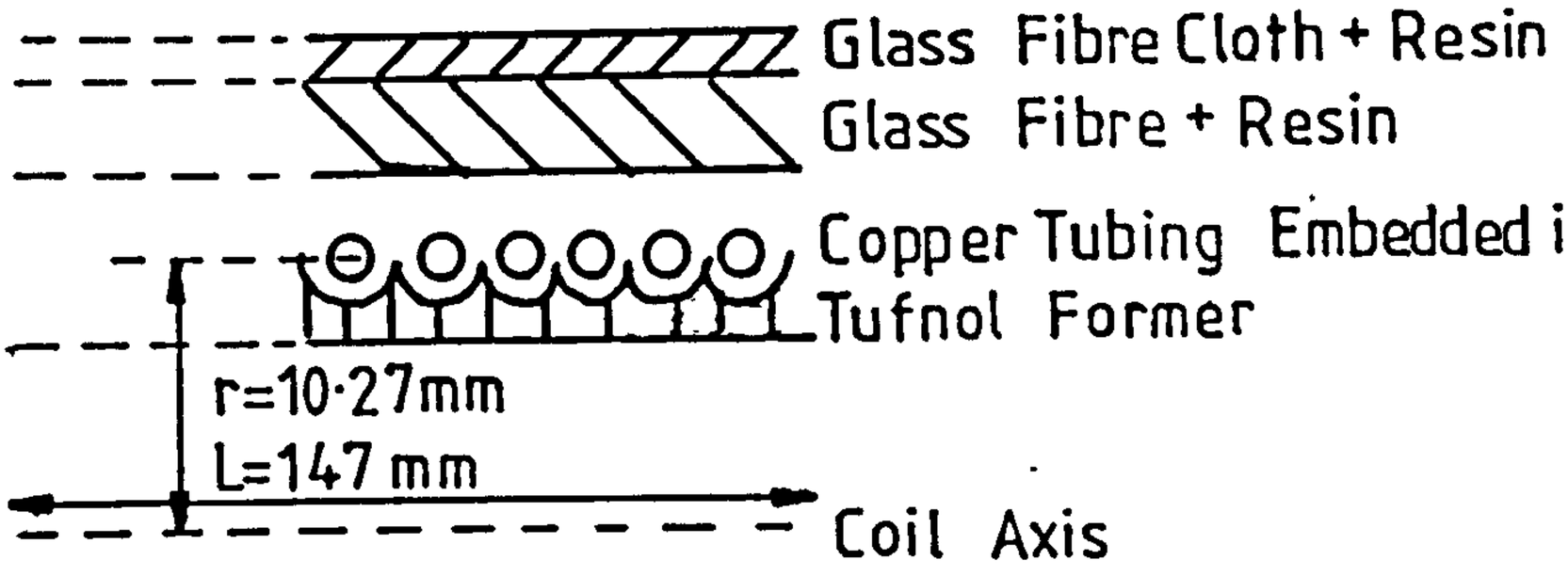


Fig.(2.3). B-field coil#1, construction and dimensions.

self-consistent analysis of the current flowing in the circuit w.r.t. time and hence predict the maximum magnetic field produced by any coil design. Before deciding on values for R, N and L the following physical constraints were taken into account.

1) The main aim of this system was to transfer as efficiently as possible the energy stored in the capacitor bank $E_C=1/2\ CV^2$, into stored B-field energy in the coil (38),

$$E_l = \frac{1}{2} L I^2 = \frac{1}{2\ \mu_0} \int_V B^2 dV, \qquad (2.6)$$

hence the smaller the coil volume the larger the B-field produced.

2) $a_1$ was limited to being larger than the cavity radius plus the coil former thickness.

3) l had to be large enough to produce a uniform B-field over a reasonable length in the case of the cavity field coil.

4) Due to the very high currents involved, >20kA, the coil had to be water cooled to avoid temperature rise between one pulse and the next. It was therefore wound using the smallest diameter copper tubing available, thus determining the maximum value of n.

5) As the particular capacitors used would not withstand having their polarity reversed, it was essential to ensure the circuit was properly damped. This imposes the restriction,

$$\frac{R^2\ C}{4\ L} \geq 1, \qquad (2.7)$$

which ensures the circuit will not oscillate.

Coil Parameters.

As a result of all these considerations the following optimum parameters were arrived at for the main coil (coil#1) and the cathode coil (coil#2).

| | Coil#1 | Coil#2 |
|---|---|---|
| wire diameter | 2.37 mm | 2.37 mm |
| mean coil radius | 10.27 mm | 42.87 mm |
| coil length | 147 mm | 63 mm |
| no. of turns | 55 | 21 |
| coil inductance | 8.08 μH | 27.19 μH |
| circuit resistance | 200 mΩ | 305 mΩ |
| circuit capacitance | .106 mF | 1.68 mF |

Table(2.1). Respective field coil parameters.

Coil Construction.

When producing such B-fields the coil experiences extremely large physical forces. To calculate the exact stress depends on the coil configuration, however an estimate may be gained by considering the magnetic field pressure,

$$P_f = \frac{1}{2\,\mu_0} ( B_1^2 - B_2^2 ). \qquad (2.8)$$

Where $B_1$ and $B_2$ are the respective magnetic fields across some boundary.

If the coil is long compared with its radius then the field outside the coil will be small, hence $B_1 \simeq 8T$ and $B_2 \simeq 0T$, giving a magnetic field pressure of approximately 260 Atmospheres.

With the geometrical factors and impulsive forces it would be difficult to calculate the yield point of the conductors and insulators used in the construction of the magnetic field coil.

The amount of mechanical reinforcement required was therefore gained from previous experience of pulsed coils constructed at Strathclyde University. The construction of coil#1 is shown in fig.(2.3). The copper tubing windings were wound on a Tufnol former and then embedded in Araldite. Around this was built a layer of epoxy resin with embedded glass fibre and then glass fibre cloth.

The cathode coil construction was of a slightly simpler design, as the magnetic field forces were significantly reduced (pressure$\propto B^2$). The coil former was made from glass fibre cloth embedded in epoxy resin. The windings were again copper tubing embedded in Araldite. On top of this a layer of glass fibre cloth and resin was built up.

Coil Circuit Triggering.

Two different methods were used to trigger the B-field circuits. Coil#2 was triggered via a compressed air driven mechanical switch. This is controlled directly from the screened room and initiates the entire firing sequence of the maser.

Coil#1 was fired electronically by an ignitron switch. Using a delay circuit, coil#1 may then be triggered after a predetermined time following the initiation of the coil#2 current

Coil Circuit Diagrams.

Both of these coils were placed in the circuits shown in fig.(2.4).

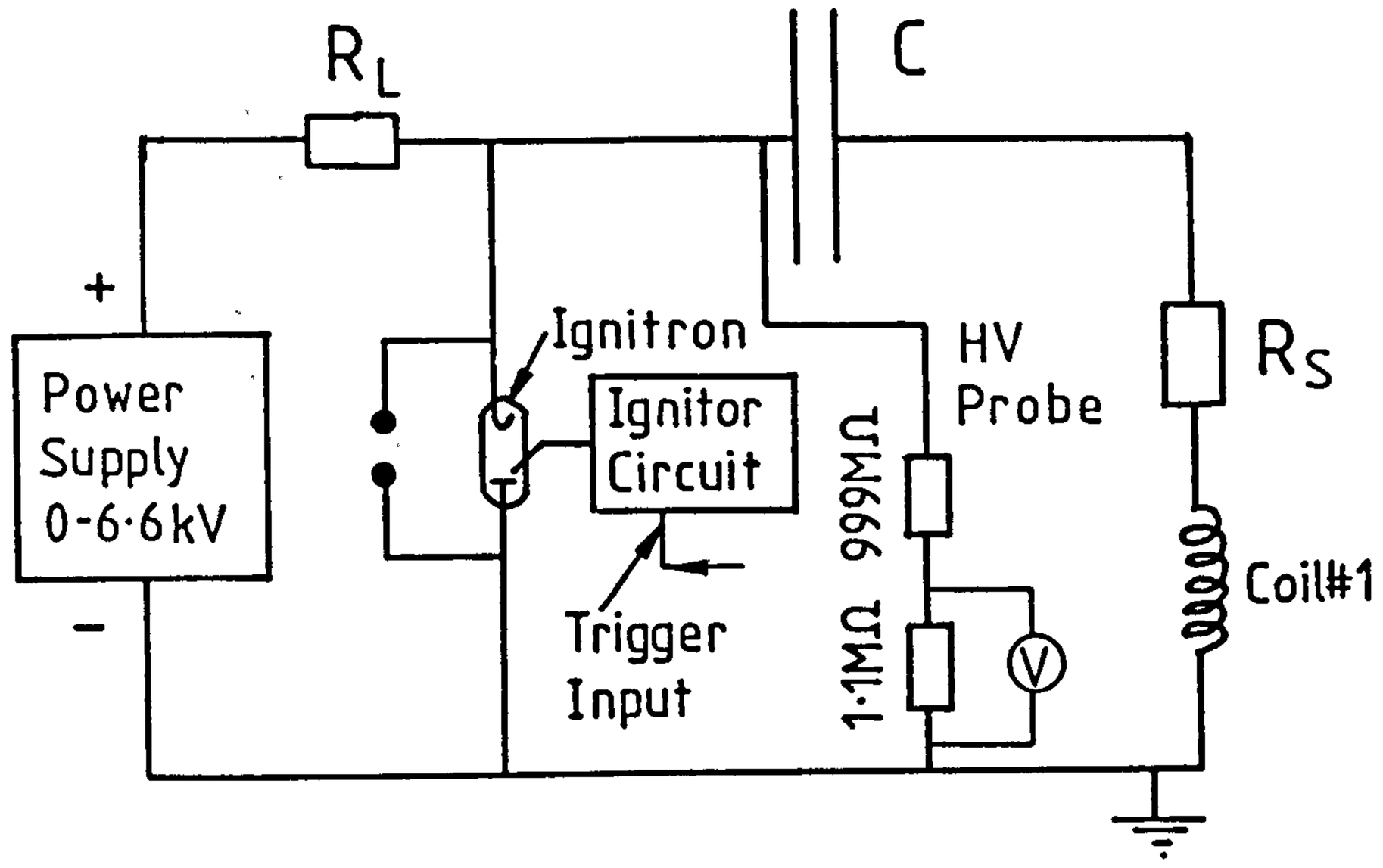


a)

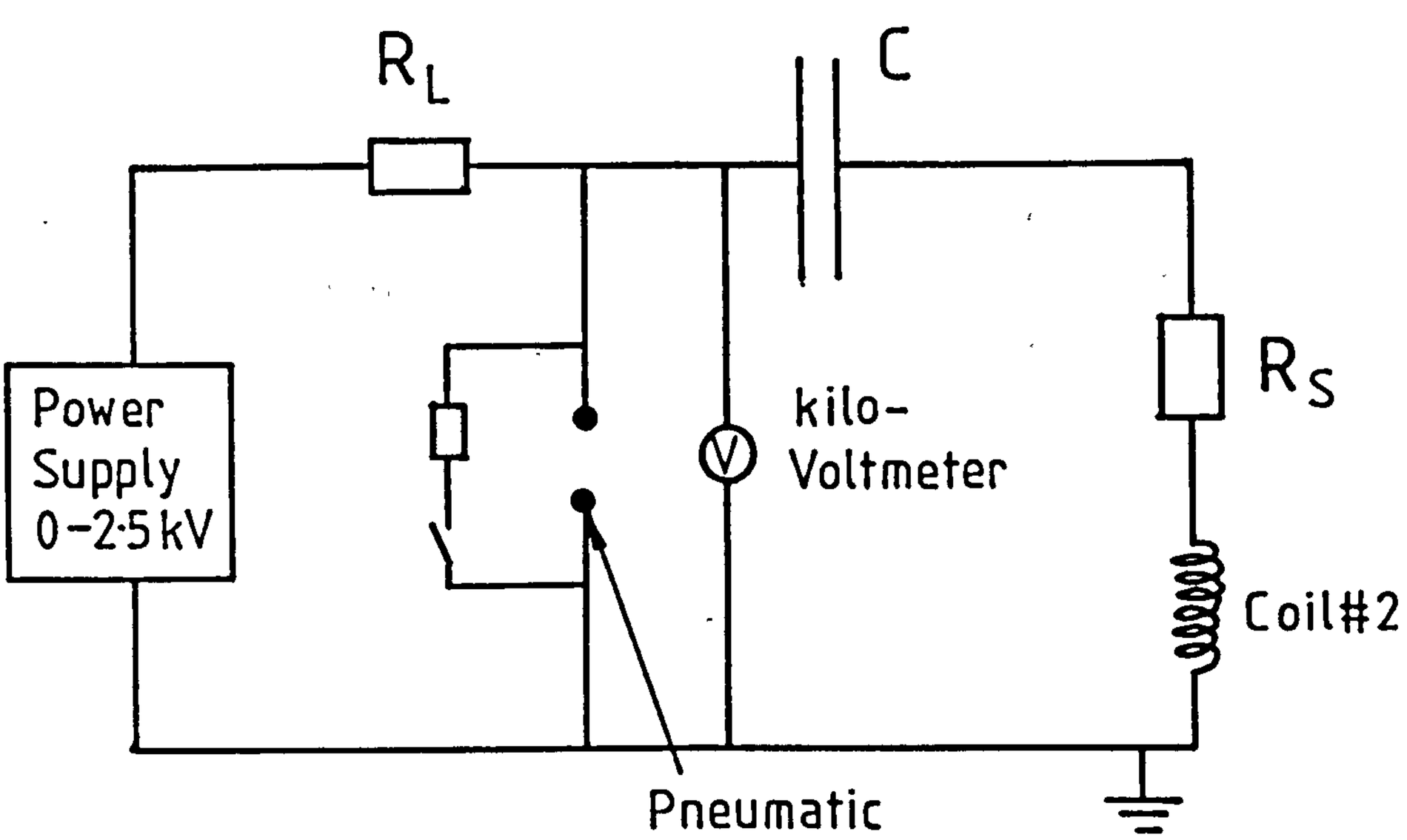


b)

Fig.(2.4). Magnetic field coil circuit diagrams.
a) Coil#1, b) Coil#2.

## 2.3 The E.C.M. Cavity

In designing the maser cavity several different considerations were taken into account.

1) Construction material.
2) Resonant frequencies of the cavity oscillation.
3) Cavity quality factor.
4) Reflection coefficients, mode conversion and output coupling.

### Cavity Theory and Design Considerations.

### Construction Material.

In past experiments at Strathclyde University, cavities have been constructed from stainless steel. This possesses two important characteristics.

1) The relatively low electrical conductivity of stainless steel, $\sigma=1.39\times10^{6}\Omega^{-1}m^{-1}$, will result in large losses in the cavity walls due to ohmic heating, reducing the overall efficiency of the maser. These ohmic losses will be mode dependent and discriminate against modes with large E-fields near the cavity wall (i.e. whispering gallery modes). The cavity will thus discriminate towards the $TE_{0n}$ modes.
2) The skin depth of the cavity walls is inversely proportional to the square root of the electrical conductivity. A low electrical conductivity will therefore minimise the B-field exclusion, allowing the pulsed magnetic field to penetrate the cavity walls.

Stainless steel will also have the mechanical strength to withstand both the atmospheric pressure, as the cavity will form part of the vacuum vessel, and the magnetic pressure, due to the B-field exclusion.

Resonant Frequencies.

The E.C.M. mechanism is predominantly concerned with the $TE_{pqs}$ modes. (In the mode designation; the first subscript indicates the number of full-period variations of radial component of field along angular co-ordinates, the second subscript the number of half-period variations of angular component of field along radial co-ordinates, and the third subscript the mumber of half-period variations of field along longitudinal co-ordinates). In the case of the $TE_{pqs}$ modes the electric field is parallel to the motion of the electrons, producing a strong interaction of the type described in chapter 1. Conversely for the $TM_{pqs}$ modes the electric field is perpendicular to the motion of the electrons and will thus experience less gain (39).

It may be shown from Maxwell's equations that the resonant frequency of a $TE_{pqs}$ mode is given by (40),

$$k_{\perp}^{2} = \omega^{2} \mu_{0} \varepsilon_{0} = \frac{\chi'^{2}_{pq}}{a^{2}} + \frac{s^{2} \pi^{2}}{l^{2}} . \qquad (2.10)$$
$$c$$

Where,

$a$ = the cavity radius,

$l_c$ = the length of the cavity,

$\chi'_{pq}$ = the $q^{th}$ root of $J_p'(x) = 0$,

$k_{\perp}$ = the perpendicular wave number within the cavity.

It is generally assumed that the electron beam will only interact with the $TE_{pq1}$ modes within the cavity. Many authors have shown that the critical starting currents increase dramatically with increasing longitudinal index, s (12,41). It is possible to understand this phenomenon by considering the gyrating electron beam interacting with a $TE_{pq2}$ mode. As the electrons gyrate through the cavity in phase with the standing wave, midway through the cavity the phases of the electrons must change by $\pi$. This obviously imposes a very strict restriction on the motion of the electrons. This condition will become even more severe for

s=3,4,5,... etc.

Reflection coefficients.

The reflection coefficients of the output couplers were calculated to determine the optimum taper angle. This influences the resonant characteristics of the cavity, the cavity Q and mode conversion in the output taper.

Considering the changing impedance as seen by a travelling wave through a taper, and the coupled wave eqns. relating a forward and backward travelling wave, with a reflection coefficient $\delta(z)$, it is possible to obtain the total reflection coefficient of an electromagnetic wave. This is given by, (40,42),

$$r = -\frac{1}{2}\left[\frac{j\,\lambda_0}{4\,\pi}\right]^u \left[\frac{\dfrac{d^u a_0}{dz^u}}{a_0\left[1-\dfrac{\chi^2}{a_0^2}\right]^v} - \frac{e^{2jJ}\cdot\dfrac{d^u a_1}{dz^u}}{a_1\left[1-\dfrac{\chi^2}{a_1^2}\right]^v}\right]. \qquad (2.11)$$

Where,

$j$ = the square root of -1,

$r$ = the amplitude reflection coefficient,

$\lambda_0$ = the free space wavelength of the radiation,

$\dfrac{d^u a}{dz^u}$ = the first non-vanishing derivative of a,

$\chi = \dfrac{\chi'_{pq}}{k_0}$, $\chi'_{pq}$ = $q^{th}$ root of $J'_p(x)=0$,

$k_0$ = the free space wavenumber of the radiation,

$J = \int_0^{z_0} k_{\parallel} dz$, $k_{\parallel} = (k_0^2 - k_{\perp}^2)^{1/2} = \dfrac{2\pi}{\lambda_0}\left[1-\dfrac{\chi^2}{a^2}\right]^{1/2}$,

$k_{\perp} a = \chi'_{pq}$, $v = 1 + \dfrac{u}{2}$,

and $a_0$, $a_1$, $z_0$ and $z_1$ are defined in fig.(2.5)

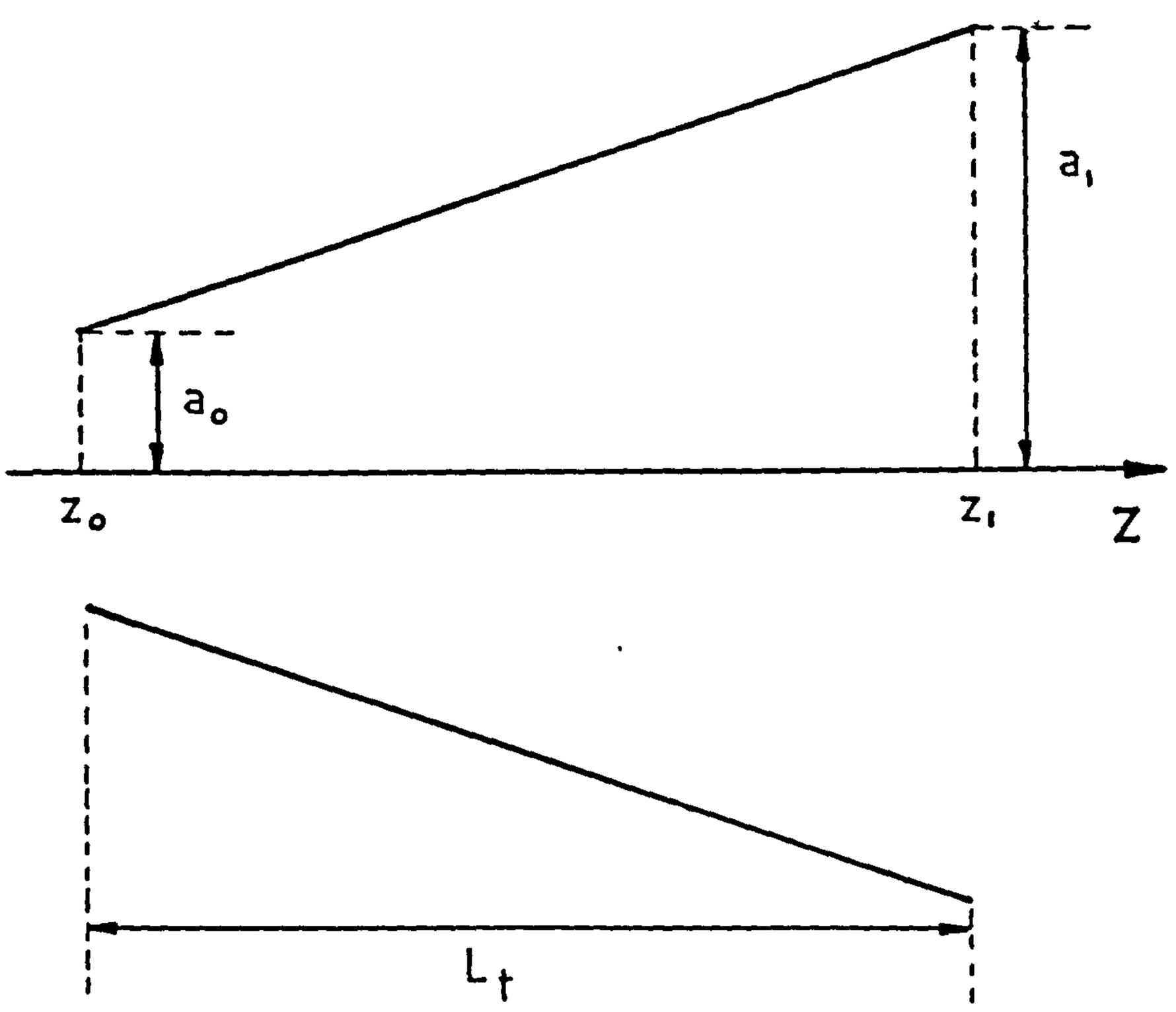


Fig.(2.5). Definition of taper parameters.

This expression was used to calculate the reflection coefficients of the respective output tapers as described in Appendix 2.

Reflection Coefficient from Step Discontinutiy.

The reflection coefficients from the output tapers were shown to be small, this results in equal amounts of energy being coupled out of both ends of the cavity, therefore only half the generated electromagnetic energy appears as useful energy. To increase the reflections from the cathode end of the cavity an abrupt change of diameter was introduced. A qualitative estimate of the reflection coefficients from the discontinuity in the cylindrical cavity may be gained from the following theory, (40).

Here the reflection coefficient from a step discontinuity in a rectangular waveguide, fig.(2.6), is calculated. In this derivation the discontinuity is not assumed small and yields a result for an incident and transmitted $TE_{10}$ mode,

$$r = \frac{4\, k_{\parallel}\, J_{11}^{2} - k_{\parallel}'\, a\, d}{4\, k_{\parallel}\, J_{11}^{2} + k_{\parallel}'\, a\, d} \,. \qquad (2.12)$$

Where,

$$k_{\parallel} = \left[ k_0^2 - \frac{p^2\pi^2}{a^2} - \frac{q^2\pi^2}{a^2} \right], \qquad (2.13)$$

$$k_{\parallel}' = \left[ k_0^2 - \frac{p^2\pi^2}{d^2} - \frac{q^2\pi^2}{d^2} \right], \qquad (2.14)$$

with a and d defined in fig.(2.6). $k_{\parallel}$ and $k_{\parallel}'$ correspond to the axial wavenumbers in the respective sections of the waveguide and,

$$J_{pq} = (-1)^{q}\, \frac{q}{\pi\, d} \cdot \frac{a^2\, d^2}{p^2 d^2 - q^2 a^2} \cdot \mathrm{Sin} \left[ \frac{p\, \pi\, d}{a} \right]. \qquad (2.15)$$

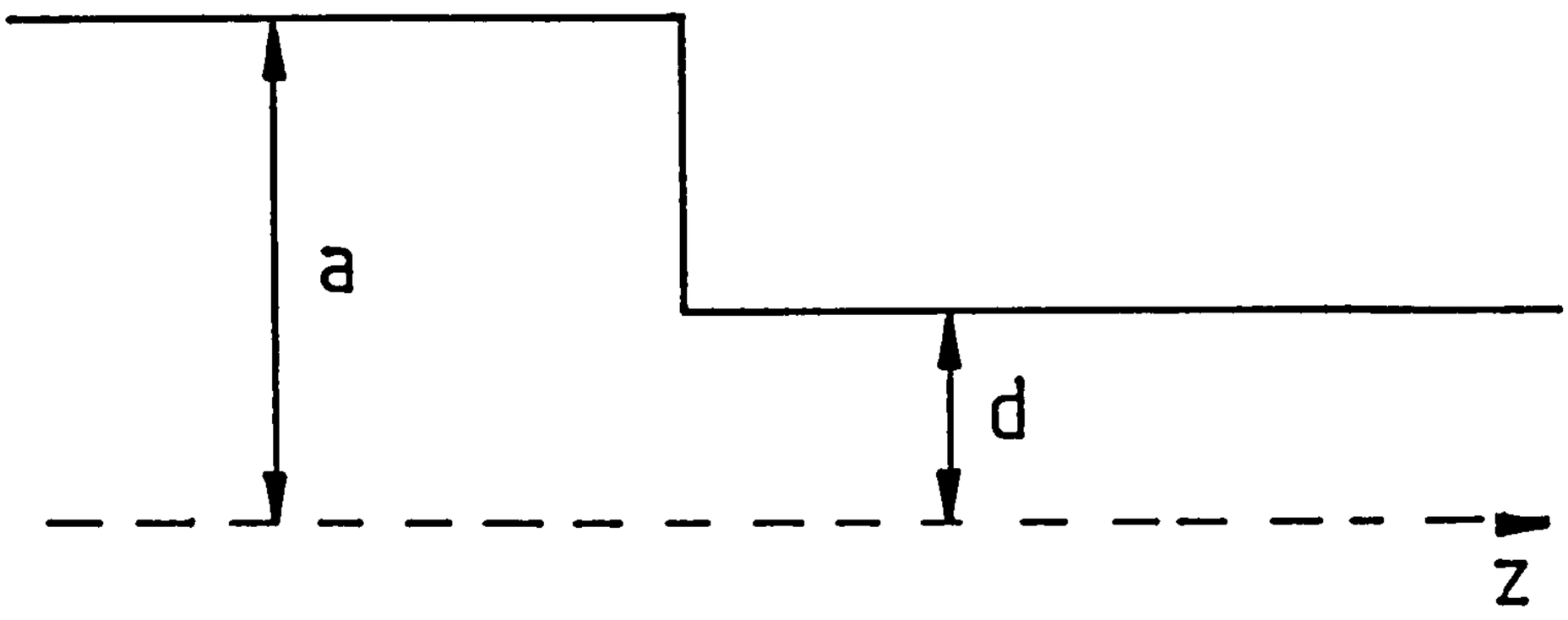


Fig.(2.6). H-plane of a rectangular waveguide with a step discontinuity.

The Cavity Quality Factor and Differential Mode Excitation.

The cavity quality factor is defined as (43),

$$Q_T = \omega \times \frac{\text{field energy stored by the resonator}}{\text{power dissipated by the resonator}} . \qquad (2.16)$$

This $Q_T$ may also be defined in more useful terms by the mode dependent ohmic quality factor $Q_\Omega$, and the diffraction quality factor $Q_D$ (12), where,

$$\frac{1}{Q_T} = \frac{1}{Q_\Omega} + \frac{1}{Q_D} . \qquad (2.17)$$

$Q_\Omega$ is defined as,

$$Q_\Omega = \omega \times \frac{\text{field energy stored by the resonator}}{\text{power dissipated in the cavity walls}} . \qquad (2.18)$$

For $TE_{pqs}$ modes in a cylindrical cavity this may be shown to be (40),

$$Q_\Omega = \frac{V_0 \ (2\omega\mu_0\sigma)^{1/2} \ \omega^2\epsilon_0\mu_0 \ \left[ 1 - \frac{p^2}{k^2 \ a^2} \right]}{\pi \left[ k^2 l_c a + \frac{2\pi^2 s^2 a^2}{l_c^2} + \frac{\pi^2 p^2 s^2}{k^2 a^2 l_c^2} (l_c - 2a) \right]} . \qquad (2.19)$$

Where,

$l_c$= length of the cavity,

a = diameter of the cavity,

$V_0$= volume of the cavity,

$\sigma$ = electrical conductivity of the cavity walls,

$ka = \chi'_{pq}$, the $q^{th}$ root of $J'_p(x)=0$.

$Q_D$ is defined as (12),

$$Q_D = \omega \times \frac{\text{field energy stored by the resonator}}{\text{radiated power output}}, \qquad (2.20)$$

which for a cavity resonator may be shown to be,

$$Q_D = \frac{4\pi \left[ \frac{l_c}{\lambda_0} \right]^2}{\left[1 - | R_1 R_2 |\right]}. \qquad (2.21)$$

Where,

$\lambda_0$ = the free space wavelength of the radiation,

and $R_1$ and $R_2$ are the intensity reflection amplitudes respectively at either end of the cavity.

In all calculations involving $Q_\Omega$, $\sigma$ has been taken to be the bulk conductivity of stainless steel ($1.39 \times 10^6 \Omega^{-1} m^{-1}$). However the following physical constraints have an influence on the value of $\sigma$, and hence on $Q_\Omega$.

1) At frequencies in the region of 100GHz the effective skin depth of stainless steel is $\simeq 3\mu m$. As the inner surface of the cavity is not polished, this value is comparable with the surface irregularities. These irregularities increase the path length of the electron current and hence reduce the effective value of $\sigma$.
2) As the cavity experiences large magnetic pressures, due to magnetic field exclusion, the cavity will experience considerable stress, which can also influence the value of $\sigma$.
3) Finally the value of $\sigma$ will be a function of the surface composition of the stainless steel, which may well vary with position.

Coupled with these physical considerations any asymmetries in the cavity will lead to the excitation of higher order modes. These in turn can produce additional ohmic losses due to increased

electric fields at the cavity walls. The result is again a reduction in the idealised calculated $Q_\Omega$. Therefore the values of $Q_\Omega$ which have been calculated should be regarded as theoretical upper limits. In practice the actual values of $Q_\Omega$ would be expected to be lower.

In any given cavity the smaller of $Q_\Omega$ or $Q_D$ will dominate. It is desirable to couple out more energy than is dissipated in the cavity walls, hence for an efficient system one requires $Q_D \ll Q_\Omega$.

These parameters will be important when considering the efficiency of an E.C.M. system (12). This may be expressed as,

$$\eta_T = \eta_{el} \eta_\perp \eta_Q . \qquad (2.22)$$

The first term, $\eta_{el}$, depends on the coupling between the perpendicular motion of the electron beam and the perpendicular E-field of a particular $TE_{pqs}$ mode. This will be dealt with in chapter 6. Only the transverse energy of the electrons is available to the E.C.M. interaction and thus $\eta_\perp$ is related to $v_\parallel / v_\perp$.

The final term is derived purely from the mode dependent quality factor and is defined by,

$$\eta_Q = 1 - \frac{Q_T}{Q_\Omega} = \frac{Q_\Omega}{Q_D + Q_\Omega} . \qquad (2.23)$$

It is therefore possible to quantify the ohmic losses in the cavity. Using the quality factor in conjunction with eqn.(2.23), it will be possible to predict which cavity modes will be preferentially excited for any given B-field. These will depend upon:

1) The cyclotron frequency of the electrons.
2) The resonant frequency of the respective modes.
3) The measured spatial coupling between the electron beam and the spatial maxima of the intracavity radiation, $\eta_{el}$.
4) Their respective quality factor values.

Mk-6 Cavity Design.

To gain preferential mode excitation and to minimise B-field exclusion stainless steel tubing was used in the construction of the maser.

A suite of programs was produced (to run on an HP9816 personal computer) which would calculate:

1) The resonant frequencies eqn.(2.10), the ohmic quality factors eqn.(2.19) and the diffraction quality factors eqn.(2.22), of the first 80 modes oscillating in a cylindrical cavity of any diameter, length and electrical conductivity of the construction material.

2) The reflection coefficient of any linear taper and step discontinuity used in conjunction with the cavity.

This allowed the determination of the following optimum parameters.

Cavity Diameter.

With increasing order, the frequency separation of each mode is reduced. If the inter mode frequency spacing is larger than the gain bandwidth of the E.C.M. interaction, then only the mode whose frequency lies under the gain line curve will experience gain. If ≤5 modes lie under the gain line curve it still may be possible to achieve single mode oscillation. If a $TE_{0n}$ mode is surrounded by whispering gallery modes and if from quality factor and beam coupling considerations these modes have prohibitive losses then all the electron beam energy will be fed into the $TE_{0n}$ mode.

It is therefore not necessary to construct a cavity which will oscillate in the fundamental mode to achieve single mode oscillation. A system operating in the fundamental mode has two distinct disadvantages.

1) It is not tunable.
2) Its power handling is reduced.

Moving to a higher frequency where there are >5 modes under the gain line curve it will become very difficult to find a group where at least two will not have low enough losses to oscillate.

To allow the study of the two distinct operating regimes mentioned above, firstly where single mode oscillation may be gained through surrounding mode suppression and secondly in the grossly overmoded regime, a cavity diameter of 10.3mm was chosen. It is expected that the maser will have a gain bandwidth of ≤10GHz. Fig.(2.7) shows the resonant frequencies of the relevant $TE_{pqs}$ modes. This demonstrates clearly the bunching of higher order modes and the possibility of single mode oscillation in the W-band (75-110GHz) and multimode operation in the G-band (150-220GHz).

Fig.(2.8) and (2.9) lists the ohmic and diffraction quality factors for the above cavity modes. As expected the cavity quality factor is dominated by the highly mode dependent $Q_\Omega$ with $Q_D \simeq 10 \times Q_\Omega$.

Cavity Length.

The effective length of the cavity is assumed to be from the small bevel at the input end of the cavity, fig.(2.12), to the end of the magnetic field coil. At this point the magnetic field is decreasing along with the gyration frequency of the electrons. This produces an impedance mismatch and defines the end of the interaction region (44).

From the coil design this will result in a cavity length of approximately 150mm. This is ≃5-10 times too long c.f. eqn.(1.3) and (2.22). This will reduce the efficiency of the system by allowing the interaction between the cavity mode and the electromagnetic wave to continue over an extended region. However previous experiments at Strathclyde have shown that useful amounts of energy may be gained from such a system.

CYLINDRICAL CAVITY
MK-6

RADIUS OF CAVITY/MM = 5.1500 LENGTH OF CAVITY/MM = 150.0000

| TE MODE (p,q,s) | | CUT-OFF | RESONANCE FREQUENCIES/GHZ | | | | |
|---|---|---|---|---|---|---|---|
| p | q | FREQ/GHZ | s=1 | s=2 | s=3 | s=4 | s=5 |
| 1 | 1 | 17.0699 | 17.0991 | 17.1866 | 17.3315 | 17.5323 | 17.7871 |
| 2 | 1 | 28.3164 | 28.3340 | 28.3869 | 28.4748 | 28.5975 | 28.7544 |
| 0 | 1 | 35.5244 | 35.5384 | 35.5806 | 35.6508 | 35.7489 | 35.8745 |
| 3 | 1 | 38.9499 | 38.9627 | 39.0012 | 39.0653 | 39.1548 | 39.2695 |
| 4 | 1 | 49.2999 | 49.3100 | 49.3404 | 49.3911 | 49.4619 | 49.5528 |
| 1 | 2 | 49.4286 | 49.4388 | 49.4691 | 49.5196 | 49.5902 | 49.6809 |
| 5 | 1 | 59.4803 | 59.4887 | 59.5139 | 59.5559 | 59.6146 | 59.6900 |
| 2 | 2 | 62.1736 | 62.1817 | 62.2058 | 62.2460 | 62.3022 | 62.3743 |
| 0 | 2 | 65.0426 | 65.0503 | 65.0734 | 65.1118 | 65.1655 | 65.2345 |
| 6 | 1 | 69.5455 | 69.5527 | 69.5742 | 69.6102 | 69.6604 | 69.7250 |
| 3 | 2 | 74.3106 | 74.3173 | 74.3375 | 74.3711 | 74.4182 | 74.4786 |
| 1 | 3 | 79.1416 | 79.1479 | 79.1669 | 79.1984 | 79.2426 | 79.2994 |
| 7 | 1 | 79.5265 | 79.5328 | 79.5517 | 79.5831 | 79.6271 | 79.6836 |
| 4 | 2 | 86.0586 | 86.0644 | 86.0819 | 86.1109 | 86.1515 | 86.2038 |
| 8 | 1 | 89.4428 | 89.4484 | 89.4651 | 89.4931 | 89.5322 | 89.5824 |
| 2 | 3 | 92.4286 | 92.4340 | 92.4502 | 92.4772 | 92.5151 | 92.5637 |
| 0 | 3 | 94.3199 | 94.3252 | 94.3411 | 94.3676 | 94.4046 | 94.4523 |
| 5 | 2 | 97.5313 | 97.5364 | 97.5518 | 97.5775 | 97.6133 | 97.6594 |
| 9 | 1 | 99.3071 | 99.3122 | 99.3273 | 99.3524 | 99.3876 | 99.4329 |
| 3 | 3 | 105.1899 | 105.1946 | 105.2089 | 105.2326 | 105.2659 | 105.3086 |
| 1 | 4 | 108.5282 | 108.5328 | 108.5466 | 108.5697 | 108.6019 | 108.6433 |
| 6 | 2 | 108.7965 | 108.8011 | 108.8149 | 108.8379 | 108.8700 | 108.9114 |
| 10 | 1 | 109.1299 | 109.1345 | 109.1482 | 109.1711 | 109.2032 | 109.2444 |
| 4 | 3 | 117.5760 | 117.5803 | 117.5930 | 117.6143 | 117.6441 | 117.6823 |
| 11 | 1 | 118.9166 | 118.9208 | 118.9334 | 118.9544 | 118.9838 | 119.0216 |
| 7 | 2 | 119.8983 | 119.9024 | 119.9150 | 119.9358 | 119.9650 | 120.0025 |
| 2 | 4 | 122.1046 | 122.1087 | 122.1210 | 122.1415 | 122.1701 | 122.2070 |
| 0 | 4 | 123.5261 | 123.5302 | 123.5423 | 123.5625 | 123.5908 | 123.6273 |
| 12 | 1 | 128.6726 | 128.6765 | 128.6881 | 128.7076 | 128.7348 | 128.7697 |
| 5 | 3 | 129.6775 | 129.6814 | 129.6929 | 129.7122 | 129.7392 | 129.7739 |
| 8 | 2 | 130.8673 | 130.8711 | 130.8826 | 130.9017 | 130.9284 | 130.9628 |
| 3 | 4 | 135.2278 | 135.2315 | 135.2426 | 135.2610 | 135.2869 | 135.3202 |
| 1 | 5 | 137.8027 | 137.8064 | 137.8173 | 137.8354 | 137.8608 | 137.8934 |
| 13 | 1 | 138.4036 | 138.4072 | 138.4181 | 138.4361 | 138.4614 | 138.4939 |
| 6 | 3 | 141.5538 | 141.5573 | 141.5679 | 141.5856 | 141.6103 | 141.6420 |
| 9 | 2 | 141.7255 | 141.7290 | 141.7396 | 141.7572 | 141.7819 | 141.8136 |
| 4 | 4 | 148.0058 | 148.0092 | 148.0194 | 148.0362 | 148.0599 | 148.0903 |
| 14 | 1 | 148.1105 | 148.1139 | 148.1240 | 148.1409 | 148.1645 | 148.1949 |
| 2 | 5 | 151.5605 | 151.5638 | 151.5737 | 151.5902 | 151.6133 | 151.6430 |
| 10 | 2 | 152.4911 | 152.4944 | 152.5043 | 152.5206 | 152.5436 | 152.5731 |
| 0 | 5 | 152.7019 | 152.7051 | 152.7150 | 152.7313 | 152.7543 | 152.7837 |
| 7 | 3 | 153.2465 | 153.2497 | 153.2595 | 153.2758 | 153.2987 | 153.3280 |
| 15 | 1 | 157.7980 | 157.8011 | 157.8106 | 157.8265 | 157.8486 | 157.8771 |
| 5 | 4 | 160.5101 | 160.5133 | 160.5226 | 160.5382 | 160.5600 | 160.5880 |
| 11 | 2 | 163.1752 | 163.1783 | 163.1875 | 163.2028 | 163.2242 | 163.2518 |
| 8 | 3 | 164.7857 | 164.7888 | 164.7979 | 164.8130 | 164.8343 | 164.8616 |
| 3 | 5 | 164.9224 | 164.9254 | 164.9345 | 164.9497 | 164.9709 | 164.9982 |
| 1 | 6 | 167.0249 | 167.0279 | 167.0369 | 167.0518 | 167.0728 | 167.0997 |
| 16 | 1 | 167.4678 | 167.4708 | 167.4797 | 167.4946 | 167.5155 | 167.5424 |
| 6 | 4 | 172.7907 | 172.7936 | 172.8023 | 172.8168 | 172.8370 | 172.8630 |
| 12 | 2 | 173.7889 | 173.7917 | 173.8004 | 173.8147 | 173.8349 | 173.8608 |
| 9 | 3 | 176.1947 | 176.1976 | 176.2061 | 176.2203 | 176.2401 | 176.2657 |
| 17 | 1 | 177.1209 | 177.1237 | 177.1322 | 177.1463 | 177.1661 | 177.1915 |
| 4 | 5 | 177.9695 | 177.9723 | 177.9807 | 177.9948 | 178.0144 | 178.0397 |
| 2 | 6 | 180.9073 | 180.9101 | 180.9184 | 180.9322 | 180.9516 | 180.9764 |
| 0 | 6 | 181.8618 | 181.8645 | 181.8728 | 181.8865 | 181.9058 | 181.9305 |
| 13 | 2 | 184.3404 | 184.3431 | 184.3512 | 184.3648 | 184.3838 | 184.4082 |
| 7 | 4 | 184.8841 | 184.8868 | 184.8949 | 184.9085 | 184.9274 | 184.9517 |
| 18 | 1 | 186.7592 | 186.7619 | 186.7699 | 186.7833 | 186.8020 | 186.8261 |
| 10 | 3 | 187.4907 | 187.4934 | 187.5014 | 187.5147 | 187.5334 | 187.5574 |
| 5 | 5 | 190.7589 | 190.7615 | 190.7694 | 190.7825 | 190.8008 | 190.8244 |
| 3 | 6 | 194.4393 | 194.4418 | 194.4495 | 194.4624 | 194.4804 | 194.5035 |
| 14 | 2 | 194.8372 | 194.8397 | 194.8474 | 194.8603 | 194.8782 | 194.9013 |
| 1 | 7 | 196.2183 | 196.2208 | 196.2285 | 196.2412 | 196.2591 | 196.2820 |
| 19 | 1 | 196.3845 | 196.3871 | 196.3947 | 196.4074 | 196.4253 | 196.4482 |
| 8 | 4 | 196.8180 | 196.8206 | 196.8282 | 196.8409 | 196.8587 | 196.8815 |
| 11 | 3 | 198.6893 | 198.6919 | 198.6994 | 198.7120 | 198.7296 | 198.7522 |
| 6 | 5 | 203.3325 | 203.3350 | 203.3424 | 203.3547 | 203.3719 | 203.3940 |
| 15 | 2 | 205.2839 | 205.2864 | 205.2937 | 205.3058 | 205.3229 | 205.3448 |
| 20 | 1 | 205.9969 | 205.9993 | 206.0066 | 206.0187 | 206.0357 | 206.0575 |
| 4 | 6 | 207.6836 | 207.6860 | 207.6932 | 207.7052 | 207.7221 | 207.7438 |
| 9 | 4 | 208.6141 | 208.6165 | 208.6237 | 208.6357 | 208.6525 | 208.6740 |
| 12 | 3 | 209.7999 | 209.8023 | 209.8094 | 209.8213 | 209.8380 | 209.8595 |
| 2 | 7 | 210.1919 | 210.1943 | 210.2014 | 210.2133 | 210.2299 | 210.2513 |
| 0 | 7 | 211.0124 | 211.0148 | 211.0219 | 211.0337 | 211.0503 | 211.0717 |
| 21 | 1 | 215.5990 | 215.6013 | 215.6083 | 215.6199 | 215.6361 | 215.6570 |
| 16 | 2 | 215.6871 | 215.6894 | 215.6964 | 215.7080 | 215.7242 | 215.7450 |
| 7 | 5 | 215.7219 | 215.7242 | 215.7311 | 215.7427 | 215.7589 | 215.7798 |
| 10 | 4 | 220.2893 | 220.2916 | 220.2984 | 220.3097 | 220.3256 | 220.3460 |
| 5 | 6 | 220.6868 | 220.6891 | 220.6959 | 220.7072 | 220.7231 | 220.7435 |
| 13 | 3 | 220.8335 | 220.8358 | 220.8426 | 220.8539 | 220.8697 | 220.8901 |

Fig.(2.7). Resonant frequencies of $TE_{pqs}$ modes in a cylindrically symmetric cavity.

CYLINDRICAL CAVITY
Mk-6

RADIUS OF CAVITY/MM = 5.1500 LENGTH OF CAVITY/MM = 150.0000

| TE MODE (p,q,s) | | CUT-OFF | MINIMUM DIFFRACTION Q | | | | |
|---|---|---|---|---|---|---|---|
| p | q | FREQ/GHZ | s=1 | s=2 | s=3 | s=4 | s=5 |
| 1 | 1 | 17.0699 | 918.54 | 231.99 | 104.85 | 60.35 | 39.76 |
| 2 | 1 | 28.3164 | 2522.12 | 632.89 | 283.03 | 160.58 | 103.90 |
| 0 | 1 | 35.5244 | 3967.77 | 994.30 | 443.66 | 250.93 | 161.73 |
| 3 | 1 | 38.9499 | 4769.24 | 1194.67 | 532.71 | 301.02 | 193.79 |
| 4 | 1 | 49.2999 | 7638.71 | 1912.03 | 851.54 | 480.36 | 308.56 |
| 1 | 2 | 49.4286 | 7678.65 | 1922.02 | 855.98 | 482.86 | 310.16 |
| 5 | 1 | 59.4803 | 11117.78 | 2781.80 | 1238.10 | 697.81 | 447.73 |
| 2 | 2 | 62.1736 | 12147.15 | 3039.14 | 1352.48 | 762.14 | 488.90 |
| 0 | 2 | 65.0426 | 13293.79 | 3325.80 | 1479.88 | 833.81 | 534.77 |
| 6 | 1 | 69.5455 | 15197.69 | 3801.78 | 1691.42 | 952.80 | 610.92 |
| 3 | 2 | 74.3106 | 17351.21 | 4340.16 | 1930.71 | 1087.40 | 697.06 |
| 1 | 3 | 79.1416 | 19680.17 | 4922.40 | 2189.48 | 1232.96 | 790.22 |
| 7 | 1 | 79.5265 | 19872.05 | 4970.37 | 2210.80 | 1244.95 | 797.90 |
| 4 | 2 | 86.0586 | 23270.05 | 5819.87 | 2588.35 | 1457.32 | 933.82 |
| 8 | 1 | 89.4428 | 25135.92 | 6286.34 | 2795.67 | 1573.94 | 1008.45 |
| 2 | 3 | 92.4286 | 26841.89 | 6712.83 | 2985.23 | 1680.56 | 1076.69 |
| 0 | 3 | 94.3199 | 27951.50 | 6990.23 | 3108.51 | 1749.91 | 1121.08 |
| 5 | 2 | 97.5313 | 29887.10 | 7474.13 | 3323.58 | 1870.89 | 1198.50 |
| 9 | 1 | 99.3071 | 30985.23 | 7748.66 | 3445.60 | 1939.52 | 1242.43 |
| 3 | 3 | 105.1899 | 34764.57 | 8693.50 | 3865.52 | 2175.73 | 1393.60 |
| 1 | 4 | 108.5282 | 37006.00 | 9253.86 | 4114.57 | 2315.82 | 1483.26 |
| 6 | 2 | 108.7965 | 37189.18 | 9299.65 | 4134.92 | 2327.27 | 1490.58 |
| 10 | 1 | 109.1299 | 37417.43 | 9356.71 | 4160.29 | 2341.53 | 1499.71 |
| 4 | 3 | 117.5760 | 43432.91 | 10860.58 | 4828.67 | 2717.50 | 1740.33 |
| 11 | 1 | 118.9166 | 44428.87 | 11109.57 | 4939.33 | 2779.75 | 1780.17 |
| 7 | 2 | 119.8983 | 45165.41 | 11293.71 | 5021.17 | 2825.78 | 1809.63 |
| 2 | 4 | 122.1046 | 46842.85 | 11713.07 | 5207.55 | 2930.62 | 1876.73 |
| 0 | 4 | 123.5261 | 47939.76 | 11987.30 | 5329.43 | 2999.18 | 1920.61 |
| 12 | 1 | 128.6726 | 52017.35 | 13006.69 | 5782.50 | 3254.03 | 2083.71 |
| 5 | 3 | 129.6775 | 52832.96 | 13210.60 | 5873.12 | 3305.01 | 2116.33 |
| 8 | 2 | 130.8673 | 53806.82 | 13454.06 | 5981.33 | 3365.87 | 2155.29 |
| 3 | 4 | 135.2278 | 57452.04 | 14365.37 | 6386.35 | 3593.70 | 2301.10 |
| 1 | 5 | 137.8027 | 59660.72 | 14917.54 | 6631.76 | 3731.74 | 2389.44 |
| 13 | 1 | 138.4036 | 60182.11 | 15047.88 | 6689.69 | 3764.33 | 2410.30 |
| 6 | 3 | 141.5538 | 62952.71 | 15740.53 | 6997.54 | 3937.49 | 2521.12 |
| 9 | 2 | 141.7255 | 63105.51 | 15778.73 | 7014.52 | 3947.04 | 2527.24 |
| 4 | 4 | 148.0058 | 68822.02 | 17207.86 | 7649.68 | 4304.32 | 2755.90 |
| 14 | 1 | 148.1105 | 68919.40 | 17232.21 | 7660.50 | 4310.41 | 2759.79 |
| 2 | 5 | 151.5605 | 72167.36 | 18044.20 | 8021.39 | 4513.41 | 2889.71 |
| 10 | 2 | 152.4911 | 73056.32 | 18266.44 | 8120.16 | 4568.97 | 2925.27 |
| 0 | 5 | 152.7019 | 73258.37 | 18316.95 | 8142.61 | 4581.59 | 2933.35 |
| 7 | 3 | 153.2465 | 73781.81 | 18447.81 | 8200.77 | 4614.31 | 2954.29 |
| 15 | 1 | 157.7980 | 78229.41 | 19559.71 | 8694.95 | 4892.28 | 3132.19 |
| 5 | 4 | 160.5101 | 80941.58 | 20237.75 | 8996.30 | 5061.79 | 3240.68 |
| 11 | 2 | 163.1752 | 83651.67 | 20915.27 | 9297.42 | 5231.17 | 3349.08 |
| 8 | 3 | 164.7857 | 85311.00 | 21330.11 | 9481.79 | 5334.88 | 3415.46 |
| 3 | 5 | 164.9224 | 85452.55 | 21365.49 | 9497.52 | 5343.73 | 3421.12 |
| 1 | 6 | 167.0249 | 87645.14 | 21913.64 | 9741.14 | 5480.77 | 3508.82 |
| 16 | 1 | 167.4678 | 88110.54 | 22029.99 | 9792.85 | 5509.85 | 3527.44 |
| 6 | 4 | 172.7907 | 93800.52 | 23452.49 | 10425.07 | 5865.48 | 3755.04 |
| 12 | 2 | 173.7889 | 94887.30 | 23724.18 | 10545.83 | 5933.40 | 3798.51 |
| 9 | 3 | 176.1947 | 97532.56 | 24385.50 | 10839.74 | 6098.73 | 3904.32 |
| 17 | 1 | 177.1209 | 98560.61 | 24642.51 | 10953.97 | 6162.98 | 3945.44 |
| 4 | 5 | 177.9695 | 99507.25 | 24879.17 | 11059.15 | 6222.15 | 3983.31 |
| 2 | 6 | 180.9073 | 102819.51 | 25707.23 | 11427.18 | 6429.16 | 4115.80 |
| 0 | 6 | 181.8618 | 103907.28 | 25979.18 | 11548.05 | 6497.15 | 4159.31 |
| 13 | 2 | 184.3404 | 106758.76 | 26692.05 | 11864.88 | 6675.37 | 4273.37 |
| 7 | 4 | 184.8841 | 107389.49 | 26849.73 | 11934.96 | 6714.79 | 4298.60 |
| 18 | 1 | 186.7592 | 109578.76 | 27397.05 | 12178.21 | 6851.62 | 4386.17 |
| 10 | 3 | 187.4907 | 110438.81 | 27612.06 | 12273.77 | 6905.37 | 4420.57 |
| 5 | 5 | 190.7589 | 114322.40 | 28582.96 | 12705.28 | 7148.10 | 4575.91 |
| 3 | 6 | 194.4393 | 118776.15 | 29696.39 | 13200.14 | 7426.45 | 4754.06 |
| 14 | 2 | 194.8372 | 119262.79 | 29818.05 | 13254.21 | 7456.87 | 4773.53 |
| 1 | 7 | 196.2183 | 120959.55 | 30242.24 | 13442.74 | 7562.92 | 4841.40 |
| 19 | 1 | 196.3845 | 121164.58 | 30293.50 | 13465.52 | 7575.73 | 4849.60 |
| 8 | 4 | 196.8180 | 121700.10 | 30427.38 | 13525.03 | 7609.20 | 4871.02 |
| 11 | 3 | 198.6893 | 124025.22 | 31008.66 | 13783.37 | 7754.52 | 4964.02 |
| 6 | 5 | 203.3325 | 129889.51 | 32474.73 | 14434.96 | 8121.04 | 5198.60 |
| 15 | 2 | 205.2839 | 132394.53 | 33100.99 | 14713.30 | 8277.60 | 5298.80 |
| 20 | 1 | 205.9969 | 133315.72 | 33331.29 | 14815.65 | 8335.18 | 5335.64 |
| 4 | 6 | 207.6836 | 135507.78 | 33879.30 | 15059.21 | 8472.18 | 5423.33 |
| 9 | 4 | 208.6141 | 136724.78 | 34183.55 | 15194.44 | 8548.24 | 5472.01 |
| 12 | 3 | 209.7999 | 138283.48 | 34573.23 | 15367.62 | 8645.66 | 5534.36 |
| 2 | 7 | 210.1919 | 138800.68 | 34702.53 | 15425.09 | 8677.99 | 5555.04 |
| 0 | 7 | 211.0124 | 139886.46 | 34973.97 | 15545.73 | 8745.85 | 5598.47 |
| 21 | 1 | 215.5990 | 146033.59 | 36510.75 | 16228.75 | 9130.04 | 5844.36 |
| 16 | 2 | 215.6871 | 146152.92 | 36540.59 | 16242.01 | 9137.50 | 5849.13 |
| 7 | 5 | 215.7219 | 146200.04 | 36552.37 | 16247.24 | 9140.45 | 5851.02 |
| 10 | 4 | 220.2893 | 152456.38 | 38116.45 | 16942.39 | 9531.47 | 6101.27 |
| 5 | 6 | 220.6868 | 153007.13 | 38254.14 | 17003.58 | 9565.89 | 6123.30 |
| 13 | 3 | 220.8335 | 153210.57 | 38305.00 | 17026.19 | 9578.61 | 6131.44 |

Fig.(2.8). Calculated diffraction quality factors for the Mk-6 cavity.

CYLINDRICAL CAVITY
Mk-6

RADIUS OF CAVITY/MM = 5.1500 LENGTH OF CAVITY/MM = 150.0000

| TE MODE (p,q,s) | | CUT-OFF | OHMIC Q | | | | |
|---|---|---|---|---|---|---|---|
| p | q | FREQ/GHZ | s=1 | s=2 | s=3 | s=4 | s=5 |
| 1 | 1 | 17.0699 | 1886.23 | 1304.28 | 871.22 | 604.12 | 441.22 |
| 2 | 1 | 28.3164 | 2117.79 | 1682.28 | 1256.83 | 932.68 | 704.67 |
| 0 | 1 | 35.5244 | 4551.91 | 4564.69 | 4585.99 | 4615.82 | 4654.22 |
| 3 | 1 | 38.9499 | 2201.72 | 1883.21 | 1519.29 | 1198.29 | 944.93 |
| 4 | 1 | 49.2999 | 2233.03 | 1994.57 | 1694.26 | 1400.80 | 1147.37 |
| 1 | 2 | 49.4286 | 5164.64 | 5132.15 | 5079.11 | 5007.12 | 4918.23 |
| 5 | 1 | 59.4803 | 2241.54 | 2057.90 | 1811.28 | 1552.00 | 1311.90 |
| 2 | 2 | 62.1736 | 5460.12 | 5398.02 | 5297.87 | 5164.25 | 5002.86 |
| 0 | 2 | 65.0426 | 6155.24 | 6160.39 | 6168.99 | 6181.02 | 6196.49 |
| 6 | 1 | 69.5455 | 2239.04 | 2093.93 | 1890.19 | 1664.18 | 1443.23 |
| 3 | 2 | 74.3106 | 5631.28 | 5558.74 | 5442.12 | 5287.24 | 5101.26 |
| 1 | 3 | 79.1416 | 6693.23 | 6689.07 | 6682.15 | 6672.53 | 6660.23 |
| 7 | 1 | 79.5265 | 2230.92 | 2113.69 | 1943.72 | 1747.46 | 1547.23 |
| 4 | 2 | 86.0586 | 5738.70 | 5664.74 | 5545.78 | 5387.70 | 5197.73 |
| 8 | 1 | 89.4428 | 2219.86 | 2123.35 | 1980.05 | 1809.41 | 1629.33 |
| 2 | 3 | 92.4286 | 7035.23 | 7020.22 | 6995.38 | 6960.95 | 6917.29 |
| 0 | 3 | 94.3199 | 7411.12 | 7414.07 | 7418.99 | 7425.88 | 7434.74 |
| 5 | 2 | 97.5313 | 5808.78 | 5737.35 | 5622.23 | 5468.85 | 5283.91 |
| 9 | 1 | 99.3071 | 2207.28 | 2126.54 | 2004.47 | 1855.56 | 1694.09 |
| 3 | 3 | 105.1899 | 7270.85 | 7248.36 | 7211.22 | 7159.92 | 7095.16 |
| 1 | 4 | 108.5282 | 7890.60 | 7890.32 | 7889.86 | 7889.21 | 7888.38 |
| 6 | 2 | 108.7965 | 5855.19 | 5787.87 | 5679.14 | 5533.78 | 5357.76 |
| 10 | 1 | 109.1299 | 2194.10 | 2125.63 | 2020.61 | 1890.05 | 1745.31 |
| 4 | 3 | 117.5760 | 7441.28 | 7414.28 | 7369.75 | 7308.35 | 7231.02 |
| 11 | 1 | 118.9166 | 2180.62 | 2121.85 | 2030.71 | 1915.63 | 1785.71 |
| 7 | 2 | 119.8983 | 5885.73 | 5823.04 | 5721.53 | 5585.36 | 5419.76 |
| 2 | 4 | 122.1046 | 8235.15 | 8230.20 | 8221.97 | 8210.50 | 8195.81 |
| 0 | 4 | 123.5261 | 8480.81 | 8482.78 | 8486.07 | 8490.66 | 8496.57 |
| 12 | 1 | 128.6726 | 2167.14 | 2116.19 | 2036.43 | 1934.46 | 1817.58 |
| 5 | 3 | 129.6775 | 7568.58 | 7539.14 | 7490.60 | 7423.75 | 7339.64 |
| 8 | 2 | 130.8673 | 5905.22 | 5847.15 | 5752.92 | 5626.09 | 5471.19 |
| 3 | 4 | 135.2278 | 8494.38 | 8485.38 | 8470.43 | 8449.61 | 8423.02 |
| 1 | 5 | 137.8027 | 8916.44 | 8916.95 | 8917.80 | 8918.99 | 8920.53 |
| 13 | 1 | 138.4036 | 2153.99 | 2109.41 | 2039.10 | 1948.26 | 1842.82 |
| 6 | 3 | 141.5538 | 7665.78 | 7635.25 | 7584.94 | 7515.66 | 7428.51 |
| 9 | 2 | 141.7255 | 5916.77 | 5863.09 | 5775.81 | 5657.97 | 5513.49 |
| 4 | 4 | 148.0058 | 8695.67 | 8683.59 | 8663.52 | 8635.61 | 8600.02 |
| 14 | 1 | 148.1105 | 2141.00 | 2101.68 | 2039.29 | 1957.97 | 1862.56 |
| 2 | 5 | 151.5605 | 9252.07 | 9250.23 | 9247.17 | 9242.88 | 9237.38 |
| 10 | 2 | 152.4911 | 5922.58 | 5872.98 | 5792.17 | 5682.76 | 5548.15 |
| 0 | 5 | 152.7019 | 9429.07 | 9430.50 | 9432.89 | 9436.23 | 9440.53 |
| 7 | 3 | 153.2465 | 7741.13 | 7710.39 | 7659.73 | 7589.96 | 7502.18 |
| 15 | 1 | 157.7980 | 2128.43 | 2093.51 | 2037.80 | 1964.65 | 1878.05 |
| 5 | 4 | 160.5101 | 8855.60 | 8841.30 | 8817.57 | 8784.59 | 8742.58 |
| 11 | 2 | 163.1752 | 5923.99 | 5878.12 | 5803.25 | 5701.65 | 5576.22 |
| 8 | 3 | 164.7857 | 7800.13 | 7769.74 | 7719.63 | 7650.60 | 7563.70 |
| 3 | 5 | 164.9224 | 9518.53 | 9514.38 | 9507.46 | 9497.80 | 9485.42 |
| 1 | 6 | 167.0249 | 9830.70 | 9831.36 | 9832.46 | 9834.00 | 9835.98 |
| 16 | 1 | 167.4678 | 2116.27 | 2085.05 | 2035.04 | 1968.95 | 1890.09 |
| 6 | 4 | 172.7907 | 8984.86 | 8969.05 | 8942.83 | 8906.39 | 8860.00 |
| 12 | 2 | 173.7889 | 5922.12 | 5879.63 | 5810.19 | 5715.73 | 5598.78 |
| 9 | 3 | 176.1947 | 7846.61 | 7816.91 | 7767.92 | 7700.39 | 7615.33 |
| 17 | 1 | 177.1209 | 2104.44 | 2076.38 | 2031.24 | 1971.28 | 1899.25 |
| 4 | 5 | 177.9695 | 9734.79 | 9728.65 | 9718.43 | 9704.16 | 9685.90 |
| 2 | 6 | 180.9073 | 10154.45 | 10153.78 | 10152.67 | 10151.11 | 10149.11 |
| 0 | 6 | 181.8618 | 10289.89 | 10290.99 | 10292.83 | 10295.40 | 10298.71 |
| 13 | 2 | 184.3404 | 5917.73 | 5878.32 | 5813.81 | 5725.87 | 5616.71 |
| 7 | 4 | 184.8841 | 9090.74 | 9073.95 | 9046.11 | 9007.44 | 8958.23 |
| 18 | 1 | 186.7592 | 2092.97 | 2067.61 | 2026.69 | 1972.08 | 1906.08 |
| 10 | 3 | 187.4907 | 7883.29 | 7854.49 | 7806.95 | 7741.39 | 7658.74 |
| 5 | 5 | 190.7589 | 9913.31 | 9905.56 | 9892.67 | 9874.69 | 9851.67 |
| 3 | 6 | 194.4393 | 10420.99 | 10418.91 | 10415.44 | 10410.59 | 10404.37 |
| 14 | 2 | 194.8372 | 5911.44 | 5874.81 | 5814.77 | 5732.78 | 5630.76 |
| 1 | 7 | 196.2183 | 10664.30 | 10664.95 | 10666.02 | 10667.53 | 10669.47 |
| 19 | 1 | 196.3845 | 2081.90 | 2058.87 | 2021.62 | 1971.70 | 1911.05 |
| 8 | 4 | 196.8180 | 9178.35 | 9160.98 | 9132.19 | 9092.20 | 9041.31 |
| 11 | 3 | 198.6893 | 7912.27 | 7884.47 | 7838.57 | 7775.24 | 7695.34 |
| 6 | 5 | 203.3325 | 10062.67 | 10053.66 | 10038.69 | 10017.80 | 9991.10 |
| 15 | 2 | 205.2839 | 5903.61 | 5869.50 | 5813.52 | 5736.96 | 5641.47 |
| 20 | 1 | 205.9969 | 2071.11 | 2050.12 | 2016.07 | 1970.28 | 1914.40 |
| 4 | 6 | 207.6836 | 10644.04 | 10640.65 | 10635.00 | 10627.10 | 10616.98 |
| 9 | 4 | 208.6141 | 9251.43 | 9233.79 | 9204.53 | 9163.89 | 9112.18 |
| 12 | 3 | 209.7999 | 7934.94 | 7908.20 | 7864.04 | 7803.06 | 7726.07 |
| 2 | 7 | 210.1919 | 10975.83 | 10975.66 | 10975.38 | 10974.99 | 10974.48 |
| 0 | 7 | 211.0124 | 11083.83 | 11084.72 | 11086.19 | 11088.25 | 11090.89 |
| 21 | 1 | 215.5990 | 2060.76 | 2041.54 | 2010.31 | 1968.18 | 1916.55 |
| 16 | 2 | 215.6871 | 5894.70 | 5862.87 | 5810.58 | 5738.95 | 5649.45 |
| 7 | 5 | 215.7219 | 10188.96 | 10179.00 | 10162.45 | 10139.37 | 10109.86 |
| 10 | 4 | 220.2893 | 9312.77 | 9295.05 | 9265.68 | 9224.89 | 9172.99 |
| 5 | 6 | 220.6868 | 10833.14 | 10828.61 | 10821.07 | 10810.52 | 10797.01 |
| 13 | 3 | 220.8335 | 7952.55 | 7926.89 | 7884.50 | 7825.92 | 7751.91 |

Fig.(2.9). Calculated ohmic quality factors for the Mk-6 cavity.

It would be possible to reduce the length of the cavity with the use of inserts. This would dramatically reduce the diffraction Q, $\propto$(cavity length)$^2$, rendering the cavity $Q_D$ dominant and reducing its selective mode damping. This would result in multimode oscillation at all frequencies.

A long interaction region will therefore be studied with the possibility of introducing inserts in future experiments, reducing the cavity length to increase the efficiency, and reducing the cavity diameter to increase mode separation.

Input/Output Tapers.

Two tapers will be used on the Mk-6 E.C.M. fig.(1.6). One will form part of the cathode chamber, the second will form the output coupler of the mm-waves. Both tapers must perform completely different roles.

1) The output coupling taper. This will have the following characteristics.

A) Low reflection coefficient. The cavity will be ohmic Q limited, hence there will be more power lost in the walls than through the output coupler. It is thus important to minimise reflections and hence $Q_D$ eqn.(2.22), coupling out as much energy as possible before it is lost to ohmic heating.

B) Minimal mode conversion. As the taper angle increases large amplitude, high order modes must be introduced in the taper to match the boundary conditions between the excited taper and waveguide modes (45). If the amplitudes of the excited high order taper modes are too large then it will be impossible to identify the cavity mode via the far and near field radiation pattern from the taper.

C) Output coupling. The taper angle must be sufficient to provide good coupling between the waveguide modes and the excited free space modes.

All of these prerequisites require a long taper with a small

taper angle. The following dimensions were chosen for the output coupler, taper length $L_{t1}$=300mm and angle $a_{t1}$=4.5°. This possesses all the characteristics of low mode conversion and excellent output coupling required in conditions B) and C) above, (17,41). Fig.(2.10) presents the calculated reflection coefficient for this taper and tapers with similar $a_{t1}$. This shows r≃1.5% and R≃.022% hence the taper also satisfies condition A).

2) Anode flange taper. This must possess the following characteristics.

A) Electron trajectories. This taper will play an important role in the determination of the electron trajectories fig.(1.6). Electrons produced at the cathode tip will be accelerated towards the anode taper. This must be designed to impart the optimum value of $v_\perp$.

B) Reflection coefficient. As all the electromagnetic energy entering the cathode chamber from the cavity is lost, it is necessary to maximise the reflection coefficient from the anode taper.

As the reflection coefficient will again be shown to be small the main consideration in the determination of the anode taper dimensions was A) above, hence $L_{t2}$=31mm and $a_{t2}$=45°. This will impart large amounts of transverse energy to the beam. The resulting reflection coefficients are shown in fig.(2.11). For this taper r≃18% and R≃3.2%.

Reflection from Discontinuity.

In an attempt to increase the useful output of the cavity a discontinuity was added at the cathode end of the cavity. A qualitative estimate of the subsequent reflection coefficient was obtained from the above theory.

In the case of the MK-6 cavity,

$a = 5.15mm$, $d = 4.10mm$, $\lambda_0 = 1.5mm$, and $k_0 = 4.19mm$.

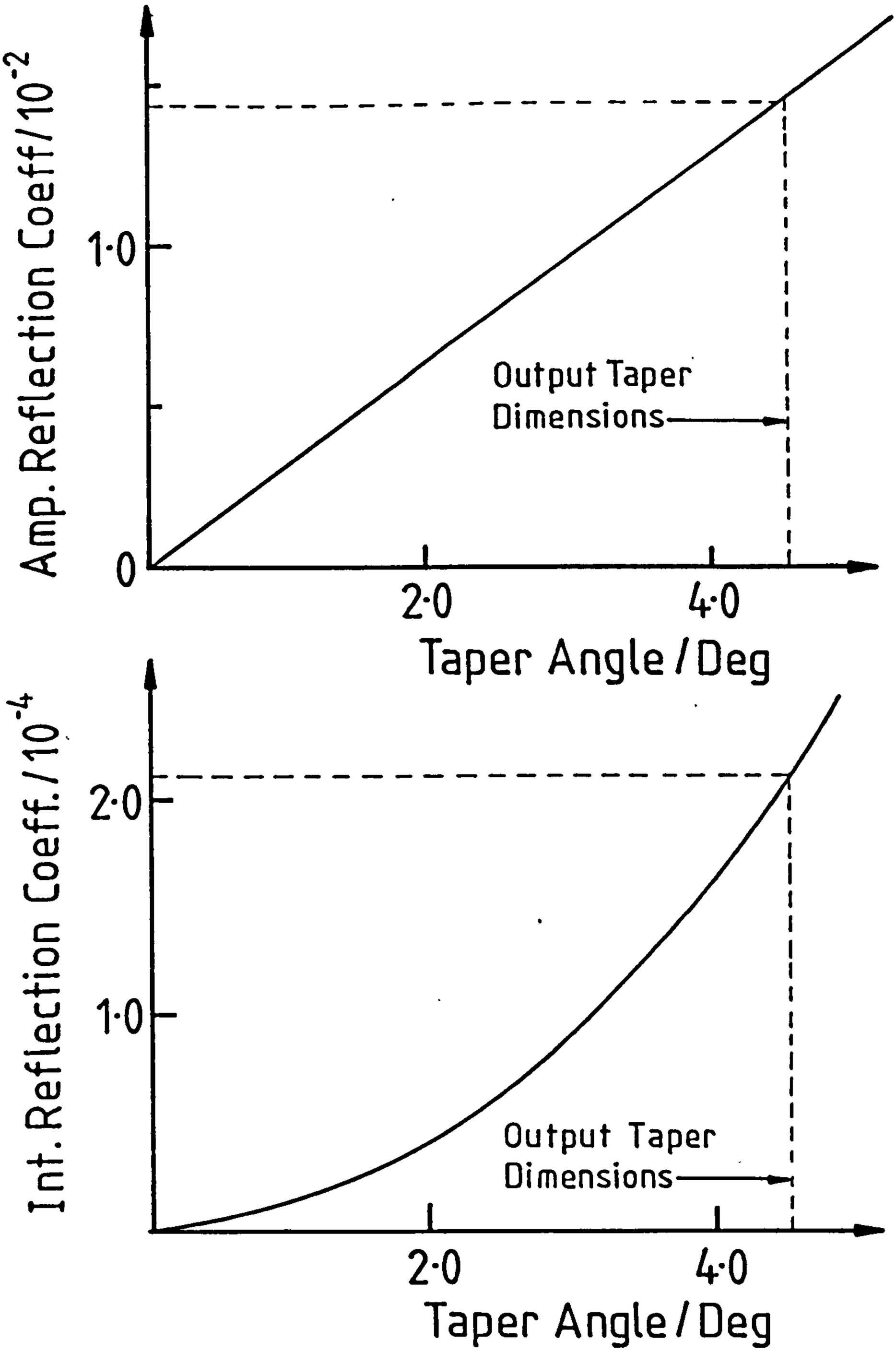


Fig.(2.10). Calculated amplitude and intensity reflection coefficients of the output coupler.

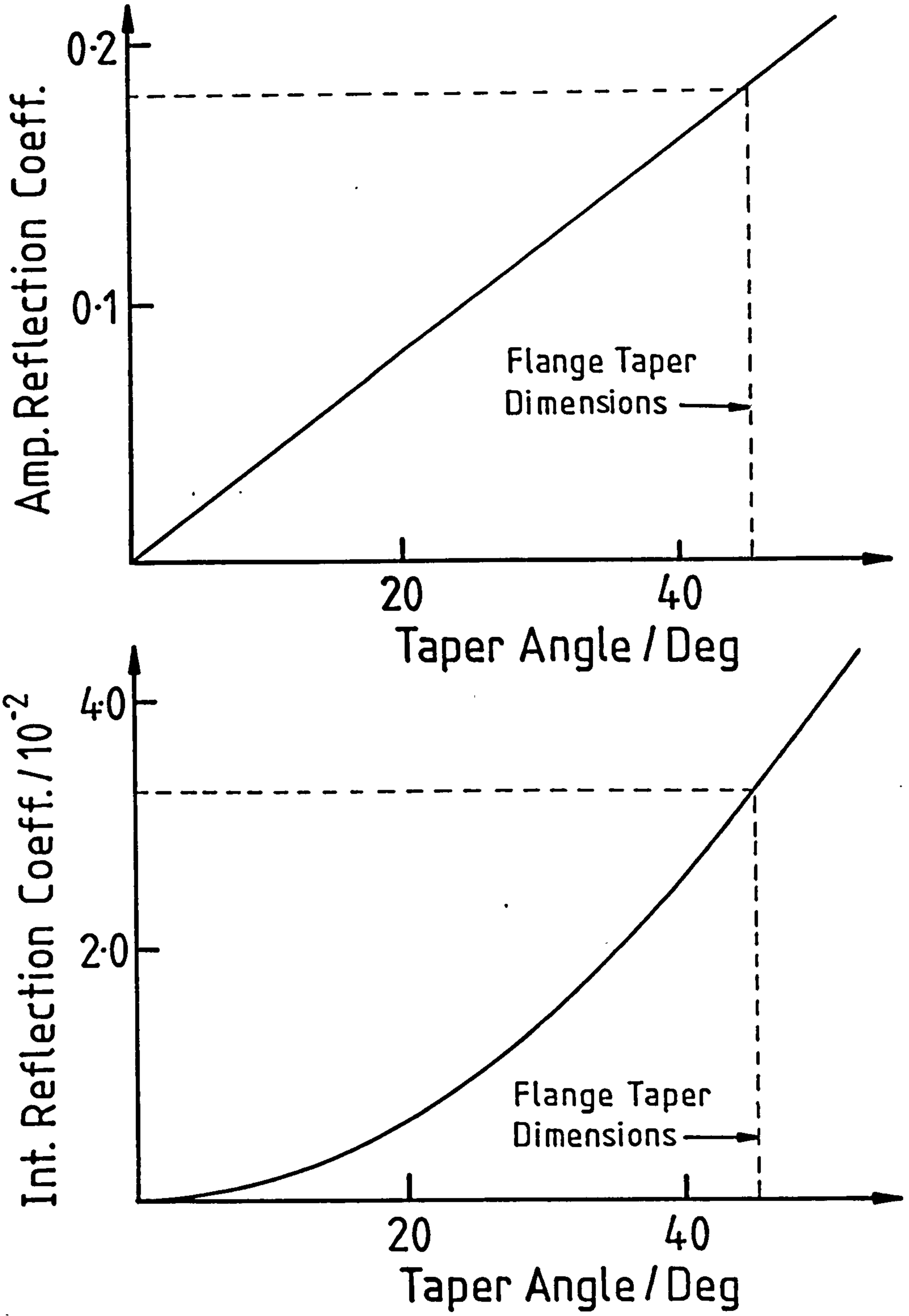


Fig.(2.11). Calculated amplitude and intensity reflection coefficients of the flange taper.

These dimensions lead to an amplitude reflection coefficient r=-7.24% and intensity reflection R=.52%. These values only served as an estimate of the reflection coefficients in the oscillating cylindrical cavity. The predicted reflection coefficients were small, therefore it is possible to conclude that adding the bevel had the desired effect, increasing the feedback and reducing the output from the cathode end of the cavity, however it was a small effect and did not influence the value of $Q_D$.

MK-6 Cavity Design Summary.

Taking into account all the previous considerations it was possible to design the maser cavity with the following characteristics.

1) Be able to oscillate multimode in the high frequency G-band regime and single moded in the low frequency W-band regime.
2) Be step tunable with the excitation of discrete cavity modes.
3) Have minimal mode conversion and low reflection coefficients.
4) Discriminate against whispering gallery modes in favour of the $TE_{0n}$ modes due to the low electrical conductivity of the cavity walls.
5) Have high gain, low feedback characteristics.
6) Have high power handling capability.

Fig.(2.12) shows the final dimensions of the constructed cavity.

## 2.4 Electron Beam Production

### Introduction

The pulsed electron beam used in the E.C.M. was produced from a field-emission, field-immersed cold cathode. A voltage of ≈72kV was generated across the anode cathode gap. Due to field enhancement, whiskers on the cathode surface explode (46) producing a surface plasma from which electrons may be drawn. The voltage used must be large enough to produce the surface electrons

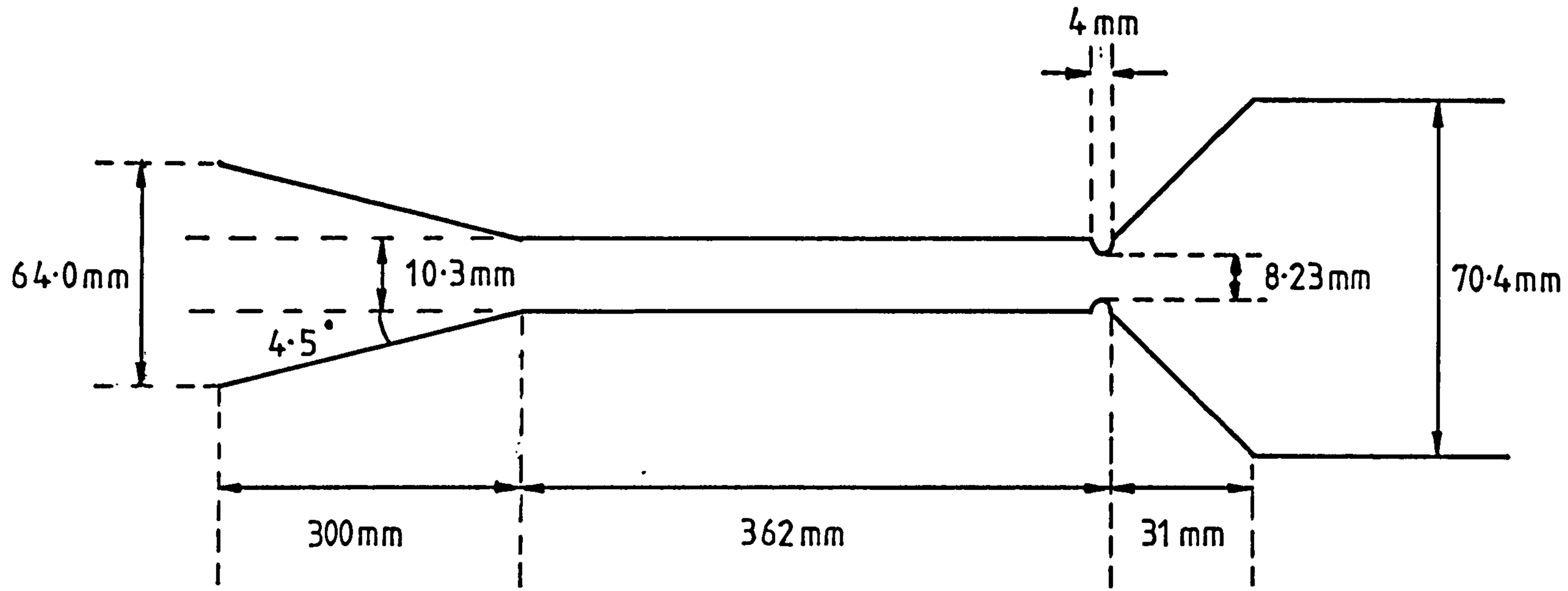


Fig.(2.12). Design and dimensions of the Mk-6 E.C.M. anode/cavity.

and make the electrons mildly relativistic, however to maximise $\omega_{ce}$, $\gamma$ must not be too large, (as will be measured in chapter 4, $\gamma$=1.14) c.f. eqn.(1.1).

The length of the electron beam pulse is governed by the gap closure time. This is the time for the plasma to travel across the anode-cathode gap (32), effectively shorting the HT voltage. Although current will continue to flow after this point it is then a low voltage arc discharge and will take no part in the E.C.M. interaction.

HT Generation

A standard Marx generator, constructed previously at Strathclyde (47,48), was used to produce the HT voltage pulse, fig.(2.13). Ten capacitors were charged in parallel and via a system of five spark gap switches discharged in series. This produces a voltage of $n(V_{charge})$, where n is the number of capacitors. Each capacitor was rated at 100kV hence the system could in principal produce 1MV. The characteristics of the Marx in conjunction with the anode-cathode gap will be investigated in chapter 4.

Cathode Design.

The cathode design is shown in fig.(2.14). It was constructed from stainless steel tubing, diameter 6.1mm, and was designed to produce an annular electron beam. The cathode tip was sharpened to maximise the electric field strength at this point. This ensures the production of a surface plasma from which electrons may be drawn.

As such a large E-field is generated at the cathode, field emission freely takes place, hence this cathode is inherently pulsed in nature. If cw operation were required, a thermionic cathode would be essential.

Anode-Cathode Configuration

The anode cathode configuration is shown in fig.(2.15) and, as

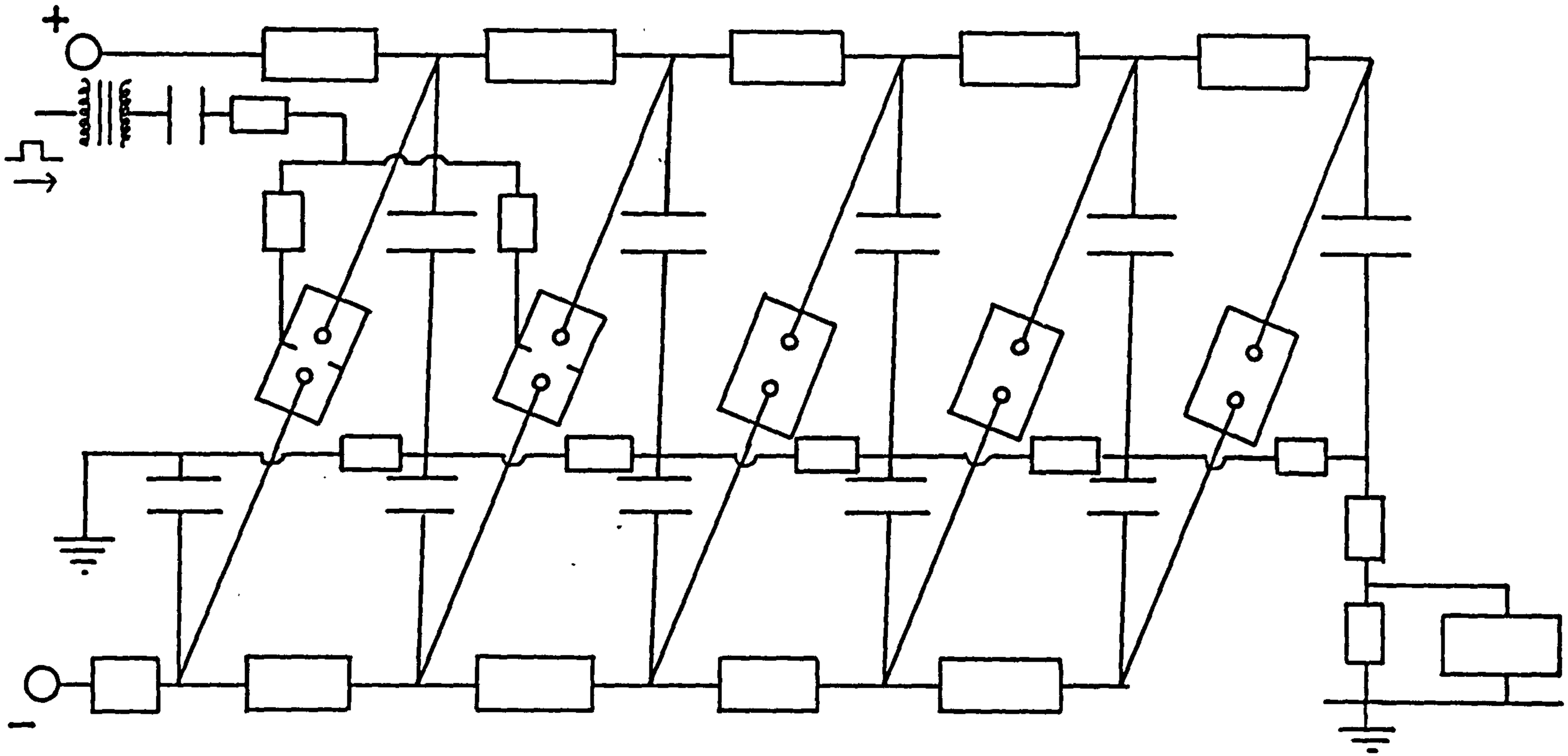


Fig.(2.13). Schematic diagram of Marx bank HT generator.

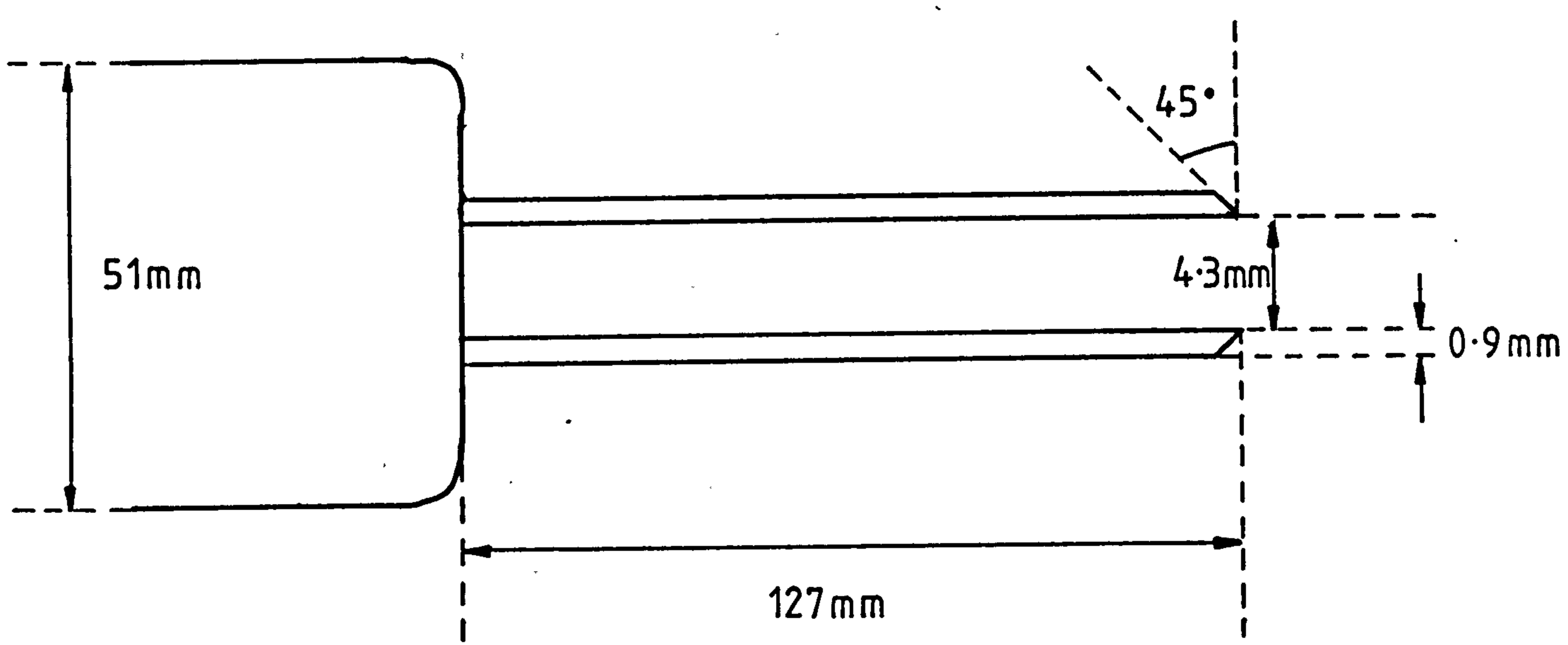


Fig.(2.14). Cathode design and dimensions.

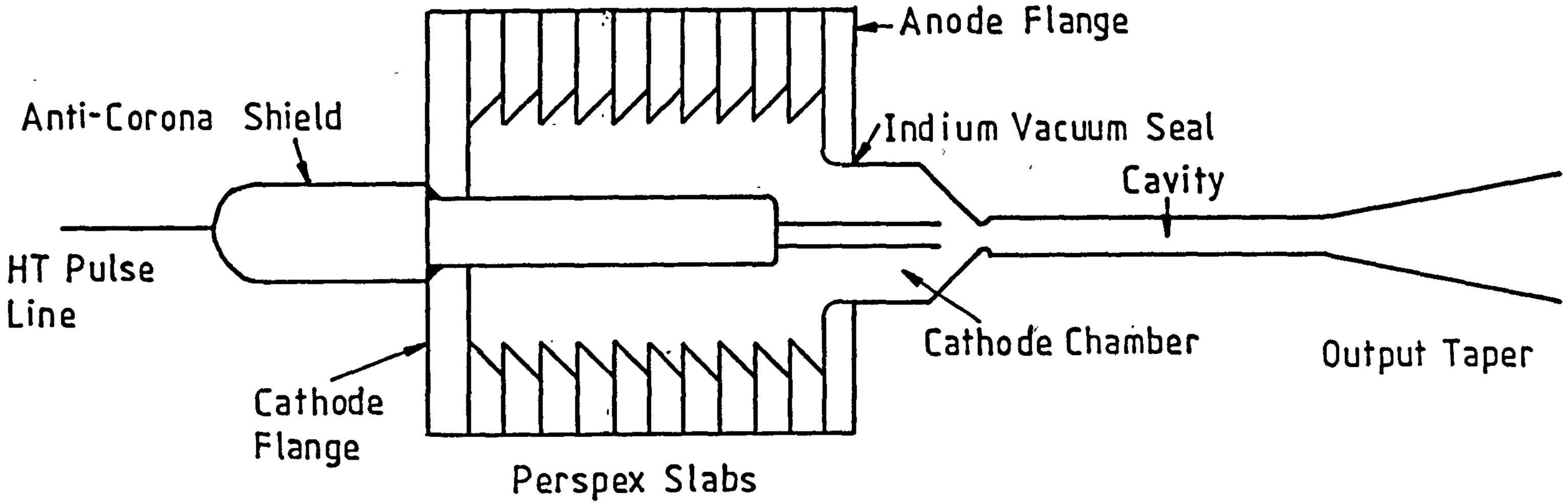


Fig.(2.15). Schematic diagram of anode-cathode configuration.

previously described, is designed to impart the optimum $v_\perp$ to the electrons. Only the $v_\perp$ energy of the electrons is available to the E.C.M. interaction.

The HT pulse line is attached to the cathode flange via an anti-corona shield. The cathode and the anode flanges are separated by nine perspex slabs. These slabs have been sawtoothed on the inside of the cathode chamber to prevent a surface flashover, effectively increasing the distance between the anode and the cathode flange and preventing secondary electrons re-impinging on the adjacent insulator. The tip of the cathode was initially placed half way along the 45° taper, this corresponds to an anode-cathode position of 0mm in subsequent chapters.

The cathode may be moved backwards or forwards with respect to the anode thus allowing the alteration of $L_{a-c}$, the anode cathode gap. It will be demonstrated that both the pulse length and the maximum output power from the maser are strong functions of $L_{a-c}$.

## 2.5 The Vacuum System.

The maser cavity and cathode chamber must be evacuated to allow the formation of the relativistic electron beam. A schematic diagram of the vacuum system is shown in fig.(2.16). The system pumps from the output end of the cavity with the cavity walls doubling as the pressure containment vessel. The cathode chamber is pumped out through the cavity.

An Edwards ED100 rotary pump was used to obtain a pressure of $10^{-3}$ torr, which was then used to back an Edwards Diffstak diffusion pump. This was used to evacuate the system to $10^{-6}$ torr.

## 2.6 The Output Window.

Any output window for the mm-waves will form part of the vacuum containment vessel, and therefore must be strong enough to withstand atmospheric pressure. In past experiments at Strathclyde University a 1.27cm section glass window was used. However when tested using a W-band source the mm-wave absorption in the window proved to be more than 10dB. Upon varying the angle of incidence

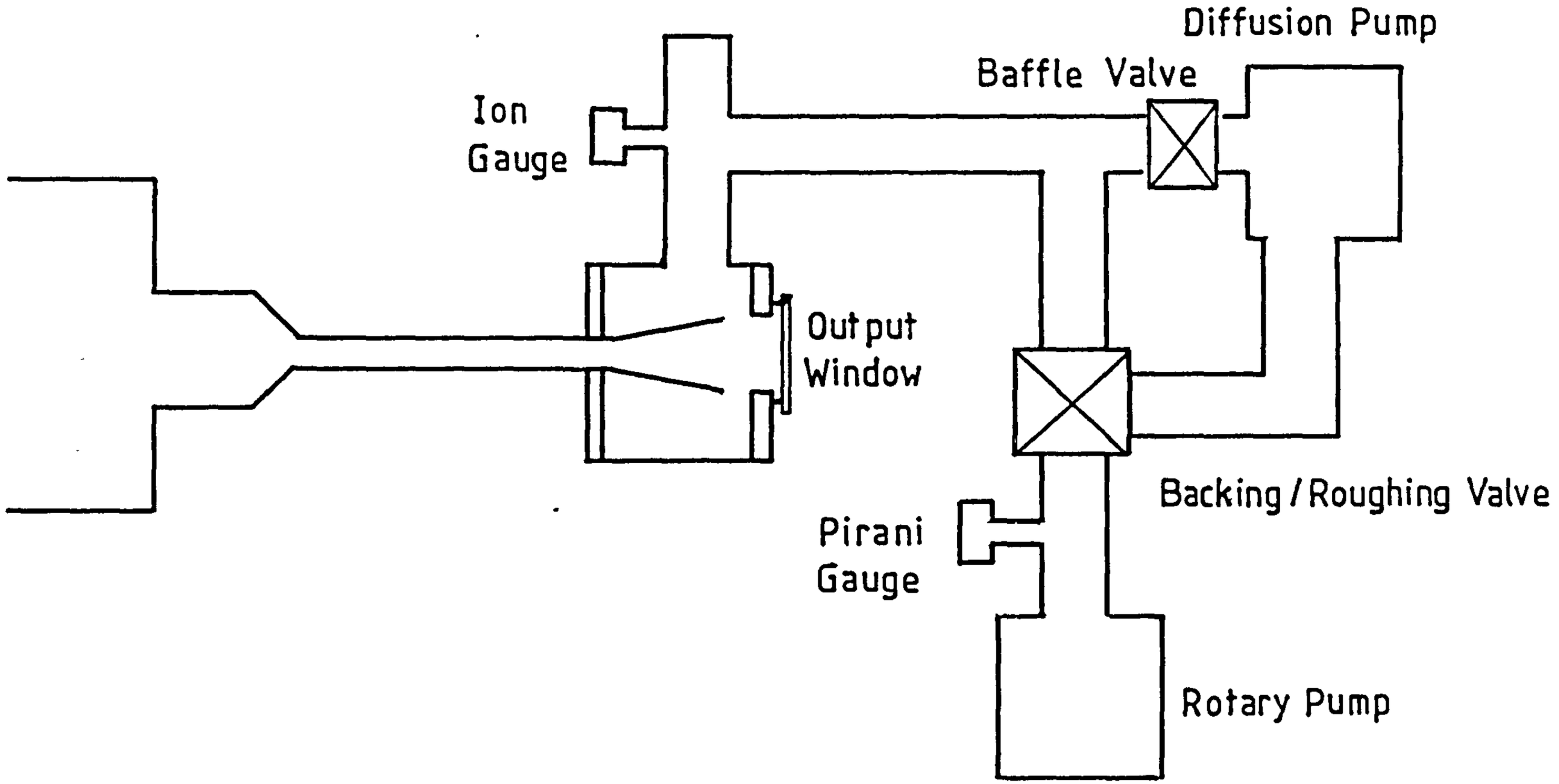


Fig.(2.16). Schematic diagram of vacuum system.

of the radiation (effectively changing the thickness of the glass) strong absorption resonances were observed. This corresponded to Fabry-Perot cavity effects between the glass faces.

To eliminate these problems a Mylar window was developed. This consisted of a .127mm thick Mylar sheet stretched over a Tufnol ring and fixed using Araldite epoxy resin. This was then bolted against an O-ring seal in the output flange, fig.(2.17).

In the construction of such a window several factors were found to be important.

1) As the Mylar window will have to withstand atmospheric pressure, the forces on the window must be uniform otherwise shear stresses will occur and the window will break. Hence care must be taken to ensure the Mylar is attached to the Tufnol ring with an even layer of epoxy resin and the Mylar stretched flat.
2) To allow even pressure to be applied by the Tufnol ring the epoxy resin must be outwith the O-ring diameter.
3) The Mylar sheet will bow inwards, hence the metal output flange must be "radiused", fig.(2.17).
4) The rotary pump must be switched on gradually to allow the Mylar sheet to take up the strain and seal against the O ring.

The resulting Mylar window had no measurable mm-wave absorption. As the thickness of the window was well below 1/4 wavelength of either the W-band or the G-band radiation no Fabry-Perot cavity effects could be detected. This resulted in a low loss broad passband output window.

## 2.7 The Electron Cyclotron Maser Configuration.

The maser configuration is shown in fig.(2.18), demonstrating the relative positions of all the components designed and constructed above.

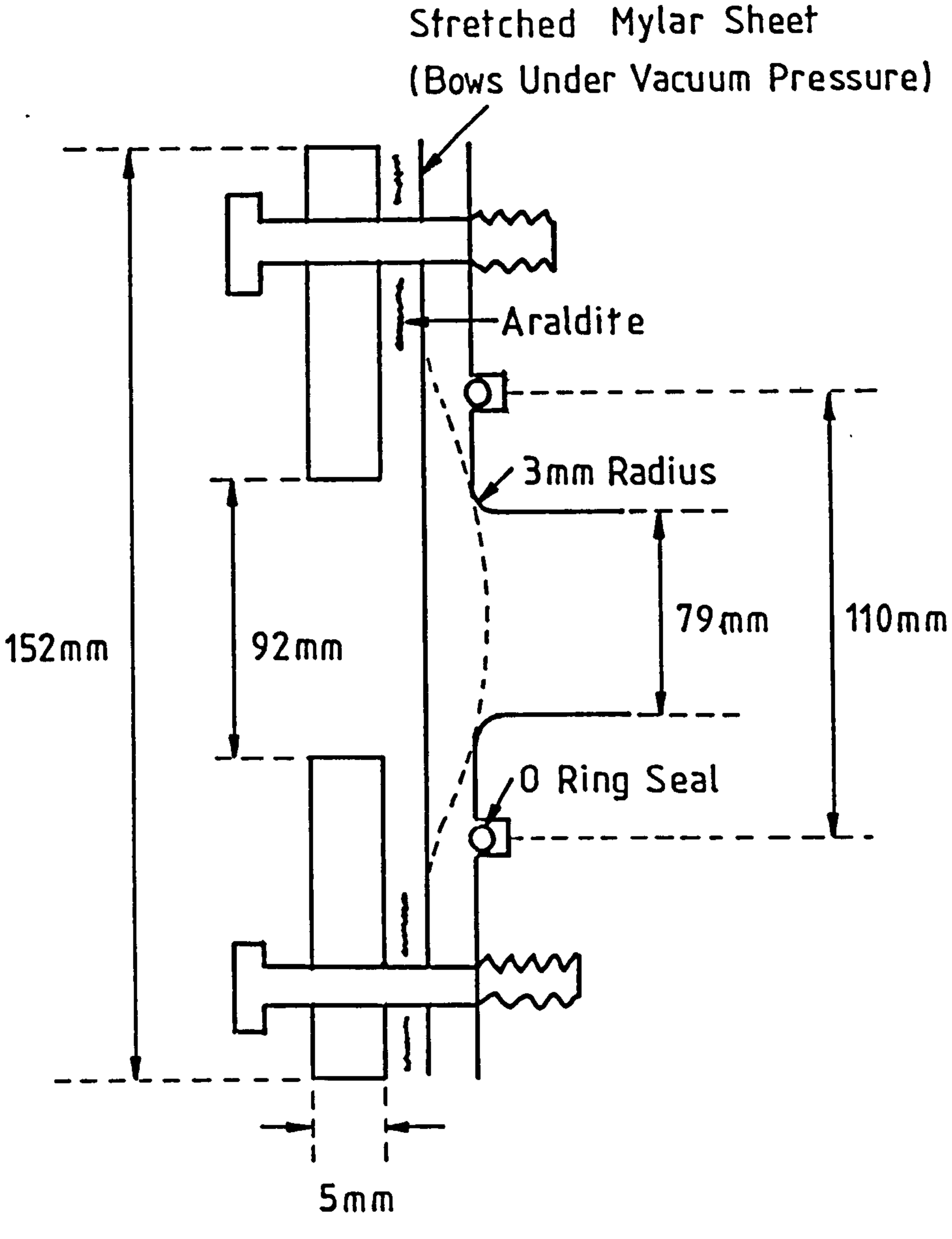


Fig.(2.17). Mylar window construction.

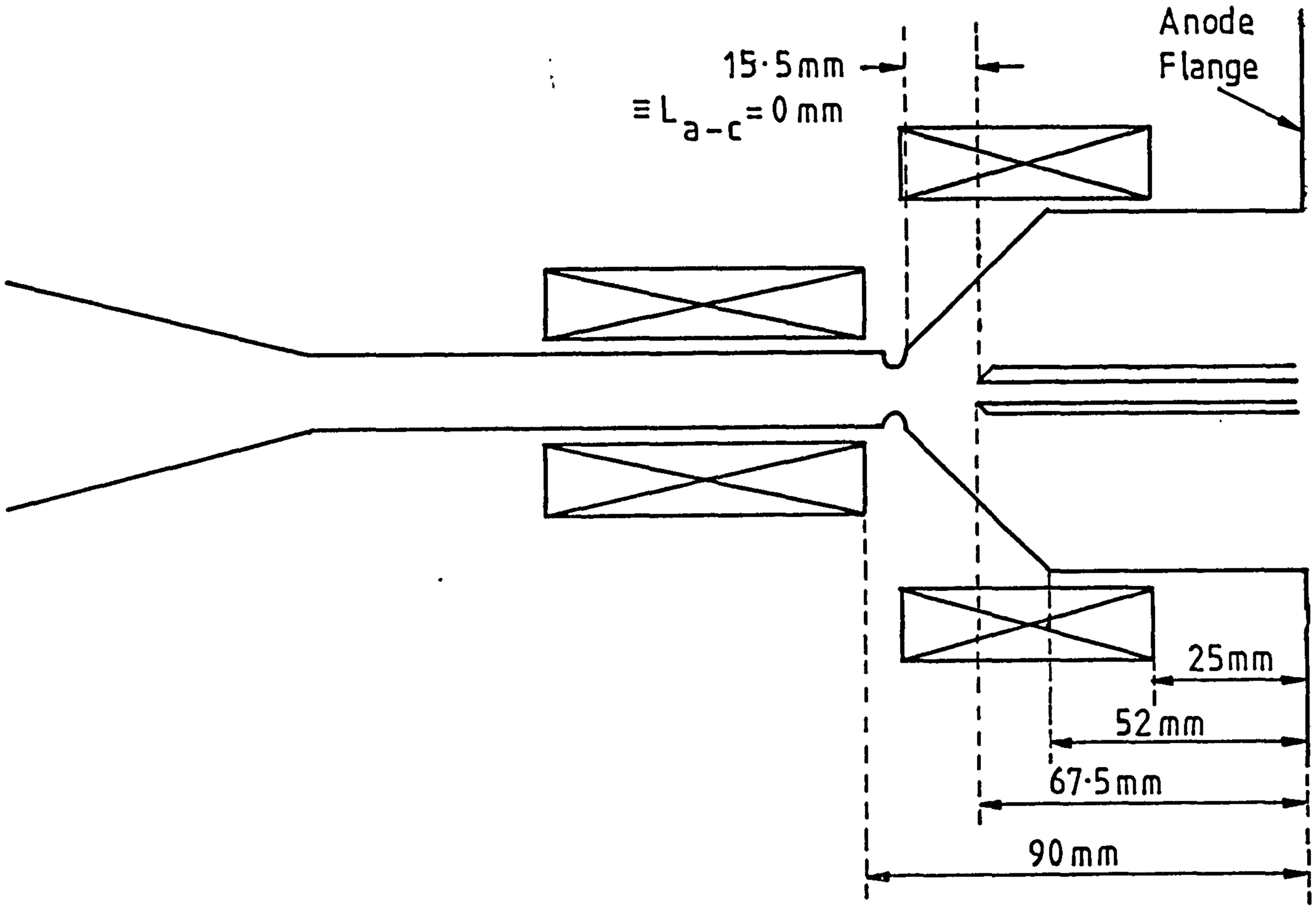


Fig.(2.18). Maser configuration.

# CHAPTER -3-

# MASER DIAGNOSTICS.

## 3.1 Introduction.

In this chapter all the diagnostics used to monitor the running and operation of the maser along with the mm-wave output characteristics, will be described.

Standard voltage dividers will be used to monitor the charging voltages on all the capacitor banks along with the diode HT voltage. Rogowski coil belts will be used to measure and monitor the current through both the field coils, the Marx discharge current and the witness plate return current. Due to the large transients associated with the capacitor discharges the entire detection system will be double screened, with measuring and recording equipment placed in screened rooms. The retrieval, storage, measurement and monitoring of data will be described.

A relativistic electron beam probe was constructed to measure the beam current, position and collimation through the cavity. Similarly a magnetic field probe coil was designed and constructed to calibrate the B-field coils and measure the B-field profile through the cavity.

In the W-band, a calibrated W-band Flann 135 rectifying crystal was used to detect the mm-wave output from the maser. In conjunction with this a Baytron V-band detector in a W-band mount was used uncalibrated to provide a constant reference while measuring the radiation pattern from the maser. In the G-band a more sensitive Flann 137 uncalibrated crystal was used. In this case the less sensitive Flann 135 crystal was used as a reference while producing the spectral analysis of the maser output.

Several different mm-wave diagnostics are used to characterise the oscillation of the maser, viz:

1) Diffraction grating spectrometer. This was constructed in the Czerny-Turner configuration, and calibrated to measure the frequency of oscillation and the frequency bandwidth of the maser output.
2) Cavity mode identification. The relevant theory and several measurement techniques were developed to measure the near and far field radiation pattern of the maser output. This may be

used to determine the cavity mode of oscillation.

3) Output power measurements. A calibrated power meter was constructed from a thermocouple array and a Flann calibrated crystal detector. The first measured the energy in any pulse and the second determined the pulse duration. From these combined measurements the power in any pulse may be calculated.

## 3.2 Voltage Dividers.

Two voltage dividers were constructed for use in this experiment, one to measure the D.C. charging voltage on the Marx bank, and one to measure the very rapidly varying Marx discharge voltage, ($\tau_{rise} \lesssim 100$ns), fig.(3.1).

The first works on the very simple and well known principle that a voltage V developed across two resistors $R_1$ and $R_2$ will result in a voltage $V_2$ being developed across $R_2$ where,

$$V_2 = V \frac{R_2}{R_1 + R_2} . \qquad (3.1)$$

If $R_1 \gg R_2$ then a large voltage V may be reduced to an easily measurable voltage, $V_2$. Care must be taken to avoid breakdown in the circuit. $R_1$ and $R_2$ may be chosen arbitrarily, though in most cases $R_1$ is made so large that the voltage divider draws almost no current from the voltage source.

In the case of the second divider, a very rapidly varying voltage has to be monitored. Hence it is essential to take into account all the stray capacitances and inductances present in choosing a value for $R_1$ and $R_2$ (49). Even though the stray capacitances may be as low as a few picofarads, $R_1$ and $R_2$ would only have to be a few kilo-ohms to make the RC time of the divider comparable to that of the rise time of the voltage pulse. If this is the case then $V_2$ will not be related to V by the simple eqn.(3.1).

It may be shown that the response time of a voltage divider is given by,

$$T_0 = \frac{R\,C_e}{6} \,. \qquad (3.2)$$

Where $C_e$ is defined in fig.(3.1) and is given approximately by,

$$\frac{C_e}{[pF]} = (10 \to 15)\,\frac{H}{[m]} \,. \qquad (3.3)$$

Where H = the height of the divider.

Thus knowing the necessary response time, a suitable value of $R=R_1+R_2$ may be chosen.

In the divider used for monitoring the Marx generator, fig.(2.13), $R_1=429\pm3\Omega$ and $R_2=.594\pm.005\Omega$, resulting in a reduction in the subsequent signal by a factor of 722±7. This may be further reduced using calibrated attenuators.

Using this technique it was possible to monitor accurately the charging voltage of the Marx and its subsequent discharge voltage across the diode.

3.3 Rogowski Coils.

A very convenient means of measuring rapidly varying currents is that of Rogowski coil belts (50). This standard method also has the advantage of measuring currents passively.

A simple diagram of a Rogowski coil belt is shown in fig.(3.2), with its eqivalent circuit in fig.(3.3). The circuit equation for this arrangement is,

$$\frac{d\,\phi}{d\,t} = L\,\frac{d\,i}{d\,t} + i(R+r) + \frac{1}{C}\int_0^t i\,dt. \qquad (3.4)$$

The Rogowski coil is commonly used in two modes of operation:-

1) The Differentiating Rogowski Coil.

In this case R is chosen such that $R \gg r$ and $R \gg L\omega$, where $\omega$ is the highest significant frequency of $\phi$, and for times $\ll RC$, it is

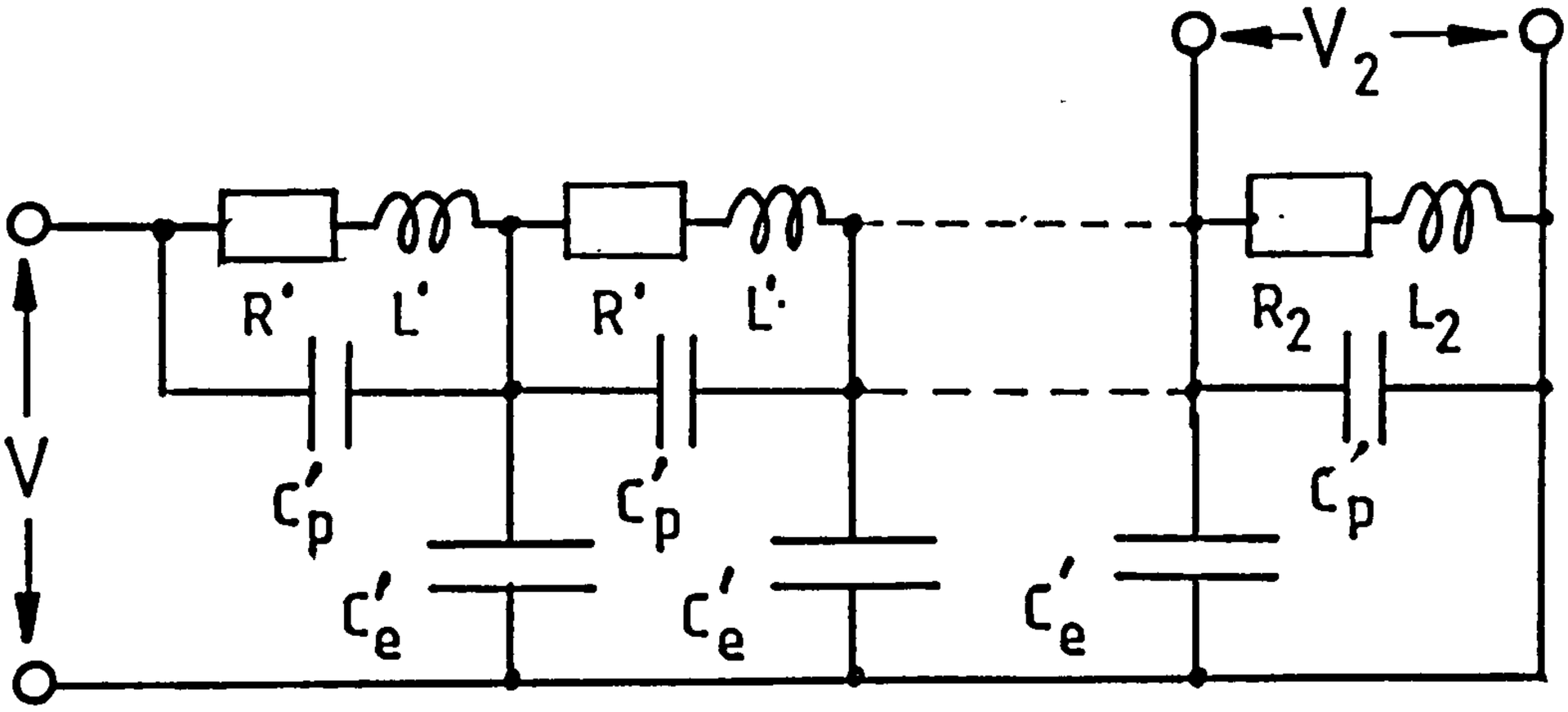


Fig.(3.1). Voltage divider showing stray capacitances and inductances. $R=nR'$, $L=nL'$, $C_e=nC'_e$, $C_p=C'_p/n$, $R_2=R'$, $L_2=L'$, $R_1=(n-1)R'$.

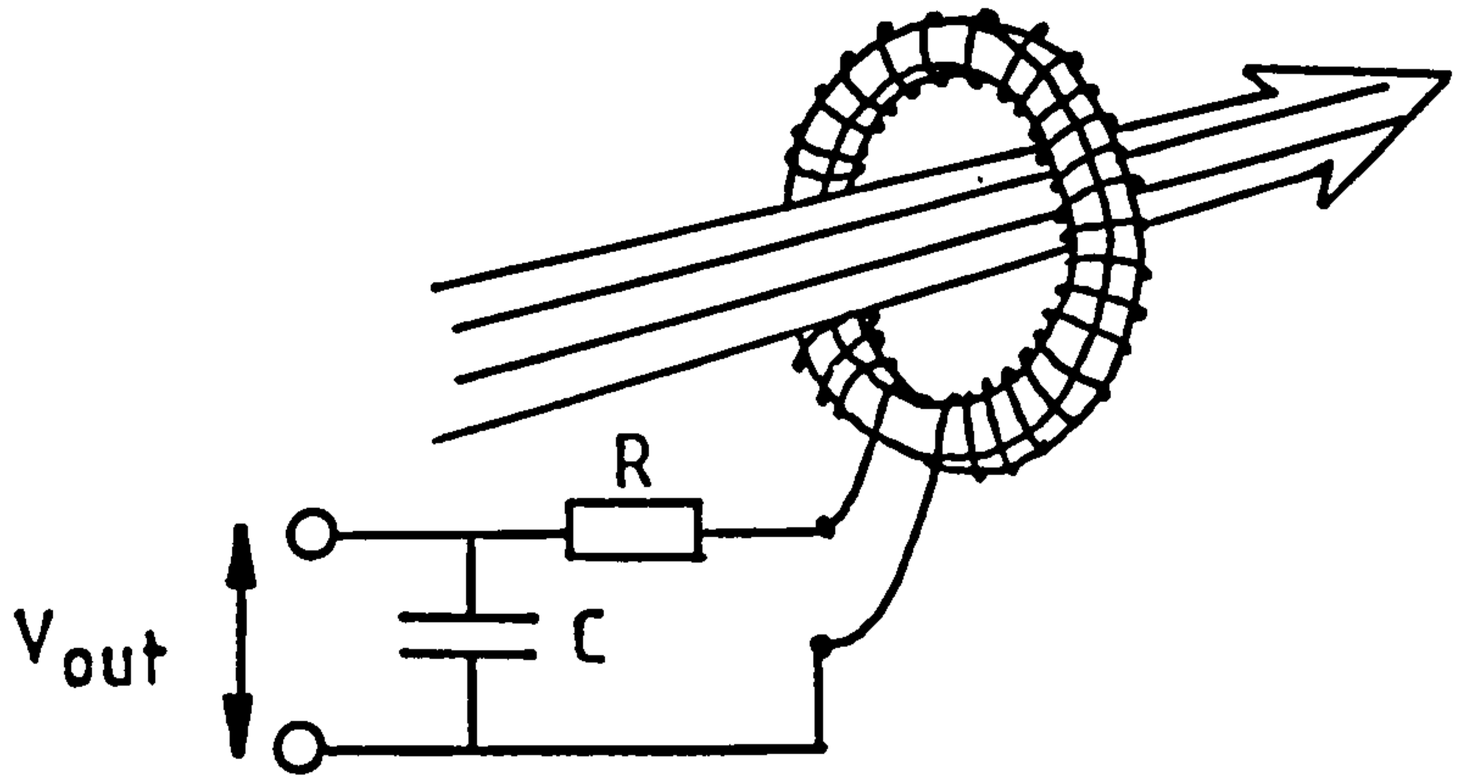


Fig.(3.2). Rogowski coil with passive integration network.

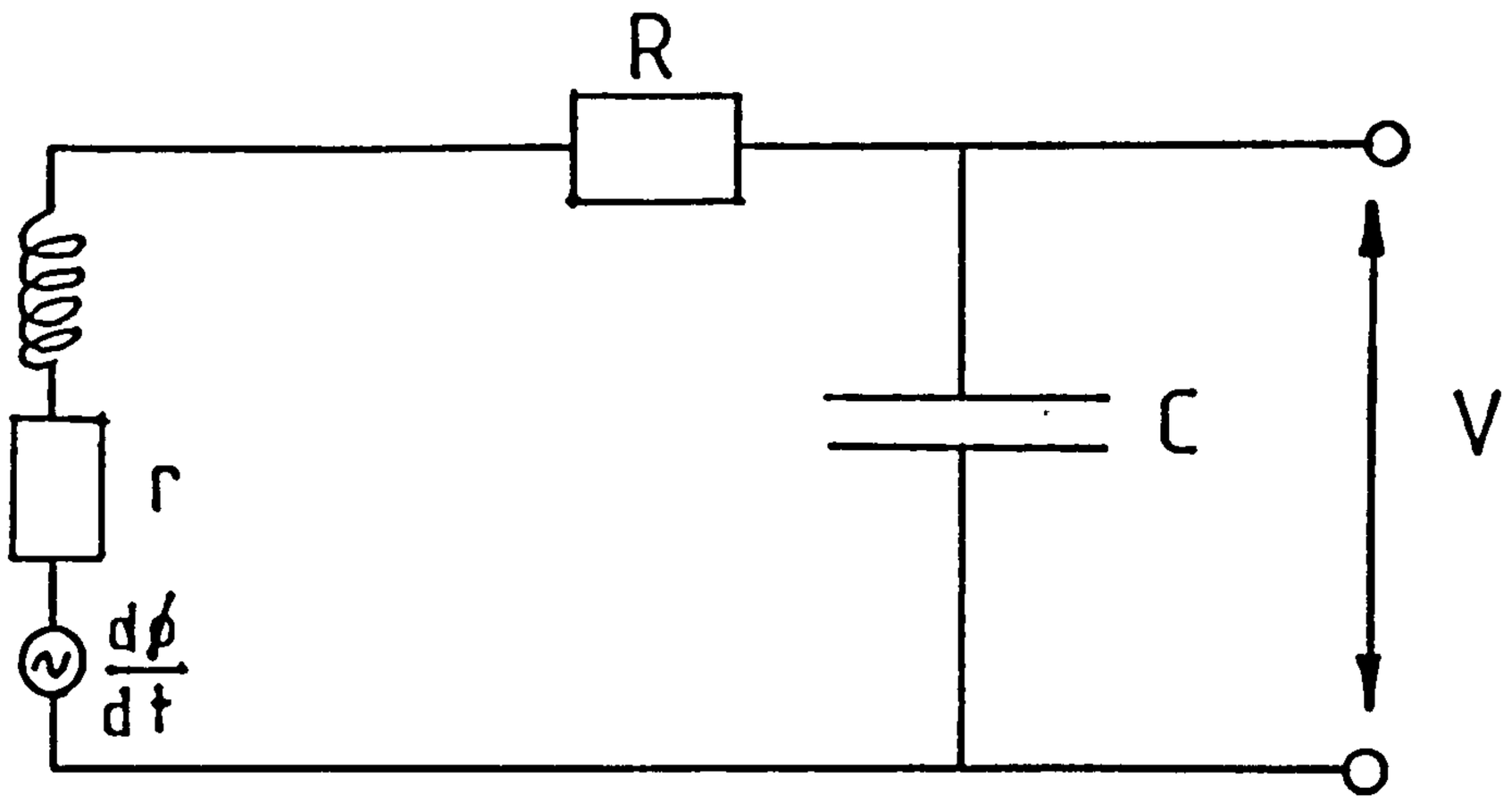


Fig.(3.3). Rogowski coil circuit with passive integrator, differentiating mode.

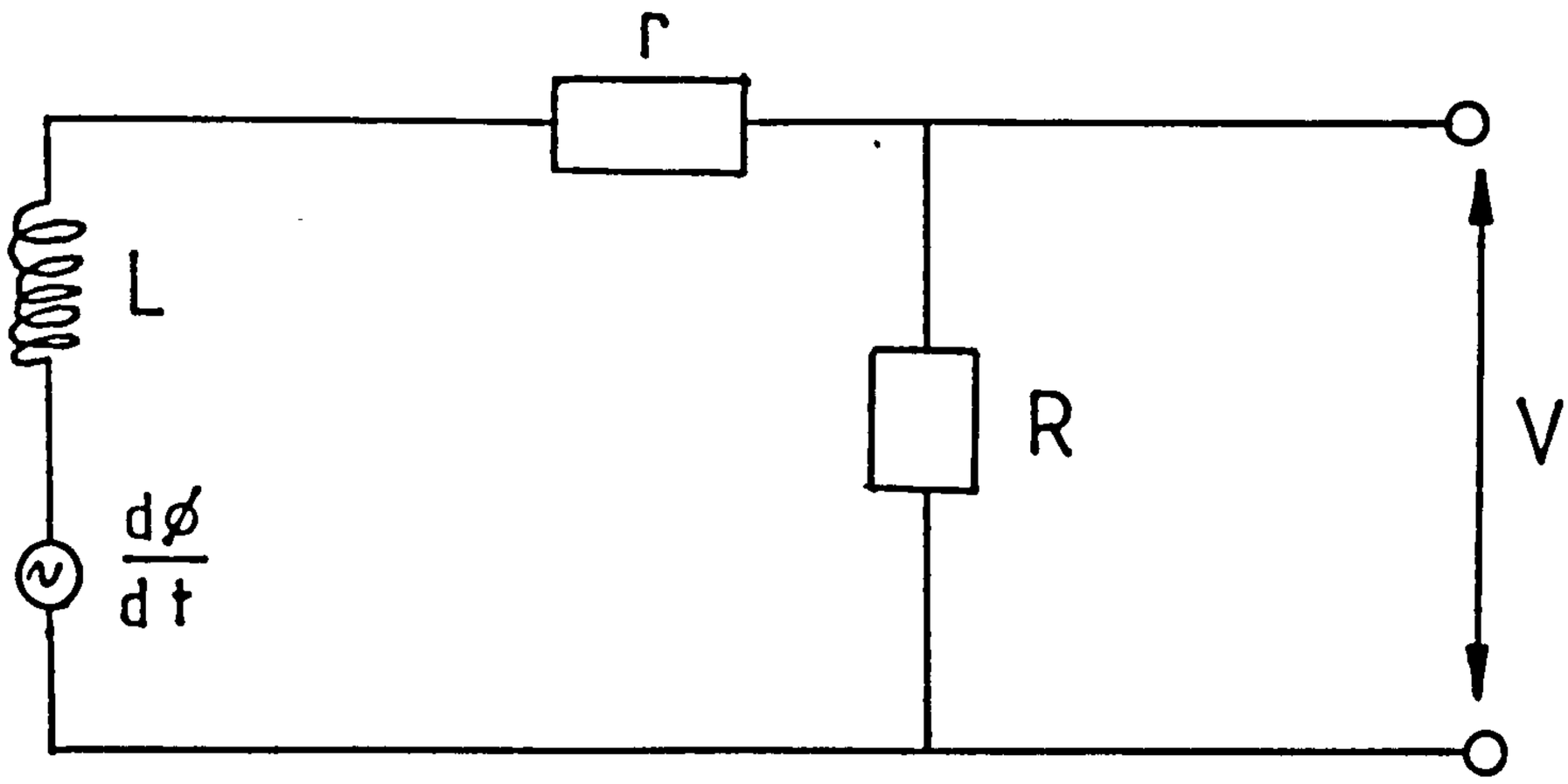


Fig.(3.4). Rogowski coil circuit, self integrating mode.

possible to show that,

$$V(t) = \frac{K\,N}{R\,C}\,I(t). \qquad (3.5)$$

Where,

I = the current flowing through the main circuit

$$K = \frac{\mu_0\,A}{s}$$

A = the cross-sectional area of the individual turns,

s = the mean circumference of the torus,

N = the total number of turns.

This type of coil is conveniently used to measure currents which are changing with typical rise times $\geq 1\mu s$. This condition is satisfied by the magnetic field circuits.

2) <u>The Self-integrating Rogowski Coil</u>.

If the measurement of faster rising pulses is required, then the coil may be used in the simpler self-integrating mode.

The relevant circuit is shown in fig.(3.4), here r is no longer assumed negligible w.r.t. R, and R is chosen such that $(R+r) \ll L\omega$. It is thus easily shown that,

$$V(t) = \frac{R}{N}\,I(t). \qquad (3.6)$$

Where again,

N = the total no of turns in the Rog. coil,

I = the current through the Rog. coil loop.

Such a coil will be used to monitor the Marx discharge current, rise time $<100ns$.

Rogowski Coils Used to Monitor the E.C.M.

Three coils were used to monitor and calibrate the operation of the electron cyclotron maser, the green, grey and black coils. The green was used exclusively in the self-integrating mode and monitored the Marx discharge current. The grey was used in both the self integrating mode, to monitor the witness plate return current (see below), and in the differentiating mode, to monitor the current through coil#1. The black coil was used in the differentiating mode to monitor the current through coil#2. The sensitivities of these coils are presented in tables (3.1) and (3.2). (To maintain a matched 50Ω working environment when using the Rogowski coils in the self-integrating mode, a 50Ω resistor could be placed in series with the low resistace Rogowski coil circuit. This matched the circuit to the 50Ω termination used in conjunction with the transient recorder used to monitor the coil output).

Using these methods the current through both field coils and the Marx discharge current may be measured and monitored during every shot of the maser.

## 3.4 Field Coil Calibration.

A magnetic field probe coil was constructed and used to calibrate the magnetic field coils (50),

It is possible to show that in a changing B-field, with the coil placed in the circuit shown in fig.(3.5),

$$V_0 = \frac{N\,A}{R\,C}\,B. \qquad (3.7)$$

Where,

N = The total number of turns

A = Probe coil radius

R C = The integration time of the circuit.

the constructed coil dimensions were,

| Rog coils : self-integrating | | $\frac{r/N}{V/kA}$ |
|---|---|---|
| Green | with matching resistor | 17.8 ± .25 |
| | without matching resistor | 35.7 ± .5 |
| Grey | with matching resistor | 23.3 ± .25 |
| | without matching resistor | 46.5 ± .5 |

Table(3.1). Self integrating Rogowski coil parameters

| Rog. coil: Diff. | $\frac{\text{RC time}}{\text{ms}}$ | $\frac{K\ N}{Nm/kA^2}$ | $\frac{KN/RC}{mV/kA}$ |
|---|---|---|---|
| Grey | 10.38 ± .01 | .873 ± .007 | 84.1 ± .7 |
| Black | 10.38 ± .01 | .812 ± .007 | 78.2 ± .7 |

Table(3.2). Differentiating Rogowski coil parameters.

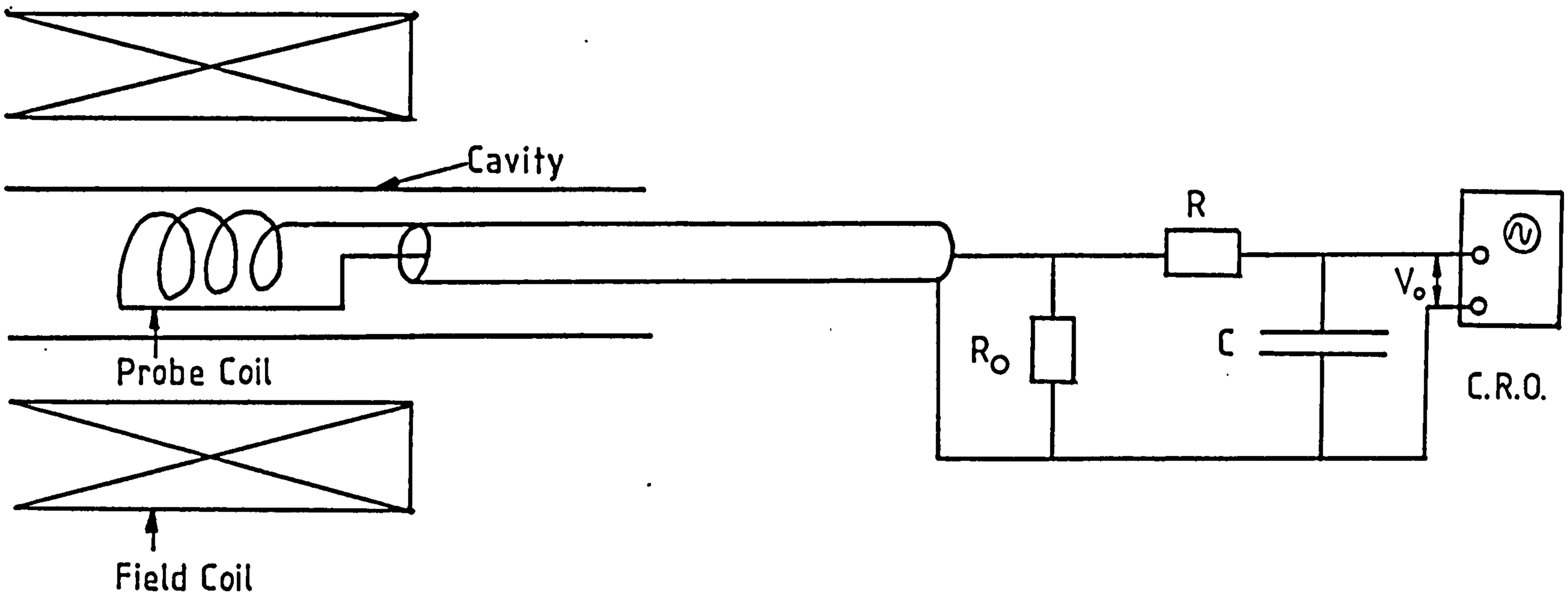


Fig. (3.5). Cavity B-field probe with associated circuit.

wire diameter = .1 mm

mean coil radius = 6.35 mm

coil length = 8 mm

No of turns = 75

Substituting these dimensions into eqn.(3.7) yields,

$$\frac{N\,A}{R\,C} = .207\,\frac{V}{T}\,. \qquad (3.8)$$

3.5 Relativistic Electron Beam Probe.

In chapter 4 it will be demonstrated that it is impossible to measure the relativistic electron beam current from the Marx discharge current. The majority of the electrons are produced from the cathode tip after the HT voltage has effectively dropped to zero. These electrons are part of a low voltage arc discharge and do not take part in the electron cyclotron maser mechanism.

In an attempt to measure the beam current a cavity probe was constructed and placed in the vacuum system, fig.(3.6). This probe consisted of a glass tube inserted in the cavity, on the end of which a copper witness plate was suspended, diameter 5.5mm. The other end of the glass was attached to a copper tube via a locating pin. The witness plate was connected electrically to the copper tube via an unshielded copper wire. The copper tube was taken out of the vacuum system via a vacuum seal and connected to earth. The probe was electrically insulated from the anode. Any electrons thus reaching the witness plate, provided no breakdown occurs, must be part of the free HT electron beam travelling through the cavity. The return current may then be measured via a self-integrating Rogowski coil.

Unfortunately it will be shown in chapter 4 that the beam probe will fail to measure the R.E.B. directly. As the Marx discharge current starts there is simultaneous breakdown between the anode, cathode and the witness plate. The probe signal is therefore swamped by a low voltage, high-current arc discharge. With the Marx discharge, the anode cathode chamber and the E.C.M. cavity

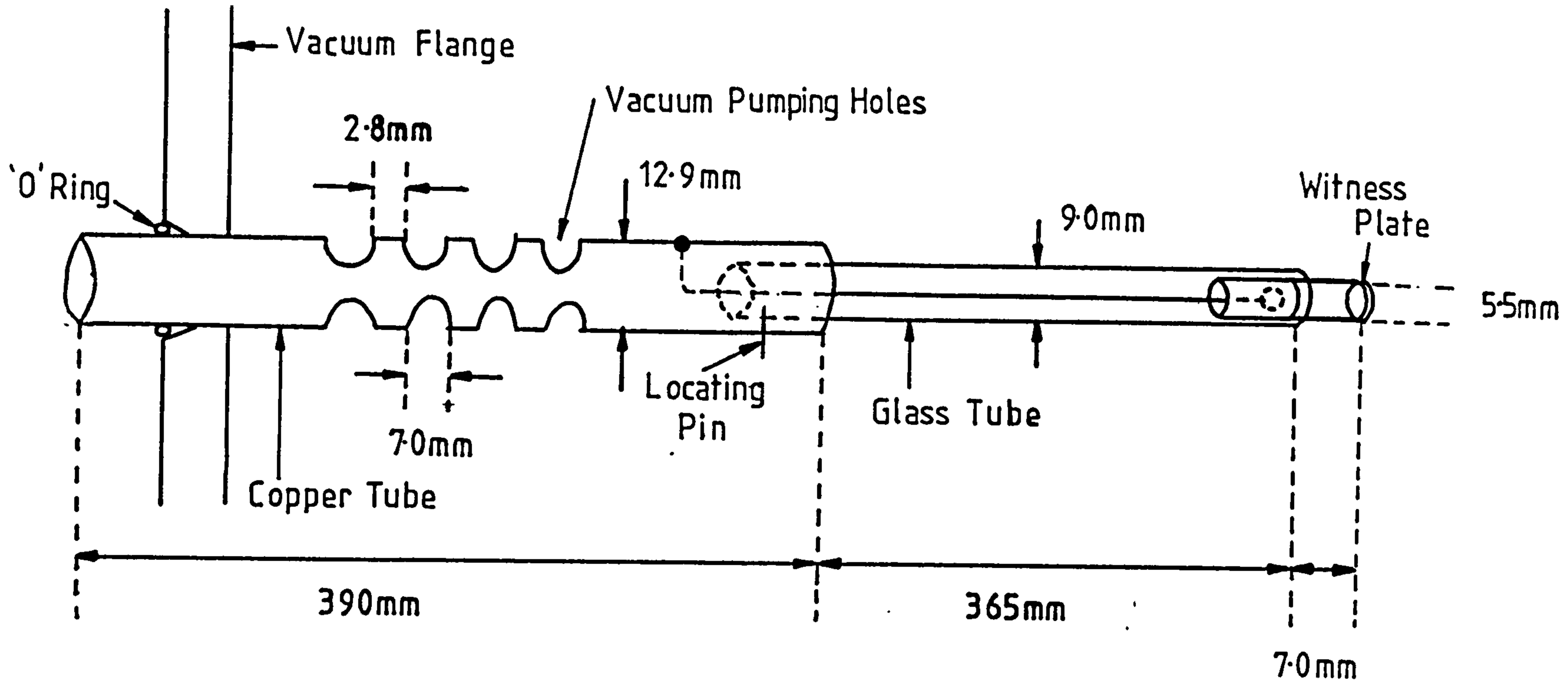


Fig.(3.6). Relativistic electron beam probe.

will fill up with highly conducting plasma after the HT voltage has dropped effectively to zero. Hence to measure the R.E.B. current directly a more sophisticated, electrostatically shielded, beam probe is required. The subsequent current would be taken to ground via a co-axial cable with only the HT electrons reaching the witness plate.

Although this probe proved unable to measure the beam current directly, this could be estimated via the substantial melting and evaporation of copper produced when the electron beam deposited its energy in the witness plate.

The probe may also be used to measure the diameter and position of the electron beam, and the relative effect on the beam, in both current and position, with the subsequent alteration of the E.C.M.'s operating parameters.

One consideration made in the design of the beam probe was that of vacuum pumping. The diffusion pump is situated at the output end of the cavity, through which the cathode chamber is pumped. Thus it was essential to ensure a pumping path existed through the copper and glass tube, past the witness plate. There is no means of measuring the pressure in the cathode chamber, however if this is not below $\simeq 10^{-5}$ torr then the pressure may be measured indirectly via adverse effects on the diode voltage.

## 3.6 Monitoring system, Screened rooms and Cable Screening.

Due to the high-voltage, high-current, transients which occur during the discharge of all the capacitor banks, a background noise level of many volts is generated in the laboratory during any shot. These transients could seriously damage components such as the computer and the transient recorders and as the output from the crystal detector is extremely low, $\lesssim$100mV, it would be very difficult to extract this signal from the much larger background noise level. To remove this problem the entire detection and monitoring system was double screened, with all the measuring and data storage eqipment placed in two screened rooms.

The monitoring system of the E.C.M. is shown in fig.(3.7). Three double screened signal lines were used to transmit the signal from

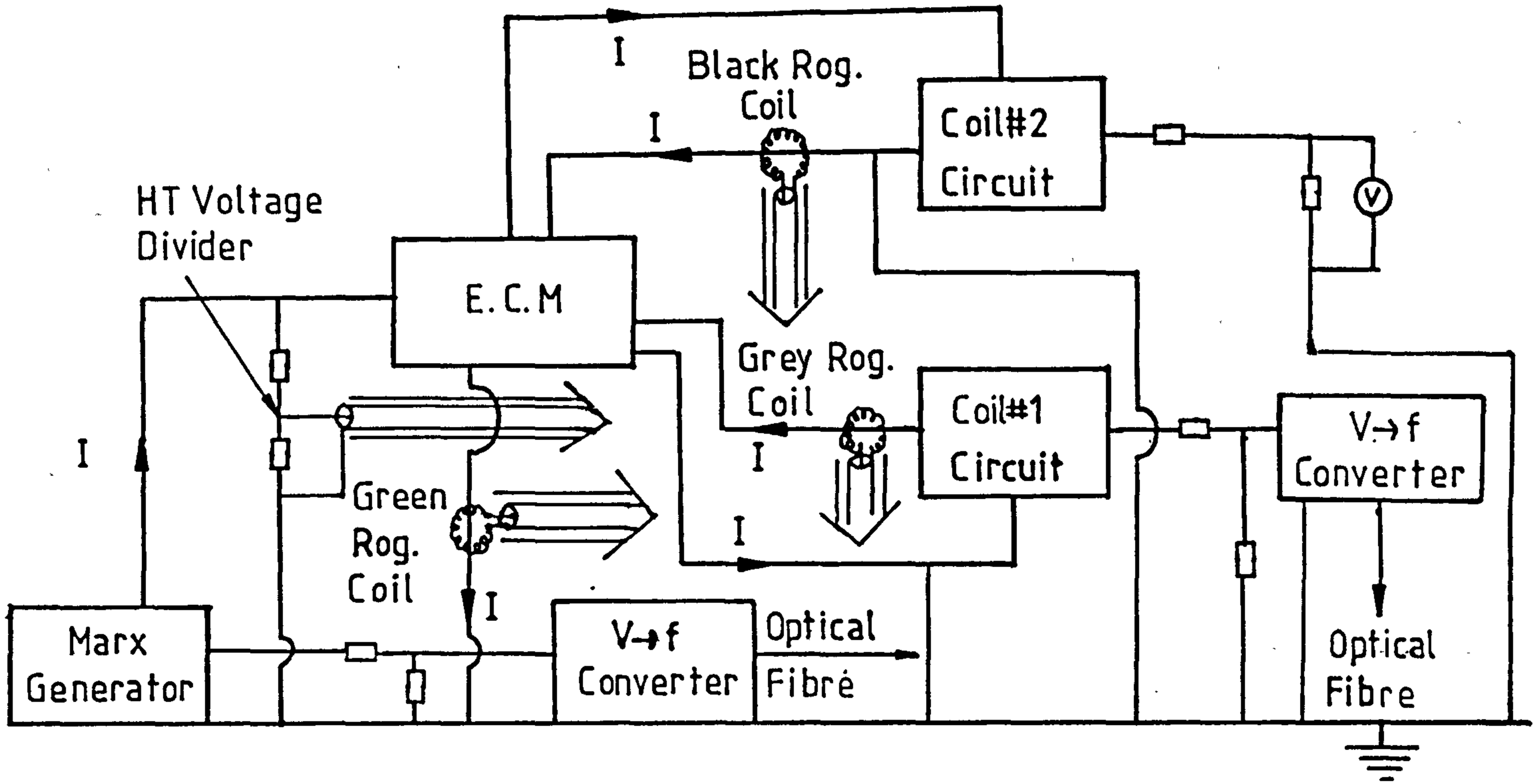


Fig.(3.7). Monitoring diagnostics of the E.C.M. All arrows lead to screened room 1

the green and grey Rogowski coils and the HT voltage divider to the screened room. In an attempt to mimimise the number of electrical signal lines entering the screened room, and hence the background noise level, the two slowly varying voltage signals, monitoring the charging of the Marx bank and of the coil#1 capacitor banks, were transmitted into the screened room via optical fibres. These measurements were made using a voltage divider and a commercially available HT probe respectively. The subsequent signals were fed through a voltage to frequency converter and transformed into an optical signal by a light emitting diode. In the screened room this information was decoded from the optical signal and monitored by the HP9816 computer.

Two screened rooms were used in conjunction with the Mk-6 maser; screened room#1 housed all the monitoring equipment and controlled the overall running of the experiment. Screened room#2 had only one input, that of the mm-wave crystal detector output. The purpose of this second screened room was to have as 'quiet' an environment as possible for the analysis of the mm-wave output of the system.

Screened Room#1.

The screened room#1, fig.(3.8), housed the HP9816 computer, the two transient recorders and the decoder for the optical input signals. This allowed the computer to monitor the Marx bank and the coil#1 capacitor bank charging voltages. When these reached a predetermined value the computer fired the maser via a compressed air operated switch. The transient recorders would then monitor the diode discharge current and voltage, and the current in both the field coils. All of these signals have magnitudes well above the noise level. The resulting data in the transient recorder could be displayed on an oscilloscope screen or transferred to the HP9816 computer. Once transferred the data may be plotted with a variable time base on the computer screen, dot matrix printer or stored for future reference on 3.5" magnetic disc.

The working noise level in screened room#1 was measured at ≈50mV. This is low enough to allow the safe use of the computer

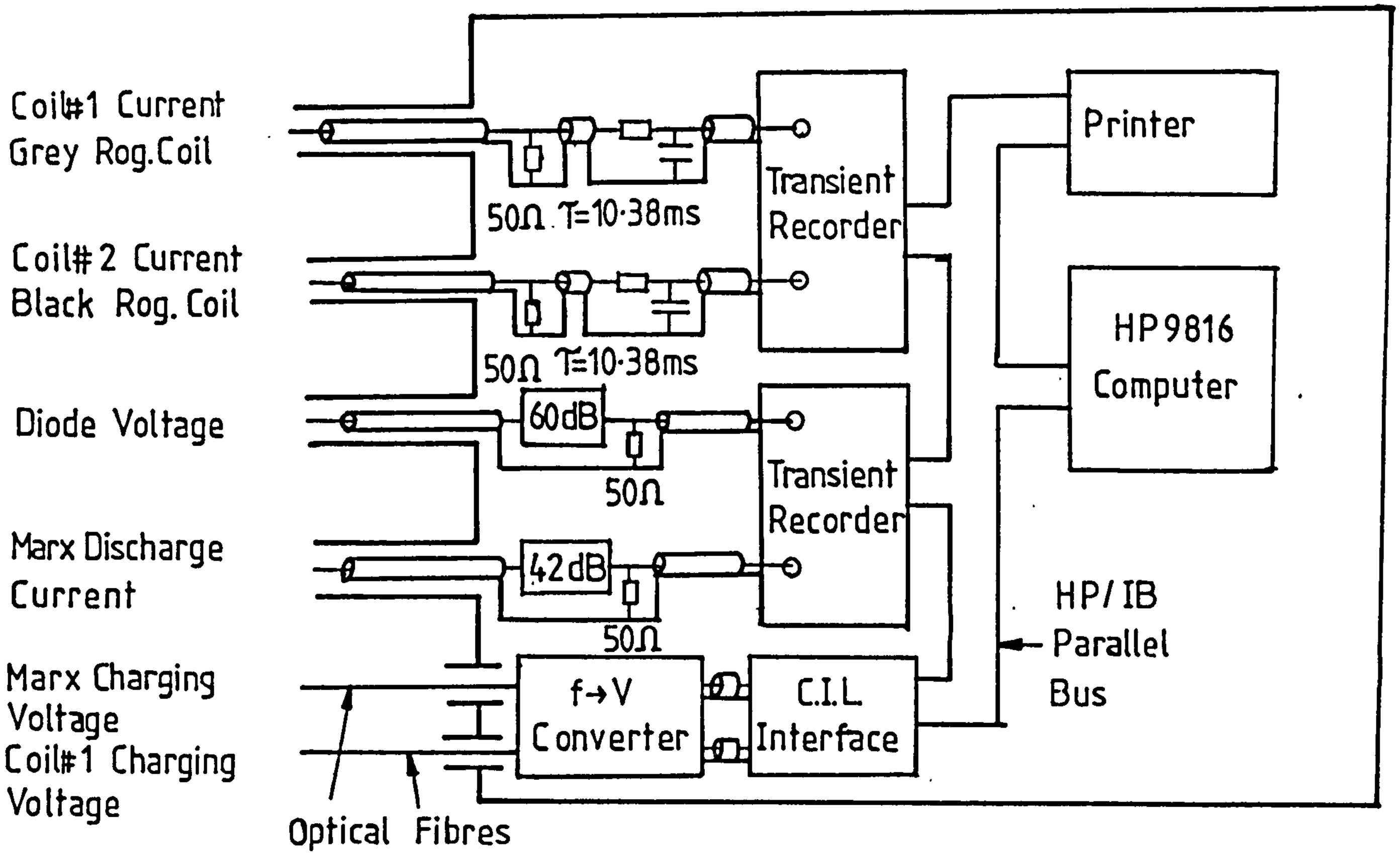


Fig.(3.8). Monitoring screened room, screened room#1.

and the transient recorders.

Screened Room#2.

In past experiments at Strathclyde University only one screened room was used, however as the maximum safe output of the crystal detector and amplifier is ≃300mV this would result in a useful dynamic range of ≃6 in screened room#1. In an attempt to increase this dynamic range screened room#2, housing only the mm-wave detection system, was used. This resulted in a quieter working environment with a measured noise level ≤5mV. A detailed description of how this screened room was used, under various experimental configurations, to measure different aspects of the maser output will be described in chapter 4.

All screened cables and attenuators were used in a 50Ω environment, thus minimising reflections in the cables. Only one central earth was used, to prevent the formation of earth loops.

## 3.7 mm-Wave Detection.

### 1) W-band.

A Flann 135 rectifying crystal detector was used for all W-band mm-wave detection. This was calibrated for both power and sensitivity versus frequency using the experimental configuration shown in fig.(3.9). A backward wave oscillator (B.W.O.) was used as a tunable W-band source. The output was fed through an isolator with an Anritsu power meter used to measure the power delivered to the detector via a 10dB coupler. The detector output was monitored on a Schlumberger digital microvoltmeter and the frequency output of the B.W.O. measured with a Flann calibrated wavemeter.

Two terminations were tested with this detector, a plunger short and a matched load termination. The plunger short reflects the mm-waves, producing a standing wave pattern at the detector. This will make the crystal sensitive, though frequency dependent. The detector sensitivity may be maximised for any given frequency by

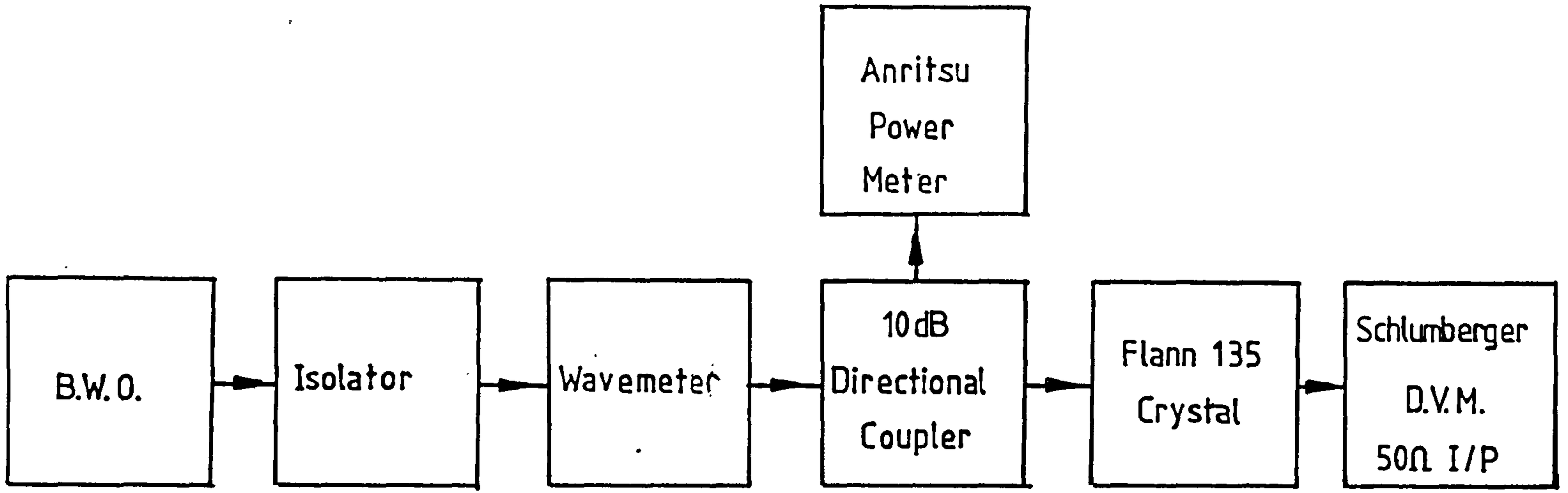


Fig.(3.9). Schematic diagram of apparatus used to calibrate W-band crystal detector.

adjusting the short position with respect to the crystal.

The load termination absorbs any mm-wave radiation incident upon it. This will result in the detector seeing a travelling wave, resulting in a flat frequency response from the detector; however the sensitivity may be reduced.

The sensitivity of the detector with respect to frequency with both terminations is presented in fig.(3.10). As the E.C.M. is a tunable system oscillating at high power throughout the W-band, the crystal will be used in all subsequent experiments with the load termination. This will make the detector less sensitive, as expected, however it will have a flat frequency response with a maximum sensitivity variation of 26% between 75GHz and 105GHz. Above 105GHz the sensitivity of the detector drops off by ≈55%.

It is also possible to calibrate the detector output for power in this frequency band, measuring the detector's linearity and sensitivity. Each crystal detector will have its own characteristic with respect to input power. At low power the detector output will be proportional to the power in (i.e. $V_{out} \propto V_{in}^2$), this is known as the square law region of the detector characteristic. At some point the detector characteristic will move into the linear region were the output will be proportional to the square root of the power in (i.e. $V_{out} \propto V_{in}$). At some subsequent higher value the detector output will saturate and finally the detector will be destroyed.

The detector power response was measured at four frequency values and the results plotted in fig.(3.11). At all four frequencies the detector output is proportional to the power in, hence it is operating in the square law region of its characteristic. From the B.W.O. experiments it is impossible to measure at what power levels the detector will move into the linear region of its characteristic, as the B.W.O. will not supply enough power. However from experiments on the E.C.M, using a calibrated attenuator, it was possible to demonstrate that the detector output remains in the square law region up to an output voltage of ≈18mV.

Although the detector has been calibrated for power this will not be utilised in subsequent experiments. This is due to the

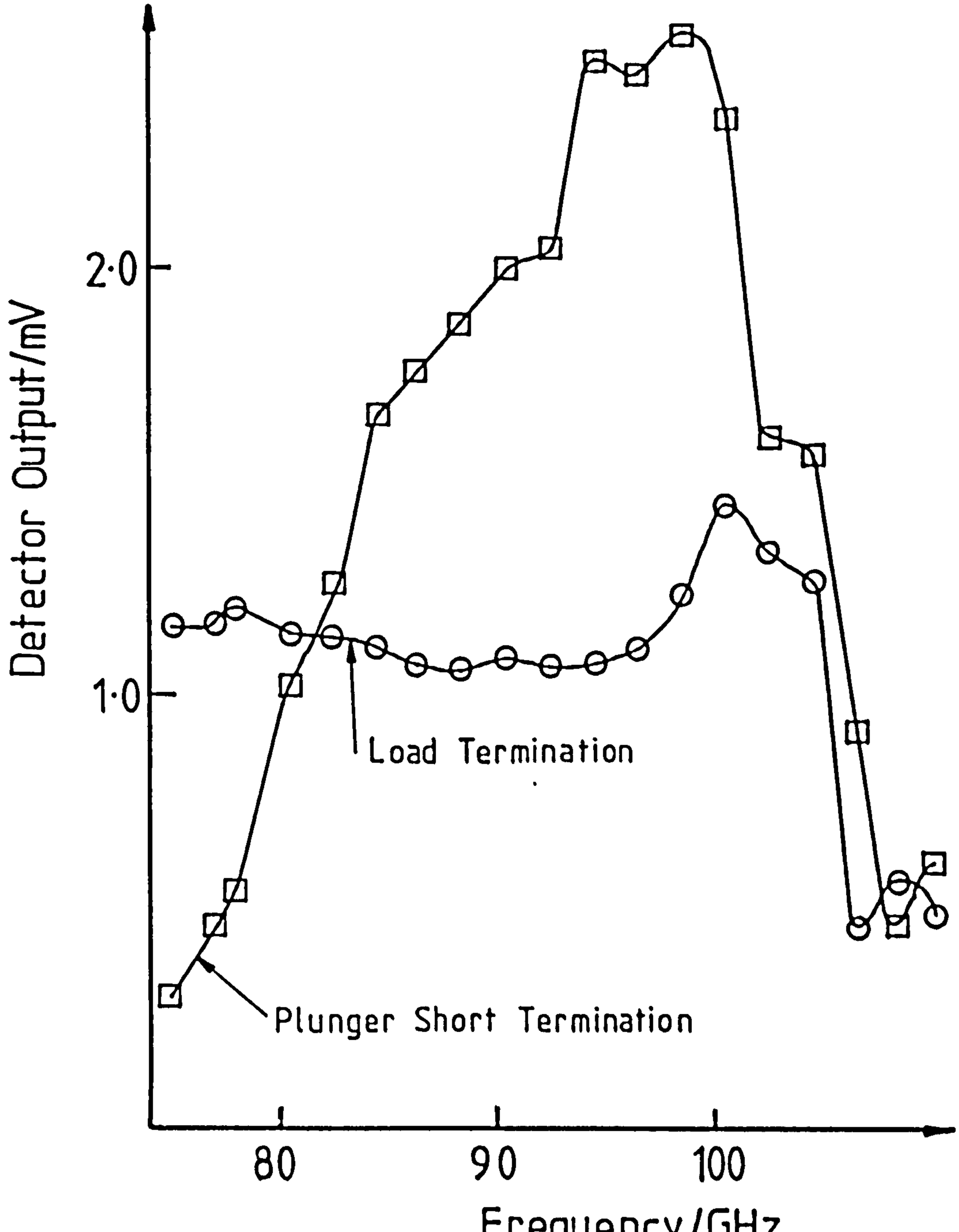


Fig.(3.10). Calibration curves of Flann 135 detector, sensitivity versus frequency, with a constant 8mW mm-wave input power.

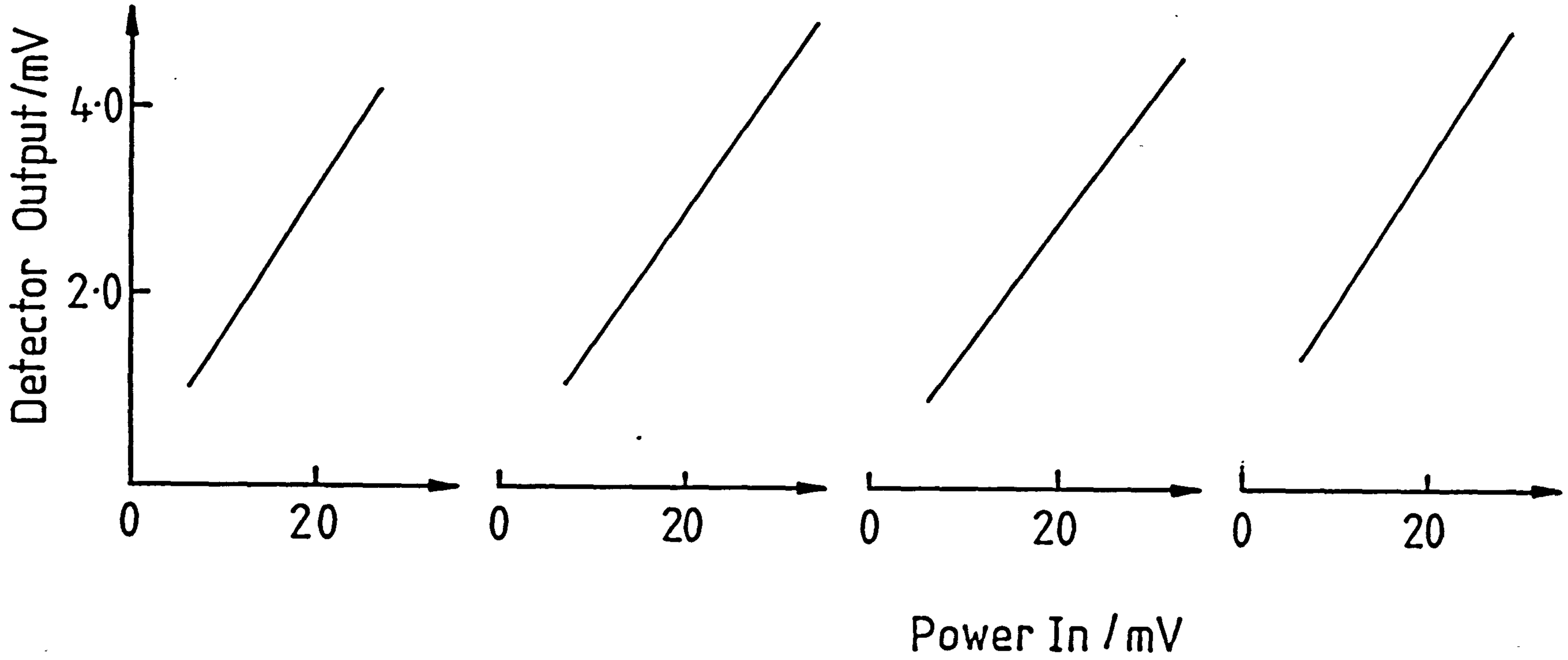


Fig.(3.11). Flann 135 detector power response.

difficulty in the calibration of the mm-wave components which will be used to collect and transmit the maser output to the crystal detector.

Great care had to be taken, via the generous use of W-band attenuators, to ensure that the detector did not receive a direct high power mm-wave signal which would have destroyed or at any rate desensitized the crystal.

As will be described in detail in chapter 4, for the first time at Strathclyde University, a two detector measurement technique was used. In the W-band this allowed the elimination of any pulse to pulse variation in the output power of the maser while measuring the radiation intensity pattern across the output window. A Baytron V-band detector in a W-band mount was used uncalibrated to produce a reference, allowing the pulse to pulse variation of the output power of the maser to be monitored.

2) G-band.

Although a G-band source was available (a frequency doubler, which could be used in conjunction with the B.W.O.), no calibrated detector or power meter, working in the G-band, was available. Hence it was difficult to directly calibrate any detector in the G-band for either power or sensitivity versus frequency. If a full analysis was to be performed on the G-band output of the maser, as was done in the W-band, then these measurements would be essential. However the aim of this project is to identify G-band oscillation and measure the frequency, without attempting mode identification or power measurements. In such a case uncalibrated detectors will be shown to be adequate, with suitable restrictions placed on the interpretation of the results

Although the Flann 135 detector, with the load termination, was suitable for making direct measurements of the maser output it was not sensitive enough to be used in the spectrometer. Hence a fresh Flann 137 crystal was used with a plunger termination. On tests with the E.C.M. output this crystal/back-short combination increased the detected output signal by ≈15dB over the Flann 135 detector.

Again, to remove the fluctuating output power of the maser, the Flann 135 crystal was used to provide a reference during the spectroscopic analysis of the maser.

The output from both the Flann 135 in the W-band and the Flann 137 in the G-band is extremely low, the maximum output (without risking damage) from both detectors being ≈18mV. These signals would have been very difficult to measure on an oscilloscope, hence a fast time response amplifier was constructed, circuit diagram fig.(3.12). This was calibrated using a pulse generator with a similar rise time and duration to that of the mm-wave pulse. The amplifier gain was measured at 16.3 and the output remained linear up to >1000mV. The rise time of the amplifier was found to be ≈100ns; this is significantly shorter than the maser pulse length (>300ns), however it cannot be used to measure the mm-wave rise time, which is itself <100ns.

## 3.8 Mode Analysis and Far Field Radiation Pattern.

As explained in chapter 1 and chapter 2 the gyrating electron beam interacts with a positive energy waveguide mode. Which mode will be excited depends on the gyration frequency of the electrons and the resonant frequency of the individual modes, along with such considerations as the mode dependent cavity quality factor and the spatial coupling of the relativistic electron beam to the E-field maxima. For many reasons and applications it is essential to be able to identify which modes are oscillating in the cavity. There are several different experimental methods of doing this, however they all rely on the ability to calculate the theoretical near- and far-field radiation patterns.

In such a radiation pattern there are three main regions defined (51). The Rayleigh region is effectively the near field where the radiation distribution reflects closely that of the intra-cavity field distribution. The Rayleigh region is a subset of the Fresnel region and ends at a distance of $\approx D^2/2\lambda$, were D is the aperture diameter. At this distance the radiation pattern is beginning to deviate significantly from the intra-cavity pattern. Throughout the

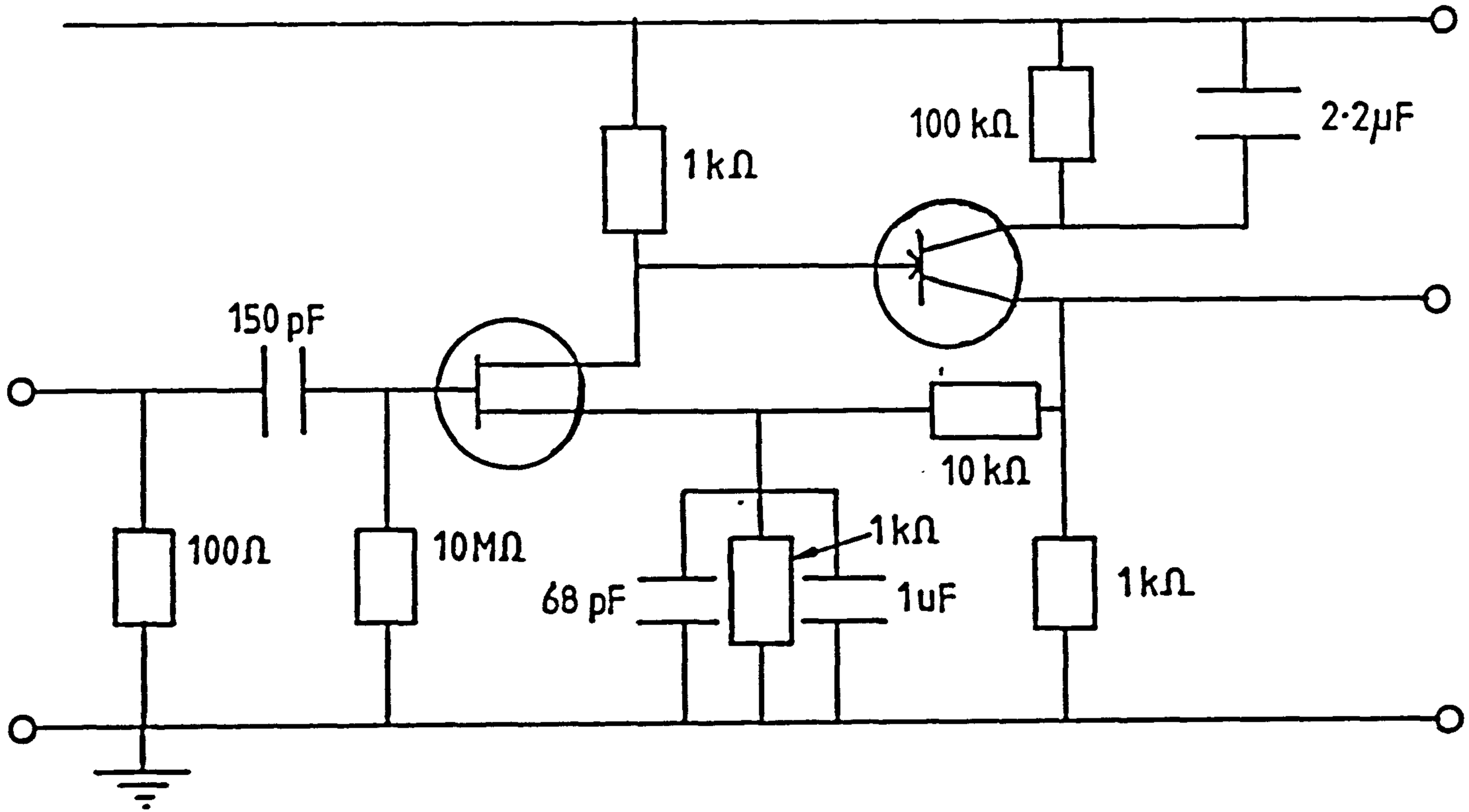


Fig.(3.12). Circuit diagram of fast time response amplifier.

rest of the Fresnel region, the mode pattern will be a complex function of distance until, at $\simeq 2D^2/\lambda$, the pattern moves into the Fraunhofer or far field region. This is defined such that the radiation pattern does not further change with distance.

Intra-Cavity Mode Structure.

This has relevance to two important aspects of the electron cyclotron maser operation.

1) If the radiation pattern is measured well within the Rayleigh region then it may be used to identify the mode oscillating in the cavity.
2) The intra-cavity mode structure may be used to qualitatively estimate the relative coupling between any mode and the R.E.B., with respect to its measured position and the calculated E-field maxima. This, along with the cavity quality factor, will be used to explain why certain modes may oscillate while others are suppressed.

To calculate the intra-cavity mode structure one must solve Maxwell's equations inside a conducting, cylindrical waveguide, this has been done by many authors (40,52) and yields the components of the E and H fields given in table(3.3).

The power flux may thus be calculated from the Poynting vector,

$$S = E \times H \tag{3.9}$$

$$\Rightarrow \quad S_z = E_r H_\theta - E_\theta H_r \tag{3.10}$$

and the normalization constants from,

$$P = \int_{r=0}^{a} \int_{\theta=0}^{2\pi} S \; r dr \; d\theta \tag{3.11}$$

where P is the power flowing down the waveguide. Eqn.(3.9) yields the results,

| $TE_{pq}$ Modes | $TM_{pq}$ Modes |
|---|---|
| $E_z = 0$ | $E_z = N J_p(k_\perp r)\cos(p\theta)$ |
| $E_r = \frac{j\omega\mu\mu_0 p}{k_\perp^2 r} N' J_p(k_\perp r)\cos(p\theta)$ | $E_r = -\frac{jk_\parallel}{k_\perp} N' J_p'(k_\perp r)\cos(p\theta)$ |
| $E_\theta = \frac{j\omega\mu\mu_0}{k_\perp} N' J_p'(k_\perp r)\sin(p\theta)$ | $E_\theta = \frac{jk_\parallel p}{k_\perp^2 r} N J_p(k_\perp r)\sin(p\theta)$ |
| $H_z = N' J_p(k_\perp r)\sin(p\theta)$ | $H_z = 0$ |
| $H_r = -\frac{jk_\parallel}{k_\perp} N' J_p'(k_\perp r)\sin(p\theta)$ | $H_r = -\frac{j\omega\epsilon\epsilon_0 p}{k_\perp^2 r} N J_p'(k_\perp r)\sin(p\theta)$ |
| $H_\theta = \frac{jk_\parallel p}{k_\perp^2 r} N' J_p'(k_\perp r)\cos(p\theta)$ | $H_\theta = -\frac{j\omega\epsilon\epsilon_0}{k_\perp} N J_p(k_\perp r)\cos(p\theta)$ |

where,

$k_\perp a = \chi_{pq}$ , the $q^{th}$ root of $J_p(x)=0$: TM modes,

$= \chi'_{pq}$, the $q^{th}$ root of $J'_p(x)=0$: TE modes

$a$ = the radius of the waveguide

and N, N' are normalization constants.

Table (3.3). E and H fields in a cylindrical waveguide

$$N' = \frac{2\,j\,\chi_{pq}'\,\sqrt{P}}{a^2\left[1-\frac{p^2}{\chi_{pq}'}\right]^{1/2} J_p(\chi_{pq})\,\sqrt{(\omega\mu\mu_0 k_{\parallel}\pi)}}, \qquad (3.12)$$

if p=0 then the 2 is replaced by √2, and

$$\text{and} \quad N = \frac{2\,j\,\chi_{pq}\,\sqrt{P}}{a^2\,\sqrt{(\omega\epsilon\epsilon_0 k_{\parallel}\pi)}\,J_n'(\chi_{pq})}. \qquad (3.13)$$

Eqn.(3.10) yields the power flux down the waveguide as a function of r and θ.

For $TE_{pq}$ modes,

$$S = \frac{4\,P}{a^2\,\pi\,J_n^{\,2}(\chi_{pq}')\left[1-\frac{p^2}{\chi_{pq}^{\,2}}\right]} \times \left[\frac{p^2}{(k_\perp r)^2}J_n^{\,2}(k_\perp r)\,\mathrm{Sin}^2(n\theta) + J_n'^{2}(k_\perp r)\,\mathrm{Cos}^2(n\theta)\right], \qquad (3.14)$$

replacing 4 by 2 if p=0, and for $TM_{pq}$ modes,

$$S = \frac{4\,P}{a^2\pi\,J_p'^{2}(\chi_{pq})} \times \left[J_n'^{2}(k_\perp r)\,\mathrm{Cos}^2(n\theta) + \frac{p^2}{(k_\perp r)^2}\,J_n^{\,2}(k_\perp r)\,\mathrm{Sin}^2(p\theta)\right]. \qquad (3.15)$$

These eqns.(3.14), (3.15) were thus coded in a program designed to run on an HP9816 personal computer (a listing of which is provided in Appendix 3). The calculations were checked against the self-consistent integral eqn.(3.11), which was solved numerically using Simpson's rule. Several examples of the output of this program are shown in fig.(3.13), with the power normalised to 1.

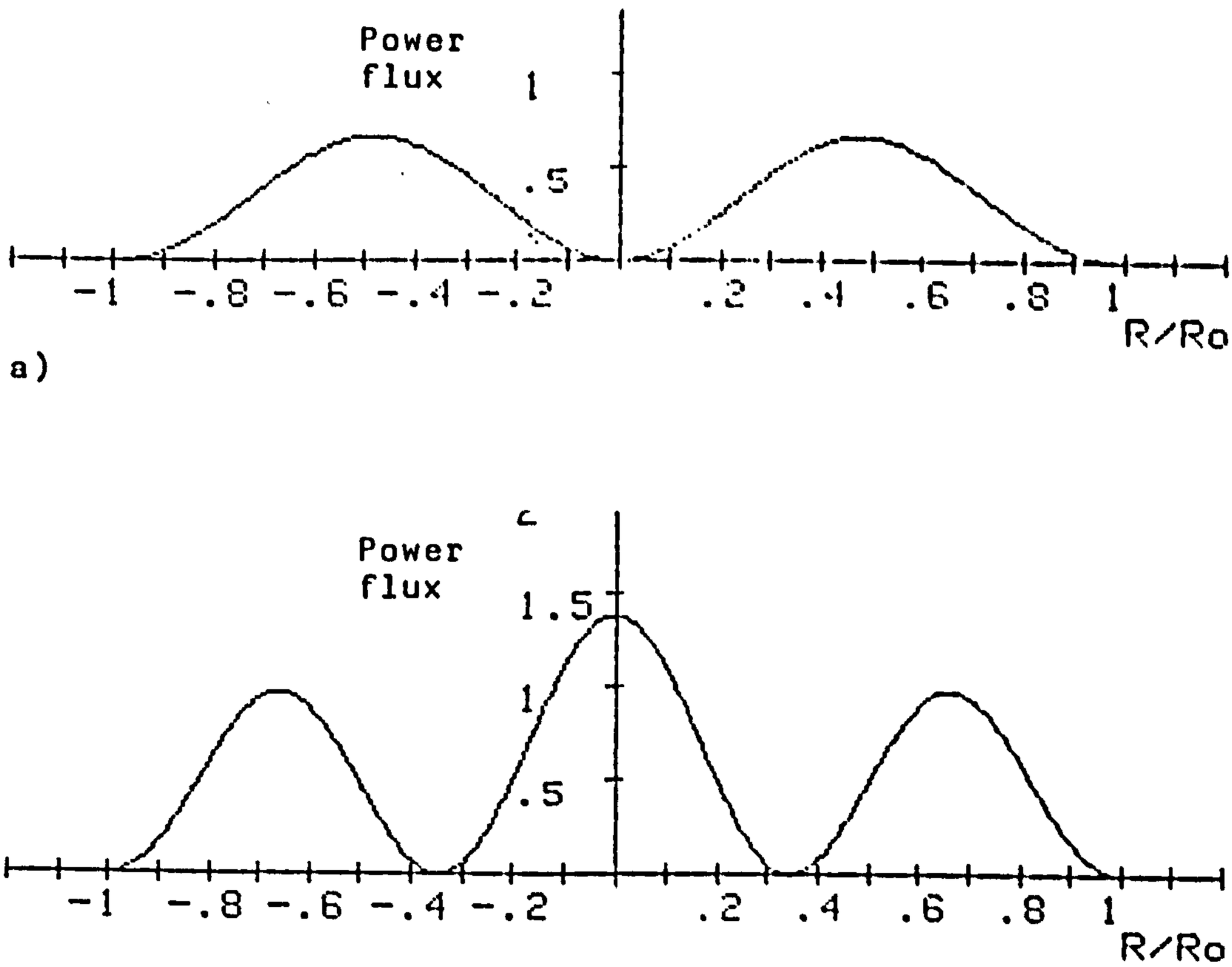


Fig.(3.13). Some typical intra-cavity mode pattern plots. a) The circularly symmetric $TE_{01}$. b) $TE_{12}$, $\phi=0°$. c) $TE_{12}$, $\phi=90°$.

Far Field Radiation Patterns (F.F.R.P.).

It may be shown that the mode pattern from an open ended, oversized, cylindrical waveguide may be expressed by the equations given in table(3.4) (53). The co-ordinate system used is shown in fig.(3.14).

The power flux density is again given by the Poynting vector,

$$S \propto (E_\theta^2 + E_\varphi^2). \qquad (3.20)$$

Hence the eqns.(3.16), (3.17), (3.18) and (3.19) were coded and checked against other published results. The program was designed to run on an HP 9816 personal computer and a listing has been provided in Appendix 4. Some typical plots of $TE_{pq}$ and $TM_{pq}$ modes are given in fig.(3.15).

Measuring the E.C.M. Radiation Pattern.

In past experiments at Strathclyde University (33,34) this has been achieved by scanning a detector across the far field radiation pattern (F.F.R.P), firing the maser at each position, keeping the operating conditions of the maser constant. This method is time consuming and laborious and depends on the reproducible excitation of one mode. If the cavity is oscillating in a regime where the resonant frequencies of the cavity modes are further apart than the gain bandwidth of the maser, then this may be possible. However at high frequencies, where the mode density increases in frequency space, mode-hopping may occur between shots or the cavity may oscillate in a multimode fashion; in either case this method will not work.

Under all considerations a single shot method of measuring the radiation pattern is desirable. This was attempted via two techniques utilising; 1) a liquid crystal sheet and, 2) an infra-red camera. (The experimental details of which are described in detail in appendix 5).

Both of these techniques worked in principle, however they required ≈25mJ/cm$^2$ incident intensity on the receiving medium for

For $TE_{pq}$ modes,

$$E_\theta = j^{p+1} \frac{p\ \omega\ \mu}{2\ R} F_{pq}(\theta)\ \mathrm{Sin}\ (p\phi)\ e^{-jk_0 R} \qquad (3.16)$$

$$F_\theta = \left[ 1 + \frac{k_\perp}{k_0} \mathrm{Cos}(\theta) + \Gamma \left[ 1 - \frac{k_\perp}{k_0} \right] \right] J_p(k_\perp a)\ \frac{J_p(k_0 a\ \mathrm{Sin}(\theta))}{\mathrm{Sin}(\theta)}$$

$$E_\phi = j^{p+1} \frac{k_0 a\ \omega\ \mu}{2\ R} f_{pq}(\theta)\mathrm{Cos}(p\phi)\ e^{-jk_0 R} \qquad (3.17)$$

$$f_{pq}(\theta) = \left[ \frac{k_\perp}{k_0} + \mathrm{Cos}(\theta) - \Gamma \left[ \frac{k_\perp}{k_0} - \mathrm{Cos}(\theta) \right] \right] x$$

$$\frac{J_p(k_\perp a)\ J_p'(k_0 a \mathrm{Sin}(\theta))}{\left[ 1 - \frac{k_0 \mathrm{Sin}(\theta)}{k_\perp} \right]}$$

and for $TM_{pq}$ modes,

$$E_\phi = 0 \qquad (3.18)$$

$$E_\theta = -j^{p+1} \frac{k_0 a}{2\ R} Q_{pq}(\theta)\ \mathrm{Cos}(p\phi)\ e^{-jk_0 R} \qquad (3.19)$$

$$Q_{pq}(\theta) = k_\perp \left[ \frac{k_\perp}{k_0} + \mathrm{Cos}(\theta) + \Gamma \left[ \frac{k_\perp}{k_0} - \mathrm{Cos}(\theta) \right] \right] x$$

$$\frac{J_p(k_0 a\ \mathrm{Sin}(\theta))\ J_p'(k_\perp a)}{\mathrm{Sin}(\theta) \left[ 1 - \left[ \frac{k_\perp}{k_0 \mathrm{Sin}(\theta)} \right]^2 \right]}$$

where $\Gamma$=the amplitude reflection coefficient from the open end of the waveguide, and all the other symbols are as previously defined.

Table(3.4). The far field electric fields from an open ended cylindrical waveguide.

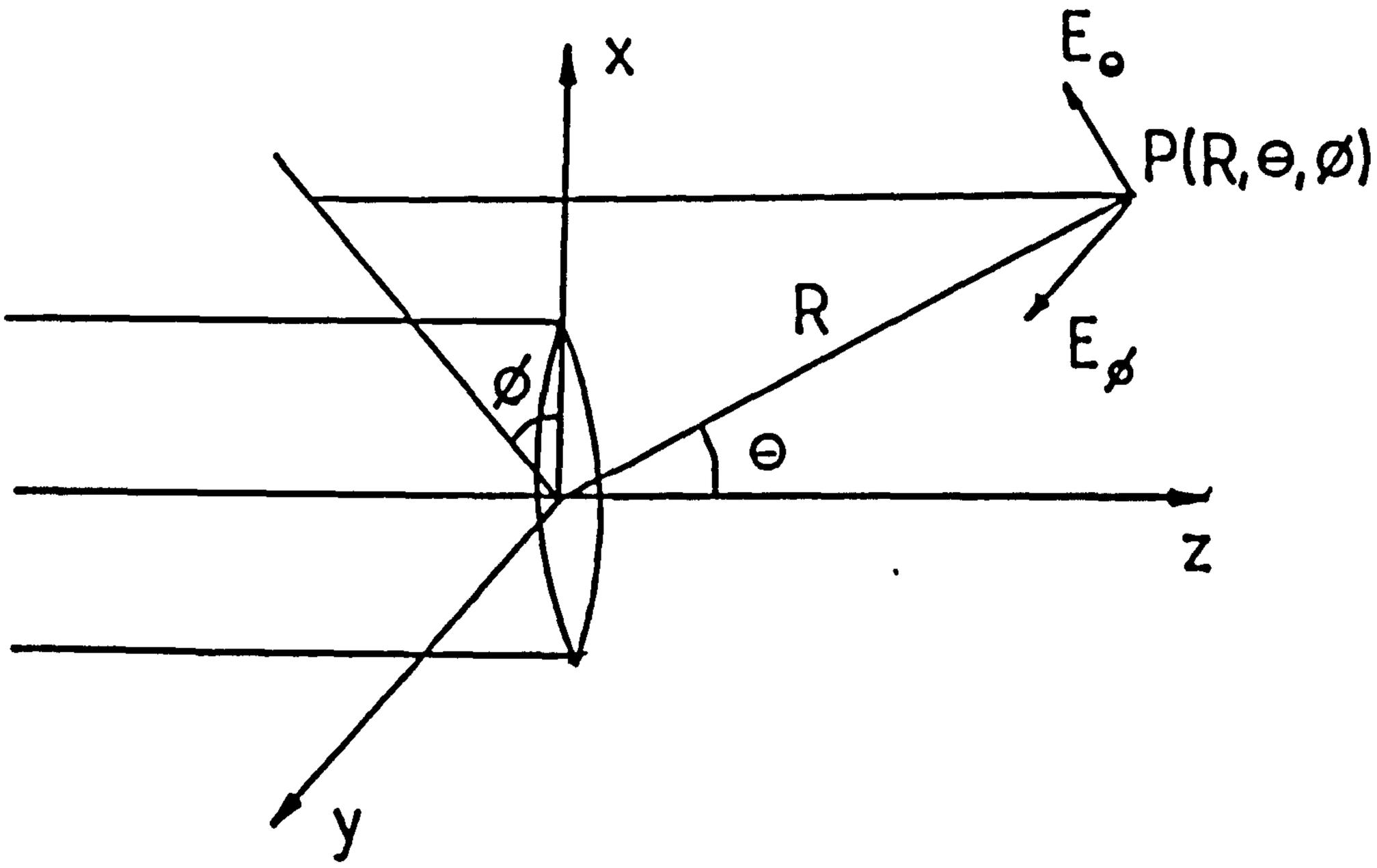


Fig.(3.14). Coordinate system used in evaluating the far field radiation pattern of the $TE_{pq}$ and the $TM_{pq}$ modes.

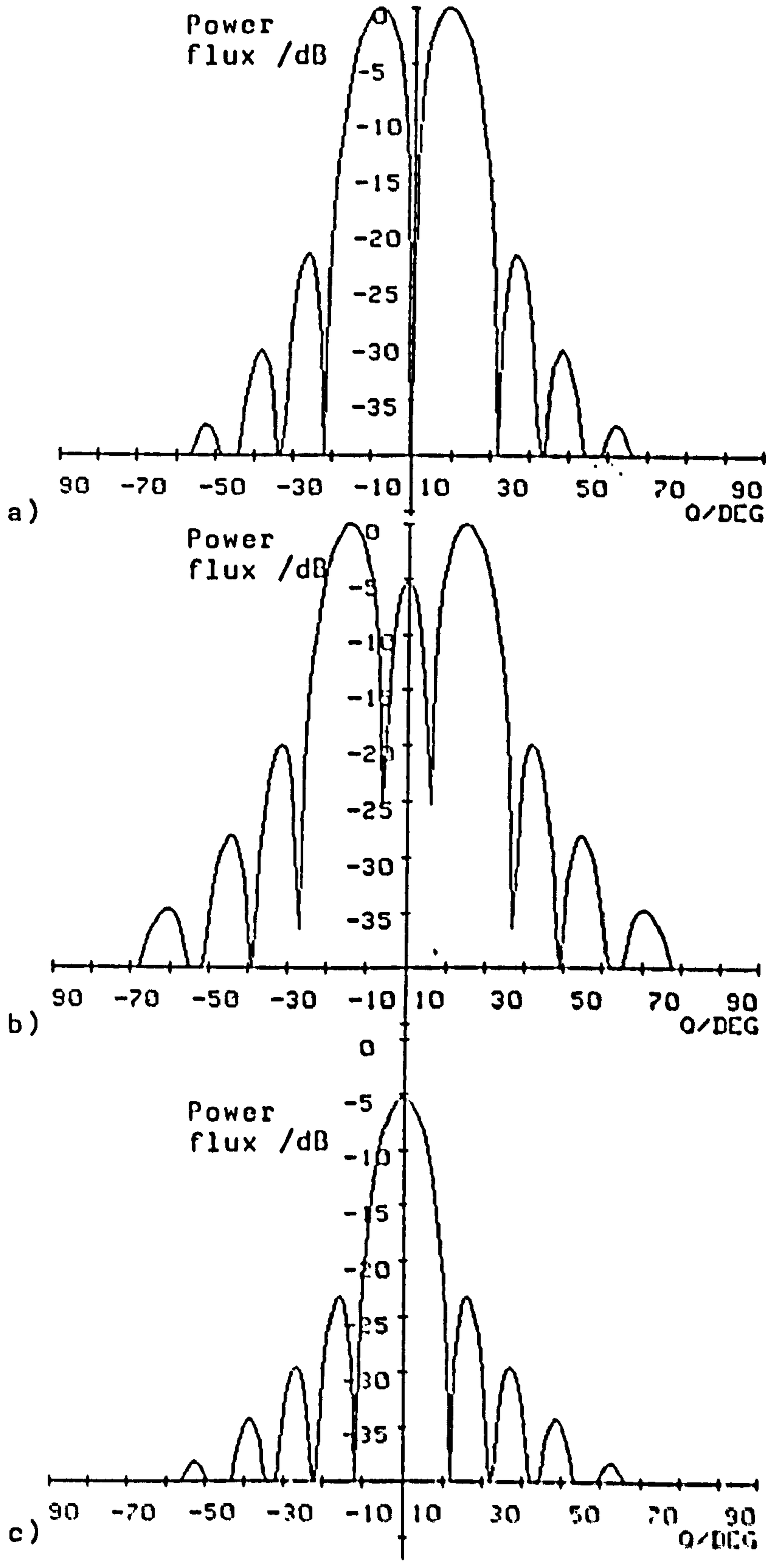


Fig.(3.15). Typical F.F.R.P. plots of waveguide modes from a cylindrically symmetric open ended waveguide. a) The cylindrically symmetric $TE_{01}$. b) $TE_{12}$, $\phi$=0°. c) $TE_{12}$, $\phi$=90°.

a temperature change to be detected. Unfortunately, as shown in chapter 6, we only measure between 10mJ to 20mJ in a typical mm-wave pulse from the maser, distributed over an aperture area of $\simeq 25cm^2$. Both methods were tried on the E.C.M, however neither had the temperature sensitivity to measure the radiation intensity distribution.

This measurement was therefore made by scanning the mm-wave detector across either the far-field or the near-field radiation pattern. Substituting the horn diameter, $\simeq$6cm, and the wavelength ($\simeq$3mm in the W-band and $\simeq$1.5mm in the G-band), into the typical lengths defined above, the F.F.R.P. will only be evident beyond distances of $\simeq$2.5m and $\simeq$5m respectively. Unfortunately these distances do not lend themselves well to the amount of space available in the laboratory. However provided the radiation pattern is measured well within the Rayleigh distance, typical lengths of 60cm and 120cm respectively, the near field radiation pattern may be measured and compared with the cavity mode patterns.

## 3.9 Spectroscopic Analysis.

The maser will oscillate at a frequency given approximately by the cyclotron frequency $\omega_{ce}=eB/\gamma m_0$. However a means must be developed by which the exact frequency and frequency bandwidth of the maser may be measured. This was achieved by means of a diffraction grating spectrometer used in the Czerny-Turner configuration, fig.(3.16). This spectrometer was designed and used in previous experiments (33,34), where three echelette gratings were produced covering the Ka, V and W frequency bands. A new G-band grating was designed to measure the high frequency, 150-220GHz, output of the MK-6 maser.

### G-Band Grating Theory and Design.

The echelette grating's operating frequency and dispersion are governed entirely by its groove spacing $a_g$, and its groove angle $\theta$. Thus considerations of frequency and dispersion may be combined

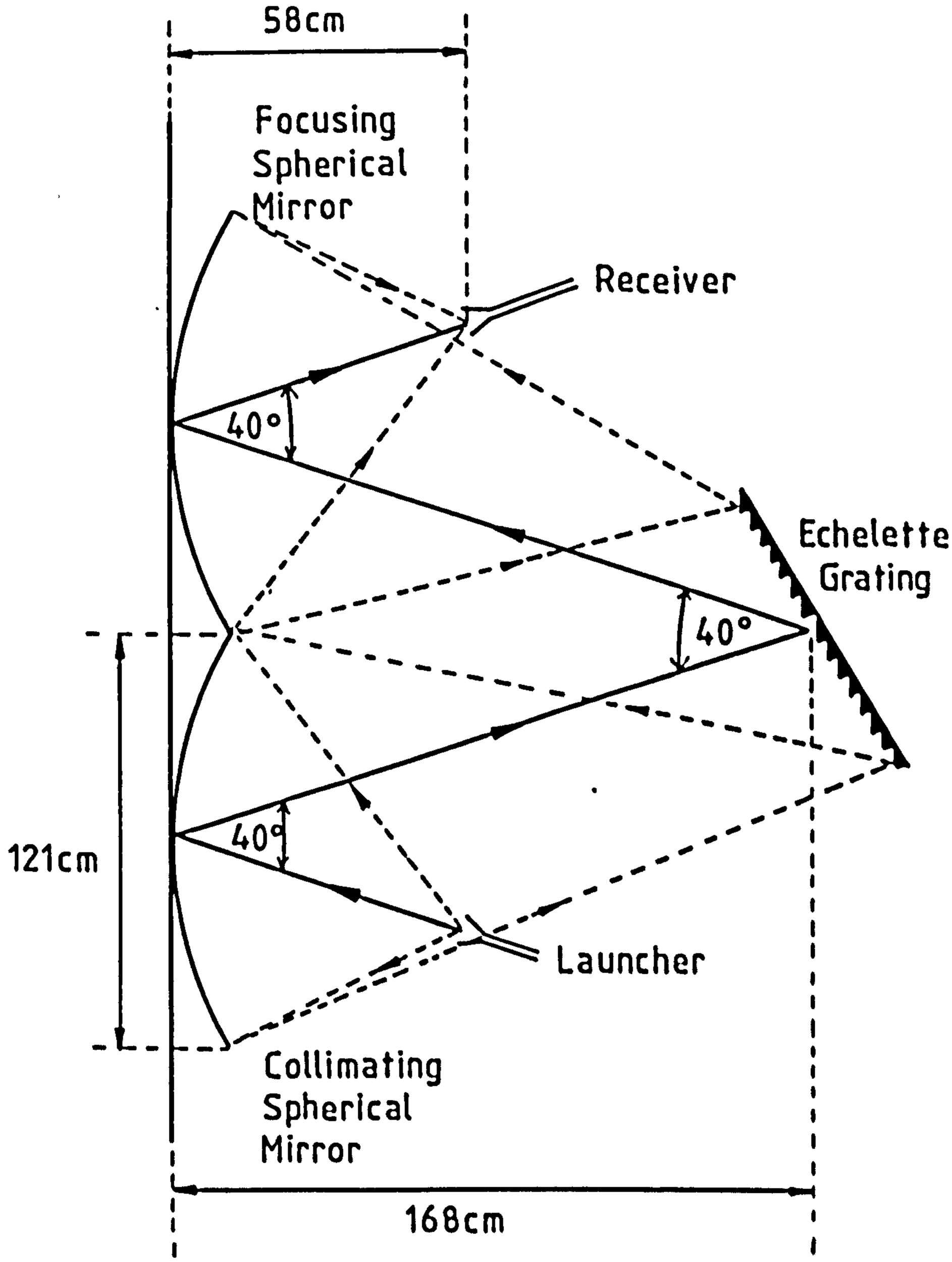


Fig.(3.16). Schematic arrangement of spectrometer in the Czerny-Turner configuration with typical dimensions as shown.

with physical parameters of the spectrometer to arrive at optimum values for $a_g$ and $\theta$ using the following equations developed from diffraction grating theory (54,55,56).

The diffraction condition, for maxima in the reflected pattern, may be stated as,

$$m\,\lambda = a_g\,(\mathrm{Sin}\,\alpha - \mathrm{Sin}\,\beta), \quad m = 0, \pm 1, \pm 2, \ldots \qquad (3.21)$$

where the terms are as defined in fig.(3.17), and the intensity distribution of the diffracted signal by,

$$\frac{I}{I_0} = \mathrm{Sinc}^2\left[\frac{b}{\lambda}(\mathrm{Sin}(\alpha+\theta)-\mathrm{Sin}(\beta-\theta))\right] \frac{\mathrm{Sin}^2\left[\frac{\pi a_g N}{\lambda}(\mathrm{Sin}\alpha-\mathrm{Sin}\beta)\right]}{\mathrm{Sin}^2\left[\frac{\pi a_g}{\lambda}(\mathrm{Sin}\alpha-\mathrm{Sin}\beta)\right]}, \qquad (3.22)$$

where N is the number of grooves in the grating and the Sinc function is defined by,

$$\mathrm{Sinc}\,(x) = \frac{\mathrm{Sin}\,(\pi x)}{\pi x}. \qquad (3.23)$$

These equations may be solved for a given wavelength $\lambda$ by imposing the following constraints,

1) intensity in the zeroth order = 0,
2) maximising eqn.(3.22) for first order,
3) the physical constraint $\alpha + \beta = \delta = 40°$.

This produces a set of simultaneous equations whose solution yields,

$$\alpha = 0\,, \quad \beta = \delta = 40°\,, \quad \theta = \frac{\delta}{2} = 20° \quad \text{and} \quad m = -1$$

with the coherence condition for the blaze wavelength, $\lambda_B$ given by,

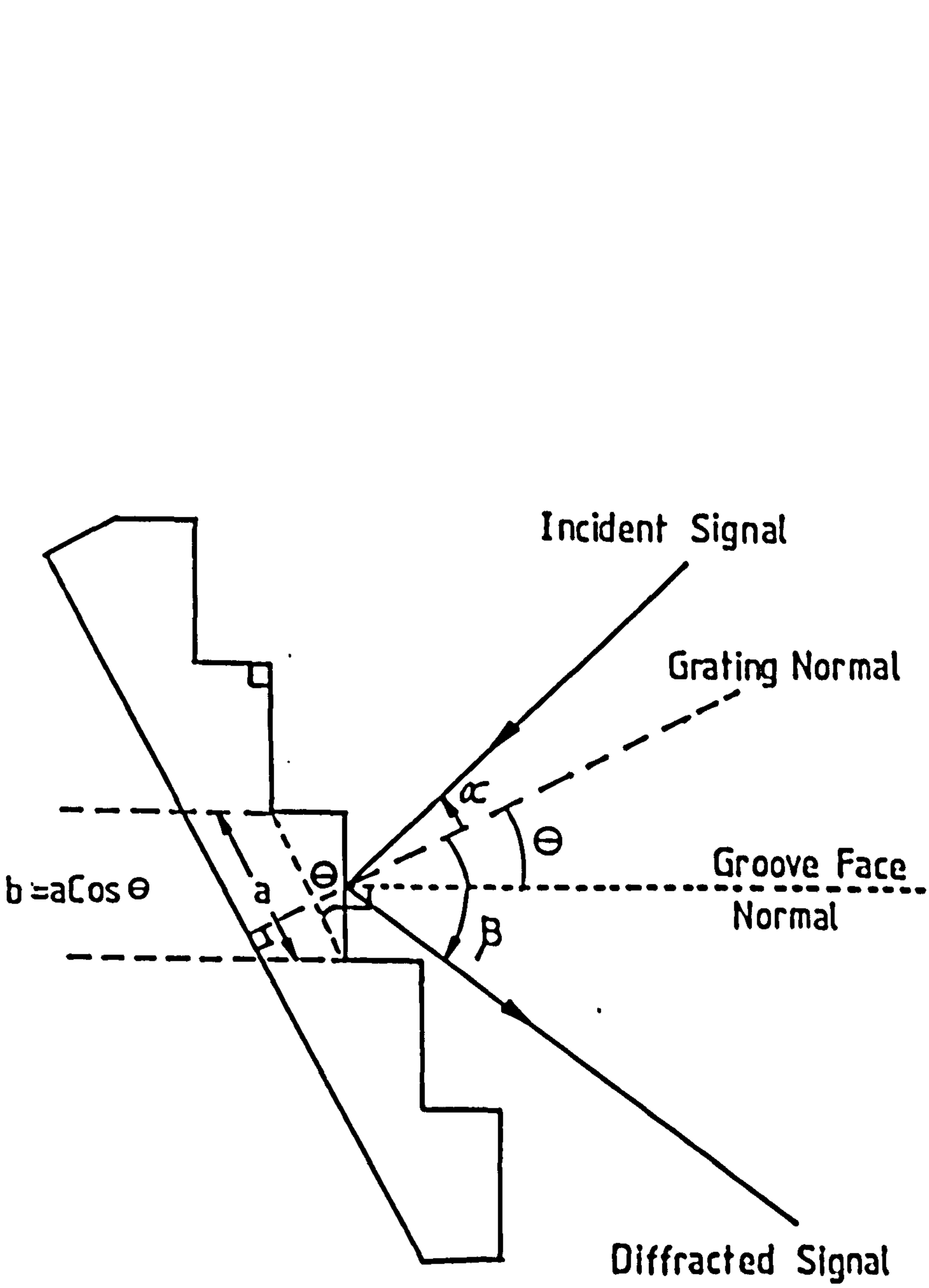


Fig.(3.17). Definition of parameters used in spectrometer theory.

$$\text{Sin } \delta = \frac{\lambda_B}{a} \quad . \tag{3.24}$$

A second set of solutions may also be shown to exist if one reverses the light path in fig.(3.17), yielding,

$$\alpha = -\delta = -40^\circ \ , \quad \beta = 0 \ , \quad \theta = \frac{\delta}{2} = 20^\circ \quad \text{and} \quad m = -1$$

with the coherence condition,

$$\text{Sin } (-2\theta) - \text{Sin } (\beta) = m' \frac{\lambda}{a_g} \ , \tag{3.25}$$

where $m' = m + 1$.

This second solution has the added advantage, considering the angular dispersion which may be derived from eqn.(3.21),

$$\frac{d\beta}{d\lambda} = \frac{m}{a_g \text{ Cos } \beta} \quad . \tag{3.26}$$

This may be minimised by setting $\beta=0$, as in the second solution. Thus, values have been arrived at for $\alpha$, $\beta$, $\theta$ and $m'$ which will maximise the signal in the first order diffracted signal at a wavelength of $\lambda_B$. However wavelengths in the neighbourhood of $\lambda_B$ will also be transmitted. Due to the physical constraints of the spectrometer the maximum value of $\Delta\beta$, centered about $\beta$ under blazed wavelength conditions, is about 20°, for which the radiation intensity for the relevant wavelength will have dropped to ≈70% of $I_{\lambda B}$.

The last parameter, $a_g$, may thus be evaluated from eqn.(3.25) which may be rewritten as,

$$\text{Sin } (2\,\theta) + \text{Sin } \beta = \frac{\lambda}{a_g} \quad . \tag{3.27}$$

Substituting the values calculated for the spectrometer,

$$\beta_{min} = -10° \rightarrow \frac{\lambda_{min}}{a_g} = \text{Sin } 40° - \text{Sin } 10° = .47,$$

$$\beta_{blaze} = 0° \rightarrow \frac{\lambda_B}{a_g} = \text{Sin } 40° = .64, \qquad (3.28)$$

$$\beta_{max} = 10° \rightarrow \frac{\lambda_{max}}{a_g} = \text{Sin } 40° + \text{Sin } 10° = .82$$

Thus for any value of $a_g$, the spectrometer $\lambda_{max}$ and $\lambda_{min}$ may be evaluated. Requiring a grating for 200GHz a value of $a_g$=2.35mm was chosen, coresponding to,

$$f_{min} = 155\text{GHz},$$
$$f_{blaze} = 200\text{GHz},$$
$$f_{max} = 273\text{GHz}.$$

Resolving Power.

The theoretical resolving power is given by,

$$\frac{\lambda}{\Delta \lambda} = N\ m. \qquad (3.29)$$

Now $\lambda$=1.5mm, $\therefore \Delta\lambda$=3.86μm $\Rightarrow \Delta f$=.515GHz.

Thus from the above theory a diffraction grating echelette may be constructed with a blaze frequency of 200GHz and a theoretical bandwidth of .52 GHz.

W- and G-Band Grating Dimensions.

As stated it is now possible to cut the G-band grating with a blaze frequency of 200GHz. Using the same method as above, a W-band grating was previously designed and constructed at Strathclyde University. The dimensions of both gratings are shown in table (3.5).

| | W-Band Grating | G-Band Grating |
|---|---|---|
| $\underline{f_{blaze}}$ GHz | 89 | 200 |
| $\underline{f_{min}}$ GHz | 65 | 155 |
| $\underline{f_{max}}$ GHz | 114 | 275 |
| $\underline{a_g}$ mm | 5.25 | 2.35 |
| Blaze Angle / Degrees | 20 | 20 |
| Width / m | .914 | .911 |
| Height / m | .914 | .911 |
| Theoretical Bandwidth / GHz | ≈.5 | ≈.5 |

Table (3.5). G- and W-band grating parameters and dimensions.

Spectrometer Calibration.

In the production of this thesis two gratings were used, the previously constructed W-band echelette and the new G-band echelette. Both must be calibrated for frequency, bandwidth and insertion losses. A different source was used in each case resulting in different experimental techniques, thus each grating will be dealt with separately.

W-band Spectrometer Grating Calibration.

Frequency Calibration.

The spectrometer was calibrated for frequency using the experimental apparatus shown in fig.(3.18). A backward wave oscillator (B.W.O.) was used as a tunable source over the entire W-band frequency range. The exact output frequency was measured using a calibrated frequency meter supplied by Flann. The signal was coupled through the spectrometer and detected using the calibrated Flann 135 rectifying diode detector.

By scanning the frequency and the grating angle, the frequency calibration graph shown in fig.(3.19) was produced.

Spectrometer Bandwidth Calibration.

The bandwidth of the spectrometer was measured keeping the frequency of the B.W.O. constant and sweeping the grating position, fig.(3.20). The bandwidth of a delta function through the spectrometer was measured at four frequencies across the W-band and was approximately 2GHz. This is significantly more than the .5GHz predicted from theory. However it was possible to show experimentally that imperfections in the mirrors and their illumination, resulting in improper illumination of the grating, created this effect

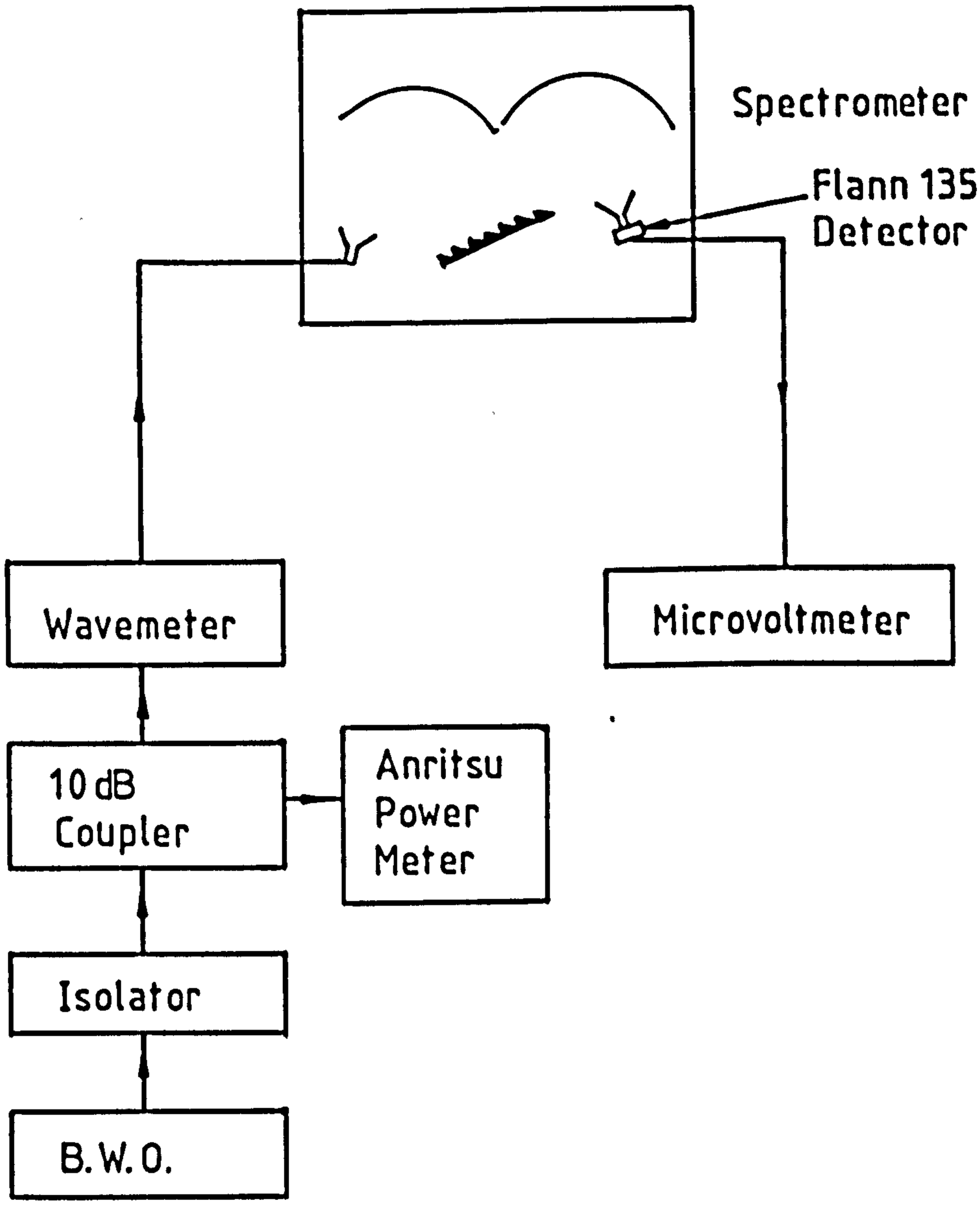


Fig.(3.18). Experimental configuration used to calibrate the W-band grating.

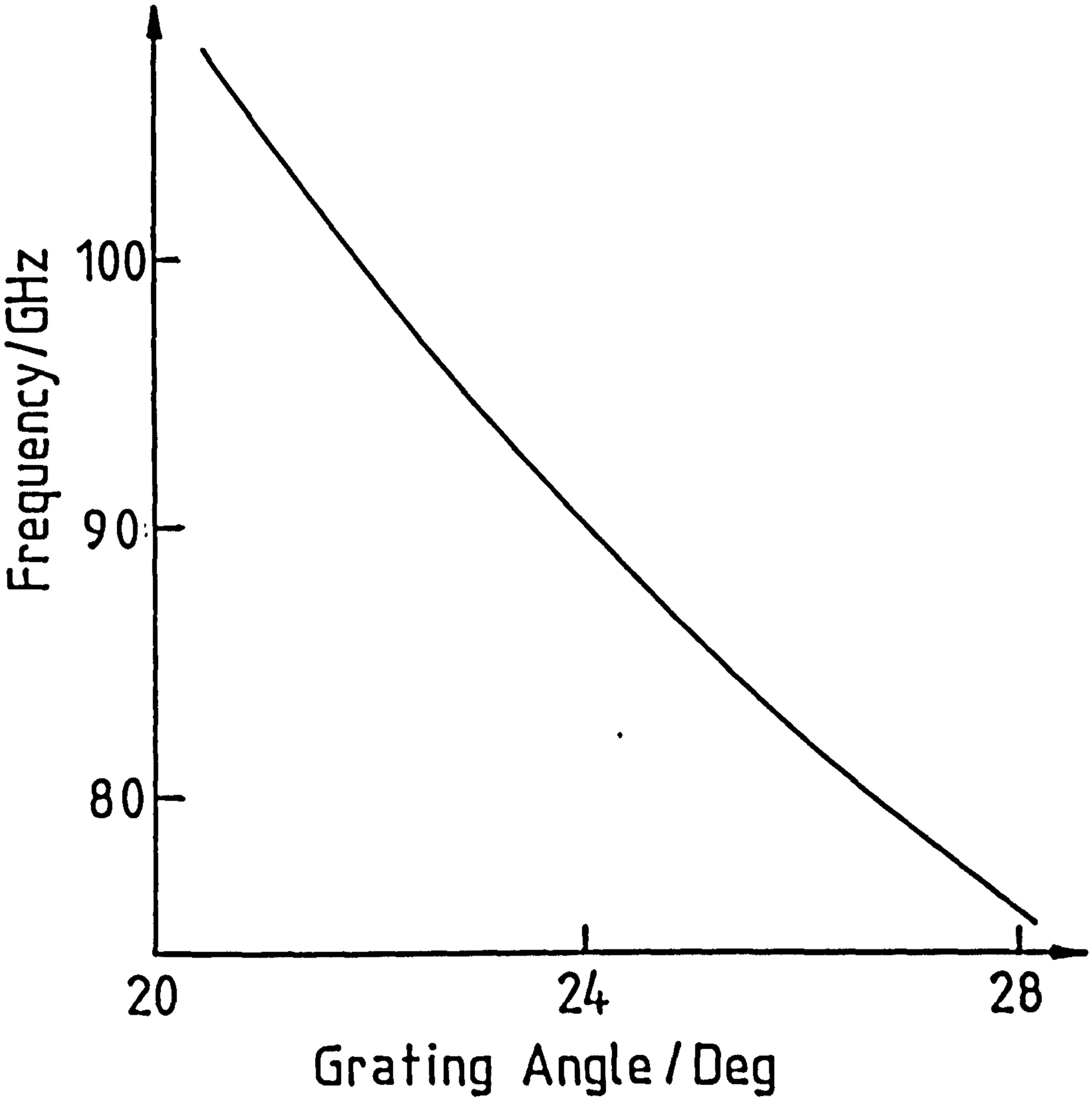


Fig.(3.19). W-band spectrometer frequency calibration.

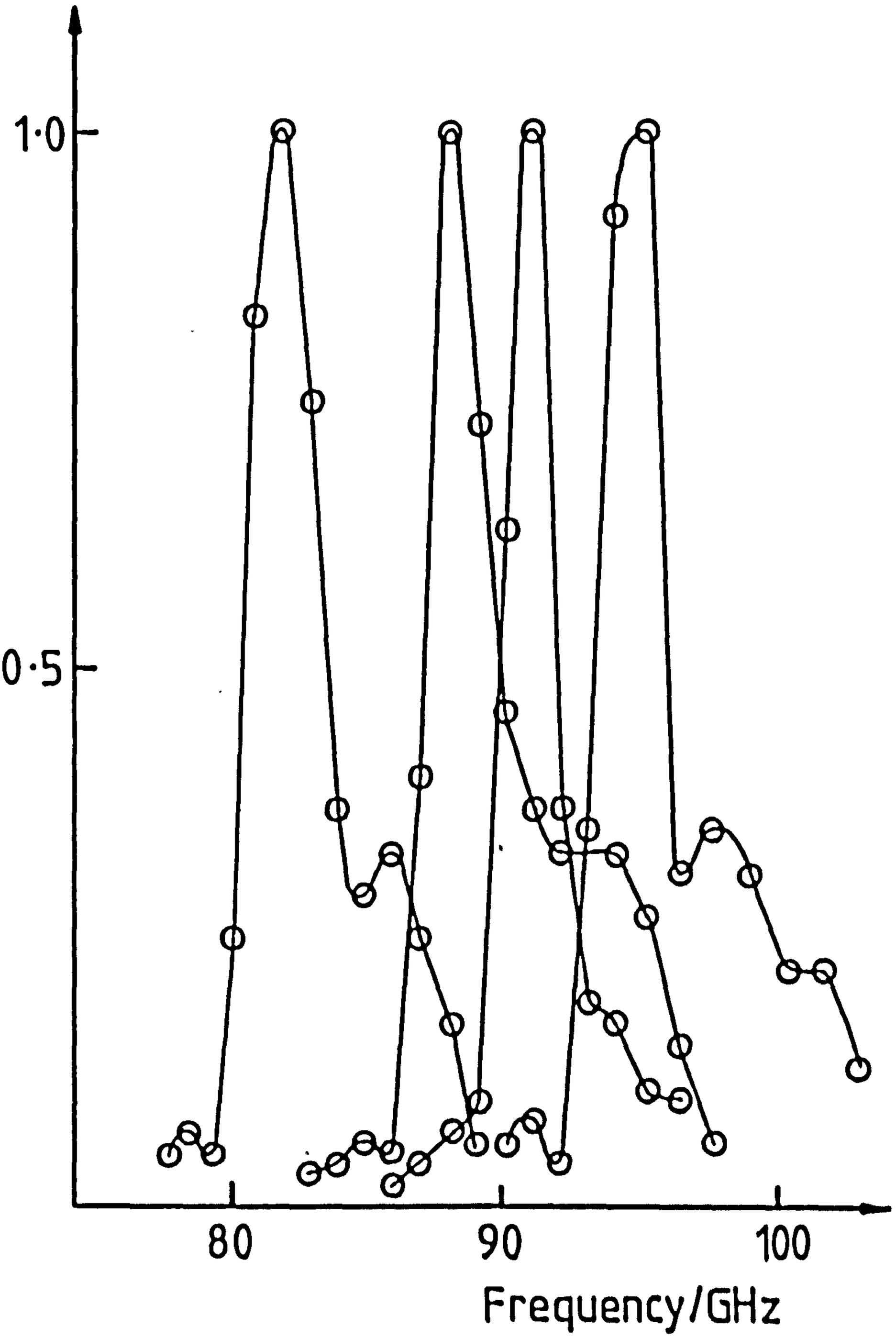


Fig.(3.20). W-band spectrometer bandwidth, shown for four separate input frequencies, 81.8GHz, 88.0GHz, 91.0GHz, 94.0GHz.

Insertion Losses of the Spectrometer.

The losses through the spectrometer will be a function of frequency and may be measured by feeding in a known frequency at a known power level. The input power was measured using an Anritsu power meter in conjunction with a 10dB Flann directional coupler. The entire insertion losses, due to both the spectrometer and the detector could thus be measured. The resulting graph is shown in fig.(3.21), which demonstrates two distinct plateaux with some irregularities being introduced above 96GHz.

The spectrometer effectively stopped working above a frequency of 103GHz, beyond which the throughput of the spectrometer became a complex function of grating position and frequency.

G-Band Spectrometer Grating Calibration.

The G-band spectrometer was an adaption of the W-band spectrometer, described above, with merely a change of diffraction grating. Limitations in the spectrometer performance mainly arose in the overmoded launching and receiving horns and imperfections in the mirrors, all of which become more critical with the reduction in wavelength. Due to limitations in the G-band source it proved impossible to complete as full a calibration of the spectrometer as in the W-band. In the G-band there are almost no sources available and we improvised by using a low power frequency doubler in conjunction with the W-band B.W.O. The output of this device was such that phase sensitive detection techniques had to be employed to detect the signal through the spectrometer. As the system was used at the limits of its working capacity and no power meter was available, no measurement of the frequency dependent insertion losses could be made. However it was possible to gain an accurate measurement of the spectrometer dispersion and bandwidth.

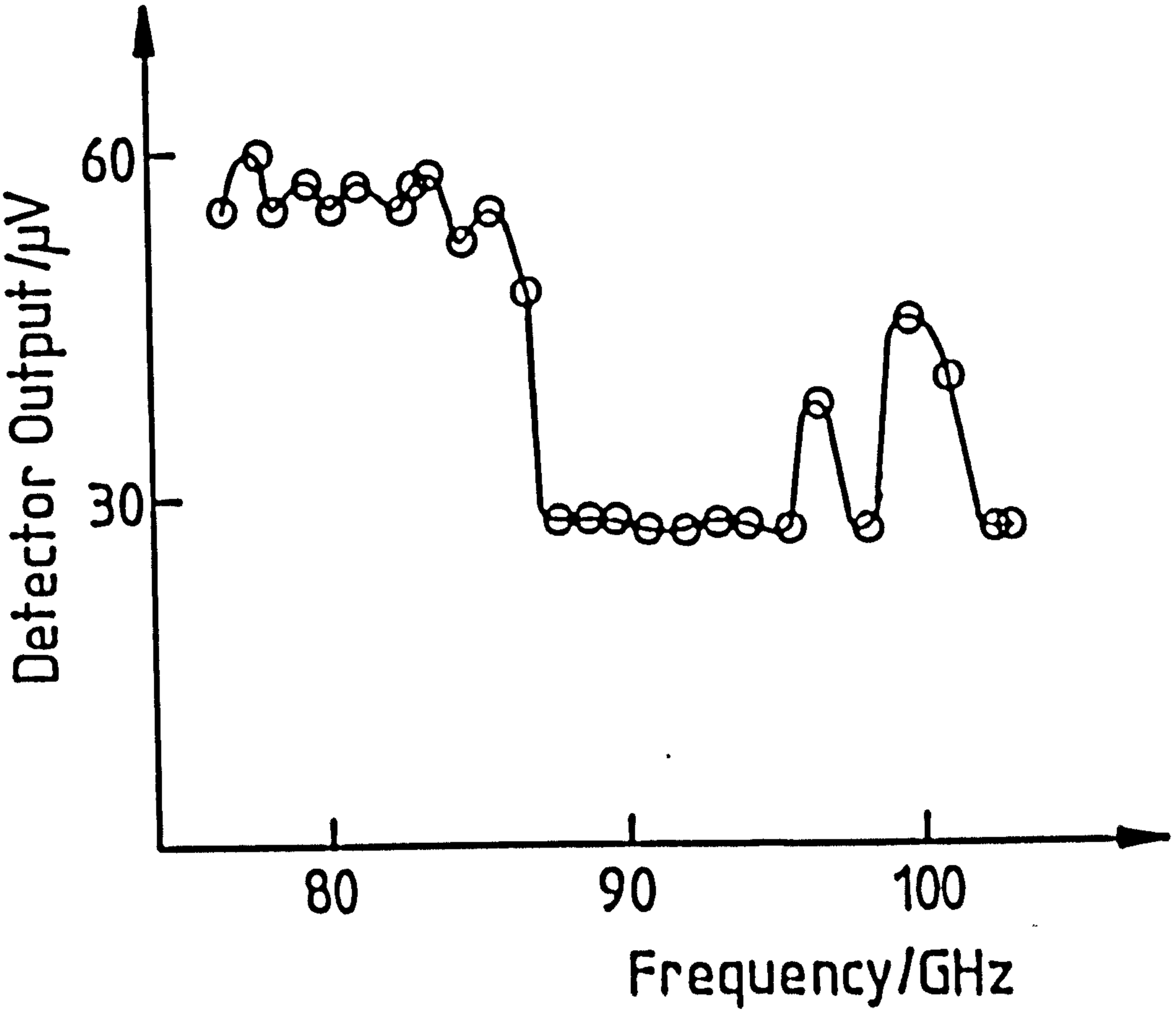


Fig.(3.21). Insertion losses of W-band spectrometer.

G-Band Source.

A commercially available Farran Technology frequency doubler was used to improvise a G-band source. This was coupled to the W-band (75-110GHz) B.W.O. mentioned above, resulting in a source capable of producing mm-wave radiation throughout the G-band (150-220GHz).

The B.W.O. produced, typically 10-20mW of power in the W-band, the frequency doubler had efficiencies of typically 10-15%, resulting in output powers from the doubler of only 1-2mW. When these low powers were combined with the relative insensitivity of the W-band detectors at these frequencies, then phase sensitive detection becomes essential, particularly with the expected 25dB attenuation through the spectrometer.

The system used to produce and monitor the G-band radiation is shown in fig.(3.22). A Flann calibrated G-band wavemeter was used to measure the frequency output from the doubler and a 10dB G-band directional coupler and uncalibrated detector used to monitor the relative output power.

Although both the B.W.O. and the directional coupler were in principle continuously tunable, this proved very difficult to achieve in practice. For any given W-band frequency the frequency doubler must be tuned for maximum output power via three orthogonal back-shorts. This is a complicated, laborious and time consuming process and must be repeated at each frequency. This tuning process is critical and care must be taken to ensure the stability of the B.W.O. as a change in the B.W.O.'s output frequency of <0.1% will effectively reduce the doubler efficiency to zero.

Detection of Calibration Signal.

From the previous section we see that the doubler only produces power of the order of 1-2mW. This signal is then reduced by another factor of ~25dB when fed through the spectrometer and when this is combined with the relative insensitivity of the W-band detectors at these frequencies simple measurement of the detector output via a microvoltmeter was not possible.

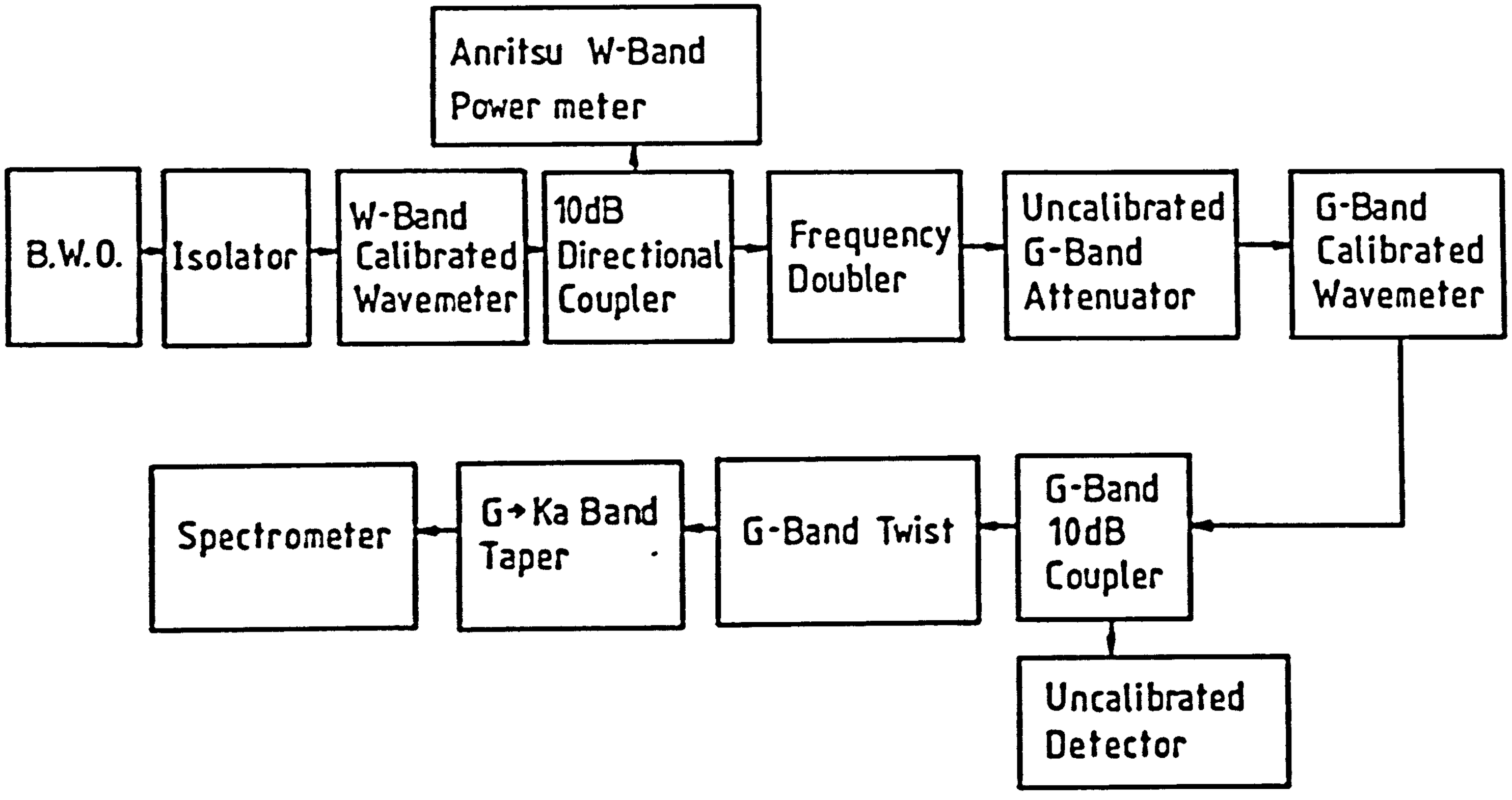


Fig.(3.22). Schematic diagram of G-band source.

The detection system used is shown in fig.(3.23). The output of the Flann W-band detector was fed into a Brookdeal low noise amplifier which could provide up to 100dB gain in power. The output of the amplifier was fed into a Brookdeal precision lock-in amplifier. This relies on locking into the frequency and phase of the modulated G-band signal.

The modulation of the G-band mm-wave output was achieved via electronically chopping the B.W.O. signal, with the electronic chopping signal also fed into the lock-in amplifier.

A schematic diagram of the entire calibration system is shown in fig.(3.24).

G-band Spectrometer Dispersion.

Using the above source and detection techniques the calibration of the spectrometer frequency throughput, with respect to grating angle, was produced and is shown in fig.(3.25).

Spectrometer Bandwidth.

The spectrometer bandwidth was measured using the same technique as in the W-band, fig.(3.26). In this case the bandwidth of a delta function through the spectrometer was measured to be ≈4GHz. Again this is significantly more than the predicted .5GHz, however it is of comparable performance to the W-band grating, both resulting in a fractional bandwidth of $\Delta f/f \approx 2\%$.

## 3.10 Power Measurements Using Calibrated Power Meter.

In previous experiments at Strathclyde no direct power measurements have been made. Instead these have been estimated by calibrating the detector for power and integrating under both the spectrometer scans and the far-field radiation patterns (33,34,57). These methods can only be used to estimate the order of magnitude of the output power. As many parts of the detection system could not be calibrated, chiefly the coupling between the maser output window and the sampling waveguide or horn, these estimates were

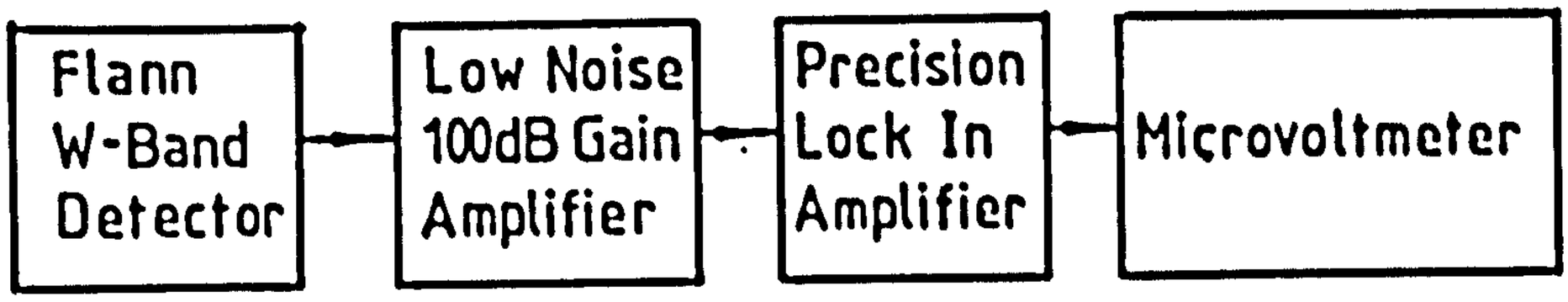


Fig.(3.23). G-band detection system

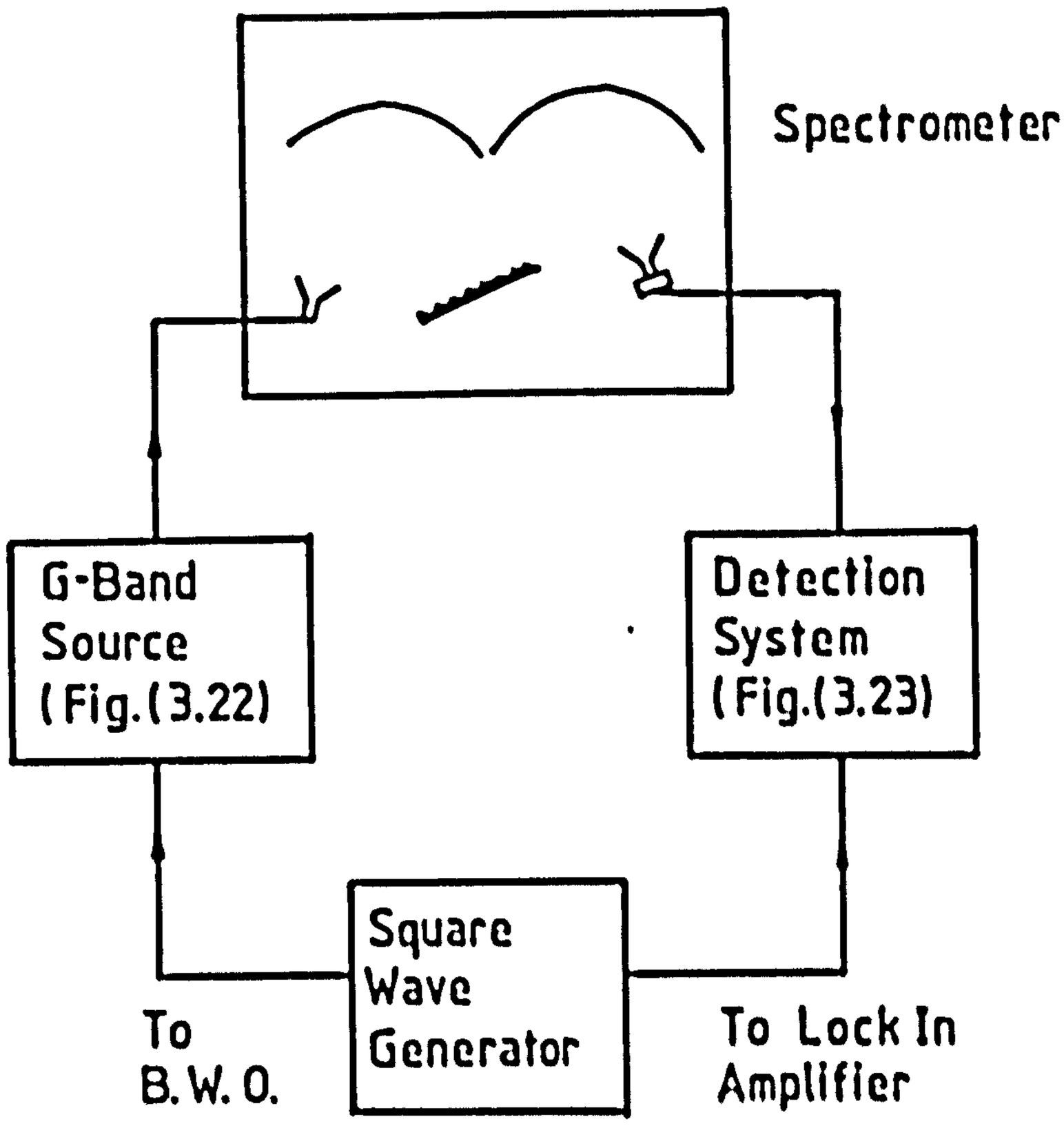


Fig.(3.24). Experimental configuration used to calibrate the G-band grating.

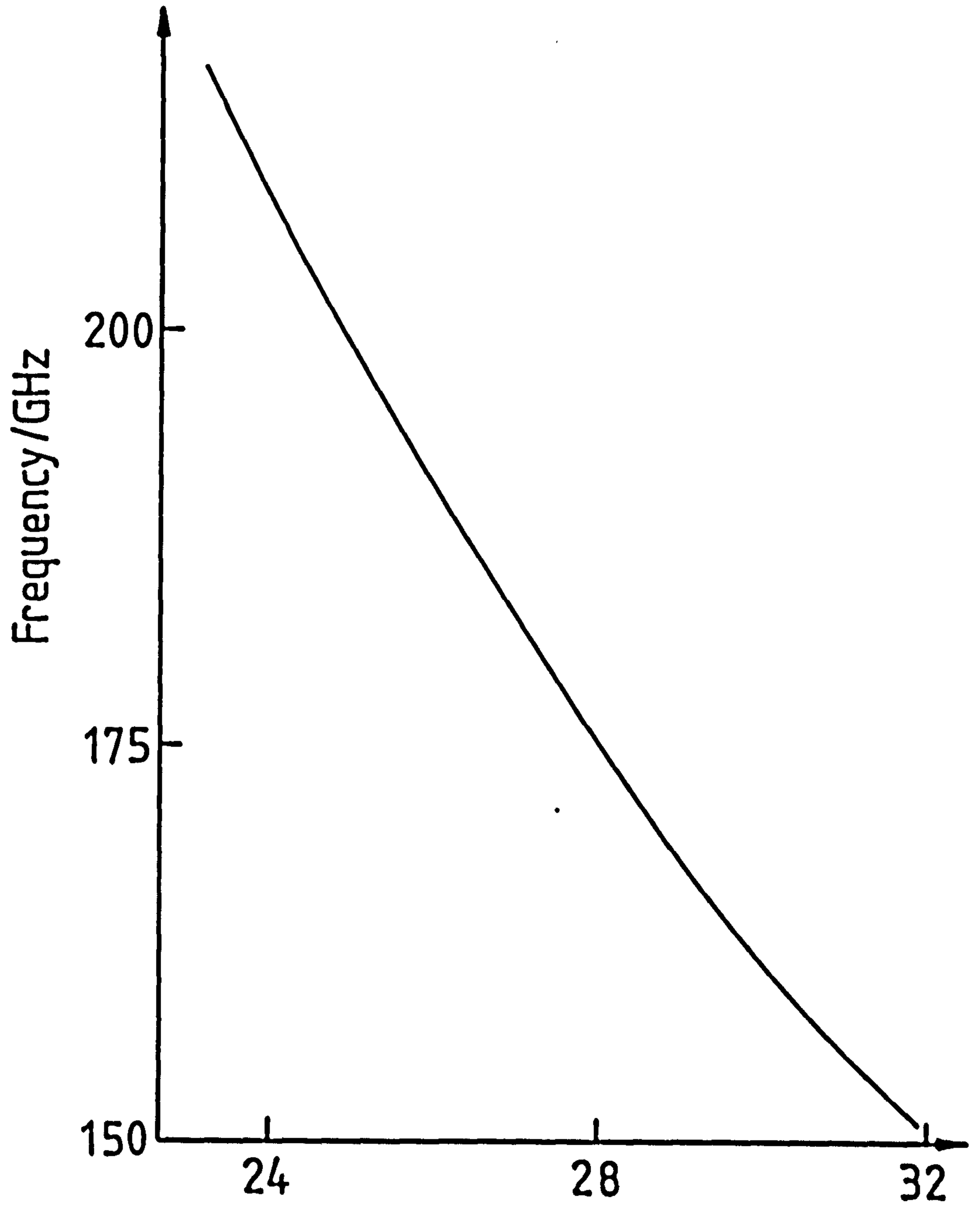


Fig.(3.25). G-band spectrometer frequency calibration.

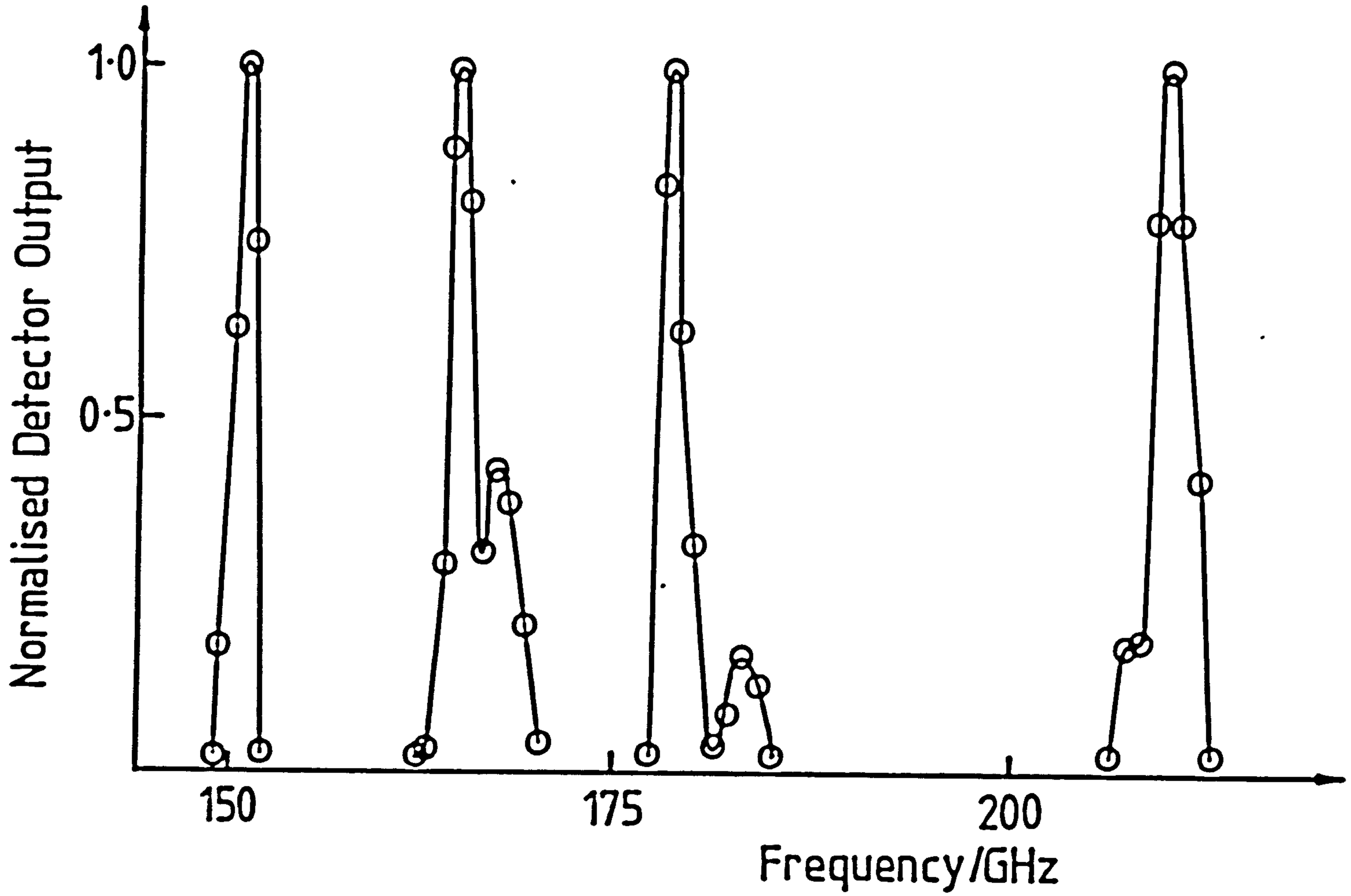


Fig.(3.26). G-band spectrometer bandwidth.

very approximate.

For this reason these techniques were rejected and a calibrated power meter used to make a direct measurement of the power out from the maser. To do this an array of thermocouples was used to measure the energy in any pulse and the calibrated Flann crystal detector used to measure the pulse length. This allowed us to calculate the output power in any pulse.

A diagram of the thermocouple array and sampling horn is shown in fig.(3.27). The array was painted with mm-wave absorbing paint. When mm-wave radiation falls on the detector the energy in the pulse is absorbed in the paint resulting in a temperature increase. This temperature increase will be transformed into a voltage rise across the output terminals of the array.

The theremocouple array was calibrated using the system shown in fig.(3.28). The B.W.O. was used as a tunable, variable power, electronically modulated source. The output power and mm-wave pulse length were measured via the calibrated Flann crystal detector in conjunction with the 10dB directional coupler. This allowed the calculation of the energy fed into the array. The output across the thermocouple array terminals was monitored on a Schlumberger digital microvoltmeter. This was connected to an HP86 computer via the HP-IB parallel bus interface. The computer monitored the thermocouple array output as a function of time, hence it was possible to calibrate the array for changes in output voltage against energy input, fig.(3.29).

The array could thus be used to measure the energy in any given pulse from the maser. The calibrated Flann crystal detector was subsequently used to measure the length of each individual pulse from the E.C.M., thus allowing the calculation of the maser output power.

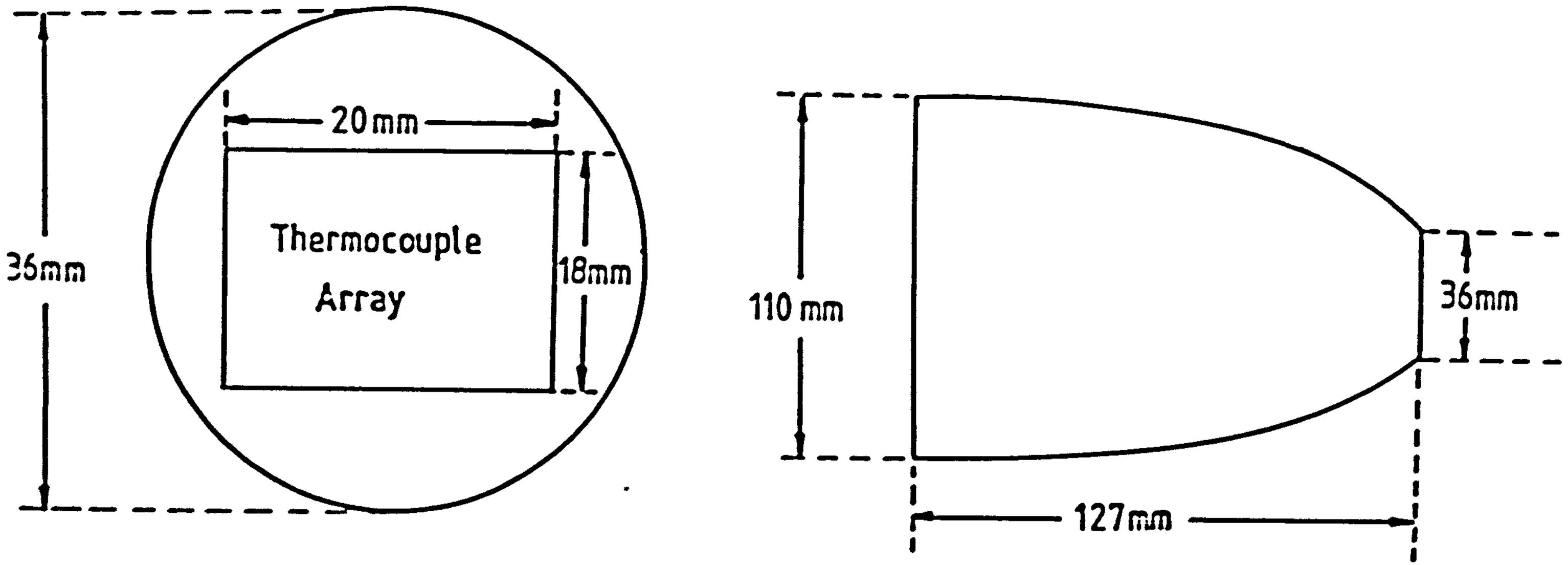


Fig.(3.27). Thermocouple array and sampling horn. Not to scale.

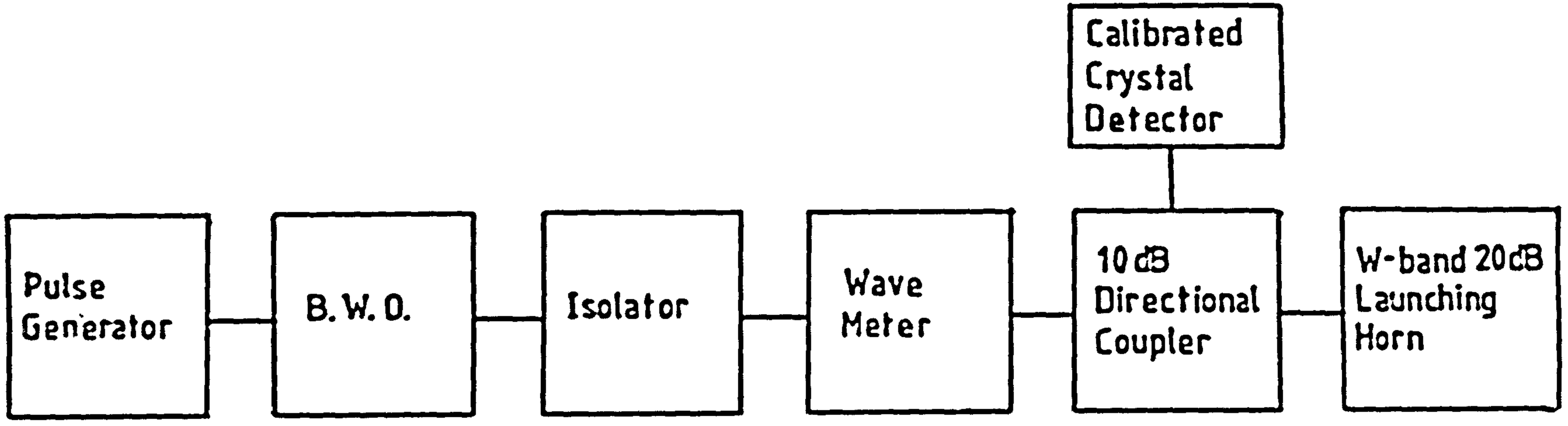


a)

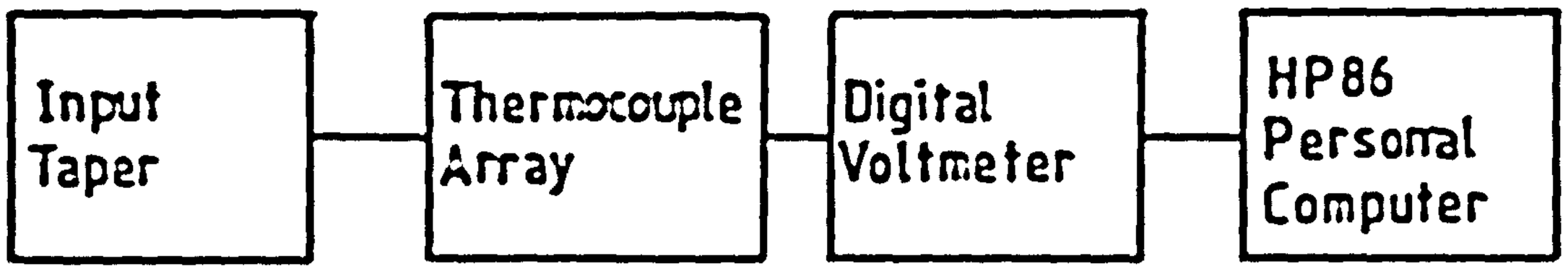


b)

Fig.(3.28). Thermocouple array calibration. a) mm-wave pulse generation. b) mm-wave energy measurement.

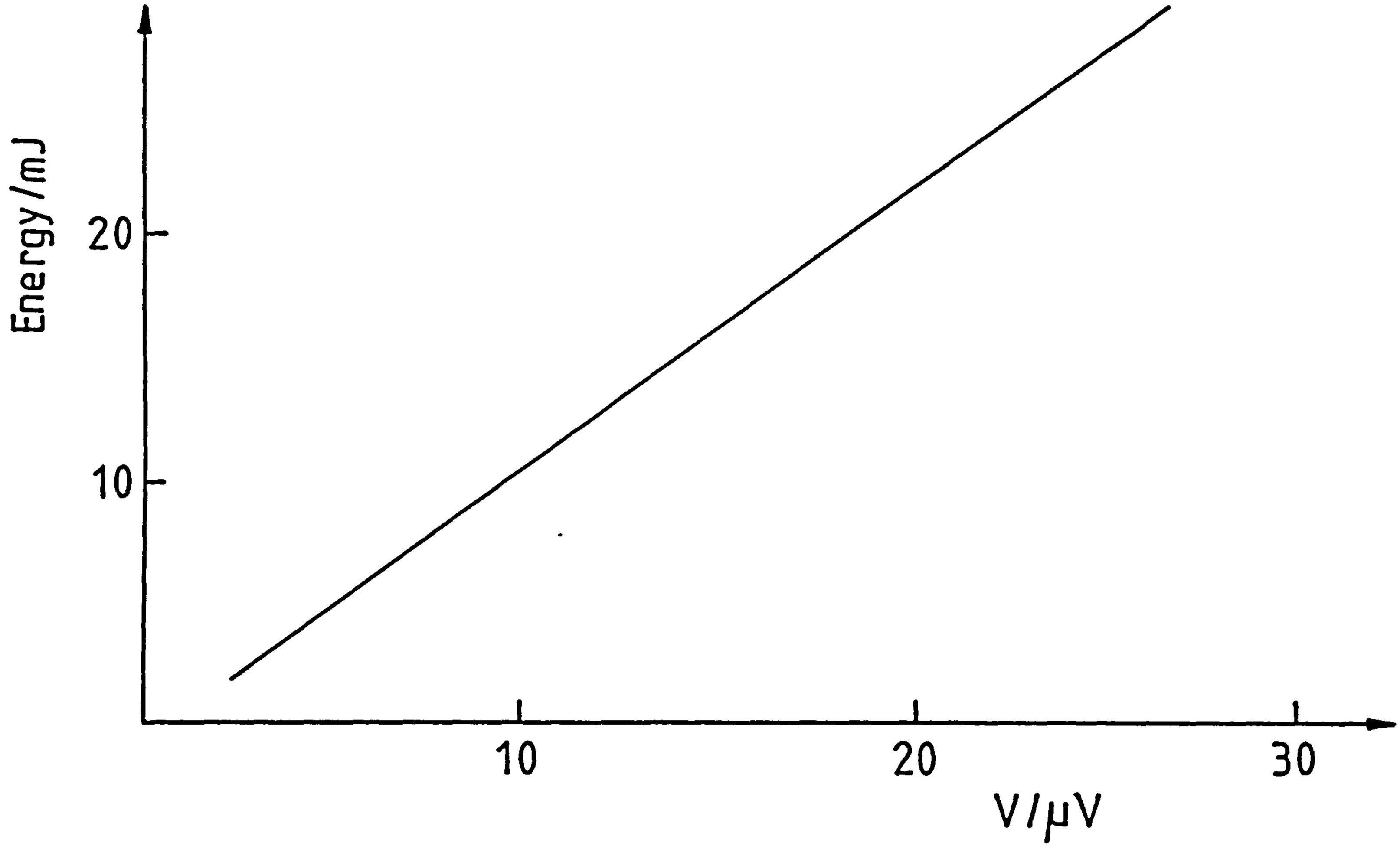


Fig.(3.29). Thermocouple calibration graph.

# CHAPTER -4-

# MASER CALIBRATION CHARACTERISATION AND EXPERIMENTAL TECHNIQUES.

## 4.1 Introduction.

The diagnostics described in the previous chapter were used to measure the operating characteristics of the maser.

This included the calibration of the magnetic field coils. Both coils must be calibrated for field production against their respective capacitor charging voltages and the current through each coil. The B-field exclusion and the time delay between the maximum current and the maximum field (both effects caused by the conductivity of the cavity walls) will also be calculated and measured. These measurements combined with the respective rise times of each coil will be used to determine the delay required to ensure the simultaneous occurrence of the maximum magnetic fields.

The I-V characteristics of the diode must be known. The voltage measurement will allow the calculation of the beam's $\gamma$-factor and will demonstrate the effects of the magnetic insulation of the diode. It is possible, via the Rogowski coils, to measure the diode discharge current, however the beam current will consist of only a small percentage of this. To measure the beam current a witness plate probe was used. Due to breakdown this was not able to measure the beam current directly, however an estimate of the beam current may be obtained from the resulting melting and evaporation of the copper surface of the witness plate.

In the analysis of the maser output four different diagnostics were used.

1) The direct power measurement using a Flann crystal rectifying diode detector.
2) The frequency measurements using a calibrated spectrometer.
3) The mm-wave intensity distribution across the output window, sampled via a W-band waveguide.
4) The direct output power measured using a calibrated power meter.

The experimental details of the above diagnostics will be described, with their respective applications, in both the W- and G-bands. (This is the first time maser oscillation over 100GHz has

been obtained). Also, for the first time at Strathclyde University, a two detector monitoring technique was used in both the G-band spectrometer measurements and the W-band intensity distribution measurements.

## 4.2 Calibration and Characterisation of Field Coils #1 and #2.

As stated in chapter two the current profile -and hence the B-field profile- with respect to time is determined entirely by the L, C and R constants of the circuit. The maximum value of the current, and hence the B-field, is governed by the charging voltage on each respective capacitor bank. It is therefore possible to produce a calibration graph of charging voltage versus B-field. This provides a convenient working relationship between easily measurable (and adjustable) parameters which relate directly to the magnetic field produced by each respective field coil. This method is however slightly unreliable if, over a length of time, the R.C.L. characteristics of the circuit change. It is very unlikely that either the capacitance or the inductance of the circuit will alter; this is not true though of the circuit resistance. There are many connections in the circuit and as such large currents are involved, (>20kA in coil#1), it is evident that only a small change in the resistance may affect the maximum B-field produced. This problem was overcome by not only calibrating the field against charging voltage but also against the current flowing through the coil. This will provide a reference with which the main charging voltage calibration can be compared.

The experimental apparatus used to calibrate both magnetic field coils and measure their combined field profile throughout the cavity and the anode cathode assembly is shown in fig.(4.1). Both coils were placed on the maser in their respective positions. The currents flowing in coil#1 and coil#2 were measured using the calibrated grey and black Rogowski coils respectively. The cavity magnetic field was measured using the probe coil described in chapter 3. All three signals were thus fed back to screened room#1. These signals were monitored on calibrated Datalab 20MHz

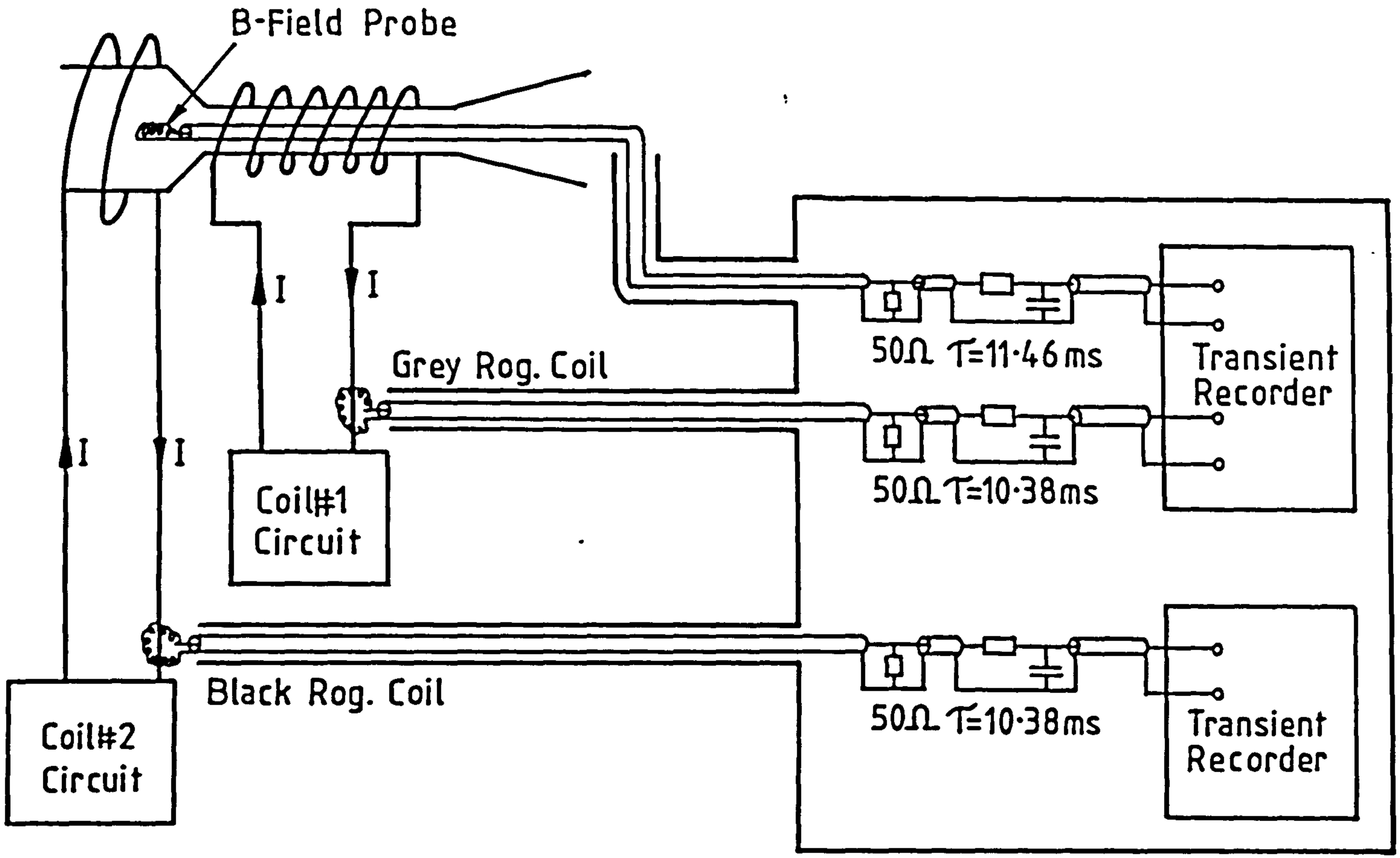


Fig.(4.1). Experimental configuration used to calibrate magnetic field coils.

digital recorders, via three integrator circuits with time constants of 10.38ms, 10.38ms and 11.46ms respectively.

All the results of this calibration are summarised in table(4.1) and fig.(4.2), (4.3) and (4.4). Fig.(4.2) and (4.3) depict the respective relationships between the measured cavity B-field and firstly, the capacitor bank charging voltage, and secondly, the respective coil currents. From these graphs the conversion factors from voltage to B-field and current to B-field, presented in table(4.1) have been calculated. Fig.(4.4) shows the coil B-field profiles with respect to the anode and the cathode positions.

Discussion and Analysis of Results.

The current rise times of coil#1 and coil#2 were measured to be 116μs and 215μs respectively, these values compared very well to those predicted by theory, i.e. 103μs and 209μs. There was a delay between the cavity B-field and the coil current as predicted due to the field exclusion of the conducting cavity walls. As the coil#1 current rises approximately twice as fast as that in coil#2, the resulting time delay is larger in the first case, with a delay of 71μs (≈60% of the current rise time), as opposed to 41μs (≈20% of the current rise time) in the second. The delay thus required between the firing of the two field circuits, to ensure the simultaneous occurence of the B-field maxima, is 69μs. This delay was used throughout all subsequent experiments described in this thesis.

The conducting cavity wall will not only introduce a time delay between the maximum coil current and the maximum intra cavity B-field (as the magnetic field takes a certain time to diffuse through the conducting stainless steel), but it will also reduce the maximum field obtained. This reduction factor may be calculated using the theoretical equation, which predicts the maximum B-field, on axis, at the centre of a coil.

$$B = \mu_0 \, n \, I \, \cos \phi,$$

Which in our case,

| | Coil#1 | Coil#2 |
|---|---|---|
| Maximum measured cavity B-field | 9.40T | 1.05T |
| Current rise time | 116μs | 215μs |
| B-field rise time | 187μs | 256μs |
| Delay | 71μs | 41μs |
| Theoretical current rise time | 103μs | 209μs |
| B-field exclusion factor | ≈8% | ≈8% |
| Delay time for field synchronisation | (256 - 187)μs = 69μs | |
| Charging voltage to B-field conversion | 1.466 $\frac{T}{kV}$ | .509 $\frac{T}{kV}$ |
| Error | 1.6% | 1.6% |
| Offset constant (c) | -.125T | .034T |
| Current to B-field conversion | .432 $\frac{T}{kA}$ | .220 $\frac{T}{kA}$ |
| Error | 1.6% | 1.6% |
| Offset constant (c) | -.020T | .013T |

Table(4.1). Results of coil#1 and coil#2 calibration experiments.

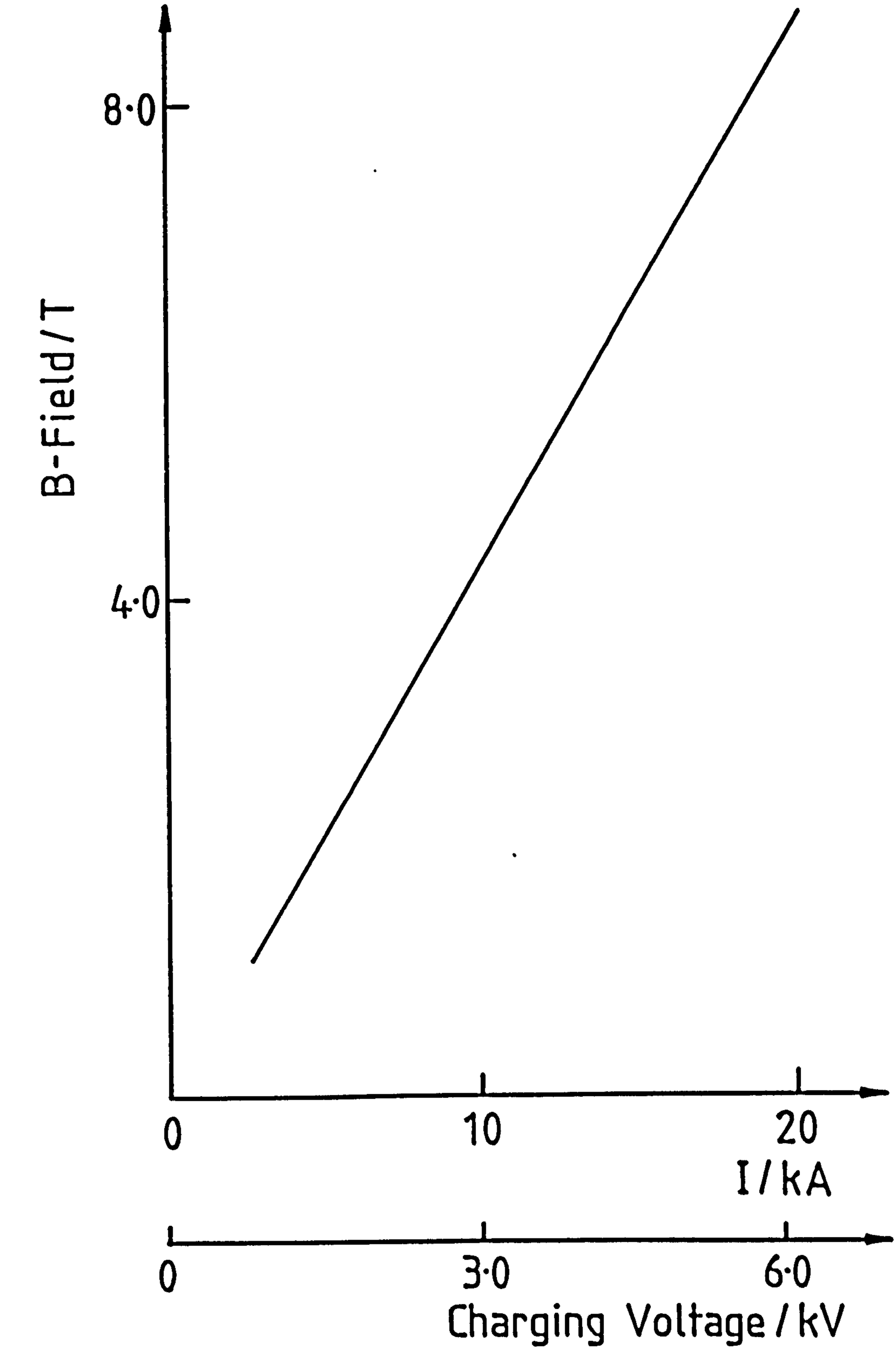


Fig.(4.2). Coil#1 field calibration.

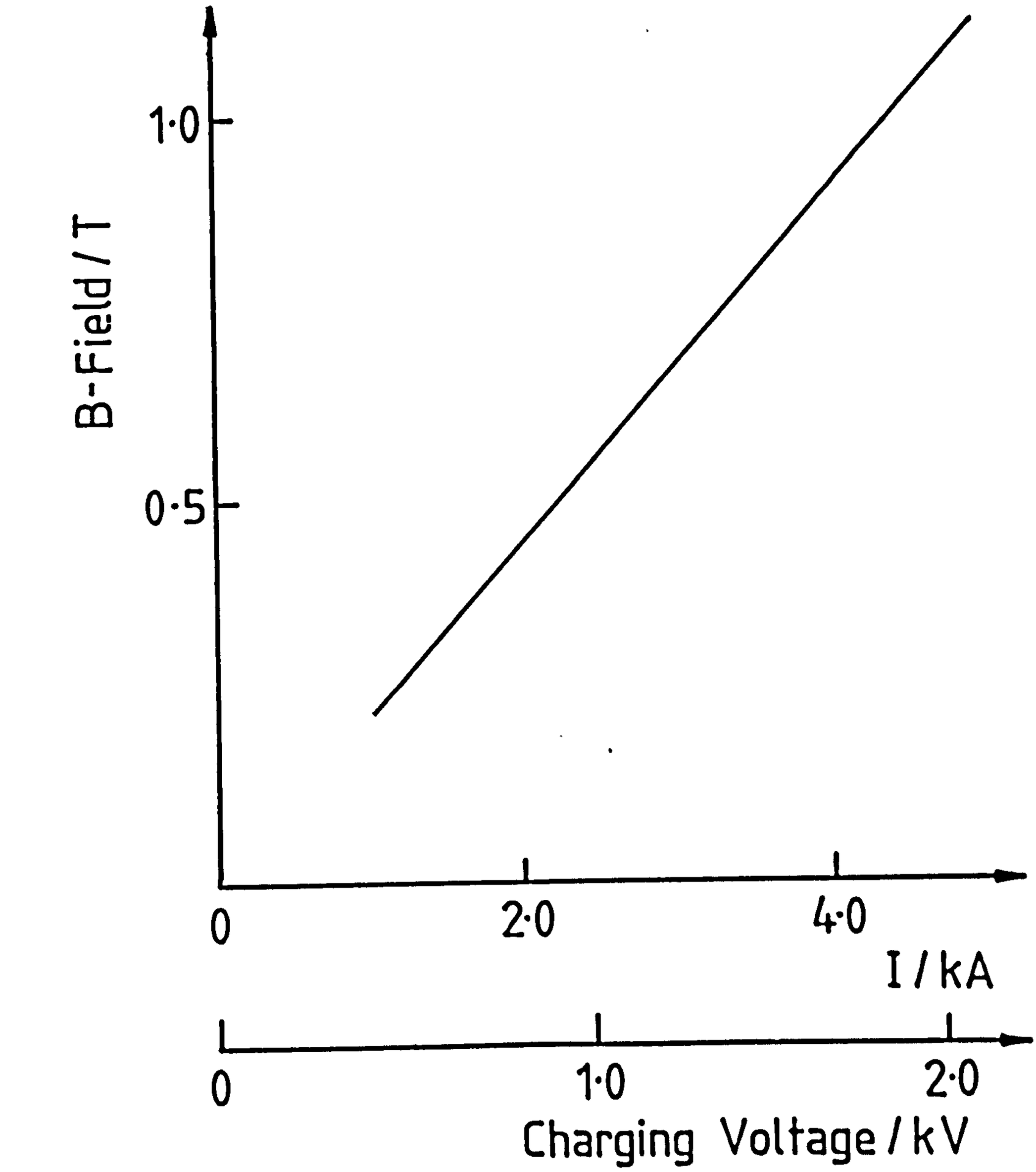


Fig.(4.3). Coil#2 field calibration.

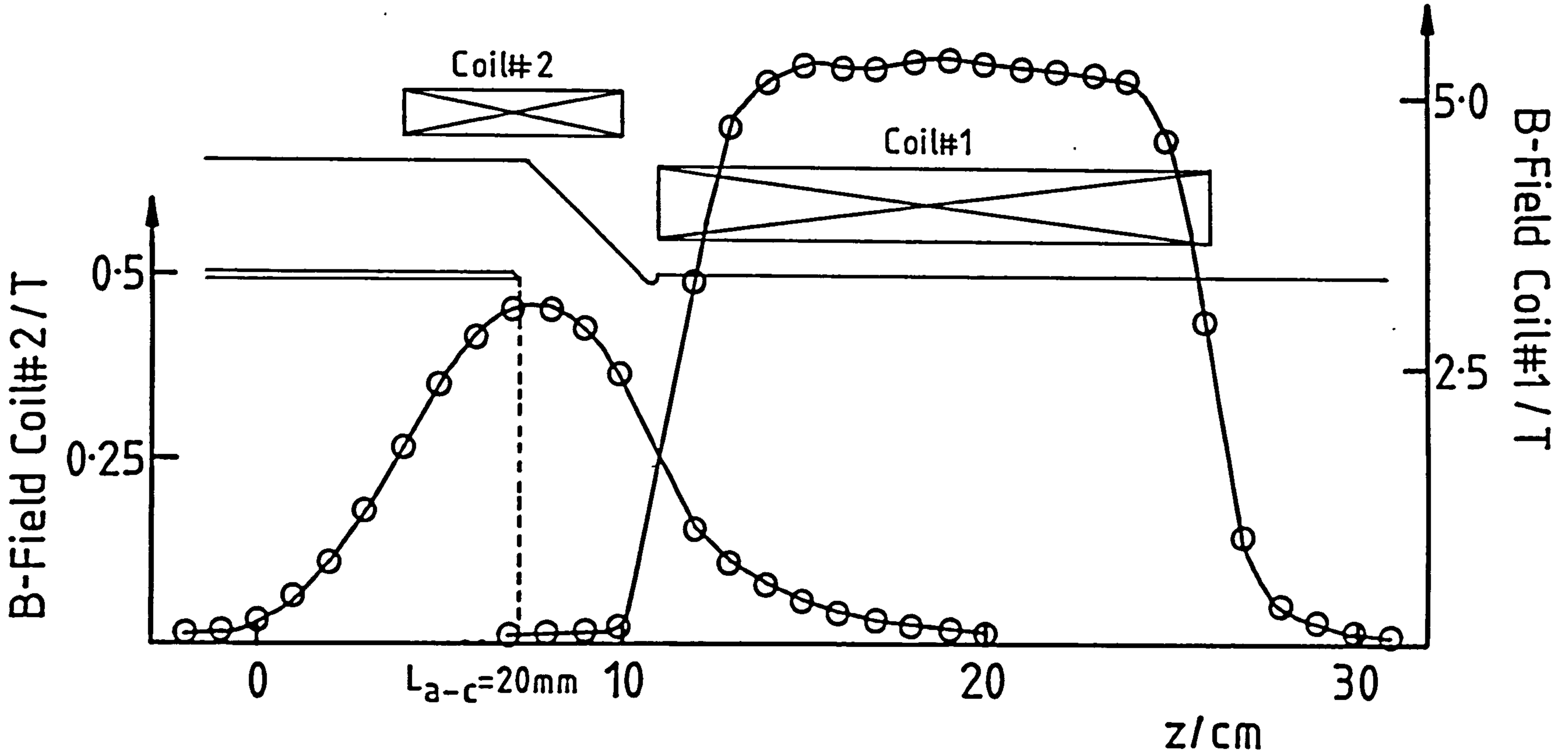


Fig.(4.4). Magnetic field profile through the cavity and cathode chamber.

$$= .4657\ (I/kA)\ T, \quad \text{for Coil\#1}$$

$$= .2479\ (I/kA)\ T, \quad \text{for Coil\#2.}$$

Where the symbols are as defined in eqn.(2.3). This value of B-field may then be compared with the measured B-field maximum and it was thus demonstrated that in both cases a field exclusion of ≃8% was evident. This reduction was allowed for in the design of both coils.

The over-riding factor in this experiment was that to generate radiation at 200GHz a magnetic field of ≃7T, (for $\gamma$=1), is required. This value was exceeded and a maximum B-field value of 9.40T was measured at the centre of the cavity. Importantly, this resulted in no damage to the field coil. This result is important in the development of this thesis, as the previous maximum magnetic field produced at Strathclyde University was 4T and it was not known whether the new field coil#1 could withstand the mechanical pressures associated with these higher B-field values. However this experiment shows coil#1 to be a complete success, accomplishing all of the objectives necessary to achieve maser oscillation at 200GHz.

Fig.(4.2) and (4.3) demonstrate the linear dependence of the magnetic field produced on both the coil current and the respective capacitor bank charging voltages. These graphs were analysed using a least squares fit method and the best straight line (y=mx+c) calculated. This allowed the evaluation of all subsequent conversion factors, with both gradient and intersection point displayed in table(4.1).

Due to the importance of these calibrations the errors at all points were kept to an absolute minimum and were calculated from each individual error arising from the entire detection system. (i.e. the probe coil dimension error=1.6%, the RC network integration time error=.26%, digital data recorder reading error=.4% and the graphical nonlinearity error=.25%). This results in an overall error in the measurement of the magnetic field of ≃1.7%.

The probe coil was also used to measure the B-field profile.

This was achieved by moving the probe coil through the cavity and the anode-cathode chamber at 1cm intervals, individually recording the field produced by both coils and keeping at all times the charging voltage on each respective capacitor bank constant. This resulted in fig.(4.4). It is evident that coil#1 produces a very uniform field over a length of ≈10cm through the cavity. This is essential to ensure the cyclotron frequency of the electrons does not vary over the length of the R.E.B./cavity mode interaction region. Due to its shorter length and greater winding diameter, the coil#2 B-field profile does not have an extended uniform region, however no prerequisites were made on its field profile. Its effect on the relativistic electron beam was not analysed in detail and the result of beam enhancement and improved efficiency was purely empirical.

## 4.3 I-V Characteristics of the Diode.

The I-V characteristics of the diode must be known as they relate directly to both the electron beam's $\gamma$-factor and current. An attempt will be made to measure this current from both the anode return current and the insulated beam probe. The experimental configuration for all of the I-V measurements is shown in fig.(4.5).

### Diode Voltage Measurements.

The diode voltage was measured using the voltage divider as described in chapter three. It was shown that,

$$V = \frac{R_1 + R_2}{R_2} V_{out},$$

which, in our case, reduces to,

$$V = (722 \pm 7)\ V_{out}.$$

A further reduction of 30dB was made to $V_{out}$ to ensure that it was a reasonable value before it was connected to the transient recorder.

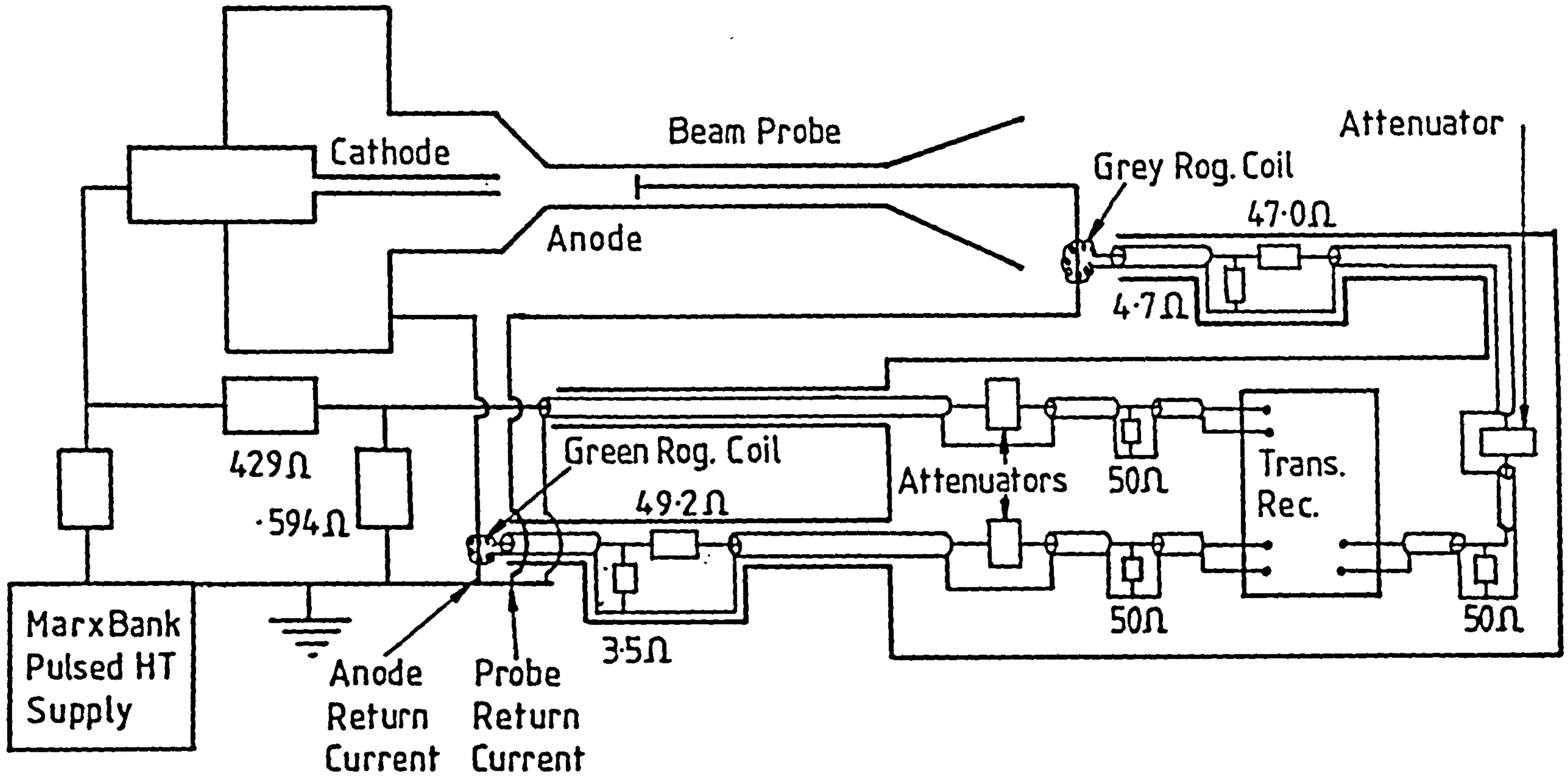


Fig.(4.5). Experimental configuration used to determine the I/V characteristics of the diode.

Using the above conversion factors, the Marx bank was fired at three different charging voltages and the following results obtained.

| $\frac{V_{charge}}{kV}$ | $\frac{V_{out}}{kV}$ |
|---|---|
| 18 | 72 ± 5 |
| 23 | 88 ± 4 |
| 26 | 89 ± 6 |

Table(4.2). Diode voltage versus Marx bank charging voltage.

These results were obtained with both field coils firing, $B_{coil\#1}$=3.04T and $B_{coil\#2}$=.26T. With an increase in charging voltage from 18kV to 23kV the discharge voltage increased from 72kV to 88kV, however a subsequent increase of the charging voltage to 26kV resulted in a mimimal increase in the discharge voltage from 88kV to 89kV.

As stated in chapter 2, an output voltage of ten times the charging voltage was expected. This did not prove correct with the resulting output being approximately four times the charging voltage. This is due to the anode-cathode gap closing before the Marx bank has reached its full discharge voltage and this effect also explains the saturation of the diode voltage at 89kV.

Magnetic Insulation of Diode.

The Marx bank was fired without the magnetic field coils#1 and #2, and the diode voltage was measured to be 6114kV. As previously stated with $B_{coil\#1}$=3.04T and $B_{coil\#2}$=.26T, keeping the Marx charging voltage constant at 18kV, the measured diode voltage rose to 72kV. This is a result of the magnetic field lines preventing the cathode plasma crossing the anode-cathode gap, resulting in

the diode remaining open circuit longer, and the Marx bank discharge rising to a consequently higher value.

This reinforces the statement above that the diode voltage is not reaching the full Marx discharge voltage due to the gap closure time being less than the Marx bank rise time.

Calculation of the Relativistic Correction Factor.

It is now possible to calculate $\gamma$, the relativistic correction factor for the electron beam. This may be done from the equation.

$$\gamma = \frac{e\ V}{m_0 c^2} + 1$$

Substituting a value of V=72±5kV yields the result,

$$\gamma = 1.14 \pm .01$$

This factor is essential in the calculation of the cyclotron frequency of the electrons as they interact with the cavity B-field.

HT Pulse Duration.

The HT pulse duration is a complex function of both the coil#2 B-field and the anode-cathode position and will be investigated fully in chapter 5 section 5.2 and 5.3. All the results presented in this chapter refer to the I/V characteristics of the diode with the anode-cathode position set for optimum pulse duration and maximum mm-wave output.

Diode Discharge Current.

This was measured with the green Rogowski coil in the self-integrating mode (fig.(4.5)). The beam probe was not present during this experiment. The maser was fired under typical

conditions, $V_{Marx}$=72kV, $B_{coil\#1}$=3.04T and $B_{coil\#2}$=.26T. Using the calibration of the Rogowski coil and taking into account the 42dB in the screened room the maximum current was measured to be 1.148±.016kA. It must be noted that the majority of the discharge current occurs after the Marx discharge current has dropped to zero; the current rise time is ≃1.7μs compared with the Marx full-width, half-maximum (F.W.H.M.) duration of ≃500ns. All of the electrons which occur after the HT pulse has effectively dropped to zero are part of a low voltage arc discharge and take no part in the electron cyclotron maser interaction. From this experiment it was impossible to determine the beam current when the diode voltage was at its maximum, however it seems to be a small fraction (<10%) of the Marx discharge current.

Beam Probe Current Measurement.

In an attempt to measure the R.E.B. current, the beam probe, as decribed in chapter 3, was introduced to the cavity. The output of the grey Rogowski coil, also used in the self-integrating mode, was fed back to the digital transient recorder in the screened room#1. This measured the current from the probe to earth. Both the green and the grey coil could be monitored simultaneously. The results of these measurements are summarised below.

| Anode return current / kA | Probe return current / kA | Total current / kA |
|---|---|---|
| .767 ± .01 | .429 ± .006 | 1.196 ± .016 |

Table(4.3). Beam probe current measurements.

The total current agrees well with that measured from the anode return current quoted above, 1.148±.016kA.

Although the witness plate is isolated from the anode under low voltage DC conditions, under HT pulsed conditions breakdown is

occurring. The probe return current was measured to have exactly the same rise time and duration as the anode return current. This again suggests that the majority of this is due to the low voltage arc discharge, with a maximum current 429A. There is no means of extracting the exact R.E.B. current from these results, however from simple analysis of the data the electron beam current must be ≤10% of the maximum probe return current.

Estimation of the Beam Current Via Witness Plate Damage.

Photographs (5.1) and (5.2) show five witness plates which have been placed in the cavity (while the R.E.B. has been pulsed) under various operating conditions of the maser. Clear damage has occurred, with surface melting evident over an area of $\simeq 0.1 cm^2$.

From this information the beam current may be estimated from theory, developed by Carslaw and Jaeger (58). Considering a semi-infinite solid with zero initial temperature at x=0, with a flux of heat raising the surface to a temperature excess T (°K) in a time t, assuming a constant flux $F_0$ per unit time per unit area then,

$$F_0 = \frac{T\ K}{2}\left[\frac{\pi}{\kappa\ t}\right]^{1/2} \qquad (4.1)$$

Where,

$\kappa = \dfrac{K}{\rho\ C}$ = The thermal diffusivity.

C = Specific heat.

$\rho$ = Density.

K = Thermal conductivity.

$$\left[\begin{array}{l}\text{i.e. the rate of flux of heat}\\ \text{per unit time per unit area}\end{array} = -K\frac{\partial T}{\partial x}\right]$$

Substituting suitable values into eqn.(4.1) ($c_{Cu}=386 JKg^{-1}\cdot K^{-1}$, $\rho_{Cu}=8.95\times10^{3} Kgm^{-3}$, $K_{Cu}=1.05\times10^{4} Wm^{-1}\cdot K^{-1}$, T=1000°K and t=100ns), results in a beam current of the order of 20A. The R.E.B. current

is a small fraction of the discharge current (≃2%) and is restricted by the narrow diameter (8.23mm) entrance to the cavity. This current may be improved in the future with an optimised anode-cathode design and B-field profile.

These results also explain why it was impossible to measure the beam current directly from either the anode or the probe return current.

Efficiency.

The beam current production is very inefficient ($\eta_{R.E.B}$=0.02). This is the product of attaching the new MK-6 maser to the previously constructed Marx bank. Had the power supplies been constructed at the same time as the Mk-6 maser, then a pulse sharpener could have been included between the capacitor bank and the diode. This would greatly increase the number of electrons in the initial high voltage pulse (at present most of the diode current is low voltage arc discharge occuring after the anode-cathode gap has closed).

The energy conversion efficiency from the R.E.B. to the output coupled electromagnetic radiation is given by eqn.(2.22),

$$\eta_T = \eta_{el}\ \eta_Q\ \ \eta_\perp \cdot \qquad (4.2)$$

From chapter 6, the peak output power from the maser was measured to be ≃50kW. Taking the beam current and voltage to be 20A and 72kV respectively, the net energy conversion efficiency (ignoring the R.E.B. production efficiency) is ≃4%.

Assuming $v_\parallel/v_\perp$=2/3, then $\eta_\perp$=0.6, and, due to the intentionally high ohmic losses in the cavity, $\eta_Q$=0.2. Thus from eqn.(4.2), $\eta_{el}$=0.33. Both $\eta_{el}$ and $\eta_\perp$ are reasonable values (0.33 and 0.6 respectively), however to further enhance these would involve the comprehensive and detailed analysis of the maser oscillation. $\eta_Q$ (which represents the ohmic losses in the cavity walls) may however be significantly improved by increasing the conductivity of the cavity surface (e.g. by silver plating).

However, our system is deliberately lossy to achieve

differential mode damping (and thus single mode oscillation), at the expense of efficiency. Although this results in a low overall efficiency, the maser has achieved very reasonable values of $\eta_{el}$ and $\eta_{\perp}$.

## 4.4 Experimental Method.

This section will be split into four parts covering the main experimental procedures used to produce the W-band and G-band results.

### 1) Direct Power Measurements Using Crystal Detector.

This experiment was designed to produce preliminary results measuring the direct power out of the maser as a function of cavity B-field, in both the W- and G-bands. This system will be used uncalibrated for sensitivity versus frequency, however it does provide an excellent qualitative preliminary analysis of the maser oscillation. The experimental configuration is depicted in fig.(4.6). The entire system is double screened, resulting in a noise level of <5mV in screened room#2. The W-band horn, attenuators, crystal detector and the amplifier were placed in a screened box looking at the maser output horn. This box was securely connected to the screened room via copper braiding. The output of the detector was monitored on a Tektronix 7844 oscilloscope via a 50Ω matching resistance.

Fig.(4.6) depicts the experimental configuration used in the W-band measurements. In the G-band the micrometer and rotary vane attenuators were replaced with a W- to G-band taper and calibrated G-band micrometer attenuator. The Flann 135 detector + load termination was changed for the more sensitive Flann 137 detector + plunger short, (chapter 3, section 3.7).

Due to the very small angle subtended by the W-band horn from the maser output, a second copper horn was added outside (though not touching) the screened box. This was an attempt to reduce the mode dependency of the coupling between the maser output and the W-band pickup horn, (the copper horn acts as a mode scrambler).

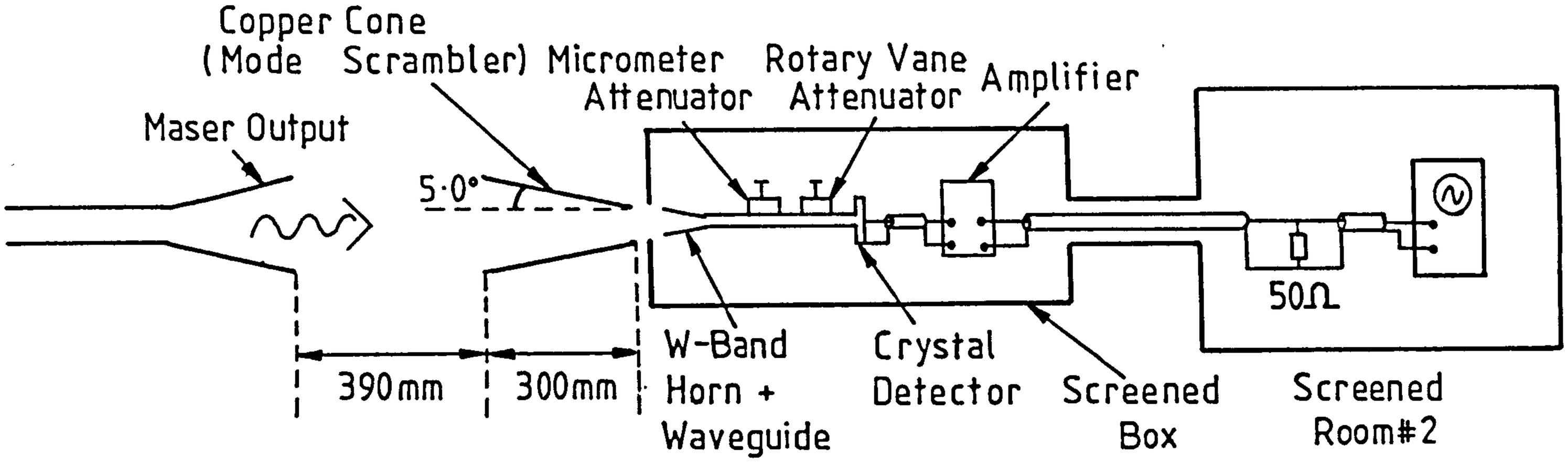


Fig.(4.6). Experimental configuration used to determine the direct maser output.

Complete control of the running of the maser was carried out by the HP9816 computer in screened room#1. The maser cavity B-field may thus be scanned through the W-band. At each field value the maser was fired several times and the detector output noted and the average taken.

2) Calibrated spectroscopic analysis of the Maser Output.

This experiment was performed to measure the frequency and the frequency bandwidth of the maser oscillation in both the W- and the G-band. A significantly different experimental configuration was used in each case and will be dealt with separately below.

1) W-band.

The experimental configuration is shown in fig.(4.7). Again the detection system is completely double screened resulting in a noise level of <10mV. The output of the maser was coupled into the Ka-band feeding waveguide via a W-band waveguide input and W-band to Ka-band taper. The W-band receiving horn, Flann 135 detector + load termination and the amplifier were placed in a screened box connected to the screened room#2 via copper tubing and flexible copper braid sheathing wrapped in aluminium foil.

2) G-band.

The more complex experimental configuration used in conjunction with the spectrometer in the G-band is shown in fig.(4.8). Due to the decrease of the sensitivity of the Flann 137 detector in the G-band and the fluctuating maser output, for the first time at Strathclyde University a two detector technique was used (in this case the two detector technique will be used to obtain the G-band spectrometer scans).

The same system was used to couple and receive the signals through the spectrometer, as in the W-band, with the exception of a Ka-band pick-up horn at the maser output and the Flann 137 detector + plunger short termination used in the screened box.

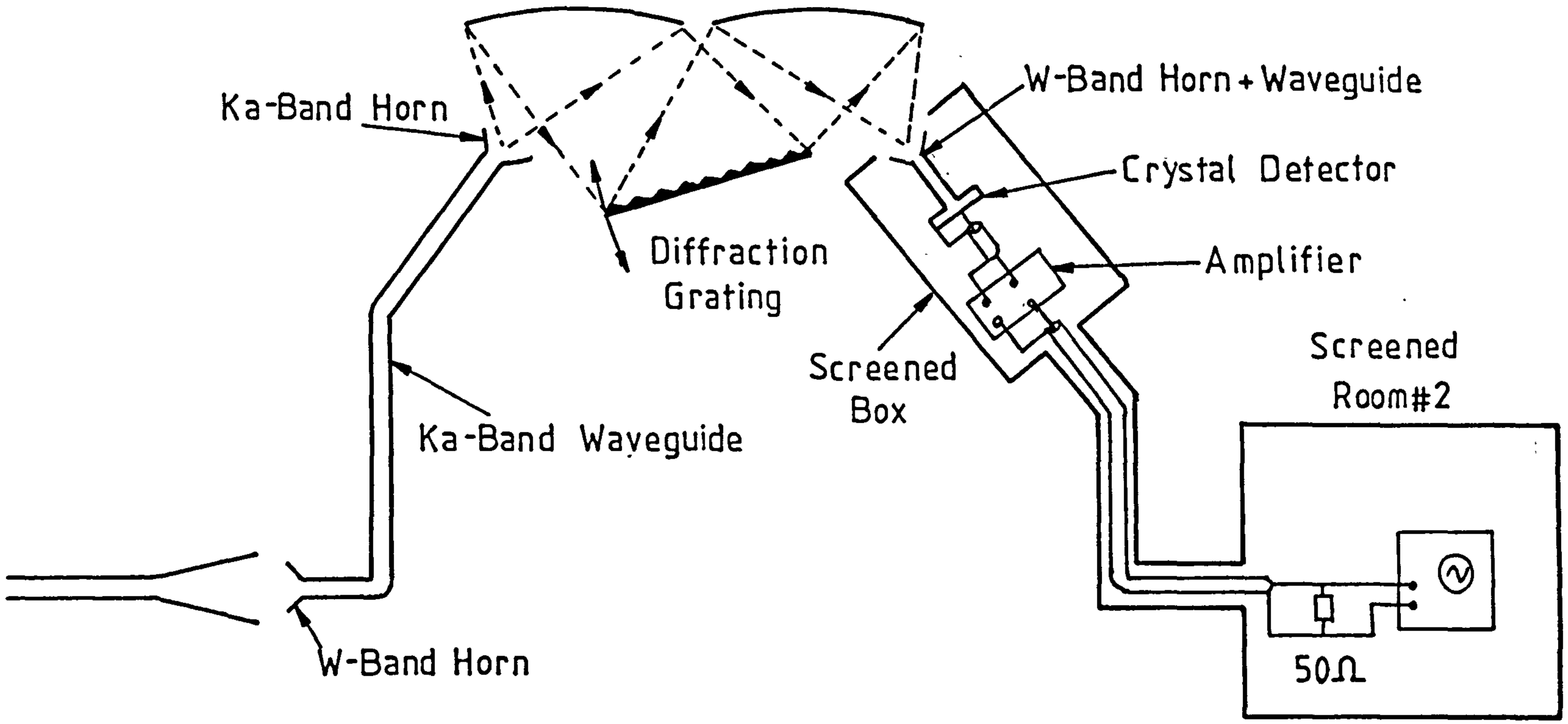


Fig.(4.7). Experimental configuration used in the W-band spectroscopic analysis of the maser output.

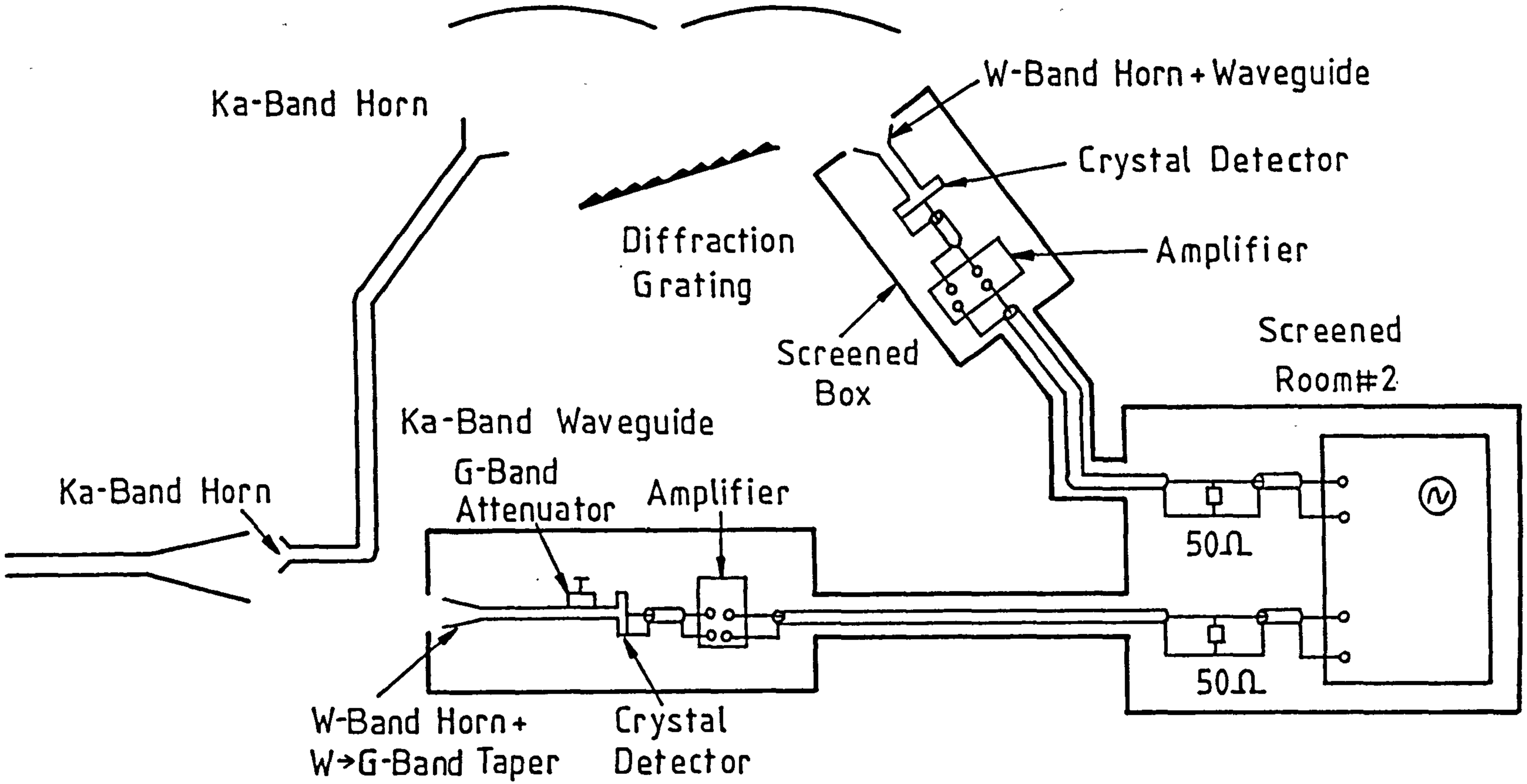


Fig.(4.8). Experimental configuration used in the G-band spectroscopic analysis of the maser output.

Coupled with this measurement, a direct reference signal was taken using a similar technique to that used in the direct power measurements above, fig.(4.6). On each shot both detector signals were simultaneously monitored and the resulting spectrometer signal normalised using the following equation.

$$\text{Adjusted detector output} = \frac{\text{Spectrometer detector output}}{\text{Reference detector output}} \times 100\text{mV}$$

Where 100mV was taken to be the average and the ratio of the two detector outputs centred at 1. (More will be said about the advantages and disadvantages of the two detector system in the next section).

The Flann 135 detector output in the W-band and both the Flann 135 + 137 detector outputs in the G-band were monitored on a Tektronix 7844 oscilloscope via 50Ω matching resistors.

The firing of the maser was controlled by the HP9816 computer in screened room#1. All the maser operating parameters were held constant while the grating was scanned through the relevant frequency band. This was repeated for several values of the B-field. At each grating position at least four shots were observed and the detector output averaged.

Although the spectrometer was fully calibrated for frequency and insertion losses, it is impossible to anticipate the mode dependent coupling of the maser output into the sampling horn. However it is reasonable to assume that the coupling of any one mode (or frequency) will be constant, i.e. sampling will always be from the same section of the output mode pattern. It will thus not be possible to integrate under the spectrometer frequency curves and estimate the output power of the maser for any given cavity B-field, nor will it be possible to gain precise information on the relative energy fed into different modes. However the measured relative output power in any one mode (with respect to itself), as the cavity B-field is gradually altered, should reflect the absolute power intensity in that mode.

Although there will be this doubt in the relative power levels of any respective mode of oscillation as measured through the

spectrometer, the frequencies measured will be accurate, with a reading error ≤2GHz.

3) Measurement of the Relative Power Intensity Across the Output Window.

In the previously described experiments, distinct resonances were expected in both the direct output measurements with respect to the cavity B-field, and the frequency measurements through the spectrometer. However, in the intensity distribution across the output window, variations in power levels of less than a factor of two have to be resolved. Such small variations might well be lost owing to the irreproducibility of any particular maser pulse. An improved, more precise, two detector technique was thus adopted for these measurements, fig.(4.9).

The varying intensity distribution signal was sampled using a W-band waveguide. This could be scanned across the output window both vertically and horizontally, via an optical bench translator. This waveguide could not be directed straight into the screened room without resulting in a measured noise level of several volts. The signal was thus coupled into the screened room using two 20dB W-band horns. Using a W-band attenuator the mm-waves were fed to the Flann 135 detctor. To ensure constant coupling between the two horns, the waveguide was clamped outside the screened room and only the sampling end of the waveguide allowed to move (the clamp effectively acted as a fulcrum for the translator).

In conjunction with this a second Ka-band sampling system was used. At all times the position of this waveguide was kept constant. This sampled signal was again coupled into the screened room using two horns, a 20dB Ka-band horn on the outside and a Ka-band to W-band taper,used as a horn, on the inside. This led directly to an uncalibrated Baytron V-band detector in a W-band mount. Both detector signals were simultaneously fed into a Tectronix 7844 oscilloscope; the Flann 135 detector (variable signal) via an amplifier and a 50Ω termination, and the Baytron detector (the reference signal) via an HF filter circuit ($\tau$=95ns) and the 1MΩ input resistance of the oscilloscope. The filter

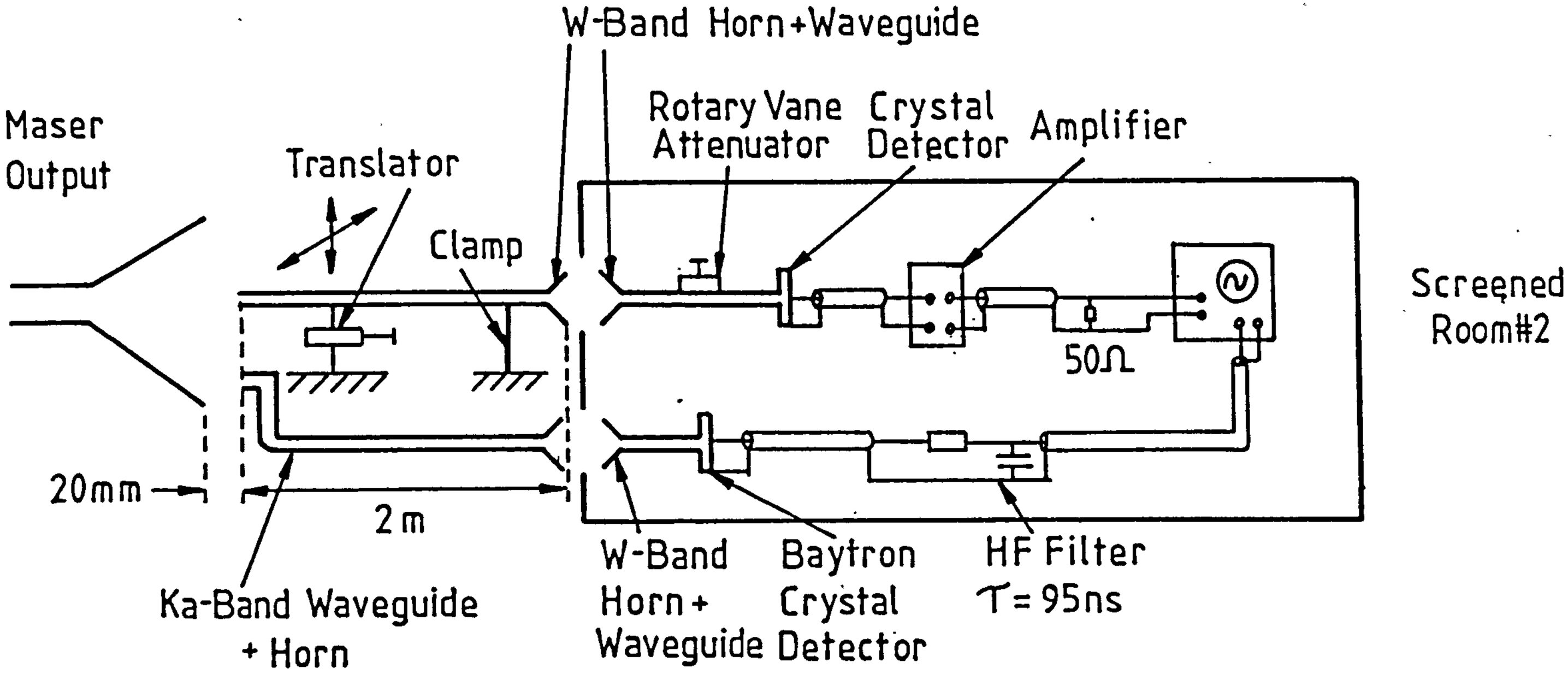


Fig.(4.9). Experimental configuration used to determine the radiation intensity distribution across the output window.

circuit was added to smooth the reference signal, aiding the simultaneous measurement of both detector outputs.

The operation of the maser was controlled entirely by the HP9816 computer in the screened room#1 and the maser was fired repeatedly under exactly the same conditions. The W-band waveguide was scanned across the output window at a distance of approximately 2cm. At each position the maser was fired at least four times and both detector outputs noted. Each pair of data points could then be normalised exactly as described in the previous section. This will, in principle (and was shown later to be true), largely remove the variations in detector output due to the irreproducibility of any given maser pulse. There are two advantages to this procedure;

A) it reduces the number of shots required to gain a reliable average, and
B) it reduces the magnitude of the error bars on any graph for a given number of shots.

This is the first time such a two-detector system has been used at Strathclyde University and we shall be able to demonstrate later that it yields very reliable results.

4) Direct Power Measurements Using a Calibrated Power Meter.

The output power of the maser was measured using a calibrated thermocouple array combined with the Flann 135 crystal detector. The thermocouple array measured the energy in each pulse and the crystal detector measured the pulse length. The experimental configuration is shown in fig.(4.10). As the signals are effectively DC (from the array of thermocouples), its transmission line has only been single-screened. An HF filter ($\tau$=95ns) and a large inductance was added between the thermocouple array and the screened room, to remove any large voltage spikes and HF noise, which may damage the digital voltmeter.

The output of the thermopile was observed on a digital multimeter, this was connected via the HP-IB parallel bus

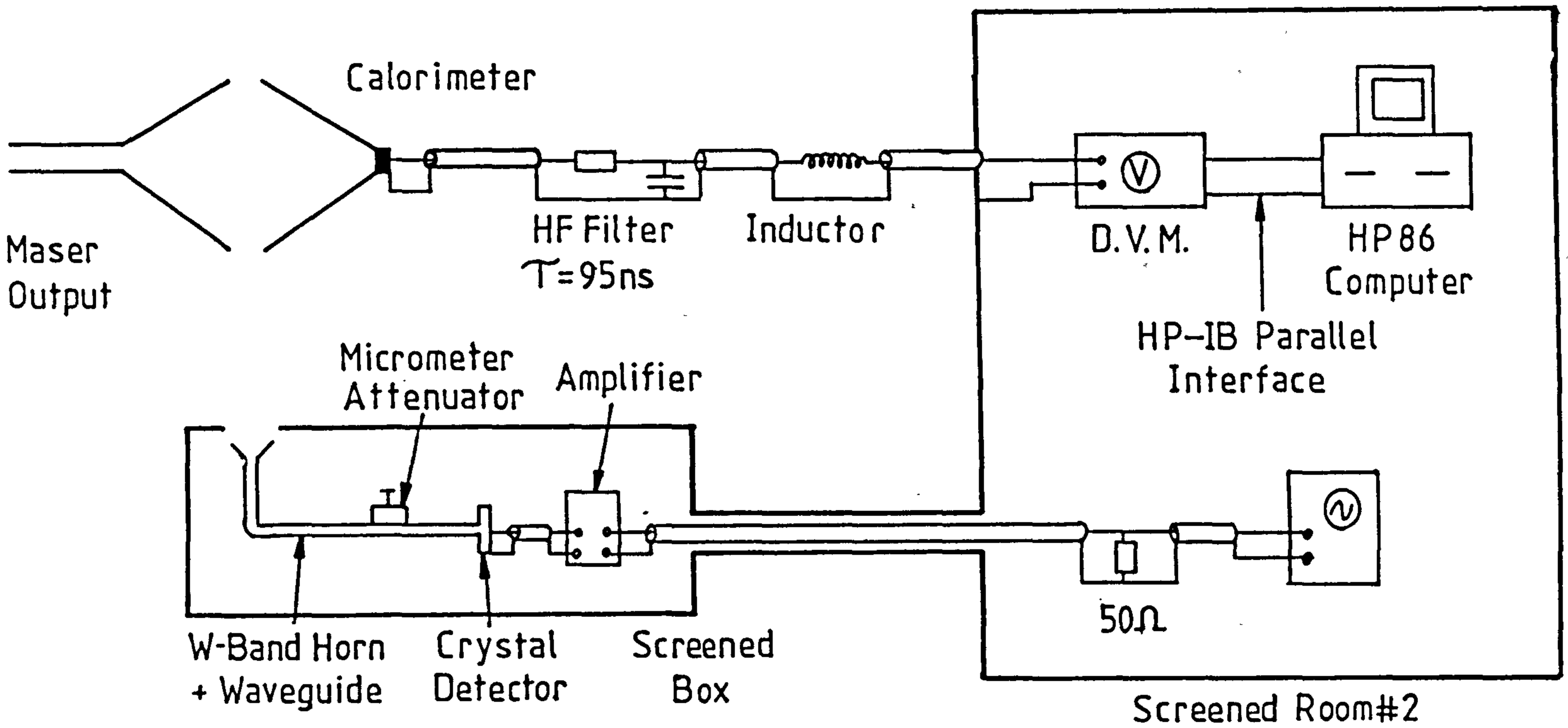


Fig.(4.10). Experimental configuration used to determine the output power of the maser.

interface to an HP86 computer which recorded the output of the thermocouple array and plotted it on a graph as a function of time.

In conjunction with this system the Flann 135 crystal detector was used in exactly the same configuration as the direct power measurements in fig.(4.6). In this instance the detector picked up scattered radiation as much as 30dB down on previous measurements. This provided a means of measuring the length of each mm-wave pulse. Using the naked eye to obesrve a non-storage oscilloscope trace, it would be impossible to determine the F.W.H.M. of each individual mm-wave output pulse; instead the length of the base was measured and taken as the total temporal duration of the pulse. This will result in measured power levels slightly less than those attained by the maser due to the approximation of the mm-wave output as a square wave form. A more realistic pulse shape may be somewhere between a triangular and a square wave output. The worst case will be used in the analysis of the experimental data (though it will be noted as such).

Again the maser was controlled via the HP9816 computer in screened room#1 and the output power measured for various cavity magnetic field values. At each point, under the defined maser operating conditions, at least six (and up to twelve) shots were measured and averaged to give the stated power out.

# CHAPTER -5-

# MASER OPTIMISATION.

## 5.1 Introduction.

The results of the optimisation of the maser output with respect to the anode-cathode position and the B-field produced by coil#2 are presented below. Two aspects of the maser optimisation were studied. Firstly the mm-wave duration; it will be shown that the anode-cathode gap closure time is a strong function of the gap spacing ($L_{a-c}$), which bears a direct relation to the duration of the R.E.B. and hence to the duration of the mm-wave output. Secondly, the output power must be optimised and this proved to be a strong function of both $L_{a-c}$ and the coil#2 B-field.

These results supplemented by beam witness plate results demonstrate both the greatly increased current when the coil#2 B-field is activated and the high degree of beam collimation over the length of the cavity.

The results in this chapter are explained in terms of the increased magnetic insulation of the diode, the beam focusing effect and the B-field compression ratio.

## 5.2 Gap Closure Time and mm-Wave Pulse Duration w.r.t. Anode-Cathode Spacing

The anode-cathode gap spacing was varied and the gap closure time along with the mm-wave pulse duration measured, fig.(5.1). These results were obtained under the following firing conditions of the maser;

$V_{Marx}$=72kV,
$B_{coil\#1}$=3.63T and,
$B_{coil\#2}$=0.21T.

The anode-cathode gap closure time increases almost linearly from 250ns to 600ns with gap spacing ($L_{a-c}$) increasing from 0 to 25mm. The mm-wave pulse duration increases correspondingly from 100ns to 425ns with $L_{a-c}$ increasing from 0 to 20mm. A reduction in the mm-wave pulse duration to 375ns was measured with a subsequent increase of gap spacing to 25mm. A peak in the mm-wave duration

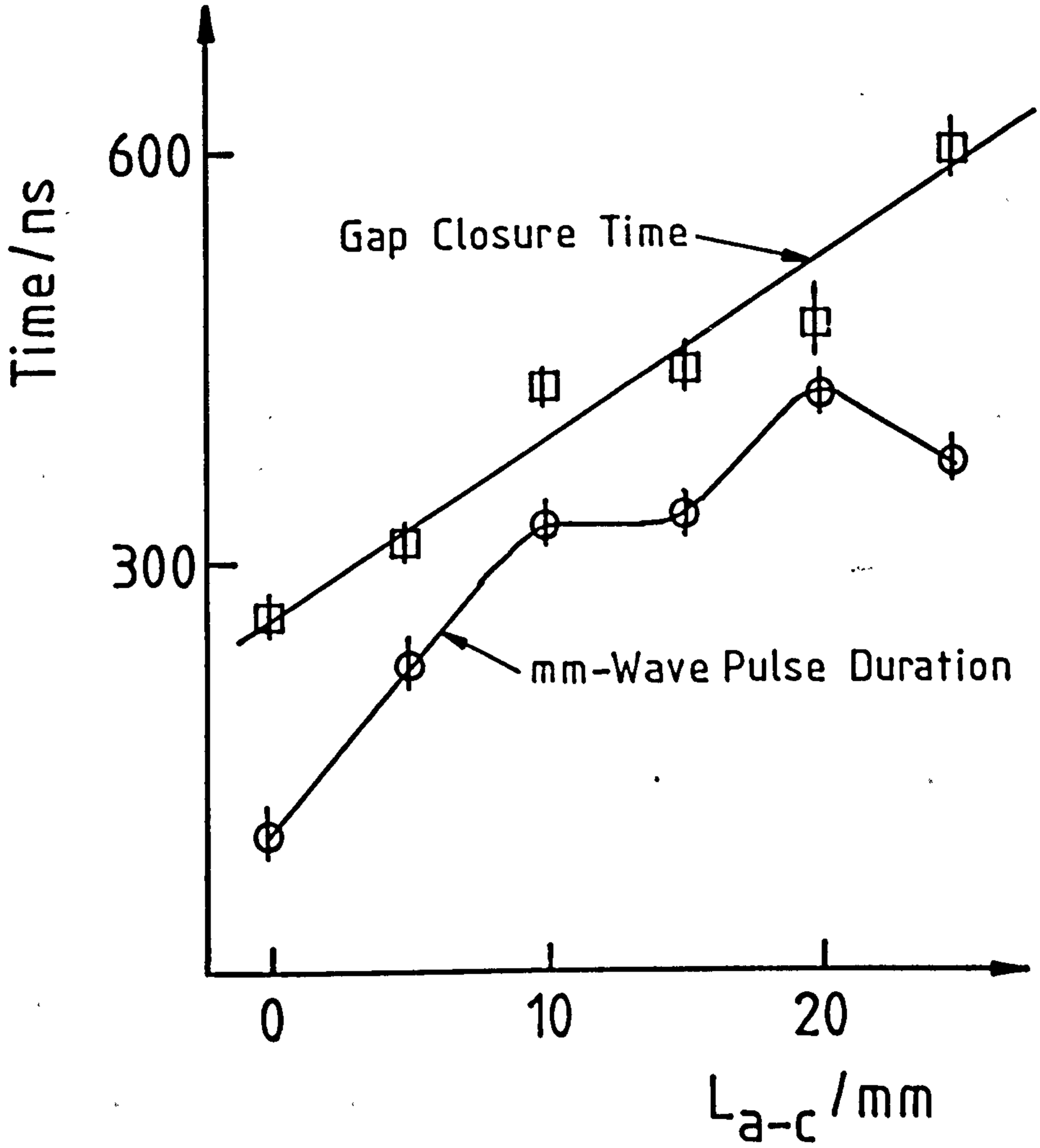


Fig.(5.1). Gap closure time and mm-wave pulse duration as a function of the anode-cathode gap spacing.

therefore occurs at $L_{a-c}$=20mm.

## 5.3 mm-Wave Pulse Duration w.r.t. Coil#2 B-field.

The mm-wave pulse length was measured as a function of the B-field produced by coil#2 (for two values of anode cathode position, viz:0 and 25mm). The magnetic field produced by coil#1 and the voltage from the marx generator were set at the same values as in the previous section. The results are presented in fig.(5.2) and show that the mm-wave pulse duration is not greatly affected by the coil#2 B-field in the range of 0.21T to 0.54T (varying by ≃10% when $L_{a-c}$=0mm and <1% when $L_{a-c}$= 25mm). Above this, however, the pulse length drops off dramatically, falling by 40% between .54T and 1.04T with $L_{a-c}$=0mm and 40% between .54T and .79T with $L_{a-c}$=25mm. Both graphs reflect the stronger dependence on the pulse length of the anode-cathode gap spacing, as depicted in fig.(5.1).

## 5.4 Maser Output Power w.r.t. Anode-Cathode Spacing and Coil#2 B-Field.

The anode-cathode gap spacing was varied and at each position the B-field produced by coil#2 was varied keeping coil#1 constant. The mm-wave output was measured and the results shown in fig.(5.3). The same firing conditions were used as in the previous section, with the coil#2 B-field being varied between .21T and 1.04T. The maser output seems to maximise and saturate at a gap spacing of ≥+15mm. As the spacing is reduced from 20mm to zero the maximum detector output falls from 350mV to 155mV. As the anode-cathode gap spacing is reduced the output becomes less dependent on the coil#2 magnetic field. The output varied from 350mV down to <5mV when $L_{a-c}$=20mm, compared with a reduction of only 155mV (to a minimum of 110mV) when $L_{a-c}$=0mm, over the same B-field range of .21T to 1.04T.

It was also noted that in all cases the mm-wave detector output is greatly enhanced by the addition of the cathode magnetic field. When coil#2's B-field was not activated the output of the maser

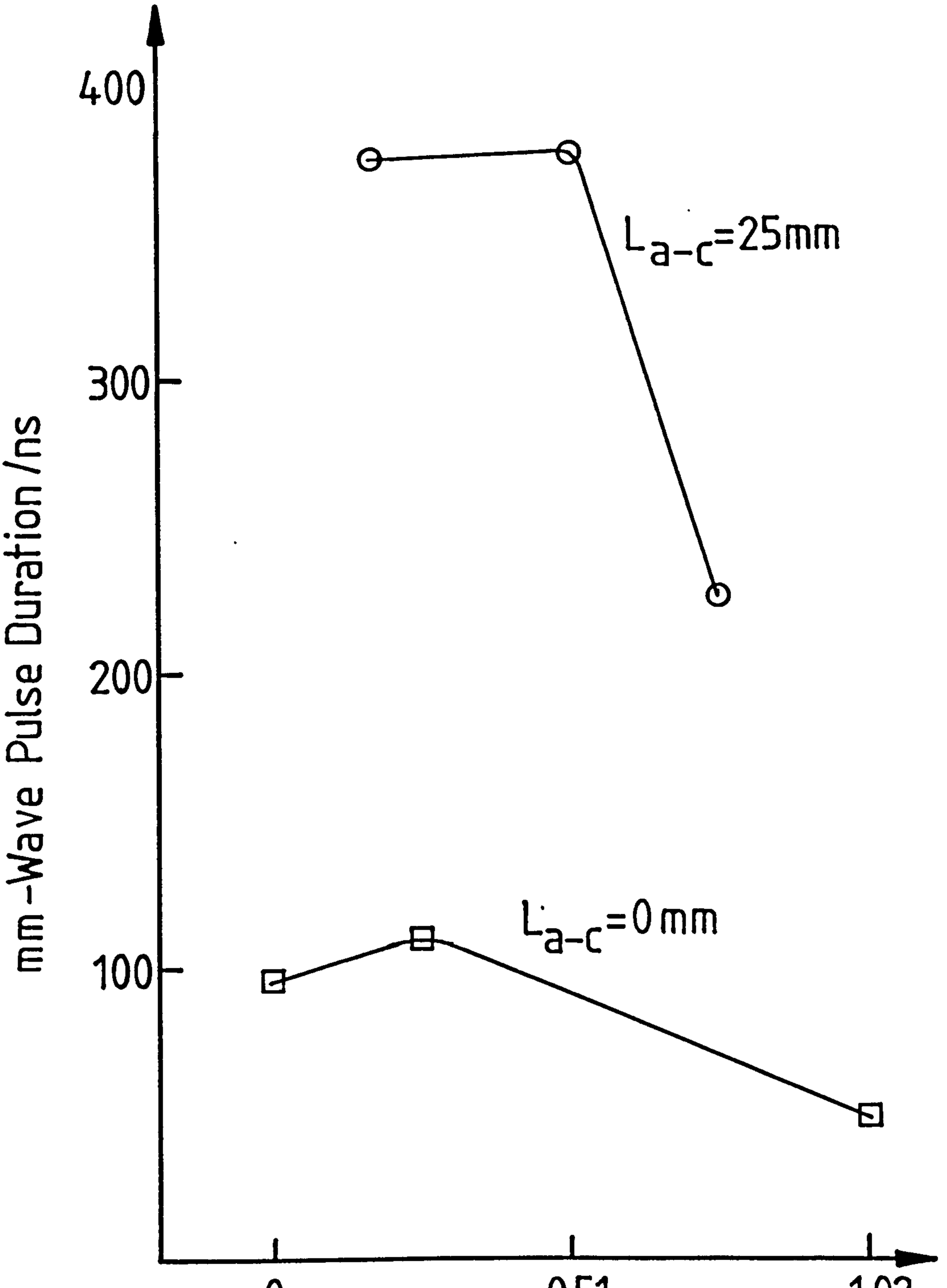


Fig.(5.2). mm-wave pulse duration as a function of coil#2 B-field at two positions of $L_{a-c}$.

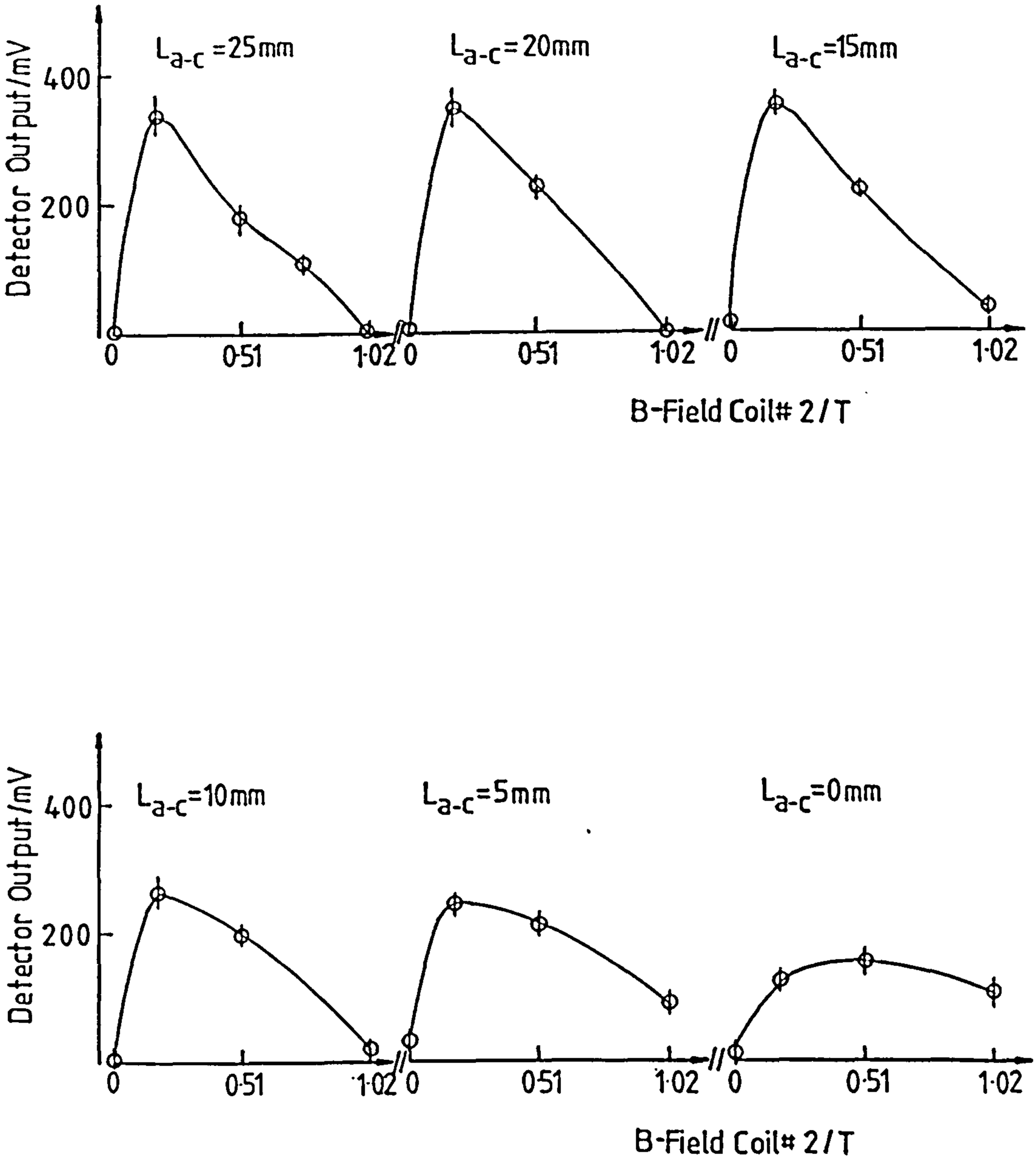


Fig.(5.3). mm-wave output against coil#2 magnetic field and anode-cathode position.

was reduced to ≃5mV for all values of $L_{a-c}$.

Exactly similar behaviour was found for all values of the coil#1 B-field.

## 5.5 Electron Beam Witness Plate Results.

The maser was fired under three different conditions with the resulting damage to the witness plates shown in photograph(5.1). In this instance each plate was placed at a position 5cm from the entrance to the cavity and received a total of twenty shots under the conditions stated.

1) Witness Plate A. R.E.B. only, $V_{Marx}$=72kV, no magnetic fields present. This has resulted in no detectable damage to the witness plate. No magnetic field lines were present to guide the electrons through the cavity, instead they will take the shortest path across the gap to the anode.

2) Witness Plate B. R.E.B. and B-field coil#1, $V_{Marx}$=72kV, $B_{coil\#1}$=3.63T. Here damage is evident on the witness plate, some melting and general darkening of the surface has occurred. An electron beam is being formed in the cavity and is reaching the plate. However from the resulting damage the flux intensity is very low.

3) Witness Plate C. R.E.B. B-field Coil#1 and coil#2. $V_{Marx}$=72kV, $B_{coil\#1}$=3.63T and $B_{coil\#2}$=.29T. In this case severe damage is seen on the plate. A 3mm diameter circular melted disc has been formed with some evaporation of the copper surface evident. Coil#2 thus has a very strong effect on the production of the R.E.B. travelling through the cavity. It is not possible to determine whether the beam is travelling in an annulus or whether it has collapsed into a solid beam. It is evident however that the beam current is greatly enhanced by the presence of the cathode B-field coil#2, improving the efficiency of R.E.B. production.

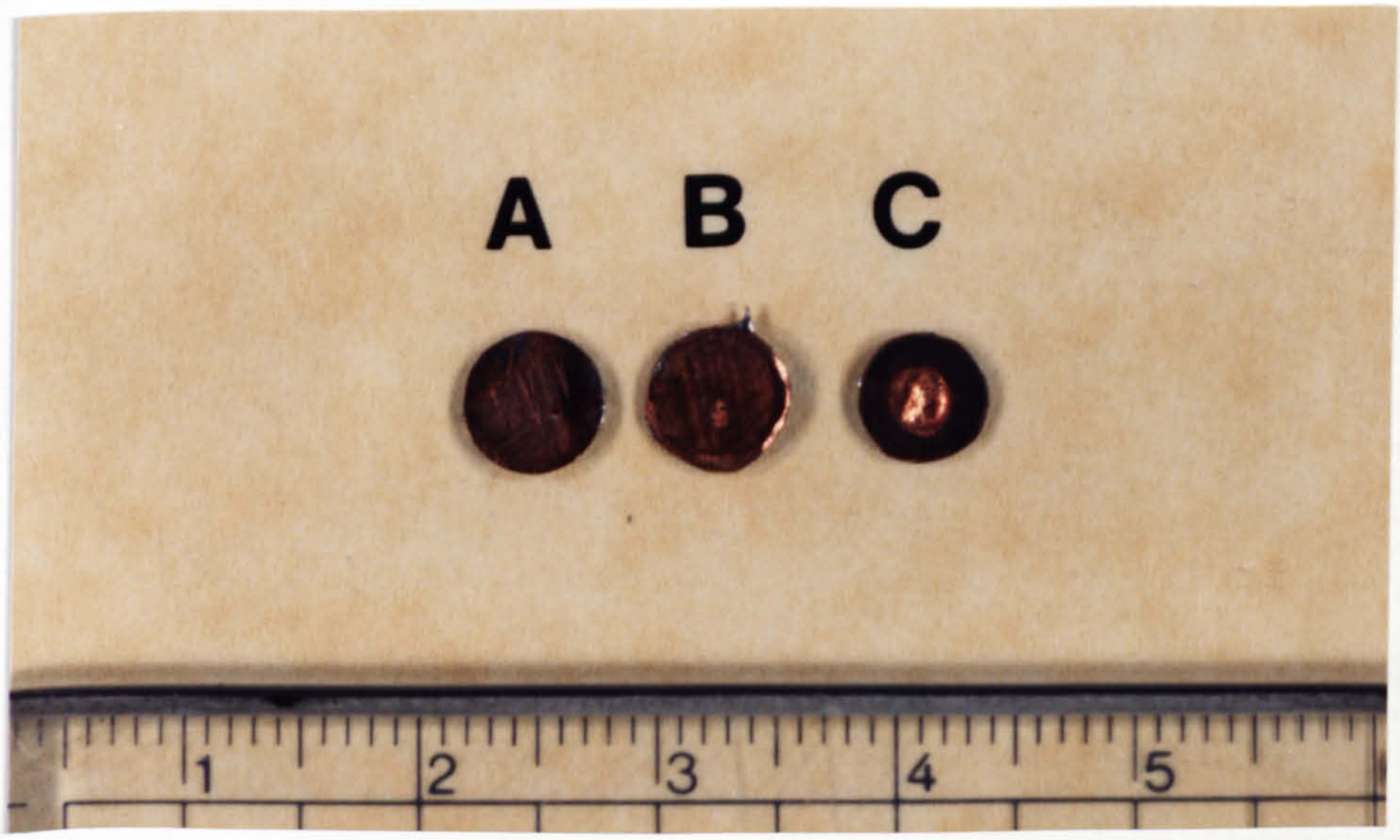


Picture(5.1). R.E.B. damage to copper witness plates under various operating conditions of the maser.

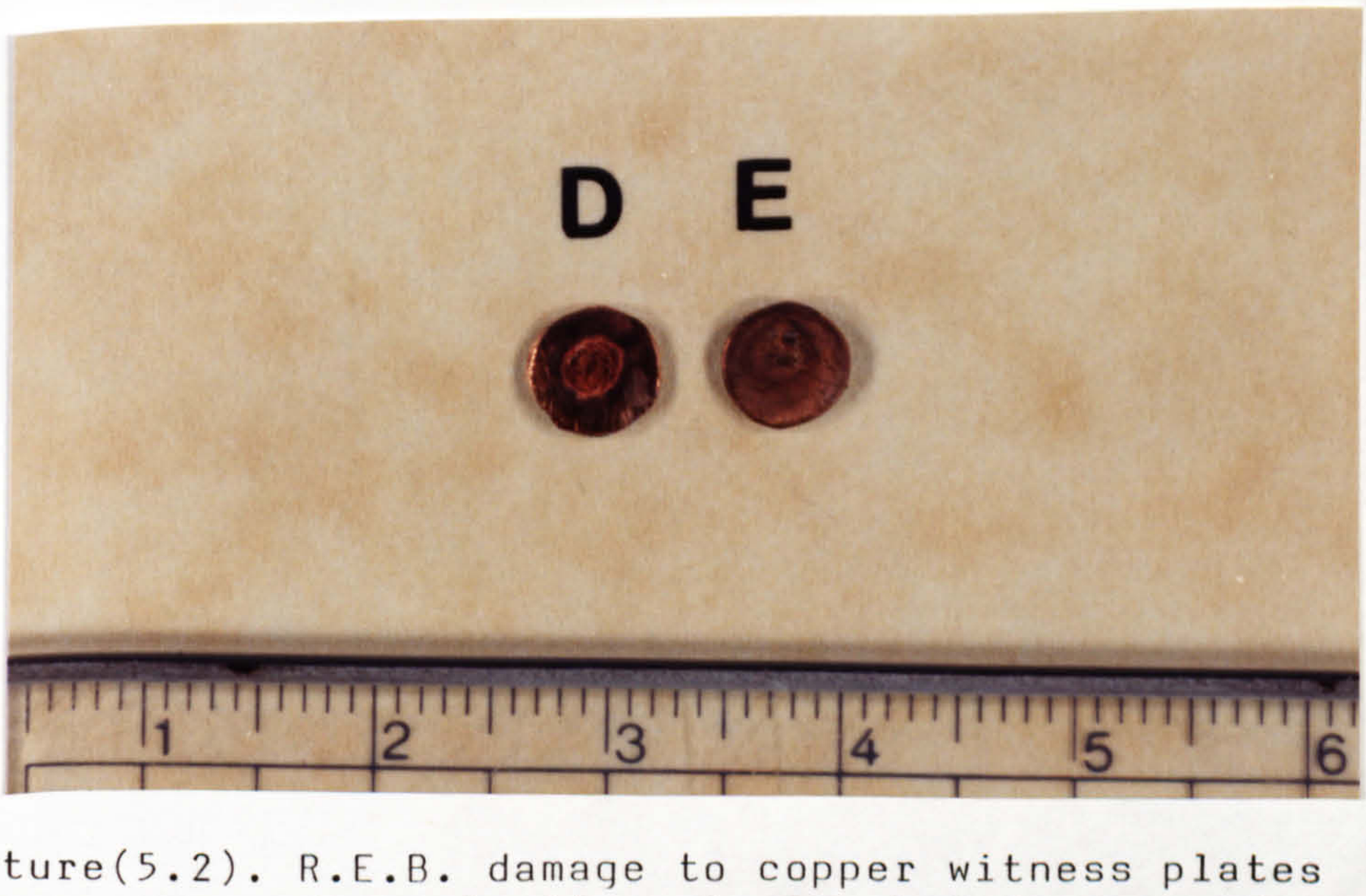


Picture(5.2). R.E.B. damage to copper witness plates demonstrating single shot damage and collimation of the beam.

A second experiment was conducted to discover whether all the damage on witness plate 3 was the result of one shot, with subsequent shots reproducing a similar amount of melting, or whether the damage was a cumulative effect of the twenty shots. The results are shown in photograph(5.2) (witness plate D). This plate was placed in the same position as all the previous plates and received 1 shot under the same conditions as plate C.

Again a circular melted disc has been formed very similar to that on plate C. It is evident that a large amount of damage occurs on each shot with subsequent shots recreating the same surface melting. This also demonstrates that the electron beam diameter is ≃3mm. (From plate three it is not clear whether the damage was produced by a broad reproducible beam or a narrow beam which changes position over many shots).

Lastly the probe was moved back to determine how well the beam was collimated. Witness plate E, photograph(5.2), received 1 shot under the same conditions as plate D, however in this case the plate was moved back away from the cathode a distance of 9cm. Here the damage is very similar to that of plate D. In this instance the plate was placed at a position where the B-field lines were begining to taper out and there is some evidence of slight divergence of the beam. However these measurements show that the R.E.B. must be well collimated throughout the cavity.

## 5.6 Analysis and Discussion.

The first stage in the operation of a system such as an E.C.M. must be the optimisation of the power output. This may be achieved systematically, commencing with the alteration of the anode-cathode gap spacing and the magnitude of the cathode coil magnetic field. These parameters will ultimately decide exactly what trajectories the electrons will follow. It would be possible, via computer simulation, to calculate the optimum position of the cathode with respect to the anode and the optimum magnitude of the cathode B-field, however with the constructed system it is possible to vary these parameters while monitoring and simultaneously maximising the mm-wave output from the maser.

To ensure maximum energy in any given mm-wave pulse, the pulse duration must be as long as possible. The length of this pulse will be governed by the length of the R.E.B., which will in turn be governed by the gap closure time.

It has been demonstrated that moving the cathode from its initial position back 25mm, fig.(5.1), has increased the gap closure time from ≃260ns to ≃600ns in an approximately linear manner. Some points do lie off this line, however this phenomenon will be due to the complex processes occurring in the discharge and the interaction with the magnetic field lines present.

With this increase in gap closure time a corresponding increase in the length of the mm-wave pulse was observed, also fig.(5.1). This has increased from ≃100ns to ≃425ns at a cathode position of +20mm. Further increase in the gap spacing results in a decrease in the pulse duration. The reason for this reduction is not obvious, however, as the cathode is pulled further back past the optimum +20mm mark the conditions necessary to direct the R.E.B. into the cavity become stricter and I would suggest that these conditions cannot now be satisfied by the anode-cathode position and cathode B-field combination.

All the results shown in fig.(5.1) are for one setting of each of the two field coils. These results proved repeatable for several values of magnetic field produced by the cavity coil#1. The gap closure time proved to be largely independent of the coil#1 magnetic field, this was however not the case for coil#2 (see fig.(5.2)). Here it was found that the length of the pulse was largely unaffected between a cathode magnetic field range of 0→.54T, (≃10% variation at $L_{a-c}$=0mm and <1% at $L_{a-c}$=25mm). However above .54T the pulse length becomes a very strong function of the coil#2 B-field, dropping by ≃50% between .54T and 1.04T with $L_{a-c}$=0mm and ≃40% between 1 and 1.5kV with $L_{a-c}$=25mm.

From all of the information stated above it is thus possible to maximise the length of the mm-wave pulse by setting the anode-cathode spacing to +20mm and firing coil#2 so as to produce a B-field between .21T and .54T.

Having optimised the length of the pulse the actual maximum

power output from the maser must be investigated w.r.t. the anode cathode spacing and coil#2 B-field. From fig.(5.3) it is evident that the maximum output of the maser increases as the cathode gap is changed from 0 to 15mm. This corresponds to a relative increase in the detector output from 150mV to 350mV. (The detector is working in the linear regime i.e. $V_{out} \propto P_{in}$ and at the moment we are only interested in relative powers as the various parameters are changed). Further increase in the gap spacing does not increase the maximum power out. It is also noted that as the gap spacing is increased the output from the maser becomes a stronger function of the coil#2 B-field, dropping from 350mV to <5mV as $B_{coil\#2}$ increases from .21T to 1.04T at $L_{a-c}$=20mm, while in the same coil#2 range at $L_{a-c}$=0mm, the output only varies by 17%. This effect can be explained as follows, as one increases the distance the electrons have to travel before they enter the cavity, the restrictions on the guiding magnetic field lines become more severe, and hence only certain values of coil#2's B-field will produce the required effect.

The maximum power out from the maser occurs, at all positions of the anode cathode spacing (except 0mm) at a coil#2 B-field of .21T.

From all the results above it is now possible to optimise the output power from the maser in both peak power and maximum pulse length. Summarising the above information:

1) To maximise pulse length requires,

$$L_{a-c}=20mm,\ B_{coil\#2}=.21T \text{ to } .54T.$$

2) To maximise peak power requires,

$$L_{a-c}=15 \text{ to } 25mm,\ B_{coil\#2}=.21T.$$

It is thus possible to mutually satisfy these conditions with an anode-cathode position of +20mm and $B_{coil\#2}$=.21T. However

$B_{Coil\#2}$=.21T would be an ideal, but critical, condition. As the output of the maser drops dramatically as the magnetic field is reduced below this value, a $B_{Coil\#2}$=.29T will be used, thus maintaining the operation of the maser away from this critical condition.

All subsequent experiments have been carried out with the above parameters as stated. The pulse length and output power have been optimised under exactly the same conditions. To maximise the pulse length an electron beam of optimum duration and stability travelling through the cavity is required. This is the same condition which will allow the electron cyclotron maser instability to develop and extract the maximum energy from the beam.

The second B-field coil has had a dramatic effect on the output of the maser, increasing the detected signal from below 5mV to 350mV, a factor of approximately 70. At the same time adjusting the anode-cathode spacing has increased the length of the pulse from 100ns to 400ns a factor of 4. Combining these results we have increased the energy in each pulse by a factor of ≈300 via the optimisation of both the anode-cathode position and coil#2 B-field.

This increase is due primarily to the optimisation of the relativistic electron beam in both current and position, as clearly demonstrated by the witness plate experiments, photograph(5.1). This shows a very great increase in the current with subsequent addition of both field coils, resulting in a well collimated beam at the centre of the cavity as measured by the amount and position of the plate damage. Witness plate A shows no damage at all. In this case there are no guiding magnetic field lines present and subesquently no observable high energy electrons reach the plate. The beam discharge, for both high and low voltage, will take the shortest route to ground by travelling straight across the gap.

Slightly more damage is evident on witness plate B, in this case only the Marx voltage and cavity B-field is present. Here there is general darkening of the plate and at one point there is clear high energy electron beam melting of the surface. Although

high energy electrons are getting to the witness plate there are two reasons why in this case the high current R.E.B. has not been formed.

1) The magnetic field at the cathode tip is too weak. From the measured cavity B-field profile, chapter 4, at an intracavity magnetic field of 3.63T, the cathode magnetic field will be .12T. In this case the B-field is not strong enough to deflect the electrons away from the anode, magnetically insulating the diode, and thereby forcing the electrons to follow the field lines through the cavity.

2) The compression ratio (defined as the ratio of the cavity magnetic field to the cathode magnetic field), is extremely large (>30). This will cause many of the electrons which have been trapped by the magnetic field lines to mirror as they approach stronger regions of field, thus severely limiting the R.E.B. current.

It is evident that both of these restrictions must be overcome to increase the efficiency of production of the electron beam. This has been achieved with the addition of the second field coil placed around the cathode. Witness plate C shows clear damage from the electron beam. The maser has been fired under exactly the same conditions as plate B with the inclusion of the second field coil. This has greatly increased the R.E.B. current by overcoming the two problems mentioned above:

1) The addition of the second field coil has increased the magnitude of the magnetic field at the cathode tip from .12T to .41T under the following conditions, $B_{Coil\#1}$=0.12T (at the cathode tip) and $B_{Coil\#2}$=.29T. Thus increasing the magnetic insulation of the diode, trapping more electrons onto the field lines.

2) Reducing the compression ratio from >30 to ≈9, under the same conditions. This will reduce the number of electrons mirroring

as they enter regions of higher field, again increasing the beam current.

Having overcome these two basic restrictions on beam formation, a third physical mechanism affecting optimum R.E.B. production becomes evident, that of beam focusing and positioning. If only the first two factors mentioned above governed the formation of the electron beam then, as coil#2's B-field was increased to some arbitrarily high value, the efficiency of the maser would go up with enhanced R.E.B. formation. This is evidently not the case. As coil#2's B-field is increased above .54T the output of the maser drops dramatically as explained in detail above, (see fig.(5.3)). This is due to;

1) the beam focusing/defocusing effect of coil#2, which will have some critical value for the formation of the optimum beam, in both current and position, in the cavity. When this criterion is not met, whether the field is too large or small, the efficiency of the E.C.M. mechanism is reduced.

2) As coil#2's B-field is increased, there may be a corresponding decrease to the electrons' $v_{\perp}$. As described in chapter 1 and 2, only the perpendicular component of the electrons' energy is available to the E.C.M. interaction. Hence a reduction in $v_{\perp}$ will result in a reduction in the overall efficiency of the system.

There is the possibility that the damage to witness plate 3 has been caused by a low voltage arc discharge between the cavity walls and the copper plate. This is unlikely for two reasons; firstly it is improbable that such a discharge would have enough energy to cause such severe damage, and secondly, the only difference between plate C and plate B is the weakening of the magnetic field at the cathode, this is unlikely to affect any low voltage discharge at the plate and thus plate two would have received the same damage.

From the witness plate experiments it is evident that not only is there a well-formed beam at the entrance to the cavity but also

that this beam remains well collimated throughout. This is demonstrated by the almost constant beam diameter (≃3mm) at two positions 9cm apart, as shown in photograph(5.2).

From all of the considerations above, the efficiency and maximum output power of the maser have been greatly increased and enhanced, primarily by optimising the anode-cathode gap, though more importantly by adding and optimising the second B-field coil. Both of these optimisations have resulted in a greatly enhanced relativistic electron beam which has a direct bearing on the overall efficiency of the electron cyclotron maser instability.

# CHAPTER -6-

# W-BAND FREQUENCY MEASUREMENTS.

## 6.1 Introduction.

This chapter will deal with the results and analysis of the W-band frequency measurements from the electron cyclotron maser.

The direct power output as a function of the varying cavity magnetic field will be presented, corresponding to an electron cyclotron frequency range of 75-110GHz. Five spectrometer scans have been produced, corresponding to cyclotron frequencies of 89.2GHz, 83.4GHz, 79.1GHz, 74.9GHZ and 73.4GHz. This set of results demonstrates the step tunability of the electron cyclotron maser. At a cyclotron frequency of 89.2GHz a very strong cavity resonance was present, suggesting the excitation of either the $TE_{03}$ or the $TE_{23}$ mode. From the radiation scan showing the power intensity across the output window, it will be demonstrated that the $TE_{03}$ mode is being excited. The output power of the maser was measured using a calibrated power meter. This showed that an average output power of 48kW, with a peak power of 100kW, was being developed in the $TE_{03}$ mode.

All of these reults will be shown to be entirely self consistent with the theory described in earlier chapters.

## 6.2 Direct Power Measurement with Varying B-Field.

The direct power out from the maser was measured as the coil#1 magnetic field was varied from 2.6-4T corresponding to a cyclotron frequency of approximately 75-110GHz, fig.(6.1). The Marx voltage was held constant at 72kV and coil#2 at .29T. The output seems to vary continuously across the band with peaks corresponding to cavity resonances. However this graph yields no spectroscopic information other than the fact that the maser will oscillate slightly above ($\lesssim$10%) the cyclotron frequency. This will be clearly demonstrated by the spectrometer frequency analysis of the maser output. For the same reason no mode identification is possible.

Although these results were obtained using an uncalibrated detection system, they do provide excellent preliminary information on the W-band oscillation of the maser. It would be extremely

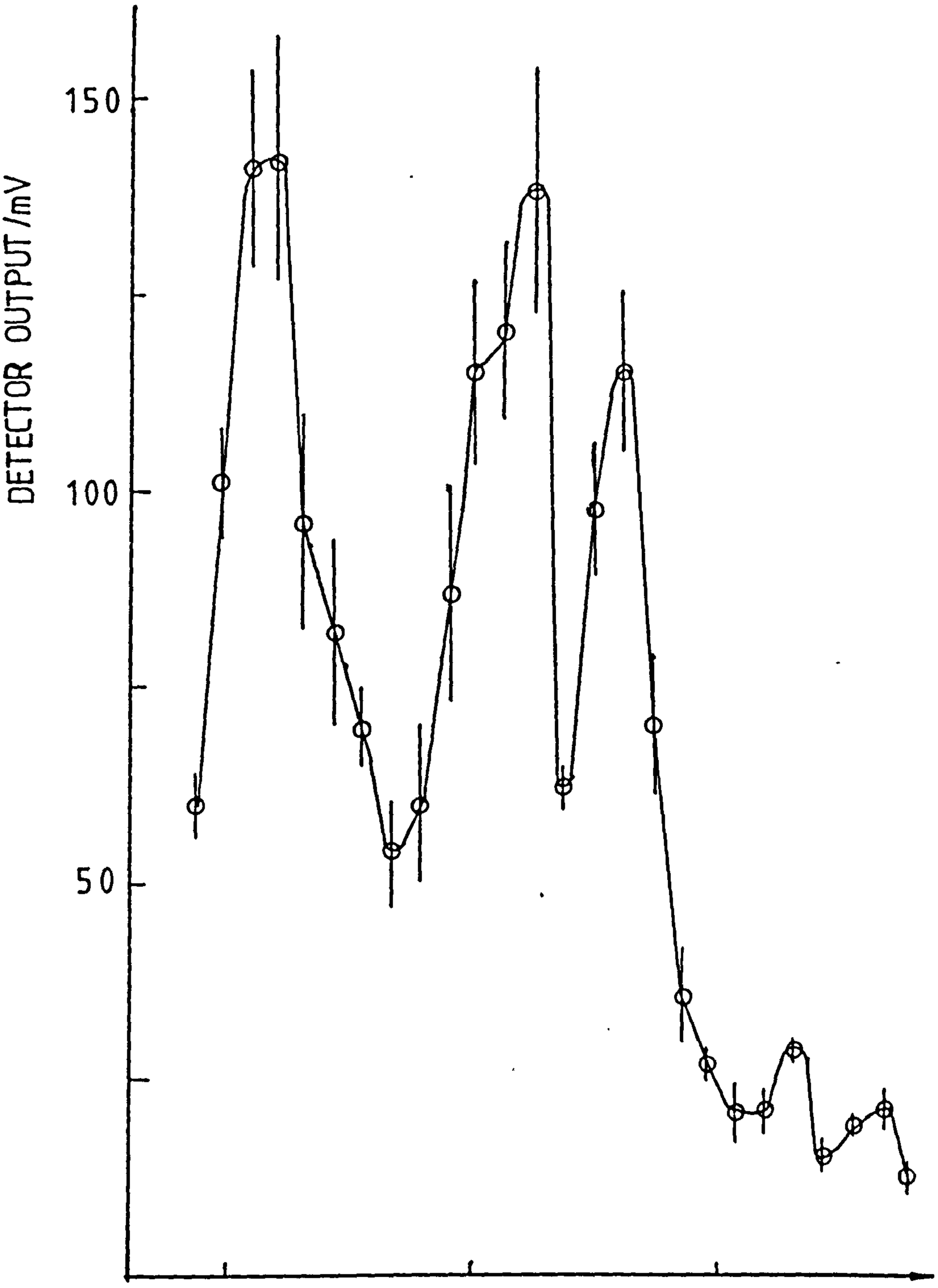


Fig.(6.1). Direct maser output as a function of coil#1 magnetic field.

difficult to calibrate this system against power and sensitivity versus frequency for two physical reasons:

1) The mode dependent coupling from the maser output into the detection system would be difficult to measure.
2) As the maser oscillating frequency is unknown, it would be very difficult to match the detector frequency response to the oscillating frequency of the maser output.

This graph does however demonstrate that mm-wave radiation is produced at all values of the cavity magnetic field. A full interpretation of the maser characteristics will only be possible with subsequent frequency analysis from a calibrated spectrometer, and the power output, for any given B-field, measured by a calibrated power meter. (See sections 6.3-6.5).

## 6.3 Spectroscopic Analysis of the Maser Output.

The frequency spectrum of the maser was investigated for five different values of coil#1's magnetic field. These results were taken keeping, at all times, the Marx bank voltage and the coil#2 B-field constant at 72kV and .29T respectively. The five values of magnetic field chosen were 3.63T, 3.40T, 3.22T, 3.05T and 2.99T corresponding to a cyclotron frequency of 89.2GHz, 83.4GHz, 79.1GHz, 74.9GHz and 73.4GHz.

The results of each of these spectrometer scans are shown in figs.(6.2)-(6.6) along with the cavity cut-off frequencies of the relevant modes. Fig.(6.2) corresponds to a spectrometer scan with equivalent cyclotron frequency of 89.2GHz. No oscillation is observed below this frequency. Above this frequency a peak is present, centralised at 95.2GHz, corresponding in frequency to the excitation of either the $TE_{03}$ or the $TE_{23}$ mode. This resonance has a F.W.H.M. of 5.5GHz. At higher frequency there seems to be another mode present, possibly the $TE_{52}$ or the $TE_{19}$.

Fig.(6.3) has an equivalent cyclotron frequency of 83.4GHz and fig.(6.4), 79.1GHz. Both of these graphs show similar characteristics to that of fig.(6.2). Although in both cases the

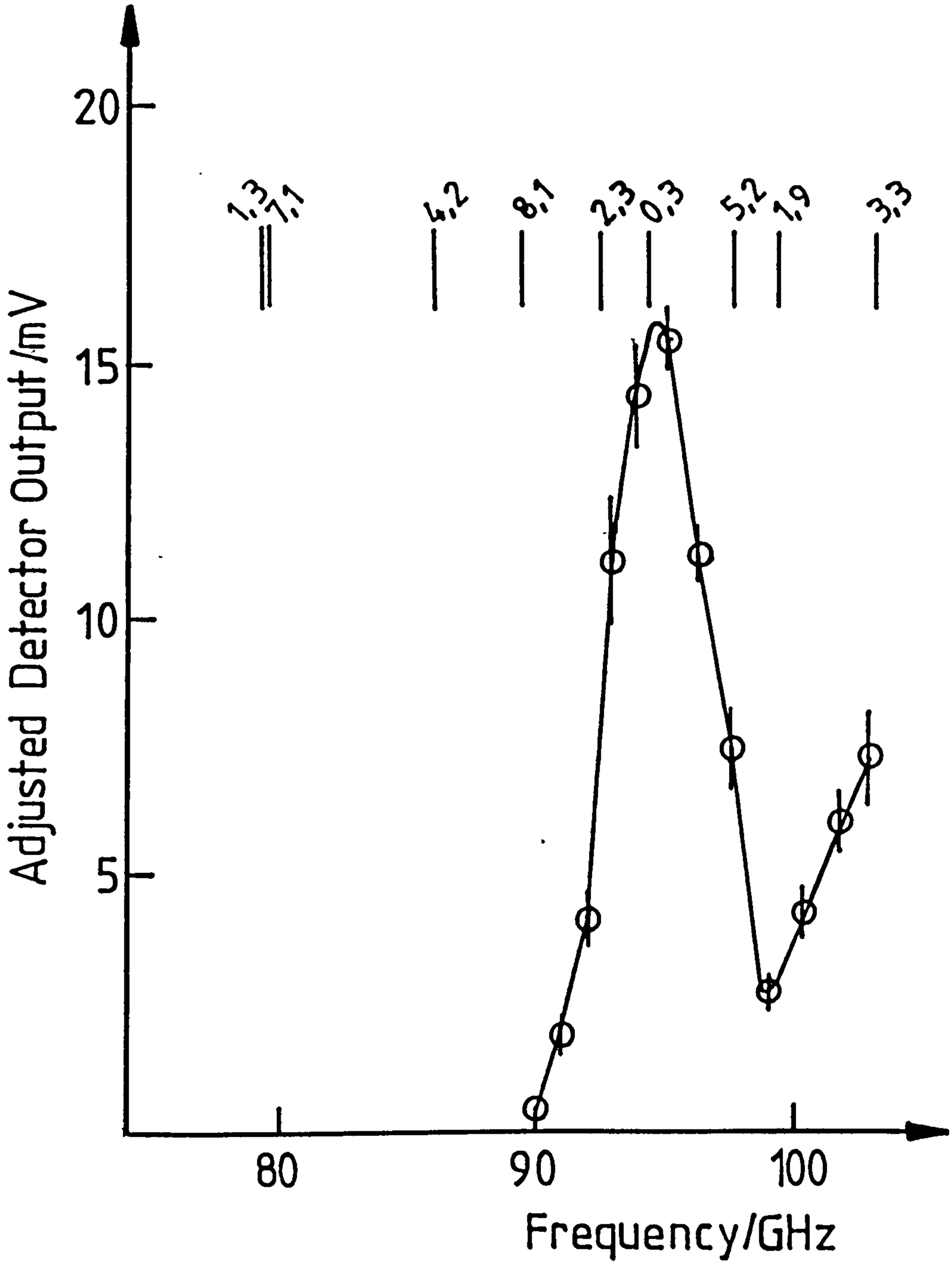


Fig.(6.2). Frequency scan, cavity B-field=3.63T, $f_{ce}$=89.2GHz.

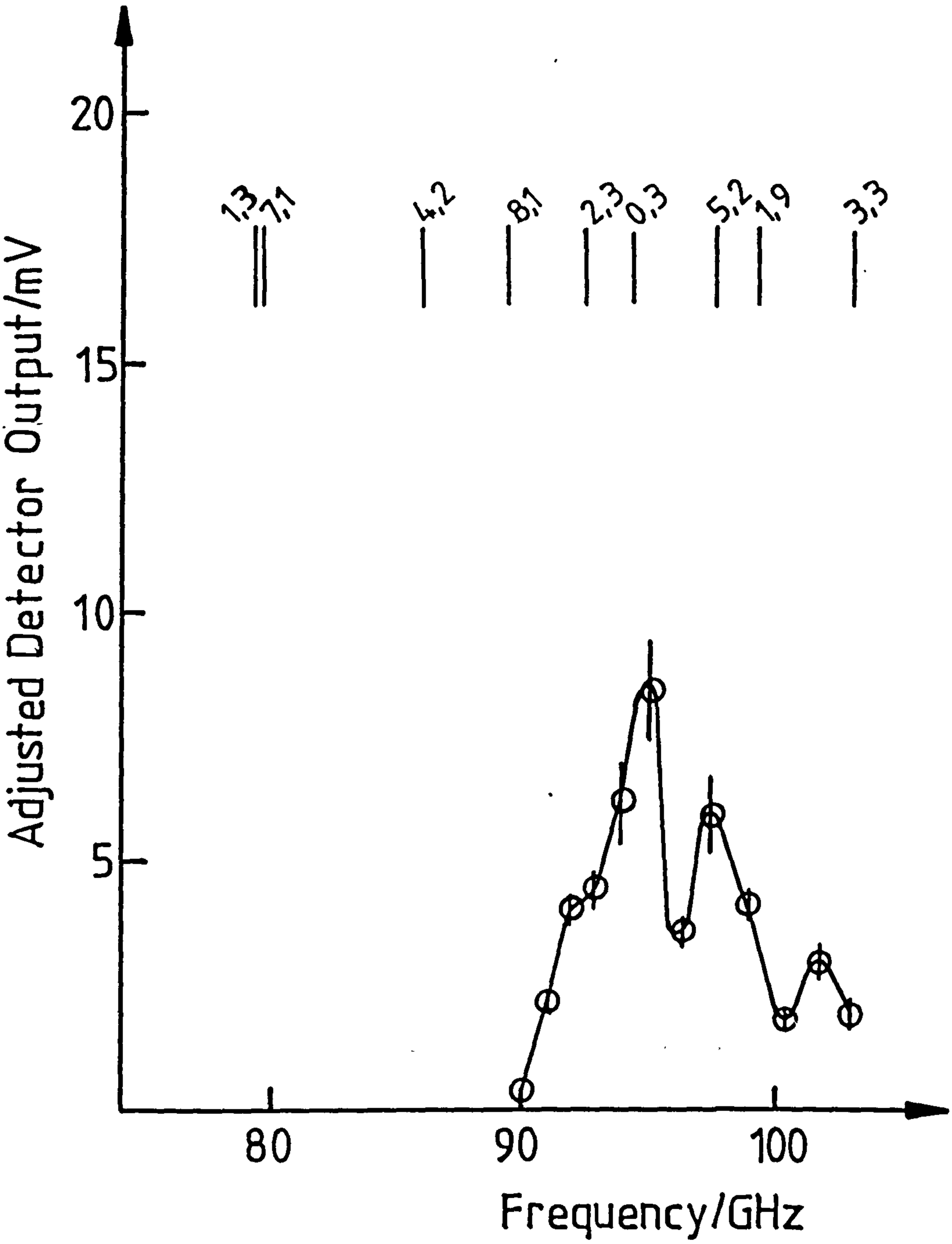


Fig.(6.3). Frequency scan, cavity B-field=3.40T, $f_{ce}$=83.4GHz.

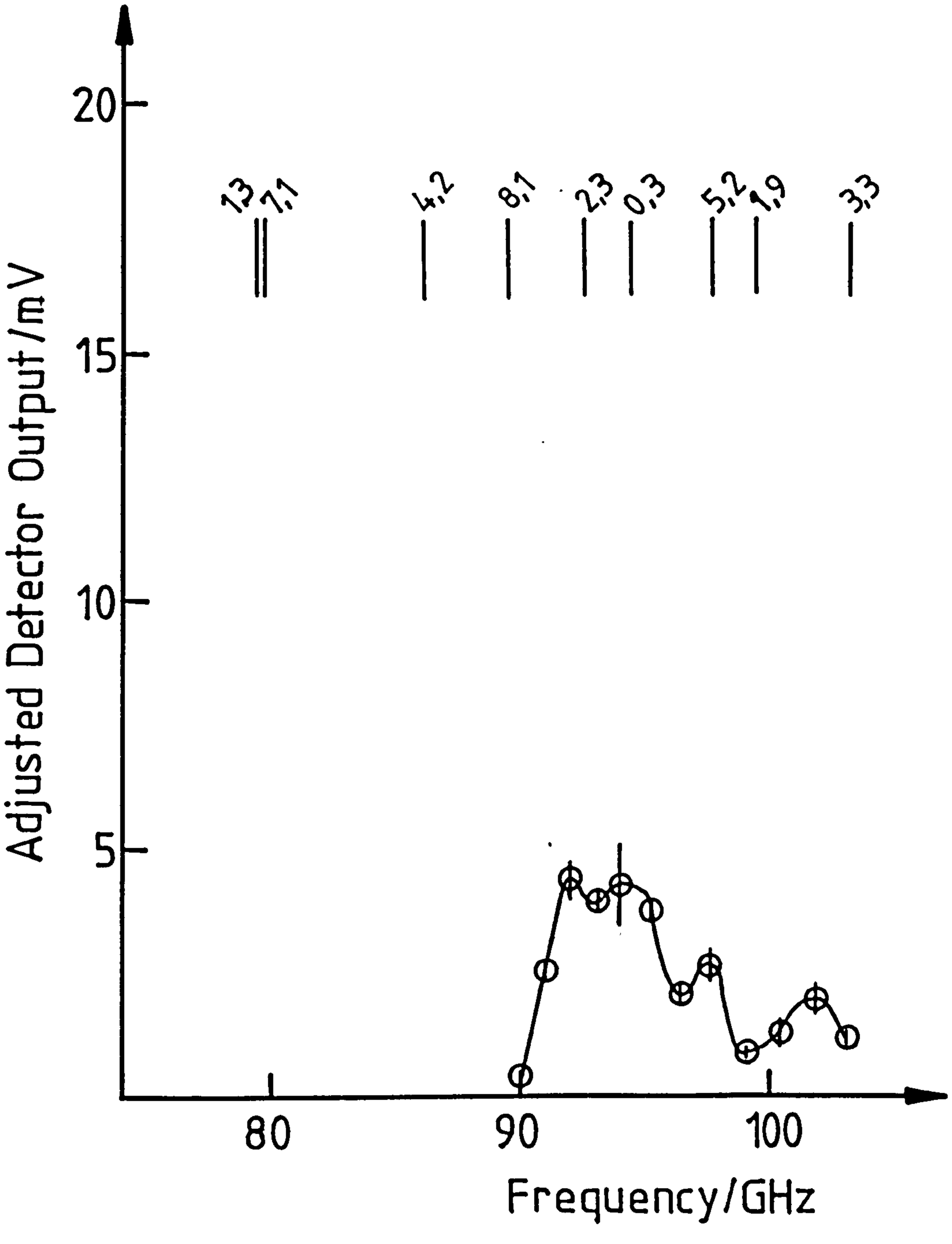


Fig.(6.4). Frequency scan, cavity B-field=3.22T, $f_{ce}$=79.1GHz.

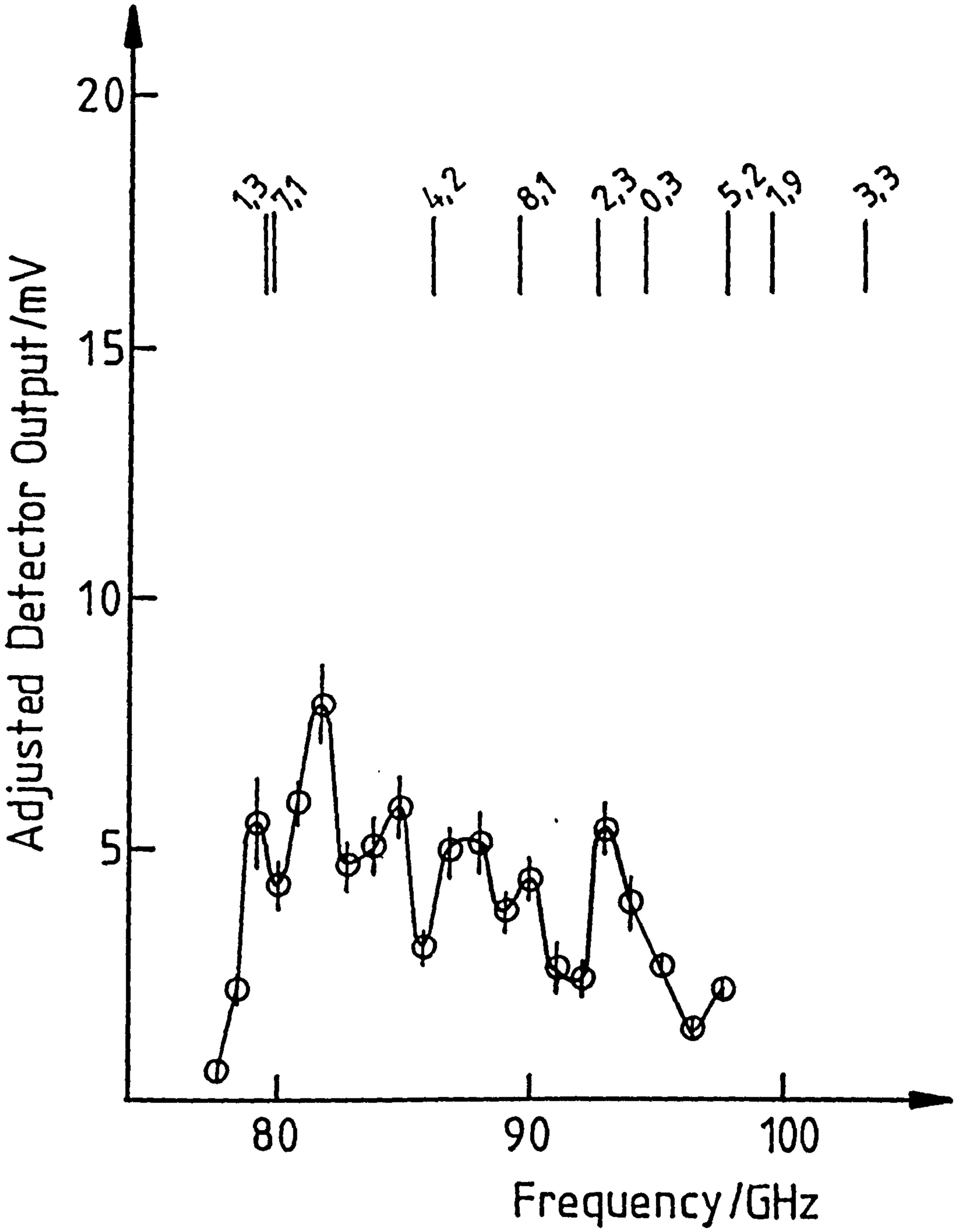


Fig.(6.5). Frequency scan, cavity B-field=3.05T, $f_{ce}$=74.9GHz.

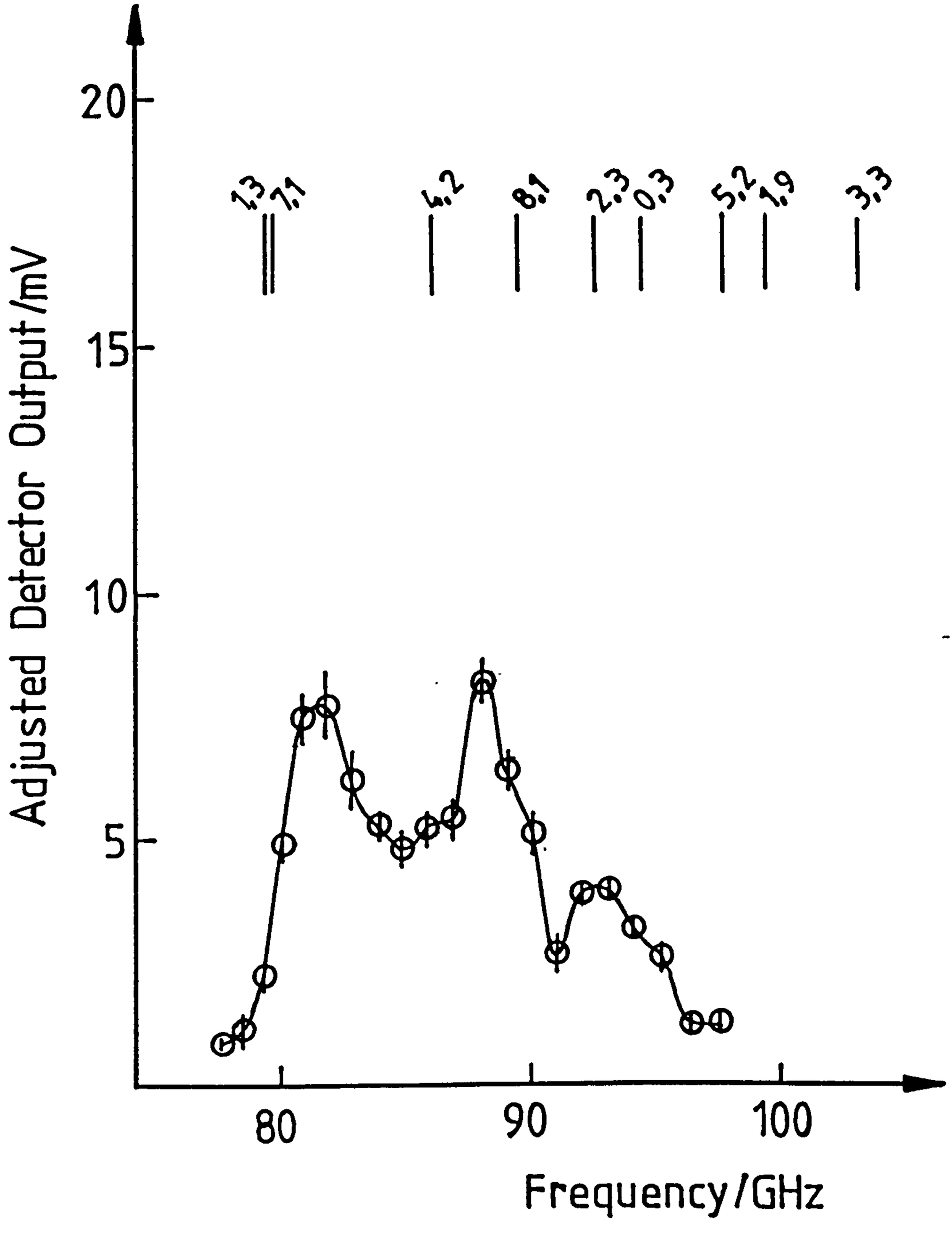


Fig.(6.6). Frequency scan, cavity B-field=2.99T, $f_{ce}$=73.4GHz.

cyclotron frequency of the R.E.B. has been reduced, no oscillation is observed below 90GHz. Above 90GHz, in all three graphs, a resonance exists which seems to suggest that either the $TE_{03}$ or the $TE_{23}$ mode is being excited. However in fig.(6.3) and fig.(6.4) the relative maximum output power is reduced as the cyclotron frequency moves further away from the resonant frequency of the excited mode.

Moving to a frequency of 74.9GHz, fig.(6.5), a new set of frequencies has started to oscillate. The $TE_{03}/TE_{23}$ mode is still clearly evident at 93.0GHz, however all the modes between 77 and 90GHz are also oscillating in a broad band fashion. There seem to be approximately similar amounts of energy being fed into each mode. In an attempt to reduce the number of modes oscillating, the cyclotron frequency was further lowered to 73.4GHz, fig.(6.6). This resulted in three peaks becoming evident, corresponding to 81.4GHz, either the $TE_{13}$ or the $TE_{71}$ mode, 88GHz, the $TE_{42}$ mode, and 93GHz, either the $TE_{23}$ or the $TE_{03}$ mode. Upon reducing the cyclotron frequency from 74.9GHz to 73.4GHz the power in the $TE_{42}$ mode has increased while in the $TE_{23}/TE_{03}$ mode it has decreased.

## 6.4 Power Intensity Distribution Across the Output Window.

From the spectrometer scans a strongly resonant mode has been identified at a frequency of 95.2GHz. In an attempt to identify this mode the maser was operated under the following conditions; $V_{marx}$=72kV, B-field coil#1=3.63T and B-field coil#2=.29T. This set of conditions is identical to those used in obtaining the results shown in fig.(6.2).

The results of scanning across the output window are shown in fig.(6.7) and (6.8). The only difference in both cases is the change in detector polarisation, shown on each graph. In fig.(6.7) six peaks were clearly detected across the window, with a clear minimum evident at the centre. Upon rotating the detector polarisation by 90°, fig.(6.8), all structure previously noted is lost. As will be shown, this information is consistent with only the $TE_{03}$ mode.

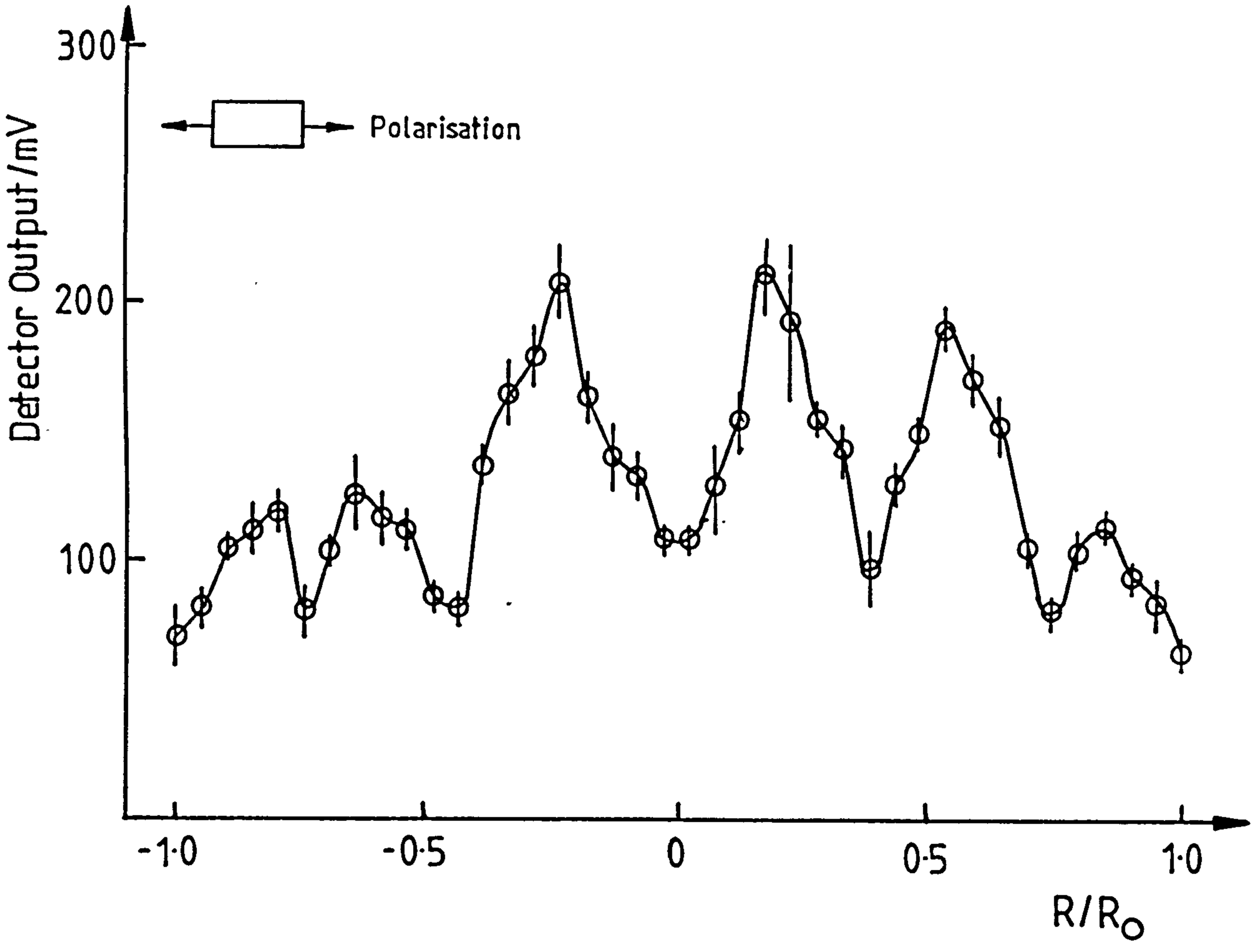


Fig.(6.7). Intensity distrobution across the output window, cavity B-field=3.63T. Polarisation as shown.

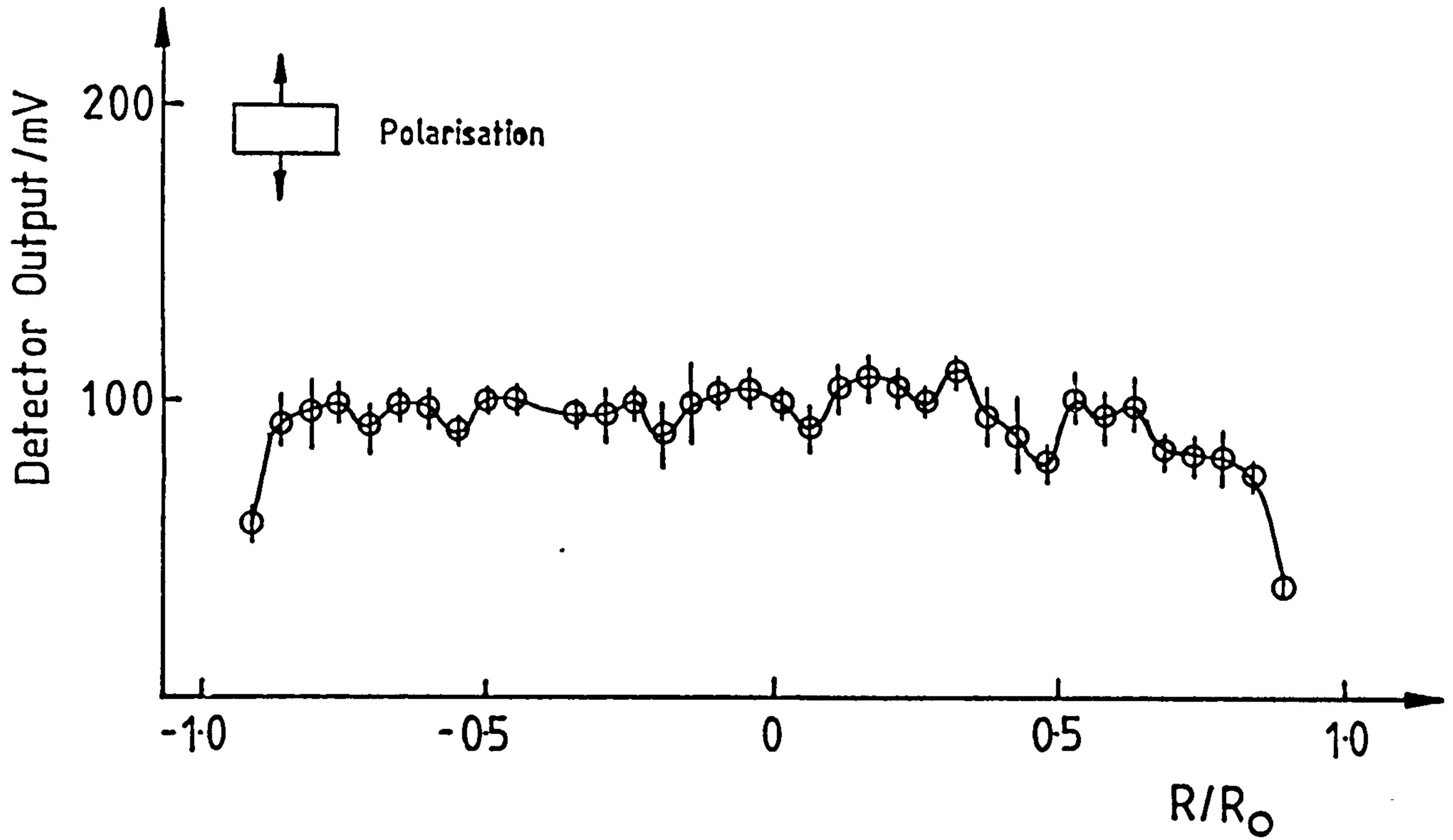


Fig.(6.8). Intensity distrobution across the output window, cavity B-field=3.63T. Polarisation as shown.

## 6.5 Maser Output Power.

All the measurements up to this point have dealt in terms of relative powers as measured by the Flann 135 crystal detector, $V_{out} \propto P_{in}$. It would in principle be possible to determine the total output power of the maser for any given cavity B-field by integrating under the spectrometer scans. This may be achieved knowing the insertion losses of the spectrometer and the sensitivity of the detector with respect to incident power. A similar calculation may also be done on the radiation pattern across the output horn, calibrating for the losses through the sampling system and knowing the power response of the detector. Both of these calculations are very difficult in practice due to the unknown mode dependent coupling from the maser output into each respective sampling waveguide.

For this reason it was decided not to use any of these methods to estimate the power output and instead measure this directly using a calibrated power meter. This was used to measure the power output at each of the cavity B-field values from which the spectrometer scans were obtained. The results are shown in table(6.1).

| Cyclotron Frequency / GHz | Power Out / kW |
|---|---|
| 89.2 | 48.3 ± 5.4 |
| 84.3 | 29.5 ± 2.5 |
| 79.1 | 24.6 ± 2.5 |
| 74.9 | 26.8 ± 2.3 |
| 73.4 | 28.3 ± 3.8 |

Table(6.1). Output power at different cyclotron frequencies

The greatest power out was measured at a cyclotron frequency of 89.2GHz corresponding to 48.3kW in the $TE_{03}$ mode. As explained in chapter 4, due to the shape of the mm-wave pulse assumed, the ouput power of the maser may be a factor of between 1 and 2 higher than those stated above.

## 6.6 Analysis and Discussion.

With the power fully optimised with respect to the anode-cathode position and coil#2 magnetic field, as described in chapter 5, it is now possible to look at the direct power out of the maser as the cavity B-field is varied using the Flann crystal detector system described in chapter 4, fig.(6.1). In previous W-band experiments conducted at Strathclyde University (Mk-5 maser), the direct output power varied over several orders of magnitude as the magnetic field was swept through the W-band frequency range. These very large changes in the mm-wave output power were almost certainly caused by the changing coupling of the electron beam into the maser cavity as the main magnetic field and thus the cathode magnetic field were altered. In the present Mk-6 case this problem has been overcome with the addition of the cathode magnetic field coil.

Fig.(6.1) shows the direct uncalibrated W-band output power of the maser. This provides excellent preliminary information on the maser oscillation. (i.e. radiation is given out uniformly, within a factor of three, between a magnetic field value of 2.95T and 3.90T. Above 3.90T the average output dropped by a factor of three, almost certainly due to detector sensitivity at these frequencies and not reducing maser output). Due to the uncalibrated nature of these results, no precise information on the relative height of peaks, frequency and mode of operation may be obtained.

Hence to gain more definite information on the resonant frequencies of the maser and its mode of oscillation more powerful diagnostics must be used, such as the calibrated spectrometer, and the radiation intensity scans across the output window.

Spectroscopic Analysis.

A spectroscopic analysis of the maser was carried out at five different values of magnetic field, 3.63T, 3.40T, 3.22T, 3.05T and 2.99T with corresponding cyclotron frequencies of 89.2GHz, 83.4GHz, 79.1GHz, 74.9GHz and 73.4GHz respectively. Considering the graphs corresponding to cyclotron frequencies of 89.2GHz, 83.4GHz and 79.1GHz, which have been plotted on the same axis in fig.(6.9), there are several different points which may be noted and explained by the theory given in earlier chapters.

1) The maser does not oscillate at or below the cyclotron frequency. This fact is predicted by all theoretical models and is a fundamental characteristic of the operation of an electron cyclotron maser. This is clearly borne out by all experimental frequency scans.

2) It is evident we are exciting either the $TE_{23}$ or the $TE_{03}$ mode in each case. As frequency is reduced neither the $TE_{81}$ or the $TE_{42}$ modes are being excited. This phenomenon is a combination of two effects. Firstly the ohmic Q, as defined in eqn.(2.19), is larger for the $TE_{23}$ and the $TE_{03}$ modes (7001 and 7375 respectively) than that of either th $TE_{81}$ or the $TE_{42}$ modes (2209 and 5710), these values combined with each mode's diffraction Q,(27370, 28502, 25631 and 23728), leads to efficiency quotients, as defined in eqns.(2.22) and (2.23) as follows.

$$\eta_Q(TE_{23})= .20,\ \eta_Q(TE_{03})= .21,\ \eta_Q(TE_{81})= .08,\ \eta_Q(TE_{42})= .19$$

Obviously the efficiency of the gain mechanism from purely cavity coupling considerations suggests that the 'non-useful' losses of the $TE_{81}$ mode will be almost three times that of the other competing modes. This mode will thus be harder to excite, requiring a comparatively higher starting current.

It must however be noted that the values of $\eta_Q$ calculated above are idealised, in that they do not take into account the physical considerations described in chapter 2 section 2.3, which would

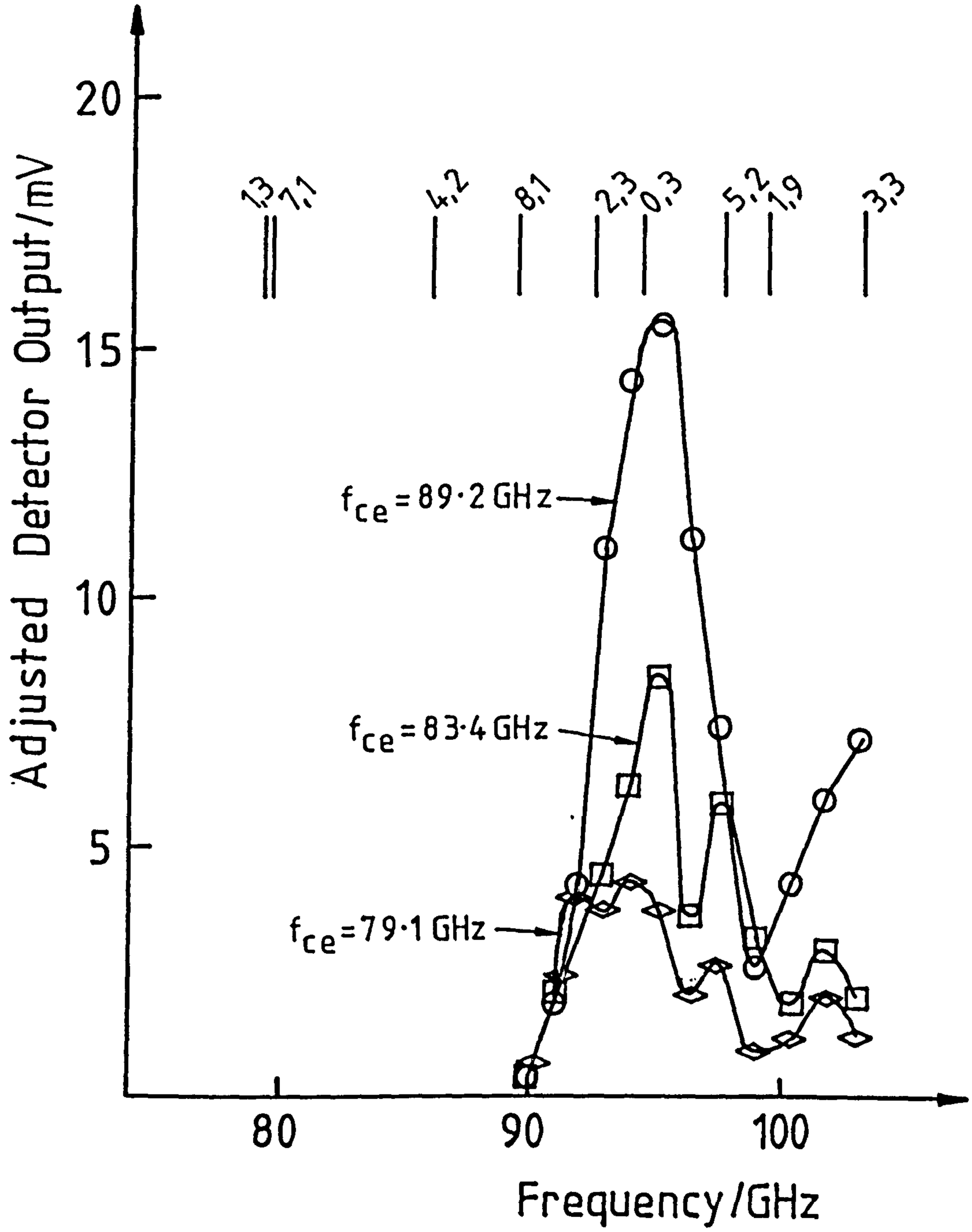


Fig.(6.9). Three spectrometer scans, as stated, plotted on the same axes.

have an influence on the calculated values of $Q_\Omega$. As these physical factors do not influence $Q_D$, the ratio of $Q_\Omega$ to $Q_D$ will also be affected, leading to potential errors in the stated values of $\eta_Q$. These calculated values of $\eta_Q$ are therefore based on an idealised model and must be treated as such. However, they do allow the experimental results to be interpreted both in this case and throughout the other experiments reported in this thesis.

The second effect determining which modes are preferentially excited is that of the spatial coupling of the electric field maxima and the corresponding position of the R.E.B. If these two do not coincide there will be weak coupling between the cavity mode and the electron beam, again resulting in low efficiency, high starting currents and hence non-excitation of the modes.

Figs.(6.10) and (6.11) show the theoretical mode pattern power density across a cavity diameter for all the modes in question. The $TE_{23}$ and the $TE_{42}$ modes have been plotted across two different azimuthal angles $\varphi_a$ to demonstrate the rotational variations of these modes. Superimposed on these plots the position of the R.E.B. has been shown. These show clearly, along with the efficiency considerations, why the $TE_{81}$ and the $TE_{42}$ modes are not being excited. In both cases the electromagnetic field energy is concentrated near the cavity walls, with the electron beam being collimated at the centre. This results in very weak coupling between the R.E.B. and the particular cavity mode.

From these two considerations the $TE_{81}$ mode will be very difficult to excite, considering its very low $\eta_Q$=8% and the complete mismatch between the maxima of the E-field and the position of the electron beam. The $TE_{42}$ mode does not suffer in such a way from cavity efficiency considerations, ($\eta_Q$ similar to that of the $TE_{03}$ and the $TE_{23}$ modes ≈20%) but again there is a high degree of mismatch between the R.E.B. position and the E-field maximum.

The $TE_{23}$ and the $TE_{03}$ modes suffer from neither of these constraints, (though a significant reduction in the non useful losses of these modes may be gained from enhanced values of $\eta_Q$ in future cavity designs), and it is thus totally consistent with the theory that these modes will be excited in preference to either

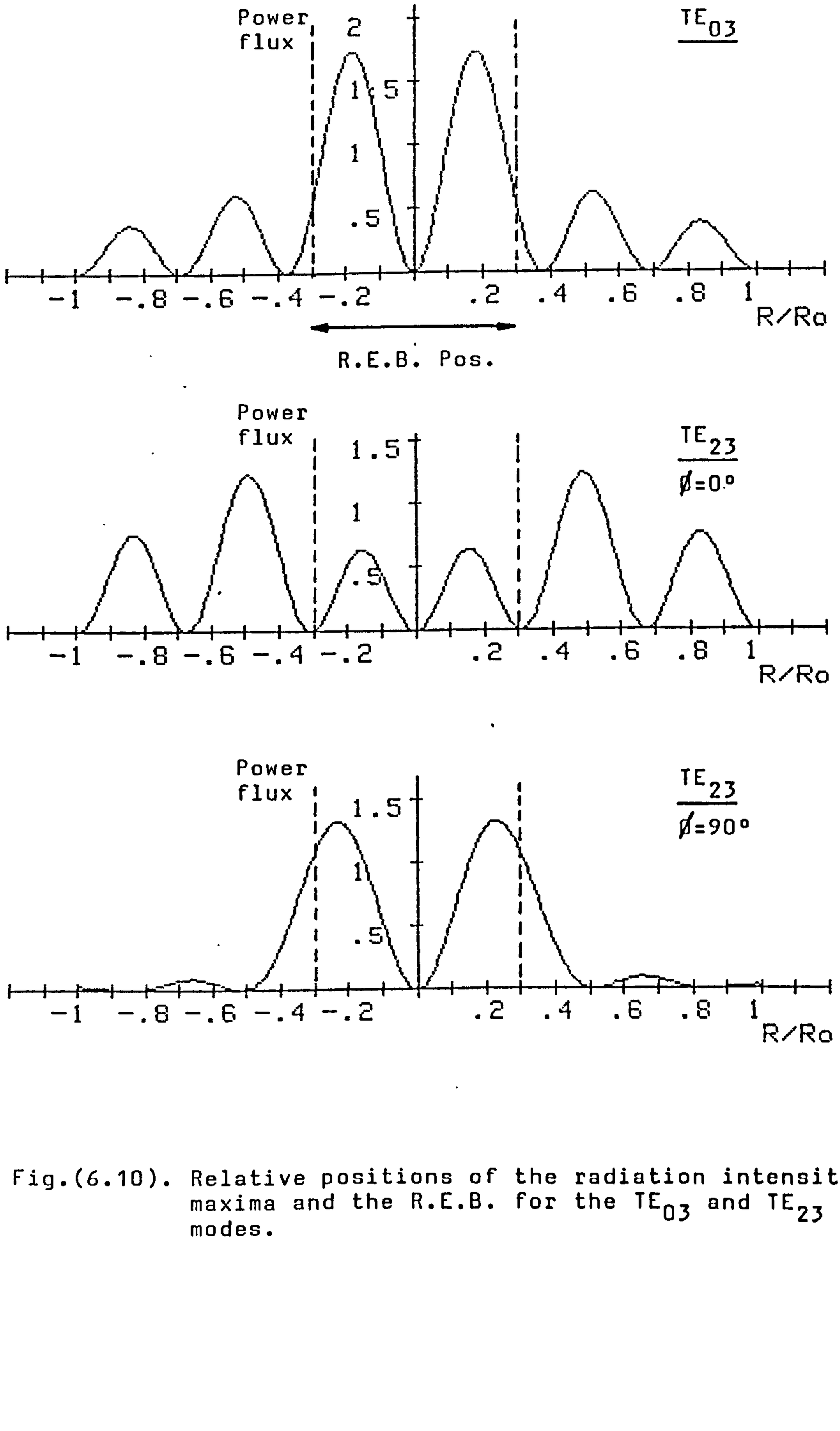


Fig.(6.10). Relative positions of the radiation intensity maxima and the R.E.B. for the $TE_{03}$ and $TE_{23}$ modes.

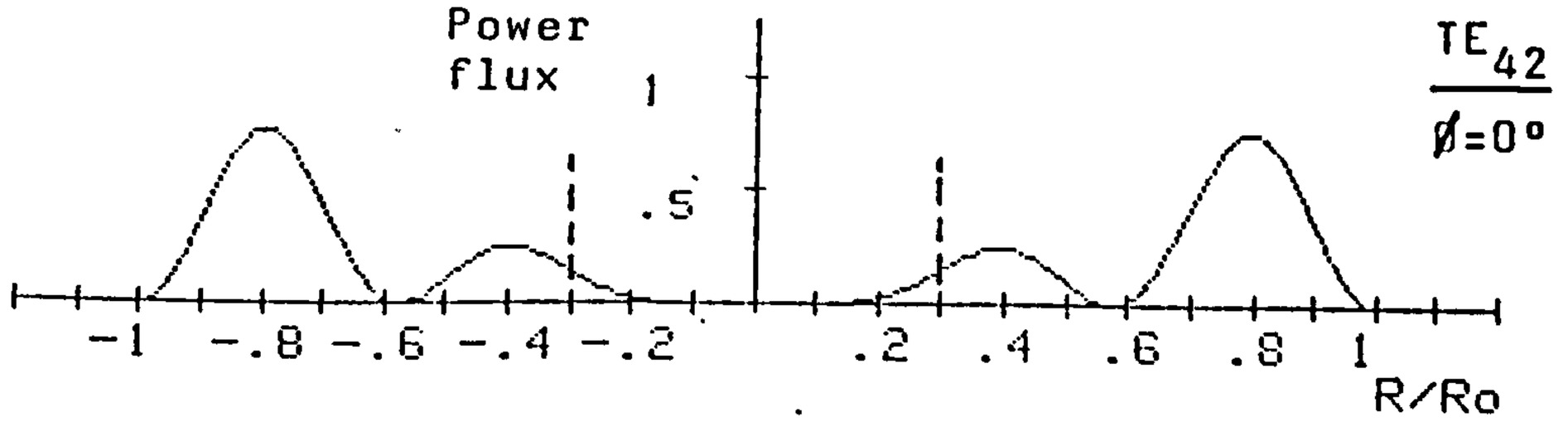


Fig.(6.11). Relative positions of the radiation intensity maxima and the R.E.B. for the $TE_{42}$ and $TE_{81}$ modes.

the $TE_{81}$ or the $TE_{42}$ modes. Both the $TE_{23}$ and the $TE_{03}$ modes have very similar $\eta_Q$'s, however it may be noted that the central maxima of the circularly symmetric $TE_{03}$ mode lies within the confines of the R.E.B. whereas the spatial coupling with the $TE_{23}$ will not be as strong. This suggests that, of the two, one would expect the $TE_{03}$ mode to be excited.

3) It is evident that as $\delta\omega=\omega-\omega_{ce}$ increases, the saturation power levels of the excited modes are reduced. This is again consistent with the theory. From chapter 1 it was stated that there were two possible saturation mechanisms. From the above information it is impossible to distinguish which is determining the final output power in each mode. However from non-linear theory it is clear that as $\omega_{ce}$ moves away from $\omega$ the saturated maximum power of any mode with resonant frequency $\omega$ will rise very quickly to some maximum ($\delta\omega\lesssim$ few percent of $\omega$). Then, via a series of complicated processes involving the efficiency of conversion of the beam energy into electromagnetic radiation, and the limitation of the growth rate as $\delta\omega$ moves past its optimum value, the peak saturation power will systematically reduce with further increase of $\delta\omega$. To calculate the saturation power would involve the numerical solution of the extremely complex non-linear equations governing the E.C.M. interaction, which is beyond the scope of this thesis. The maser does however behave qualitatively exactly as one would expect, with the saturation power level starting off at some maximum, corresponding to a $\delta\omega/\omega$ of $\simeq$5%, and subsequently reducing with increasing $\delta\omega$.

4) The modes in question are oscillating with a $\Delta\omega$, F.W.H.M. $\simeq$5GHz, corresponding to $\Delta\omega/\omega\simeq$6%. This broad bandwidth oscillation is due to the ends of the cavity, comprising low reflection output couplers (chapter 2), not being well defined. As the resonant frequency of a mode is a function of the cavity length, the excited cavity modes in the Mk-6 maser will run broad-band.

Having studied the three graphs corresponding to cyclotron frequencies of 89.2GHz, 83.4GHz and 79.1GHz the B-field was

further reduced, resulting in the graphs produced from corresponding cyclotron frequencies of 74.9GHz and 73.4GHz. These have been replotted on the same axis in fig.(6.12).

Under these conditions three modes of oscillation were observed simultaneously, one at 81.4GHz, either the $TE_{13}$ or the $TE_{71}$ mode, one at 88.0GHz, the $TE_{42}$ mode, and one at 93GHz, either the $TE_{03}$ or the $TE_{23}$ mode. In the 74.9GHz case the $TE_{81}$ mode with a resonant frequency of 89.4GHz may also be present. (Although it has been demonstrated above that the $TE_{42}$ and the $TE_{81}$ modes will have high ohmic losses and poor coupling with the electron beam, under certain conditions and via mode conversion these modes may still oscillate). These two graphs (fig.(6.12)), are very similar with an almost identical frequency bandwidth of 77GHz to 96GHz. However in the graph corresponding to a cyclotron frequency of 73.4GHz the individual mode excitation seems to be more pronounced, due to the slightly enhanced coupling of the beam energy into each respective mode, and the suppression of the resonance occuring at 89.4GHz.

Studying the relative field intensity distribution of the $TE_{13}$, $TE_{71}$ and the $TE_{42}$ modes with respect to the R.E.B. position, fig.(6.13), along with their relative $\eta_Q$'s (viz: $\eta_Q(TE_{13})=.25$, $\eta_Q(TE_{71})=.09$ and $\eta_Q(TE_{42})=.19$), it is possible to understand the maser output at a cyclotron frequency of 73.4GHz in terms of its behaviour at higher frequencies. The $TE_{13}$ mode is being initially excited in preference to either the $TE_{71}$ (exceptionally low $\eta_Q$ and poor coupling between E-field maxima and R.E.B.) and the $TE_{42}$ (poor coupling between the cavity mode and R.E.B.). The $TE_{42}$ mode is then oscillating parasitically with mode conversion between the $TE_{13}$ and the $TE_{42}$ modes, resulting in energy being fed from the first to the second. The existence of a peak at a frequency of 93GHz shows power is still being fed into the $TE_{03}$ or the $TE_{23}$ modes.

It would be extremely difficult to identify any of these modes via their radiation intensity pattern across the output window. Any attempt to measure the radiation pattern would result in a distribution made up of a superposition of the three modes.

This spectroscopic analysis also demonstrates the crude

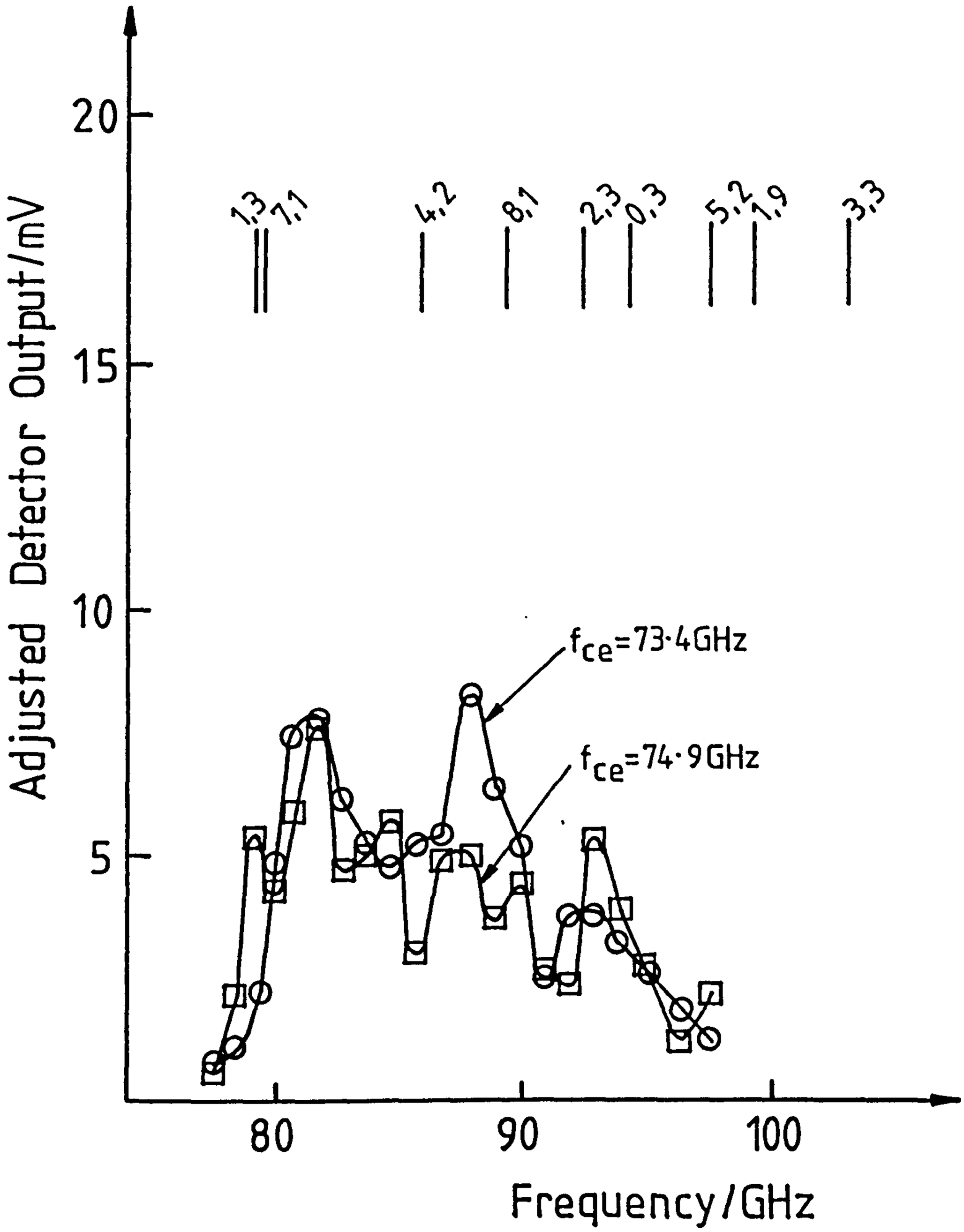


Fig.(6.12). Two spectrometer scans, as stated, plotted on the same axes

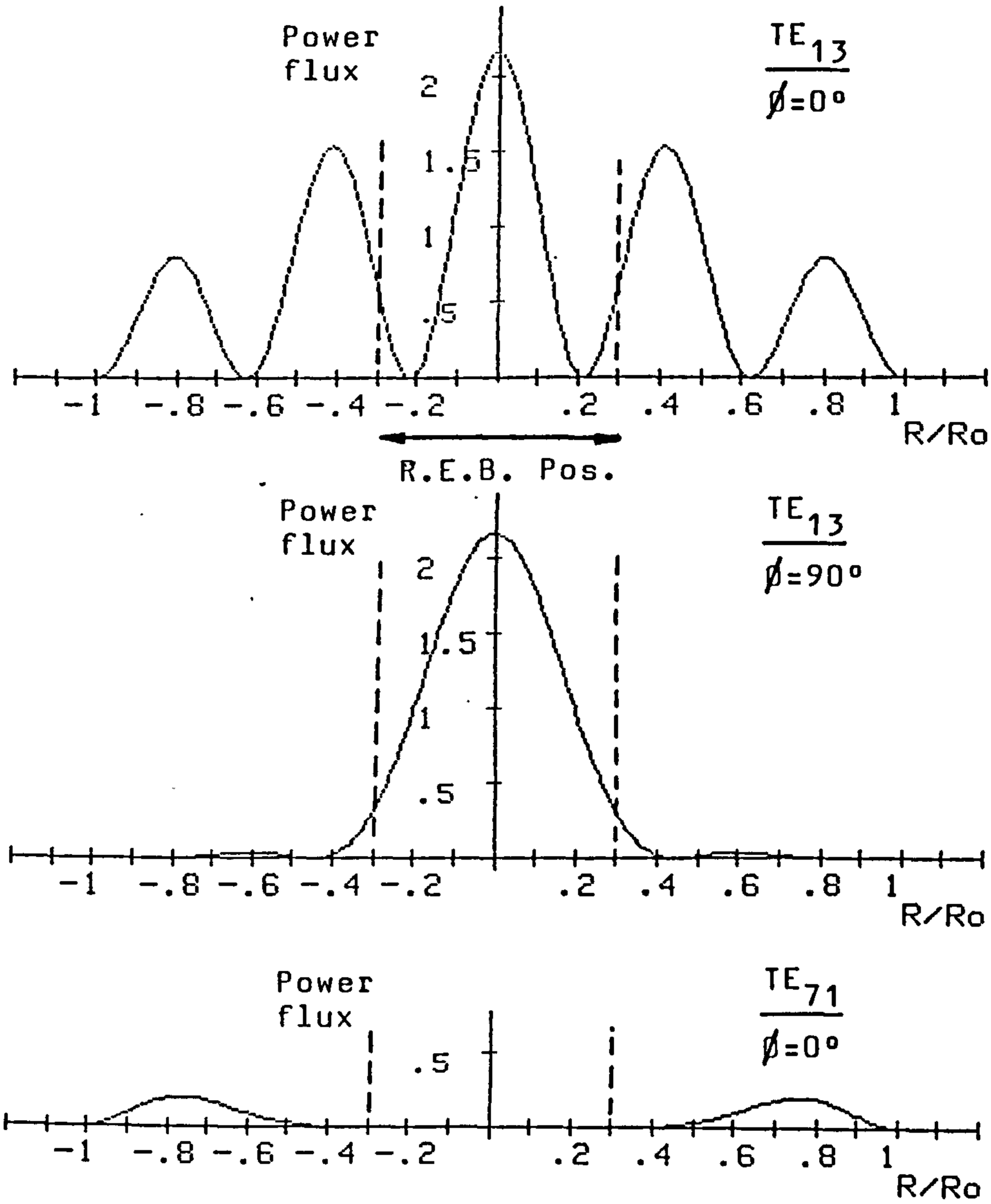


Fig.(6.13). Relative positions of the radiation intensity maxima and the R.E.B. for the $TE_{13}$ and $TE_{71}$ modes.

step-tunability of the maser in the W-band. At a cyclotron frequency of 89.2GHz a resonance was excited at a frequency centered on 95.2GHz. With a subsequent tuning of the magnetic field to a cyclotron frequency of 73.4GHz, although a component of the resulting radiation is still at ≈95GHz, two new frequencies , 81.4GHz and 88.0GHz, are now present. Hence as predicted the maser is step-tunable via differential mode excitation.

Mode Identification From Radiation Intensity Distribution.

It has been shown from spectroscopic analysis that either the $TE_{23}$ or the $TE_{03}$ modes are being excited with theoretical considerations favouring the $TE_{03}$. From fig.(6.7) and (6.8) and comparing these with theoretical mode plots shown in fig.(6.10), all of which have been replotted in fig.(6.14) and (6.15), there is conclusive evidence that the $TE_{03}$ mode is the one which is oscillating. These results were obtained under the same operating conditions as the spectroscopic scan corresponding to a cyclotron frequency of 89.2GHz, i.e. $V_{Marx}$=72kV, $B_{coil\#1}$=3.63T and $B_{coil\#2}$=.29T. Studying fig.(6.14a) it is seen that the three intensity peaks on the left hand side are in almost exactly the same relation, in both position and magnitude, as those on the theoretical plot, fig.(6.14b). The central two peaks are very strong with a well-defined hollow centre. The middle peak on the right hand side of the measured intensity distribution is larger than expected, this may be due to slight mode conversion in the output taper, (mode conversion has been minimised but will still occur). However overall the measured pattern almost exactly mirrors the theoretical intensity distribution.

Upon rotating the polarisation, fig.(6.15a) all the intensity variations have been lost leaving a flat intensity distribution. Again this is exactly mirrored by theory which predicts the $TE_{03}$ mode should have no radial component of electric field, fig.(6.15b), hence no mm-wave radiation should be detected. As the detectors are not 100% polarised and there will exist low intensity, high order modes in the output taper, a background mm-wave signal has been detected. This background signal is higher

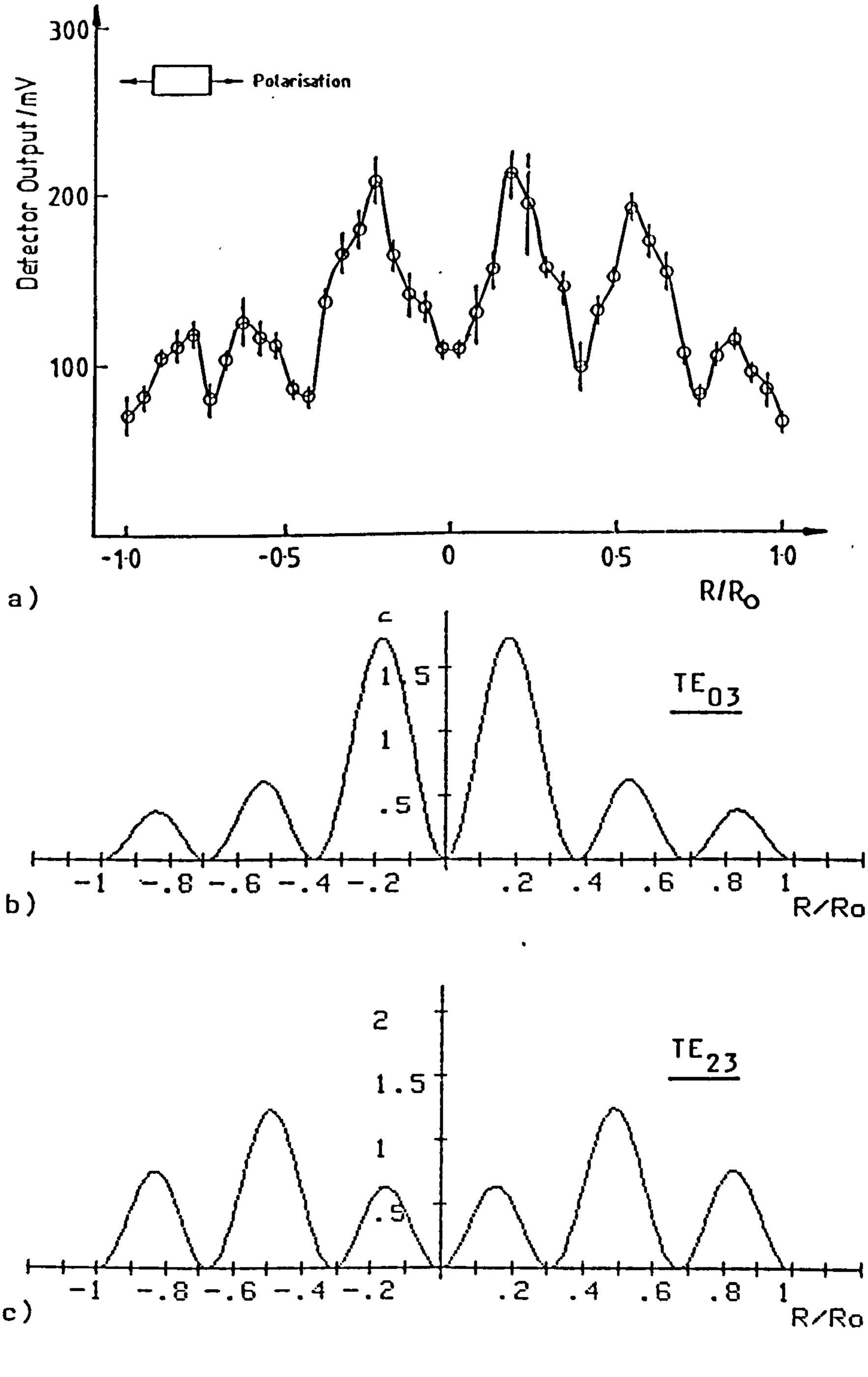


Fig.(6.14). Comparison of measured intensity distribution against intra-cavity mode pattern plots. b) $TE_{03}$ mode, c) $TE_{23}$ mode. Polarisation as shown.

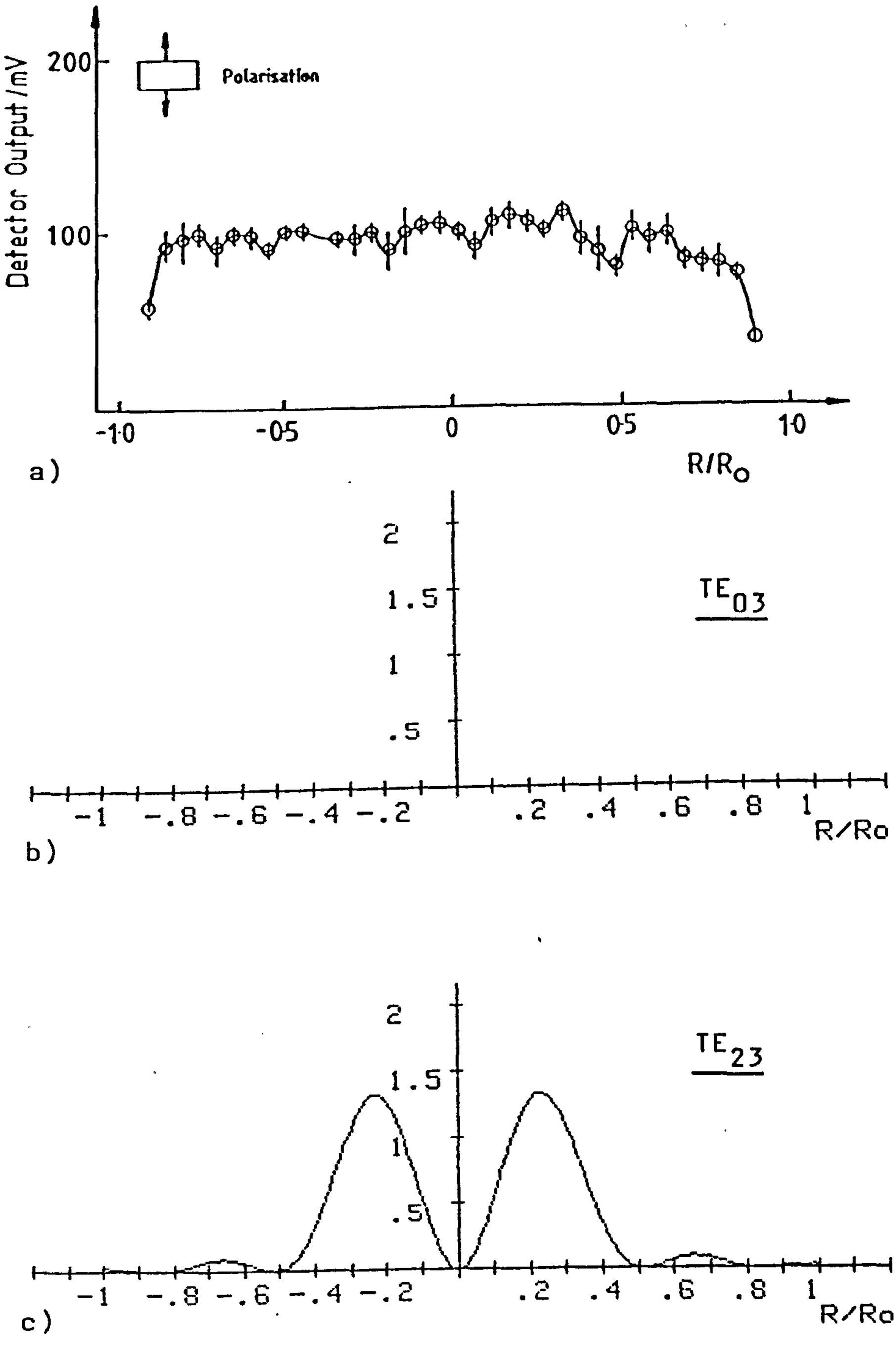


Fig.(6.15). Comparison of measured intensity distribution against intra-cavity mode pattern plots. b) $TE_{03}$ mode, c) $TE_{23}$ mode. Polarisation as shown.

than expected, though it shows no intensity variations.

All of this information discriminates against the $TE_{23}$ mode in two main instances:

1) The central two peaks should be less intense than the second and fifth in the $TE_{23}$ mode, fig.(6.14c), and
2) The $TE_{23}$ mode has a radial component of its electric field with a very marked intensity distribution, fig.(6.15c), which would have been detected upon rotating the polarisation of the detector.

It has thus been possible to unambiguously identify the $TE_{03}$ mode oscillating in the maser cavity. Both from spectroscopic analysis and from the radiation pattern across the output window.

Output power from the Electron Cyclotron Maser in the W-Band.

This was measured using a calibrated power meter as described in chapter 3 and 4. The thermocouple array measured the total energy in each pulse and the crystal detector measured the pulse duration. From this information the power given out in any pulse may be easily calculated.

The results of this experiment are shown in fig.(6.16) and (6.17). In fig.(6.16) the spectrometer scans produced earlier in the chapter have been replotted, this time with their respective output powers noted with each curve. The power stated in this case corresponds to the total power integrated over all frequencies under each curve. Each power measurement was made with the maser operating under exactly the same conditions as each spectrometer scan.

The results given above have been averaged over many shots. It was however noted that at a cyclotron frequency of 89.2GHz a maximum output power of 100kW was measured. Obviously the efficiency of the system may be doubled if the exact firing conditions of this particular shot could be reliably reproduced.

These results mirror almost exactly the relative power levels predicted via the calibrated spectrometer, with the maximum output

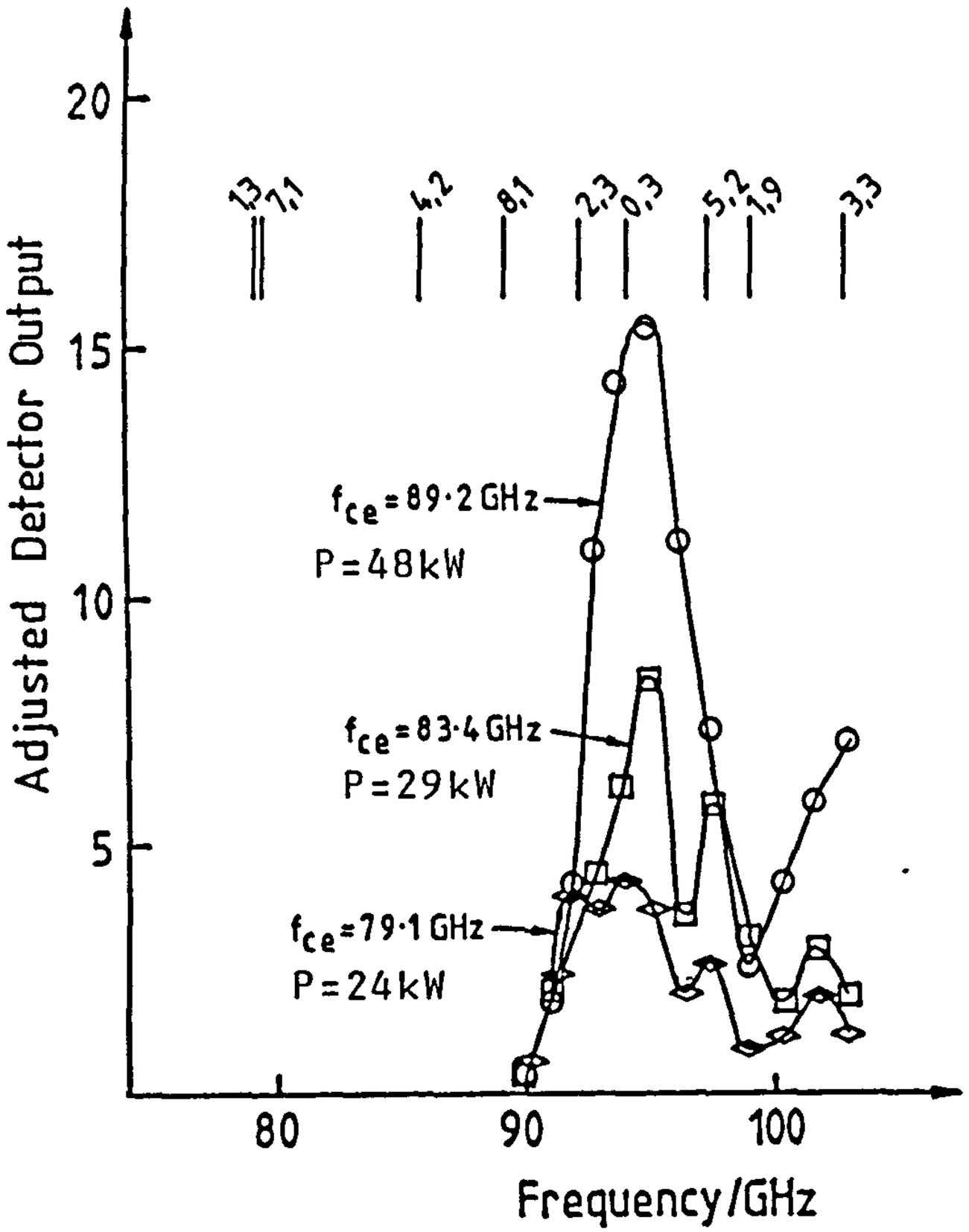


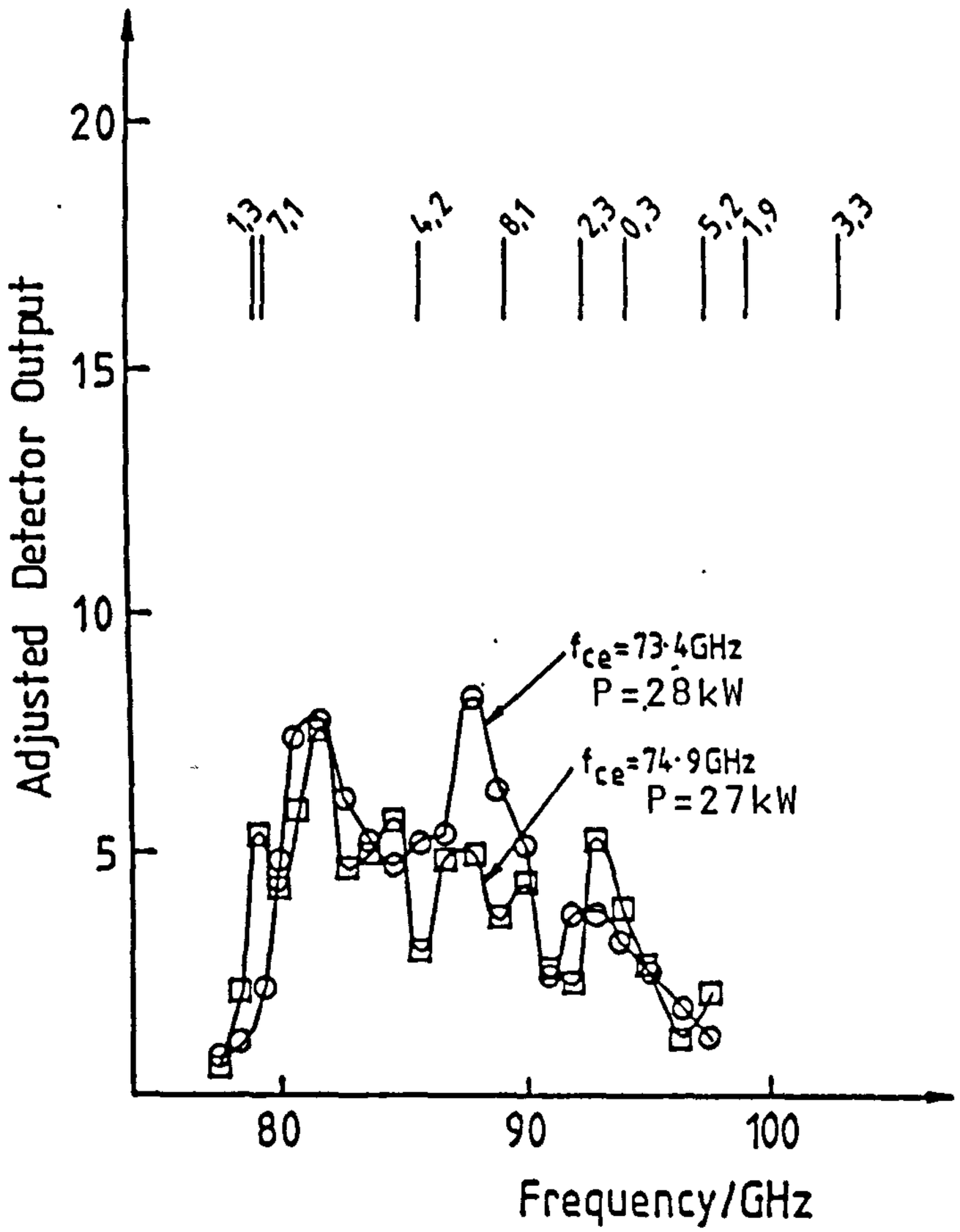


Fig.(6.16). Comparison of spectral intensities with calibrated power measurements.

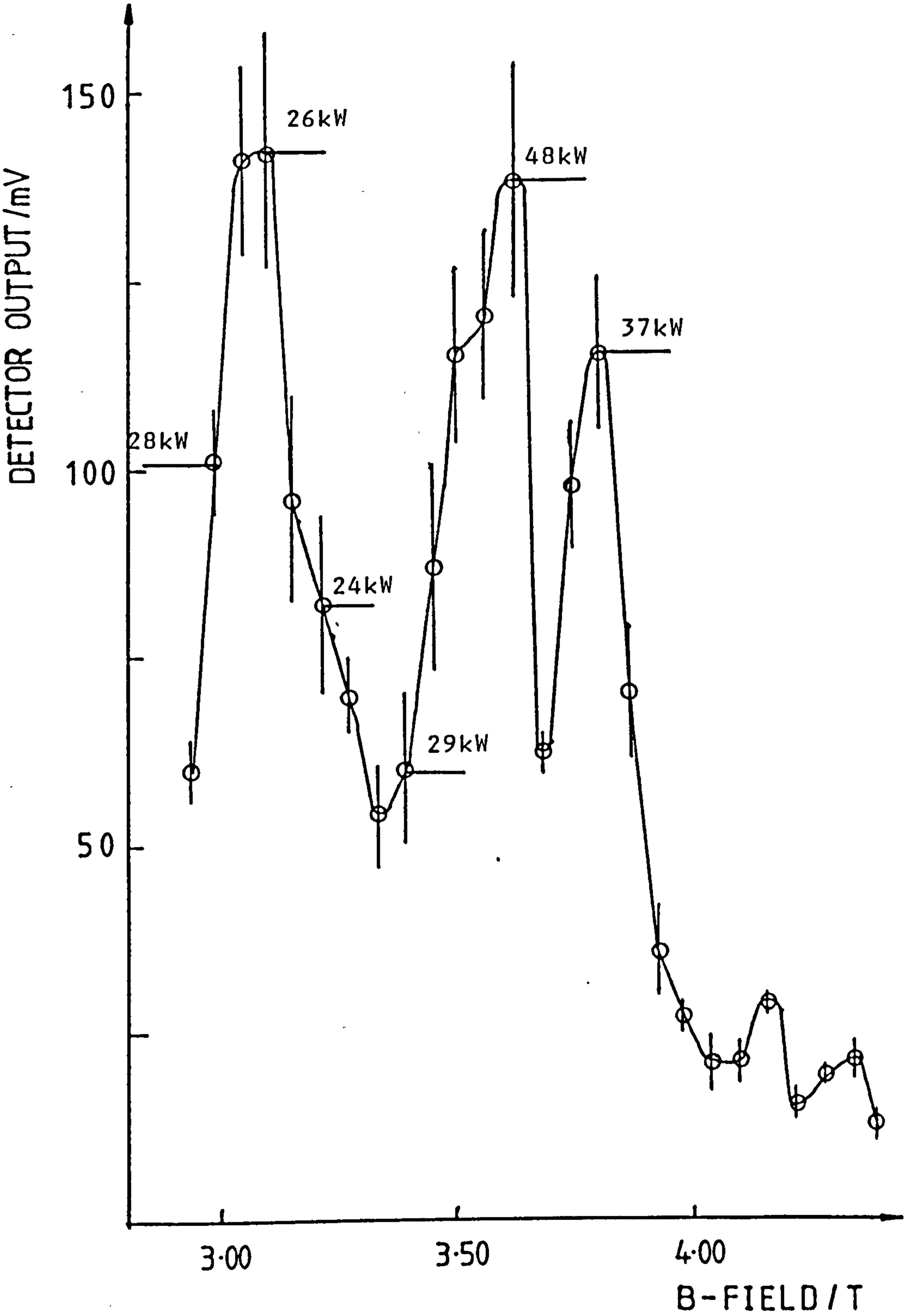


Fig.(6.17). A relative comparison of the direct power measurements made using the crystal detector and the calibrated power meter.

power being developed in the $TE_{03}$ mode with a cyclotron frequency of 98.2GHz. Again as $\delta\omega$ increases the power in the $TE_{03}$ mode is reduced to 29.6kW at a cyclotron frequency of 84.3GHz and is further reduced to 24.6kW at a cyclotron frequency of 79.1GHz.

As the cyclotron frequency is again reduced to 73.4GHz the output power rises as expected to 28.3kW with the excitation of both the TE13 and the $TE_{42}$ modes.

Again all of these results are entirely self-consistent with theory and previous work. The direct power measurements from both the crystal detector and the calibrated power meter are shown in fig.(6.17). In this case the relative magnitudes of the respective points do not agree. This may be seen at the three main resonances evident at magnetic field values of 3.10T, 3.63T and 3.81T. From the crystal detector results the first two peaks seem to be of comparable magnitude, however from the more reliable power meter it is clear there is approximately a factor of two difference in their respective amplitudes. There are similar discrepancies between all points depicted on the graph.

Although in quantitative terms the uncalibrated direct power measurements have been shown to be approximate, in qualitative terms the relative power measurements are only a factor of $\simeq 2$ out across the W-band. Also, if radiation is detected at a certain cyclotron frequency then the maser must be oscillating with a frequency upshift $\lesssim 10\%$ of this frequency. Hence, the uncalibrated direct power measurements do provide an important preliminary macroscopic analysis of the maser oscillation. (i.e. radiation is emitted from the system across the entire bandwidth with the relative magnitude of each point correct to within a factor of $\simeq 2$). Once maser oscillation has been identified using this technique, the resulting output may be characterised using more specific diagnostics.

## 6.7 Summary of W-band Results.

It has been possible to absolutely identify the $TE_{03}$ mode oscillating in the maser cavity at a frequency centered at 95.2GHz (with a corresponding cyclotron frequency of 89.2GHz). This mode

has been identified from both spectroscopic analysis and radiation intensity distribution scans across the output window.

The step-tunability of the maser has also been demonstrated via discrete mode excitation. This has resulted in the subsequent simultaneous excitation of the $TE_{13}$ and the $TE_{42}$ modes centered at frequencies of 81.4GHz and 88.0GHz. Due to the multimode oscillation of these modes, no mode identification from their radiation intensity distributions is possible. From spectroscopic analysis, however, comparison of the R.E.B. position and electric field intensity distribution and each mode's $\eta Q$, it seems certain that the above mentionad modes are being excited in preference to the $TE_{71}$ and the $TE_{81}$ modes respectively.

It also seems certain that the maser is oscillating in the $TE_{13}$ and the $TE_{42}$ modes simultaneously. In the past it has been unclear whether multimode oscillation has been the result of mode hopping between shots, with only one mode oscillating at any one time, or whether two or more modes may be able to run simultaneously. From the above information it seems the latter is true. The $TE_{42}$ mode proved impossible to excite on its own and only appeared as a parasitic mode when the $TE_{13}$ mode was oscillating, resulting in both modes running concurrently.

The output power of the maser has bèen measured, with a maximum occuring with the excitation of the $TE_{03}$ mode. The average output power was measured to be 48kW with a maximum peak power of 100kW.

It is satisfying to note that all these results are in complete agreement with theory presented in earlier chapters.

# CHAPTER 7.

# PRELIMINARY G-BAND MEASUREMENTS.

## 7.1 Introduction.

This chapter deals with the preliminary G-band measurements. These are the first measurements over 100GHz to have been achieved in our E.C.M. programme at Strathclyde University.

The direct power measurements are presented first and were obtained using an uncalibrated crystal detector. The subsequent measurements of the output frequency of the maser are shown graphically, and were measured using the calibrated G-band grating. These results demonstrate the varying frequency of oscillation as a function of the cavity magnetic field. They do, of course, also demonstrate the successful achievment of one of the main aims of this thesis, that of maser oscillation at 200GHz.

Due to the limitations of the G-band calibration source and the multimode oscillation of the maser at these frequencies, a comprehensive study of the maser operation at these frequencies is not possible. However, the results do present features of the maser operation which allow positive identification of the E.C.M. interaction and confirm that we have, in fact, observed maser oscillation at 200GHz.

## 7.2 Direct Power Measurements with Varying Cavity Magnetic Field.

The direct output power was measured as the intracavity magnetic field was varied from 6.06T to 8.18T, corresponding to a cyclotron frequency of 149GHz to 201GHz, fig.(7.1). The Marx discharge voltage was held constant at 72kV and the coil#2 B-field at .29T. (In chapter 5 .29T was found to be the optimum value for the cathode magnetic field for W-band oscillation. The relationship between the maser output power and the cathode magnetic field in the G-band was measured. This experiment reproduced the results presented in fig.(5.3)).

As in the W-band, obvious peaks and resonances are evident, however care must be taken in their interpretation as they may not correspond to maxima in the absolute output power of the maser (this phenomenon was described in detail in chapter 6). Radiation is again produced (within a factor of ≃3) across the entire

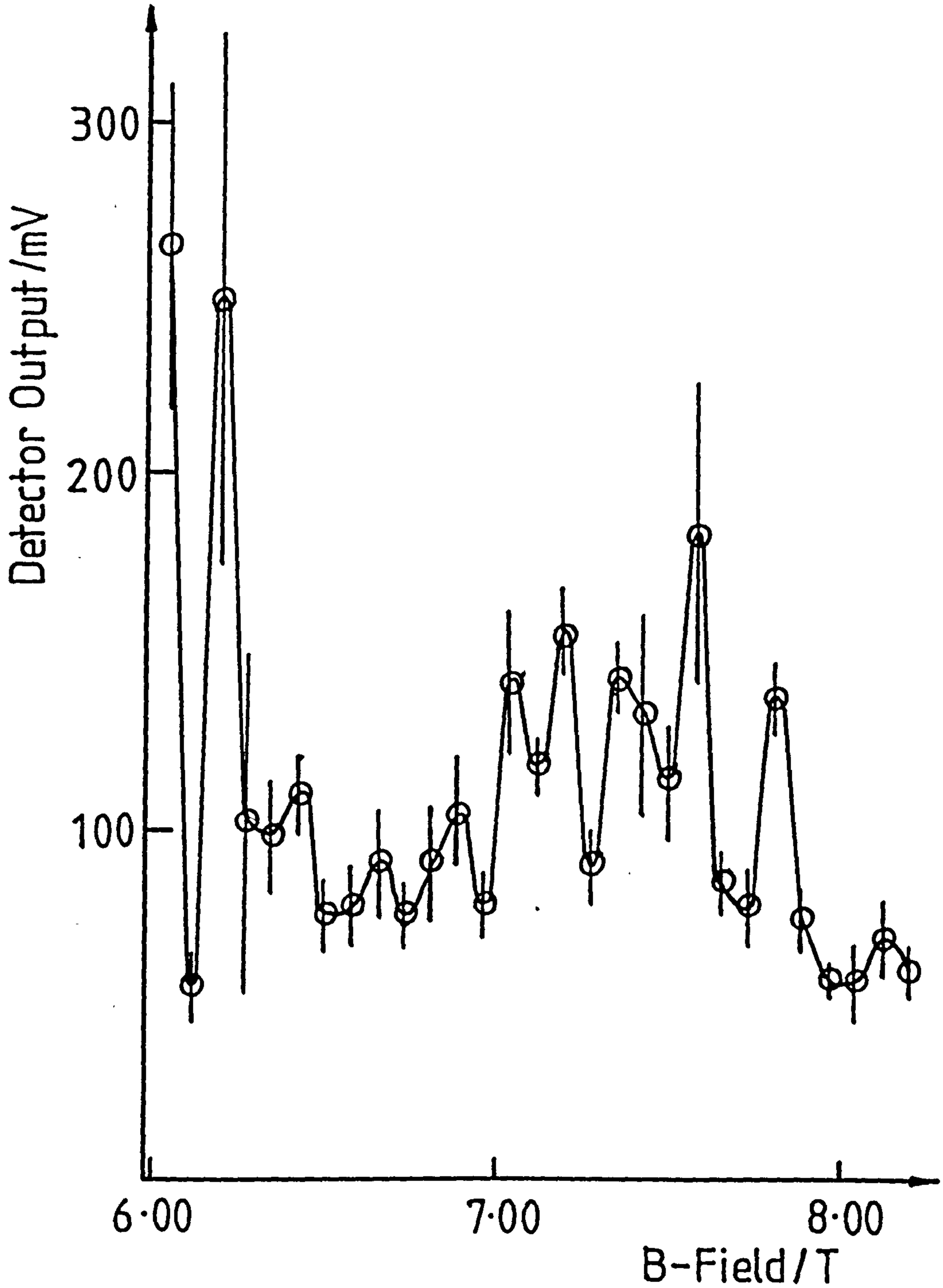


Fig.(7.1). Direct maser output as a function of the cavity B-field.

G-band. This suggests that the maser is oscillating (albeit in a multimode manner) across the entire band.

Again no spectroscopic information is contained in this data other than the fact that if it is the E.C.M. interaction being observed then one would expect the maser to oscillate at and above the equivalent cyclotron frequency.

## 7.3 Spectroscopic Analysis of the G-Band Output.

Measurement of the frequency dependent insertion losses has so many practical difficulties (the extemely low power produced by the G-band calibration source (chapter 3), the complexity of the detection technique (used in conjunction with the G-band test source), having no G-band power meter or calibrated detector available and the difficulties involved fine tuning the G-band source), as to render the measurement of the insertion losses of the spectrometer impossible with the hard-ware available a Strathclyde University. Hence, the frequency dependent insertion losses have not been taken into account in the presented frequency scans in this section. It is important to state that although the frequency dependent insertion losses of the spectrometer have not been measured, the frequency throughput versus grating angle calibration of the spectrometer has.

Five spectrometer scans are presented and described below. Each scan shows the expected multimode oscillation of the maser and the characteristic frequency shift with the magnitude of the intra-cavity magnetic field. Marked on each graph are all the relevant cut off frequencies of the $TE_{pq}$ modes.

During all scans the Marx discharge voltage was held constant at 72kV and the coil#2 magnetic field at .29T.

### Spectrometer Scans.

### Intra-cavity B-Field=6.21T (≡152GHz), fig.(7.2).

Broadband oscillation was observed between 151GHz and 160GHz (i.e. with an oscillating bandwidth, $\Delta f$=9GHz). Four peaks were

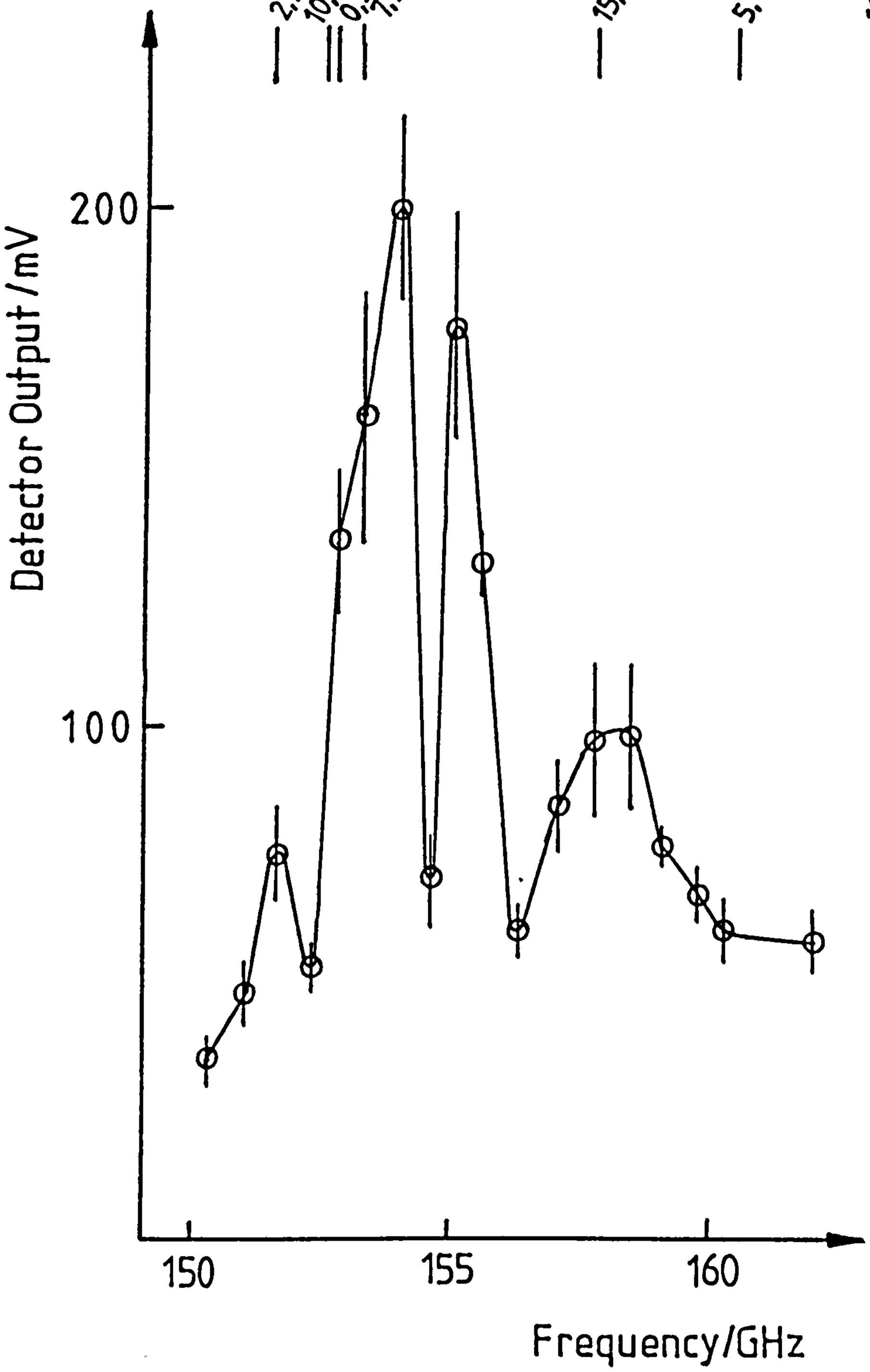


Fig.(7.2). Frequency scan, cavity B-field=6.12T, $f_{ce}$=152GHz.

observed with the two largest centered at 154.0GHz and 155.1GHz. Due to the high losses of the $TE_{10,2}$ and $TE_{7,3}$ whispering gallery modes, it seems that either the $TE_{2,5}$ or the $TE_{0,5}$ modes, or both, were being excited. (A given mode should oscillate at a frequency slightly above its cut-off frequency).

Intra-cavity B-Field=6.67T (≡163GHz), fig.(7.3).

In this instance the maser oscillated between 162GHz and 176GHz (i.e. $\Delta f$=14GHz). No strong individual resonances are present with energy being fed evenly into many of the possible modes at these frequencies. This results in the maser acting like a broadband amplifier.

Intra-cavity B-Field=7.22T (≡176GHz), fig.(7.4).

Broadband oscillation was observed between 177GHz and 186GHz (i.e. $\Delta f$=9GHz). The detected power in these frequencies was significantly lower than in other regions of the G-band, with detected signals reduced by a factor of approximately 2. Three peaks are evident, 177.6GHz and 179.6GHz corresponding in frequency to either the $TE_{9,3}$, $TE_{17,1}$ or the $TE_{4,5}$ modes and at 183.3GHz, in close proximity to the oscillating frequency of the $TE_{0,6}$ mode.

Intra-cavity B-Field=7.58T (≡186GHz), fig.(7.5).

At this magnetic field value radiation was observed between 185GHz and 198GHz (i.e. $\Delta f$=13GHz). A strong resonance was observed at 187.7GHz corresponding in frequency to either the $TE_{13,2}$ or the $TE_{7,1}$ modes. A broad-band excitation region between 188.3GHz and 195.6GHz is evident, due to the oscillation of perhaps two indistinguishable modes such as the $TE_{10,3}$ and the $TE_{5,5}$.

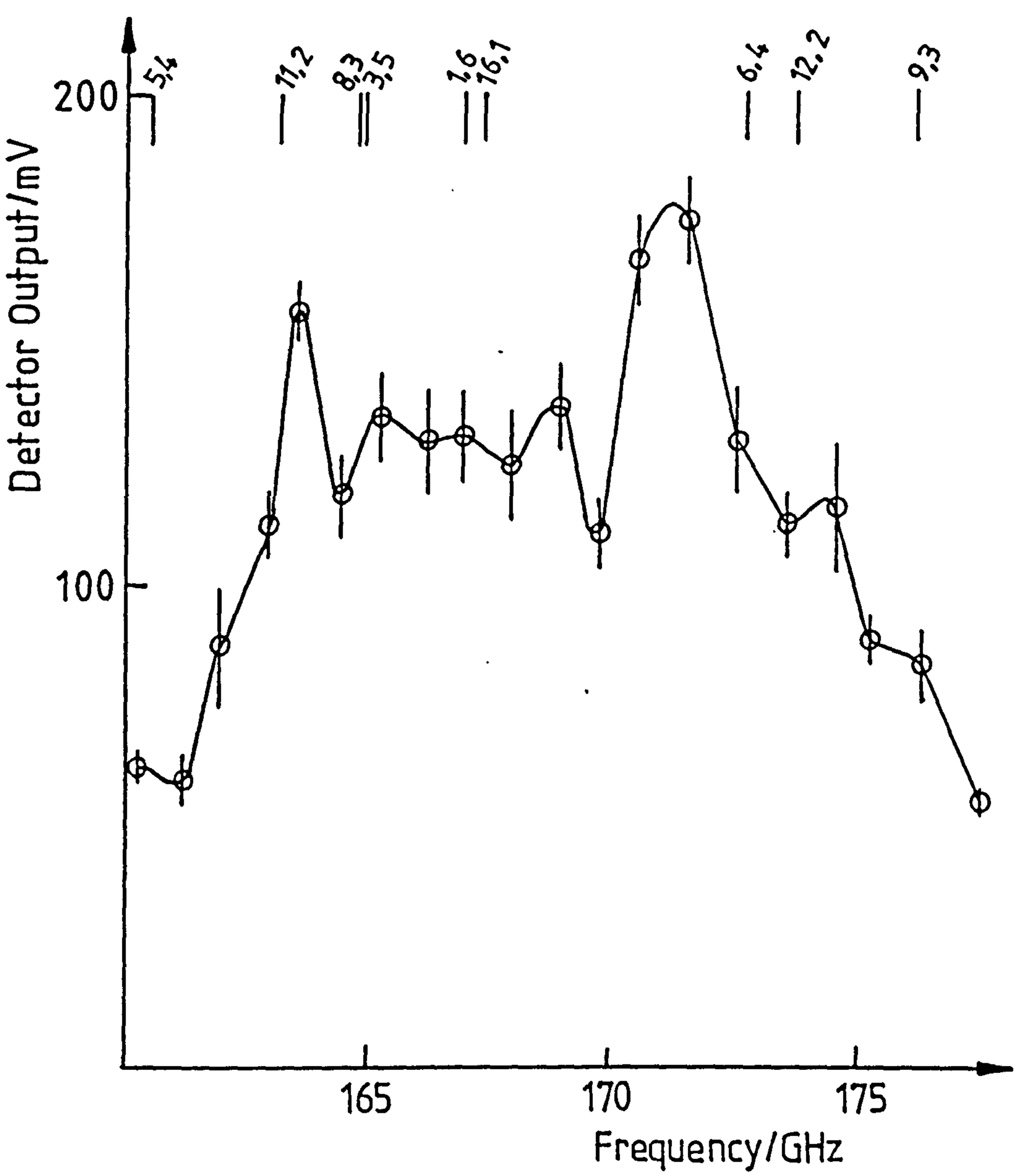


Fig.(7.3). Frequency scan, cavity B-field=6.67T, $f_{ce}$=163GHz.

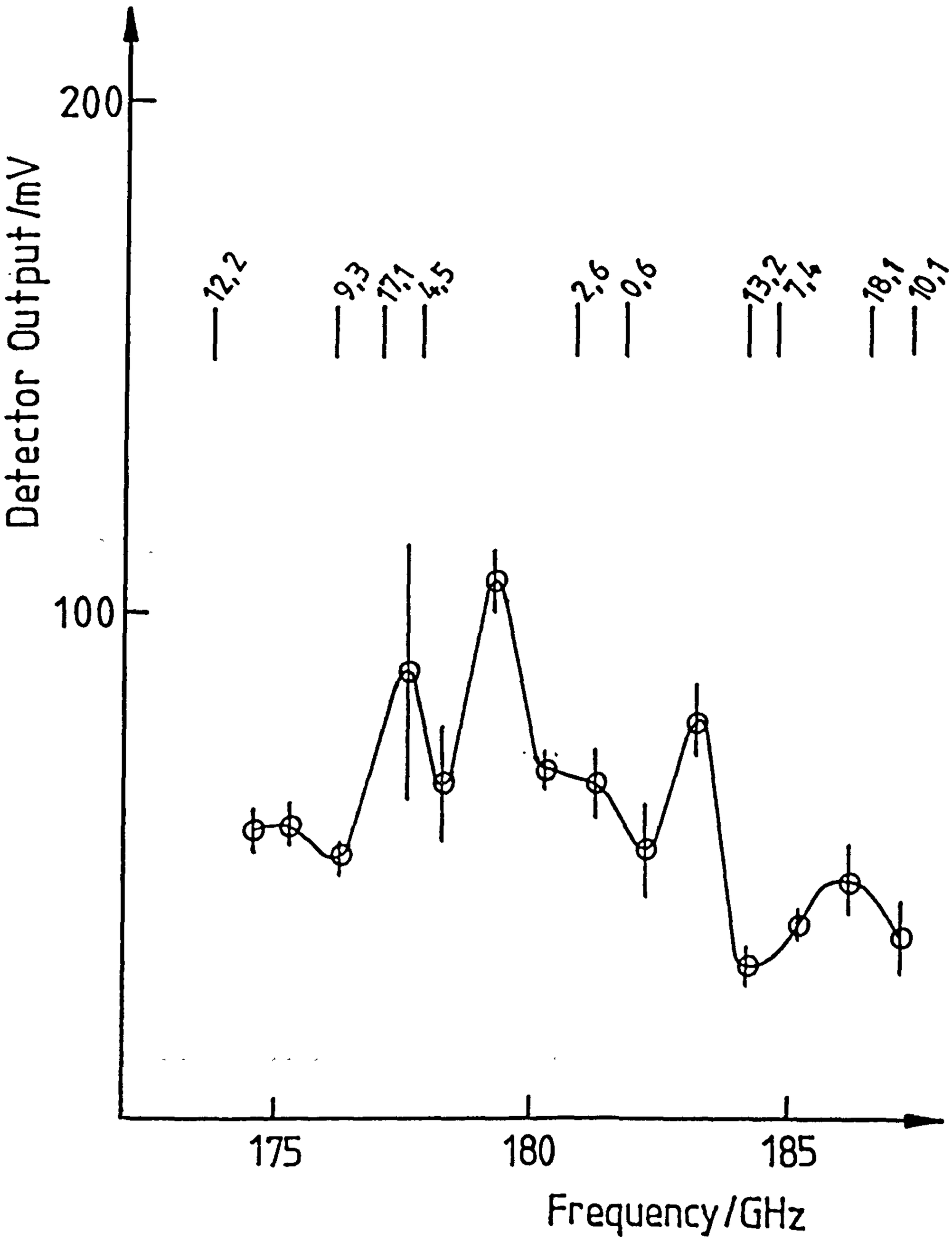


Fig.(7.4). Frequency scan, cavity B-field=7.22T, $f_{ce}$=176GHz.

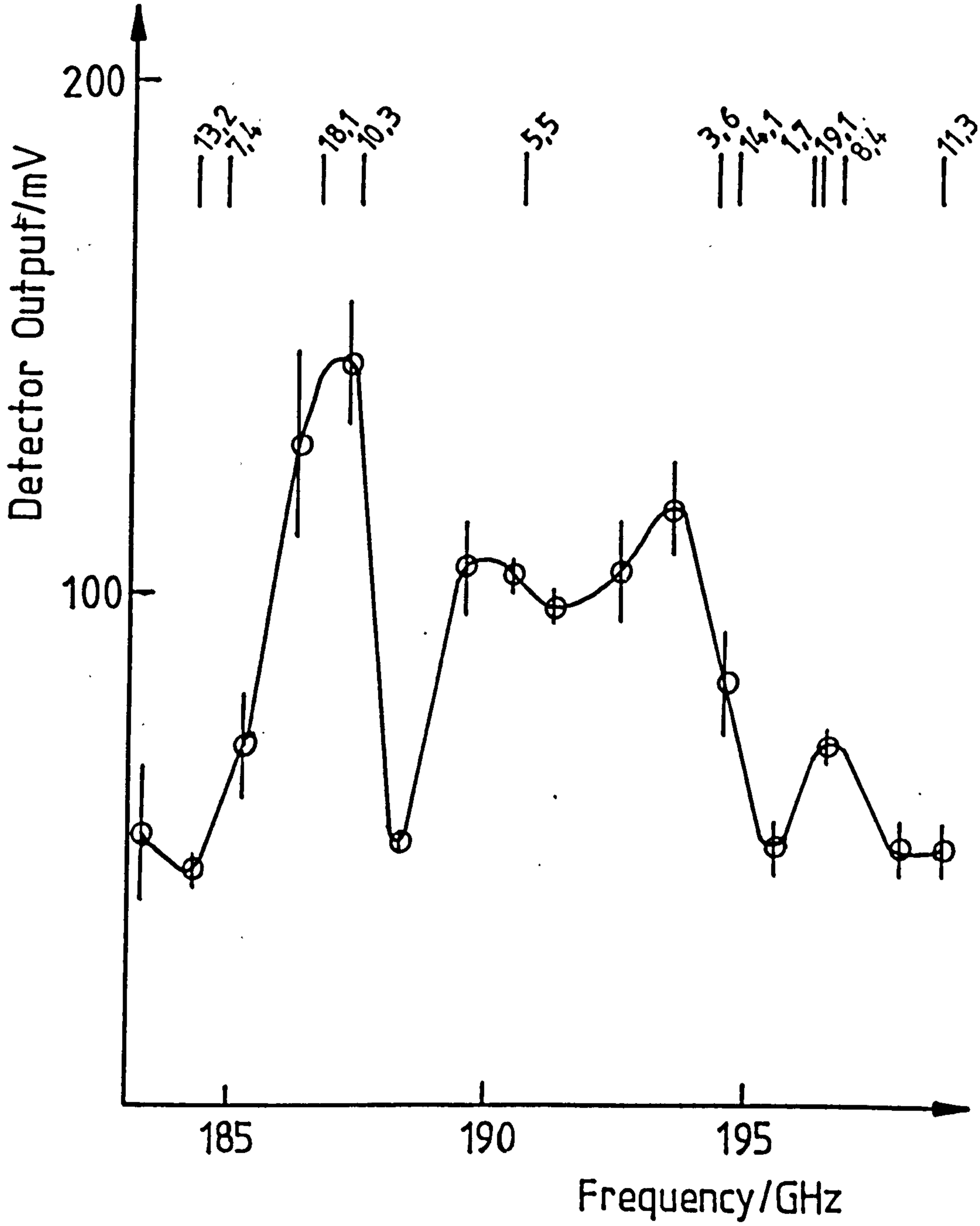


Fig.(7.5). Frequency scan, cavity B-field=7.58T, $f_{ce}$=186GHz.

Intra-cavity B-field=7.81T (≡191GHz), fig.(7.6).

Radiation was observed between 189GHz and 202GHz (i.e. Δf=13GHz). No particular resonances are evident and once again we observe broad-band gain associated with most of the possible modes across this frequency range. This graph does, however, show maser oscillation at 200GHz, a significant result in the development of the Strathclyde University maser (and for E.C.M. development in general). It would seem from the graph that the $TE_{11,3}$ mode is oscillating at 200GHz.

## 7.4 Analysis and Discussion.

Although no detailed information on the maser oscillation may be obtained from the direct power measurements, they do demomstrate clearly that our maser is capable of oscillating at frequencies throughout the G-band. Also, as these results were obtained with 25dB attenuation between the receiving horn and the crystal detector, they removed any possibility that the maser output power in the G-band coupled with the insensitivity at these frequencies of the W-band detectors, would not allow the detection of signals through the minimum 25dB insertion losses of the spectrometer.

In the previous section a detailed analysis of the maser output at each value of the cyclotron frequency was presented. At no cyclotron frequency did this suggest single mode oscillation and it was only possible to speculate which modes were being excited. It also proved impossible to derive information about the oscillating linewidth of any one mode. However the overall behavior can be seen clearly when all the above spectrometer scans are replotted on the same axes, fig.(7.7). The following points should be noted.

1) The measured gain bandwidth of the E.C.M. varies between 9GHz and 14GHz. To calculate theoretically the gain bandwidth would involve the numerical solution of the complex non-linear plasma physics equations or the self-consistent numerical calculation of the electron trajectories in the presence of

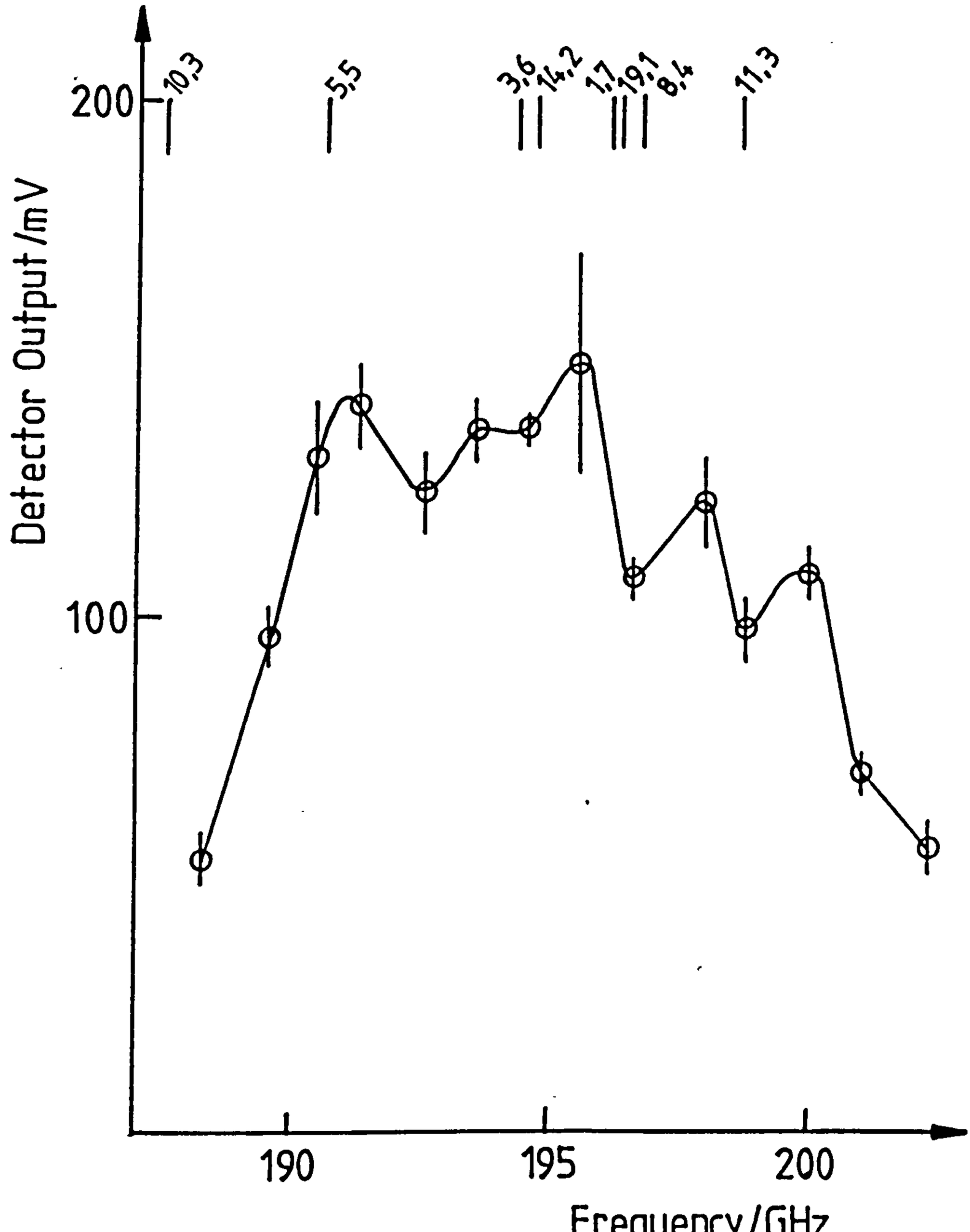


Fig.(7.6). Frequency scan, cavity B-field=7.81T, $f_{ce}$=191GHz.

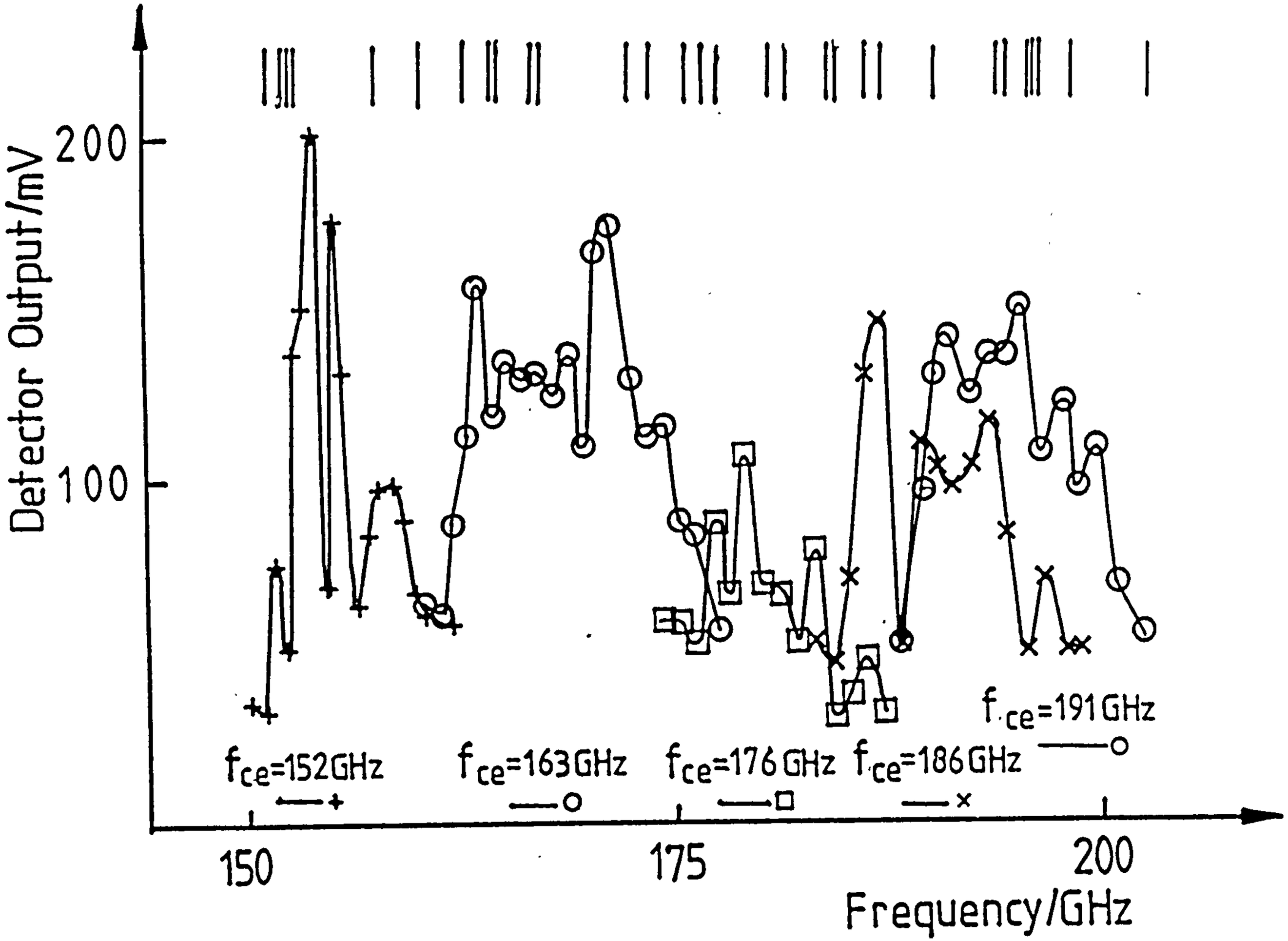


Fig.(7.7). The five G-band spectrometer scans plotted on the same axes.

the DC electric and magnetic fields and the RF intra-cavity electromagnetic radiation; which is beyond the scope of this thesis. However a similar gain bandwidth was observed in both the W-band and the G-band. In the G-band the greatly increased mode density has resulted in many modes experiencing similar gain at each value of the cyclotron frequency. In the W-band the inter-mode spacing was greater and low-loss, low-order modes could extract energy from the electron beam, suppressing adjacent lossy modes.

2) The frequency shift of the maser with electron cyclotron frequency is clearly evident. In each case the oscillation of the maser is observed to begin at, or above, the cyclotron frequency. This demonstrates the existence of the majority of the gain curve above this frequency. This behaviour is typical and indicative of the E.C.M. gain mechanism and is evident at all frequencies.

3) The above two conditions result in an almost continuously tunable system. In the W-band the maser was crudely step-tunable, however the increased number of modes below the gain line curve (in the G-band) produces a system which, by comparison, is quasi-continuously tunable.

4) As stated above one of the main aims of this project was to obtain oscillation at 200GHz. As is evident in fig.(7.6) and (7.7), this has been achieved. In principle there was no reason why the frequency could not have been pushed higher, as the magnetic field produced by the main field coil could be increased by a further 1T. However as the system was beginning to reach its design limits and all stated aims had been achieved it was decided not to risk possible damage to, or destruction of, the machine.

5) The two frequency scans, fig.(7.5) and (7.6), overlap in frequency and show in detail the effects of a small shift in the cyclotron frequency, 5GHz. In moving from an intra-cavity

magnetic field of 7.58T to 7.81T, a frequency shift of 4GHz was evident. This has the effect of eliminating the resonance centered at 197.3GHz. The remaining higher frequency modes received more energy, which was then available from the electron beam with the increase of $f_{ce}$. There is also a corresponding frequency shift of 4GHz at the high frequency end of the gain line curve.

6) Although the spectrometer has been calibrated for frequency output (using the incident angle on the grating) and the associated bandpass width, it was not possible with the apparatus available to calibrate for the frequency dependent insertion losses. However this additional piece of information would only result in the alteration of the relative height of each peak. Hence any frequencies detected by the spectrometer must actually be present in the maser output. (No matter how large their absolute relative intensities are).

7) As the output power of the G-band calibration source was typically <.5mW it was impossible to calibrate the thermocouple array as in the W-band. As a result no absolute power measurements on the G-band maser output were possible. Also as the insertion losses of the spectrometer were unknown, no indirect estimates of the maser output could be made.

Considering fig.(7.1), these results were taken in exactly the same way as the equvalent W-band measurements, with approximately the same attenuation (25dB) placed between the receiving horn and the crystal detector. In this case a more sensitive W-band detector was used in the G-band (Flann 137 with plunger short termination) to that used in the W-band (Flann 135 with load termination). However this detector will be correspondingly less sensitive in the G-band. It is reasonable therefore to assume that the maser output power is still reaching reasonable levels, certainly many kW if not 10's of kW.

## 7.5 Summary.

After a comprehensive and self consistent analysis of the W-band operation of the maser, the first preliminary results in the G-band have been presented. Although not designed to be as detailed as those previously described they do however clearly highlight the following characteristics.

1) Millimetre-wave production in the G-band.
2) Expected multimode oscillation.
3) Existence of finite gain bandwidth.
4) Shifting frequency of oscillation with cyclotron frequency.
5) The existence of the gain line curve almost wholly above the cyclotron frequency.
6) High power operation.
7) 200GHz oscillation.

All of which are self-consistent with, the general E.C.M. gain mechanism and with our Mk-6 E.C.M. in particular.

# CHAPTER -8-

## SUMMARY AND DISCUSSION.

## 8.1 Introduction.

The Mk-6 E.C.M., which forms the subject of this thesis, is part of an on-going programme of E.C.M. development being performed at Strathclyde University. This previous work culminated in the Mk-5 E.C.M., which produced single mode oscillation in the Ka-band and multi-mode oscillation in the W-band. The previous research and development was however almost entirely empirical in nature, with no self-consistent analysis used to describe the maser oscillation. Hence the Mk-6 E.C.M. develcpment had three main aims,

1) Production of single mode oscillation in the W-band, ≃100GHz.
2) Production of high frequency, multi-mode oscillation in the G-band, ≃200GHz.
3) A completely self-consistent analysis of the maser oscillation.

As has been demonstrated in the previous chapters all of these aims were met in full and will be briefly summarised below.

## 8.2 The Intra-Cavity Magnetic Field.

As was demonstrated the maser oscillated at a frequency determined by the intra-cavity magnetic field. To first order, this frequency is given by the cyclotron frequency of the electron beam; with a more comprehensive analysis it is possible to show that the system should oscillate at a frequency slightly above this, and this proved to be the case.

To gain oscillation up to 200GHz a field coil was designed to produce a continuously variable magnetic field up to ≃10T. This had to be mechanically strengthened to withstand the expected mechanical field pressures (up to 260 Atmospheres). The current (≃20kA) flowing through the coil windings, created heat dissipation problems which were overcome by using hollow tube windings (suitably cooled).

The coil was constructed as described in chapter 2 and calibrated as described in chapter 4. The coil satisfied all the

design aims, producing a maximum magnetic field of ≃9T when in situ on the cavity. The position of the coil was significant due to the pulsed nature of the field and the electrical conductivity of the cavity walls, the combination of which results in a significant (10%) field exclusion.

The construction and testing of the field coil was essential to the work described this thesis, as it permits the successful operation of the Mk-6 E.C.M. over all the frequency ranges stated.

## 8.3 Cavity Design.

The following theoretical considerations were taken into account in the design of the Mk-6 maser cavity.

1) Resonant frequencies and relative mode spacing with respect to the cavity diameter.
2) Reflection coefficients from the output tapers and the step discontinuity, along with mode conversion considerations in the output taper.
3) The ohmic and diffraction quality factors.

These considerations allowed the determination of the optimum cavity diameter. With the relative mode density increasing with frequency the cavity diameter was chosen such that it would allow single mode oscillation at 100GHz and multi-mode oscillation at 200GHz. This is the first time that the items listed under 2) above had been quantitatively considered in the work at Strathclyde. With the subsequent calculated reflection coefficients (<1% intensity reflection in both cases), the taper angle in the output taper was determined to satisfy minimal mode conversion and, for the flange taper, to optimise the R.E.B.'s $v_\perp$. This resulted in an oscillating system with high gain, low feed-back characteristics and with a low mode conversion output coupler.

The anode-cathode system was designed to impart the optimum $v_\perp$ to the electron beam. An inherently pulsed field-immersed field-emission cold cathode was used. This utilised a two electrode configuration, as opposed to the three electrode M.I.G.

electron gun used in many other systems (16.17,18). However the pulsed nature of the work undertaken at Strathclyde University makes the two electrode configuration ideal, with its light weight, heaterless construction and high-voltage, high-current capability.

## 8.4 Diagnostics.

Along with the complete redesign of the maser, significant improvements were also made to the diagnostics. The diagnostics were split into two different systems, both housed in separate screened rooms.

### E.C.M. Monitoring Diagnostics.

These fed information to screened room#1 and were monitored by an HP9816 personal computer. For the first time the pulse to pulse running of the maser was entirely controlled by computer. Via the monitoring diagnostics, the computer monitored the charging of the respective capacitor banks, the HT diode voltage and the discharge currents through both the magnetic field coils. This ensured reliable, repeatable operation of the maser.

### mm-Wave Output Diagnostics.

These were monitored in screened room#2, which had a noise level a factor of ≃10 less than that in screened room#1. These diagnostics were split into four groups.

1) Direct power measurements, which were made using an uncalibrated detection system. This was used to provide preliminary information on the maser output as a function of the cavity magnetic field.
2) Frequency measurements, which were made using a calibrated diffraction grating spectrometer. These allowed the determinaton of the frequency of oscillation and the frequency bandwidth of the maser for any predetermined cavity magnetic

field.

3) Radiation pattern measurements. Several practical and theoretical methods for determining the cavity mode of oscillation were considered. The radiation pattern measurements were made by scanning a detector across the near-field radiation pattern and relating this to the cavity mode of oscillation via the theoretically calculated intra-cavity mode pattern plots.

4) Direct absolute power measurements. These were made using a calibrated thermocouple array in conjunction with a crystal detector.

All the above mm-wave diagnostics were designed to allow the complete determination of the oscillating characteristics of the E.C.M. In conjunction with these measurements, for the first time, a two detector system was used in both the G-band spectrometer measurements and the W-band radiation pattern mesurements. In both cases this allowed the removal of the shot-to-shot fluctuations of the maser and greatly increased the precision and signal-to-noise ratio of the respective diagnostics.

## 8.5 Further Improvements to the E.C.M. System.

Having completely redesigned the E.C.M. and upgraded the control and diagnostics systems, two further significant improvements were made to the maser.

1) The cathode magnetic field coil. This coil was designed to produce a continuously variable magnetic field of up to ≃1T at the cathode tip. This was included to enhance and optimise the electron beam production.
2) The output window. Due to the high losses and frequency dependent absorption of the glass window used previously, a completely novel Mylar output window was developed. This had no frequency dependent transmission losses and was shown to increase the transmitted energy from the system by a factor of ≃10.

## 8.6 Maser Optimisation.

When keeping the intra-cavity magnetic field constant there are two important factors which determine the output power of the maser; the anode-cathode spacing and the cathode magnetic field.

1) Anode-cathode spacing. Adjusting $L_{a-c}$ from 0 to 20mm increased the mm-wave pulse length by a factor of ≃4 to ≃400ns. This also resulted in a factor of ≃2 increase in the maximum output power.
2) Cathode magnetic field. This had a much stronger influence on the overall efficiency of the maser, increasing, by a factor of ≃70, the maximum output power, when the cathode field coil was activated. This very large increase in the output power was shown to be due entirely to the optimised efficiency of the R.E.B. production.

Both these factors proved to have a very large influence on the overall efficiency of the E.C.M., which (combined with the low-loss, broad passband output window), produced a fully optimised system. This optimised E.C.M. was then used to study in detail, the maser oscillation in both the W-band and the G-band.

## 8.7 W-Band Results.

A complete and self-consistent analysis of the W-band oscillation of the maser is presented in chapter 6. This identified the following salient features:

1) Single mode oscillation was identified, in the $TE_{03}$ mode, from both the frequency scans and the near-field radiation pattern. This mode oscillated at a frequency centred on 95.2GHz.
2) The system was also shown to be crudely step-tunable, with the excitation of modes such as the $TE_{13}$, at a frequency of 81.4GHz, and the $TE_{12}$ mode, at a frequency of 88.0GHz.

3) It was also possible to explain the differential excitation of the $TE_{03}$ mode, in preference to the neighbouring $TE_{31}$, $TE_{42}$ and the $TE_{23}$ modes, in terms of their respective ohmic losses and the relative spatial coupling of the measured R.E.B. position, combined with the theoretically calculated electric field distribution of each individual mode.
4) The output power was measured at several different frequencies, having a maximum of ≈50kW at 95.2GHz (corresponding to the observed excitation of the $TE_{03}$ mode).

## 8.8 G-Band Results.

Due to the severe limitations in the calibration equipment available at Strathclyde (chapters 3 and 7), a comprehensive analysis of the G-band oscillation was not possible. However the following characteristics of the maser oscillation in the G-band were positively identified.

1) Multi-mode oscillation was observed, which was entirely self-consistent with the increased mode density at those frequencies.
2) The maser was shown to be quasi-continuously tunable, again due to the reduced frequency separation of the modes.
3) 200GHz oscillation was observed.

This is the first time oscillation at frequencies over 100GHz have been observed at Strathclyde University.

## 8.9 Conclusions and Future Work.

The initial theory described in chapter 1, identified the E.C.M. interaction and predicted several important aspects of that phenomenon. The E.C.M. interaction was shown, fundamentally, to be a mechanism by which energy from free relativistic electrons may be coupled to an electromagnetic wave. The description shows how the relativistic mass dependence causes electron phase bunching, resulting in power conversion from the R.E.B. to the radiation

field and a frequency upshift of the resulting radiation with respect to the cyclotron frequency of the electrons. The analysis was used predominantly as a basis for this research program, however the theory itself, of course, was largely device independent.

It follows that in the production of a practical maser, several parameters both quantitative and qualitative must be taken into account. These design criteria are used to describe and determine the oscillating characteristics of a particular device and include such parameters as: the resonant frequencies of any particular cavity, the cavity quality factor, the theoretical, intra-cavity, mode-dependent radiation field distribution, the experimental measurement of the R.E.B. position in the cavity, the reflection coefficients from each end of the cavity and the relative mode conversion in the output taper.

Using these device-dependent parameters and studying practical gyrotron development, both at Strathclyde and at many other centres around the world, the Mk-6 E.C.M. was developed. The design incorporated a novel pulsed electromagnet producing the necessary high intra-cavity magnetic field and a two electrode system incorporating a field-immersed, field-emission, cold cathode.

The E.C.M. was subsequently optimised by purely empirical means. This process involved the addition of a novel Mylar window and the adjustment of both the anode-cathode position and the magnetic field produced by tuning coil placed arround the cathode. As none of the calculations developed above were detailed enough to specify optimum magnetic field values at the cathode tip, optimum cathode position or optimum R.E.B. position in the cavity, all of these parameters were optimised experimentally during the development phase.

Having successfully optimised the system, it was then possible, by adjusting the intra-cavity magnetic field, to comprehensively study the maser oscillation in the W-band and to produce a preliminary study in the G-band. On obtaining these results it proved possible to define an entirely self-consistent analysis of the maser oscillation in terms of both the plasma theory (which

predicted many of the general aspects of the maser behaviour) and the device-dependent theory. The latter could be used to explain more particular aspects of the maser oscillation, such as the differential mode excitation, multi-mode and single-mode oscillation, and the step tunability of the cavity.

An experimental measurement of the cavity quality factor would make an important improvement to the above analysis. The values of $Q_\Omega$ were calculated using an idealised model, and thus any consequent interpretation of the experimental results has limitations. The use of Q in explaining the experimental data would be strengthened if an experimental measurement of the cavity Q were made.

This work leads us, in a logical progression, to a self-consistent analysis of the E.C.M. interaction, commencing with predictions from general theory and then developing a device-dependent set of calculations allowing the determination of experimental details. The combination of these considerations with practical experience gained both at Strathclyde and elsewhere, led to the development, construction and testing of a practical device and allowed the explanation of the subsequent results in terms of the initial theory and calculations.

This thesis thus represents the culmination of an important stage of E.C.M. development at Strathclyde University. The work has now reached a stage where a test system has been developed, which has been shown to be capable of producing pulsed, high-power mm-waves over a very large frequency range, 75 to 200GHz. This general development work creates an ideal situation where the experience gained could be used to develop a use-specific E.C.M. for any one of the many practical applications which have been proposed or implemented elsewhere.

Having developed the general principles of operation and obtained experimental experience, future developments might well include:

1) High average power oscillation for E.C.R.H. This would involve the development of a high average power electron gun and suitable heavy-duty heat dissipation processes. With the use

of suitable power supplies and electron gun this work would build on the cavity design and optimisation work contained in this thesis. This work is not entirely suited to a university environment however due to the very high average power consumption this experiment would generate.

2) Plasma diagnostics. These usually require a high power which may be pulsed. Some diagnostics also require a very narrow line width. This second condition may be met with the combination of a very well defined cavity coupled with an extremely stable intra-cavity magnetic field. Such a device would probably incorporate a superconducting magnet producing the stable magnetic field. All of the above requirements would be a feasible extension and development of the work contained in this thesis.

3) High-power, high-frequency, short-range radar. Again high pulsed power and narrow line-width would be essential requirements. This work however would also require a very well defined beam, hence development work would also be required to convert the maser output mode into a well defined Gaussian beam.

4) Further theoretical development. To understand more fully the E.C.M. process and to be able to predict more efficient anode-cathode designs, magnetic field profiles, cathode tip shapes and possible cavity tapers, a more comprehensive theoretical description of the maser must be produced. It is unlikely that this information will be gained from analytical results, instead they will almost certainly come from mathematical modelling and computer simulation. This involves calculating, via numerical techniques, the relativistic electron beam trajectories in the presence of the DC magnetic field, the accelerating DC electric field, the high frequency RF fields and the varying self-field effects.

The further developments outlined above are essential in the production of a user-specific E.C.M. However the apparatus described in this thesis has been an extremely useful test system, as it allowed the investigation of all the relevant physics, both

theoretical and experimental, while keeping the necessary engineering (and power consumption) to a minimum. Having gained all the relevant information from this system one is now in a position to go on to develop a more sophisticated E.C.M. for a particular practical application.

# APPENDICES.

## APPENDIX 1.

Table(A1.1) defines the μ-wave and mm-wave frequency bands, with their corresponding designations and waveguide dimensions, used throughout this thesis.

| Frequency Range / GHz | Designation | Internal Dimensions / mm |
|---|---|---|
| 8.2 - 12.4 | X-Band | 23.0 x 10.0 |
| 26.5 - 40 | Ka-Band | 7.1 x 3.6 |
| 50 - 75 | V-Band | 3.8 x 1.9 |
| 75 - 110 | W-band | 2.4 x 1.3 |
| 140 - 220 | G-Band | 1.3 x .65 |

Table(A1.1). Definition of frequency bands.

## APPENDIX 2.

Eqn.(2.11) was used to calculate the reflection coefficients from both tapers at either end of the cavity via the following technique.

In each case a linear taper will be used which will have the form,

$$a = m\,z + b.$$

Obviously the first derivative will be non-vanishing,

$$\frac{d\,a}{d\,z} = m\ , \qquad \text{where } m = \text{constant.}$$

Hence u = 1 and v = 3/2 and eqn. (2.11) becomes,

$$r = -\frac{j\,\lambda_0}{8\,\pi}\left[\frac{m}{a_i\left[1-\frac{\chi^2}{a_i^2}\right]^{3/2}}\;\frac{e^{-2jJ}\cdot m}{a_2\left[1-\frac{\chi^2}{a_i^2}\right]^{3/2}}\right]. \qquad \text{(A2.1)}$$

This eqn. may be split into a real and an imaginary part by writing the exponential term as the sum of a cosine and sine, yielding,

$$\text{Re}\,(r) = \frac{\lambda_0\,m}{8\,\pi}\cdot\frac{\text{Sin}(2\,J)}{a_i\left[1-\frac{\chi^2}{a_i^2}\right]^{3/2}}\ , \qquad \text{(A2.2)}$$

$$\text{Im}(r) = -\frac{\lambda_0\,m}{8\,\pi}\left[\frac{\text{Cos}\,(2J)}{a_i\left[1-\frac{\chi^2}{a_i^2}\right]^{\frac{3}{2}}}-\frac{1}{a_0\left[1-\frac{\chi^2}{a_0^2}\right]^{\frac{3}{2}}}\right]. \qquad \text{(A2.3)}$$

To interpret these eqns. the definition of r must be considered. In the derivation, r was taken to be the reflected amplitude coeff. i.e.

$$r = \frac{U_2(0)}{U_1(0)} \,. \qquad \text{(A2.4)}$$

Where,

$U_1(0)$ = initial wave amplitude at z=0,

$U_2(0)$ = reflected wave amplitude at z=0.

But the only detectable quantity is $U.U^*$ (43), multiplying eqn.(A2.4) by its complex conjugate yields,

$$r\,r^* = \frac{U_2(0).\,U_2^*(0)}{U_1(0).\,U_1^*(0)} \,. \qquad \text{(A2.5)}$$

Thus $r.r^*$ is the detectable intensity reflection coeff. given by,

$$r\,r^* = Re^2(r) + Im^2(r). \qquad \text{(A2.6)}$$

Hence combining eqns.(A2.2), (A2.3) and (A2.6) it is possible to evaluate $rr^*$, the reflected intensity, R.

## APPENDIX 3.

The program which was used to generate the electromagnetic field distribution in a cylindrically symmetric waveguide is listed. Along with calculating the field distribution of any $TE_{pq}$ and $TM_{pq}$ mode in a smooth waveguide, it will also calculate the mode structure of any $HE_{pq}$ and $EH_{pq}$ modes, which propagate in a corrugated waveguide.

The $HE_{11}$ mode is of particular interest as it has a pure Gaussian beam profile.

The program will run on an HP 9816 personal computer and was written in HP Basic.

```
10    ! ***************************************************************
20    ! ***                                                         ***
30    ! ***     PROG. PRODUCES PLOTS OF TEnm AND HEnm MODE STRUCTURES***
40    ! ***        IN A CYLINDRICALLY SYMMETRIC CIRCULAR WAVE GUIDE ***
50    ! ***                AND CORRUGATED WAVE GUIDE                ***
60    ! ***                                                         ***
70    ! ***************************************************************
80    DIM U(20,20),U1(20,20)
90    ! ********** SET SIZE OF GRAPH AND EQNS. TO BE USED ***************
100   ! ** Mode=1 FOR TEom MODES;Mode=2 FOR HEnm MODES;Mode=3 FOR TEnm MODES ***
110   ! ********** MODE =4 FOR TMnm MODES;MODE=5 FOR EHnm MODES **********
120   Gratype=2
130   ! ********** INIT. VARS. AND DRAW GRAPH AXES **********************
140   Init(U(*),U1(*),Gratype)
150   Mode=3
160   ! ********** SET nm MODES AND AT ANGLE Q **************************
170   N=0
180   M=3
190   Q=0
200   ! ********* DEF. FREE SPACE WAVELENGTH Lo AND DIAM. A **************
210   Lo=2.9979250E+8/6.0E+10
220   A=.05
230   ! ********** SET POWER,P, FLOWING IN WAVEGUIDE *********************
240   P=1
250   ! ************ CAL. NORMALIZATION COEF. ***************************
260   Coef=FNCoef(U(*),U1(*),N,M,Lo,A,Mode,P)
270   Coef=(Coef/800)
280   ! ***** DOUBLE INTEGRATION TO TEST NORMALIZATION *****************
290   GOTO 330
300   GCLEAR
310   Simpsons_rule(U(*),U1(*),N,M,Mode,Q,Coef)
320   STOP
330   ! ********** PLOT S OF MODE FIELD **********************************
340   ! **** PLOTING (X,Y) AND REFLECTION (-X,Y) ***********************
350   X=.01
360   Y=FNMode(U(*),U1(*),N,M,X,Mode,Q,Coef,A)
370   MOVE X,Y
380   Oldx=0
390   Oldy=Y
400   FOR T=1 TO 100
410     X=T/100
420     Y=FNMode(U(*),U1(*),N,M,X,Mode,Q,Coef,A)
430   ! PRINT X,Y
450     DRAW X,Y
460     MOVE -Oldx,Oldy
470     DRAW -X,Y
480     MOVE X,Y
490     Oldx=X
500     Oldy=Y
510   NEXT T
520   END
530   SUB Init(U(*),U1(*),Gratype)
540     FOR N=0 TO 3
550       FOR M=1 TO 10
560         READ U(N,M)
570       NEXT M
580     NEXT N
590     DATA 2.40482,5.52007,8.65372,11.79153,14.93091
600     DATA 18.07106,21.21163,24.35247,27.49347,30.63460
610     DATA 3.83171,7.01559,10.17347,13.32369,16.47063
```

```
620       DATA 19.61586,22.76008,25.90367,29.04683,32.18968
630       DATA 5.13562,8.41724,11.61984,14.79595,17.95982
640       DATA 21.11700,24.27011,27.42057,30.56920,33.71652
650       DATA 6.38016,9.76102,13.01520,16.22347,19.40942
660       DATA 22.58273,25.74817,28.90835,32.06485,35.21867
670       FOR N=0 TO 8
680         FOR M=1 TO 10
690           READ U1(N,M)
700         NEXT M
710       NEXT N
720       DATA 3.83171,7.01559,10.17347,13.32369,16.47063
730       DATA 19.61586,22.76008,25.90367,29.04683,32.18968
740       DATA 1.84118,5.33144,8.53632,11.70600,14.86359
750       DATA 18.01553,21.16437,24.31133,27.45705,30.60192
760       DATA 3.05424,6.70613,9.96947,13.17037,16.34752
770       DATA 19.51291,22.67158,25.82604,28.97767,32.12733
780       DATA 4.20119,8.01524,11.34592,14.58585,17.78875
790       DATA 20.97248,24.14490,27.31006,30.47027,33.62695
800       DATA 5.31755,9.28240,12.68191,15.96411,19.19603
810       DATA 22.40103,25.58976,28.76784,31.93854,35.10392
820       DATA 6.41562,10.51986,13.98719,17.31284,20.57551
830       DATA 23.80358,27.01031,30.20285,33.38544,36.56078
840       DATA 7.50127,11.73494,15.26818,18.63744,21.93172
850       DATA 25.18393,28.40978,31.61788,34.81339,37.99964
860       DATA 8.57784,12.93239,16.52937,19.94185,23.26805
870       DATA 26.54503,29.79075,33.01518,36.22438,39.42227
880       DATA 9.64742,14.11552,17.77401,21.22906,24.58720
890       DATA 27.88927,31.15533,34.39663,37.62008,40.83018
900       U1(1,6)=18.0155
910       U1(15,1)=17.0203
920       U1(16,1)=18.0633
930       U1(17,1)=19.1045
940       U1(6,4)=18.6374
950       U(6,4)=20
960       U1(12,2)=18.7451
970       U1(1,7)=21.16437
980       U1(3,6)=20.97248
990       U1(10,4)=23.7607
1000      U1(0,7)=22.76008
1010      U1(4,4)=15.96411
1020      U1(4,5)=19.19603
1030      U1(6,2)=11.73494
1040      U1(6,3)=15.26818
1050      U1(6,1)=7.50127
1060      U1(9,3)=19.0046
1070      GINIT
1080      GRAPHICS ON
1090    ! **** DRAWS GRAPH AXES CORRESPONDING TO VAR. GRATYPE **********************
1100      Graph(Gratype)
1110    SUBEND
1120    ! ************** FN. RETURNS Jn(X) N=ORDER,MUST BE INTEGER *****************
1130    DEF FNJn(N,X)
1140      REAL R
1150      J=0
1160      Jold=0
1170      R=0
1180      REPEAT
1190        Jold=J
1200        J=J+(-X*X/4)^R/(FNFact(R)*FNFact(R+N))
1210        R=R+1
```

```
1220      UNTIL ABS(J-Jold)<.00001
1230      RETURN (.5*X)^N*J
1240    FNEND
1250    ! ********** FN. RETURNS X! ***************************************************
1260    DEF FNFact(X)
1270      REAL Y,Z
1280      Z=1
1290      FOR Y=1 TO X
1300        Z=Z*Y
1310      NEXT Y
1320      RETURN Z
1330    FNEND
1340    ! ********** FN EVALUATES S (R,THEETA) ***************************************
1350    ! ********** Mode=1:FOR TEom,Mode=2:FOR HEnm,Mode=3:FOR TEnm *************
1360    ! ************* MODE=4:FOR TMnm,MODE=5:FOR EHnm ****************************
1370    DEF FNMode(U(*),U1(*),N,M,X,Mode,Q,Coef,A)
1380      SELECT Mode
1390      CASE 1
1400        RETURN (FNJn(1,X*U(0,M)))^2
1410      CASE 2
1420        Temp=FNJn(N-1,X*U(N-1,M))
1430        Eq=(Temp*COS(Q))^2
1440        Er=(Temp*SIN(Q))^2
1450        RETURN (Eq+Er)*Coef
1460      CASE 3
1470        Eq=(FNJnd(N,X*U1(N,M))*COS(N*Q))^2
1480        ! *************** N.B. X=R/A ***********************************
1490        Er=((FNJn(N,X*U1(N,M))*SIN(N*Q))*N/(X*U1(N,M)))^2
1500      ! PRINT Eq,Er
1510        RETURN Coef*(Eq+Er)
1520      CASE 4
1530        Er=(FNJnd(N,X*U(N,M))*COS(N*Q))^2
1540        Eq=((FNJn(N,X*U(N,M))*SIN(N*Q))*N/(X*U(N,M)))^2
1550        RETURN Coef*(Er+Eq)
1560      CASE 5
1570        Temp=FNJn(N+1,U(N+1,M)*X)^2
1580        RETURN Coef*Temp
1590      END SELECT
1600    FNEND
1610    ! *************** SUB DRAWS AXES ***************************************
1620    SUB Graph(Gratype)
1630      GRAPHICS ON
1640      GINIT
1650      SELECT Gratype
1660      CASE 1
1670        WINDOW -1.2,1.2,-.4,2
1680        AXES .1,.2
1690        FOR X=2 TO 10 STEP 2
1700          MOVE X/10-.1,-.15
1710          LABEL X/10
1720          MOVE -X/10-.08,-.15
1730          LABEL-X/10
1740        NEXT X
1750        FOR Y=2 TO 20 STEP 2
1760          MOVE -.3,Y/10-.1
1770          LABEL Y/10
1780        NEXT Y
1790        MOVE 1,-.26
1800        LABEL "R/Ro"
1810        MOVE -.5,1.9
```

```
1820      LABEL "E^2"
1830    CASE 2
1840      WINDOW -1.2,1.2,-.8,4
1850      AXES .1,.5
1860      FOR X=2 TO 10 STEP 2
1870        MOVE X/10-.1,-.3
1880        LABEL X/10
1890        MOVE -X/10-.08,-.3
1900        LABEL-X/10
1910      NEXT X
1920      FOR Y=5 TO 40 STEP 5
1930        MOVE -.25,Y/10-.2
1940        LABEL Y/10
1950      NEXT Y
1960        MOVE 1,-.5
1970        LABEL "R/Ro"
1980        MOVE -.45,3.75
1990        LABEL "'S'"
2000    END SELECT
2010  SUBEND
2020  ! ************** FN RETURNS Jn'(X) N=ORDER,MUST BE INTEGER ******************
2030  DEF FNJnd(N,X)
2040    REAL R
2050    J=0
2060    Jold=0
2070    R=0
2080    REPEAT
2090      Jold=J
2100      J=J+(-1)^R*(N+2*R)*X^(N+2*R-1)/(2^(N+2*R)*FNFact(R)*FNFact(N+R))
2110      R=R+1
2120    UNTIL ABS(J-Jold)<.00001 AND R>1
2130    RETURN J
2140  FNEND
2150  ! *** SUBRUTINE PERFORMS DOUBLE INTEGRAL TO TEST NORMALIZATION ***********
2160  SUB Simpsons_rule(U(*),U1(*),N1,M,Mode,Q,Coef)
2170  ! ******** FIRST INTEGRATION IS ALONG R SECOND Q ***************************
2180    RAD
2190    N=10
2200    A1=.0001
2210    B=1
2220    H=(B-A1)/N
2230    X=B
2240    Yn=FNSimpsons_rule2(U(*),U1(*),N1,M,X,Mode,Coef)
2250    X=A1
2260    Yo=FNSimpsons_rule2(U(*),U1(*),N1,M,X,Mode,Coef)
2270    Igl=0
2280    Cnt=1
2290    FOR T=0 TO N-2
2300      X=X+H
2310      PRINT X
2320      Y=FNSimpsons_rule2(U(*),U1(*),N1,M,X,Mode,Coef)
2330      IF Cnt=1 THEN
2340        Cnt=Cnt-1
2350        Igl=Igl+4*Y
2360      ELSE
2370        Cnt=Cnt+1
2380        Igl=Igl+2*Y
2390      END IF
2400    NEXT T
2410    Integral=H/3*(Igl+Yo+Yn)
```

```
2420    PRINT Integral
2430  SUBEND
2440  DEF FNSimpsons_rule2(U(*),U1(*),N1,M,X,Mode,Coef)
2450    RAD
2460    N=20
2470    A1=0
2480    B=PI/2
2490    H=(B-A1)/N
2500    Q=B
2510    Yn=FNMode(U(*),U1(*),N1,M,X,Mode,Q,Coef,A)*X
2520    Q=A1
2530    Yo=FNMode(U(*),U1(*),N1,M,X,Mode,Q,Coef,A)*X
2540    Igl=0
2550    Cnt=1
2560    FOR T=0 TO N-2
2570      Q=Q+H
2580      PRINT Q
2590      Y=FNMode(U(*),U1(*),N1,M,X,Mode,Q,Coef,A)*X
2600      PRINT N1,M,X,Q
2610      IF Cnt=1 THEN
2620        Cnt=Cnt-1
2630        Igl=Igl+4*Y
2640      ELSE
2650        Cnt=Cnt+1
2660        Igl=Igl+2*Y
2670      END IF
2680    NEXT T
2690    Integral=H/3*(Igl+Yo+Yn)
2700    RETURN Integral*4
2710  FNEND
2720  DEF FNCoef(U(*),U1(*),N,M,Lo,A,Mode,P)
2730  ! ********** EVAL.NORMALIZATION COEF. **********************************
2740    IF Mode=3 AND N<>0 THEN
2750      Coef=4*P/(A*A*PI*FNJn(N,U1(N,M))^2*(1-(N*N)/(U1(N,M)*U1(N,M))))
2760    ELSE
2770      IF Mode=3 AND N=0 THEN
2780        Coef=2*P/(A*A*PI*FNJn(N,U1(N,M))^2)
2790      END IF
2800    END IF
2810    IF Mode=4 AND N=0 THEN Two=2
2820    IF Mode=4 AND N<>0 THEN Two=4
2830    IF Mode=4 THEN
2840      Coef=Two*P/(A*A*PI*FNJnd(N,U(N,M))^2)
2850    END IF
2860    IF Mode=2 THEN Coef=2*P/(A*A*PI*FNJnd(N-1,U(N-1,M))^2)
2870    IF Mode=5 THEN Coef=2*P/(A*A*PI*FNJnd(N+1,U(N+1,M))^2)
2880    RETURN Coef
2890  FNEND
```

## APPENDIX 4.

The following program listing will produce the far-field radiation pattern plots of the $TE_{pq}$, $TM_{pq}$, $HE_{pq}$ and the $EH_{pq}$ modes.

The program was written in HP Basic and will run on an HP 9816 personal computer.

```
10    ! ***************************************************************
20    ! ***                                                         ***
30    ! ***       PROG. PLOTS THE FAR FIELD RADIATION PATTERNS OF THE ***
40    ! ***          TEnm,TMnm,HEnm,EHnm MODES FROM AN OPEN ENDED   ***
50    ! ***                      CIRCULAR WAVEGUIDE                 ***
60    ! ***                                                         ***
70    ! ***************************************************************
80    DEG
90    ! **** INITIALISE ALL VARIABLES AND ARRAYS ************************
100   DIM U(10,10),U1(10,10),Ymax(8,10,10)
110   Gratype=2
120   Init(U(*),U1(*),Gratype,Ymax(*))
130   ! **** Mode,N,M DECIDES WHICH MODES TO CALCULATE¡THE FAR FIELD PATTERN ***
140   ! **** Mode=1 FOR TMnm MODES , Mode=2 FOR TEnm MODES ********************
150   ! **** DIFF.METHOD 1 Mode=3 FOR HEnm MODES Mode=4 FOR EHnm MODES *********
160   ! **** DIFF.METHOD 2 Mode=5 FOR HEnm MODES Mode=6 FOR EHnm MODES *********
170   ! **** F.T. METHOD 3 Mode=7 FOR HEnm MODES                    *********
180   Mode=2
190   N=1
200   M=3
210   ! ****** PHYSICAL PARAMETERS OF WAVEGUIDE AND E/M WAVES ****************
220   R=.58
230   Thy=90
240   Lo=2.9979250E+8/6.0E+10
250   A=.0825
260   Ka=18.62
270   K=Ka/A
280   Bnmk=SQR(1-(U(N,M)/Ka)^2)
290   Gamma=.05
300   W=2*PI*6.0E+10
310   ! ********* POWER P IN MODE ***************************************
320   P=1
330   ! *** DOUBLE INTEGRATION TO EVALUATE NORMALIZATION COEF. ************
340   GOTO 380
350   GCLEAR
360   Simpsons_rule(U(*),U1(*),N,M,Mode,R,Coef)
370   STOP
380   ! ********** PLOT S OF MODE FIELD *************************************
390   ! **** PLOTING (X,Y) AND ITS REFLECTION (-X,Y) ************************
400   X=.000000001
410   Y=FNMode(U(*),U1(*),N,M,X,Mode,R,Thy,Coef,A,Ka,K,Gamma,Bnmk,W)
420   PRINT X,Y
430   Y=10*LGT(Y/Ymax(Mode,N,M))
440   IF Y<-40 THEN Y=-40
450   MOVE X,Y
460   Oldx=.000000001
470   Oldy=Y
480   FOR X=1 TO 90
490     Y=FNMode(U(*),U1(*),N,M,X,Mode,R,Thy,Coef,A,Ka,K,Gamma,Bnmk,W)
500     PRINT X,Y
510     Plot(X,Y,Oldx,Oldy,Gratype,Ymax(*),Mode,N,M)
520   NEXT X
530   END
540   SUB Init(U(*),U1(*),Gratype,Ymax(*))
550     FOR N=0 TO 3
560       FOR M=1 TO 10
570         READ U(N,M)
580       NEXT M
590     NEXT N
600     DATA 2.40482,5.52007,8.65372,11.79153,14.93091
```

```
610     DATA 18.07106,21.21163,24.35247,27.49347,30.63460
620     DATA 3.83171,7.01559,10.17347,13.32369,16.47063
630     DATA 19.61586,22.76008,25.90367,29.04683,32.18968
640     DATA 5.13562,8.41724,11.61984,14.79595,17.95982
650     DATA 21.11700,24.27011,27.42057,30.56920,33.71652
660     DATA 6.38016,9.76102,13.01520,16.22347,19.40942
670     DATA 22.58273,25.74817,28.90835,32.06485,35.21867
680     FOR N=0 TO 3
690       FOR M=1 TO 10
700         READ U1(N,M)
710       NEXT M
720     NEXT N
730     DATA 3.83171,7.01559,10.17347,13.32369,16.47063
740     DATA 19.61586,22.76008,25.90367,29.04683,32.18968
750     DATA 1.84118,5.33144,8.53632,11.70600,14.86359
760     DATA 18.01553,21.16437,24.31133,27.45705,30.60192
770     DATA 3.05424,6.70613,9.96947,13.17037,16.34752
780     DATA 19.51291,22.67158,25.82604,28.97767,32.12733
790     DATA 4.20119,8.01524,11.34592,14.58585,17.78875
800     DATA 20.97248,24.14490,27.31006,30.47027,33.62695
810     U1(0,5)=16.4706
820     U1(7,3)=16.5294
830     U1(15,1)=17.0203
840     U1(5,4)=17.3128
850     U1(11,2)=17.6003
860     U1(8,3)=17.7740
870     U1(3,5)=17.7887
880     U1(1,6)=18.0155
890     U1(16,1)=18.0633
900     U1(6,4)=18.6374
910     U1(12,2)=18.7451
920     U1(9,3)=19.0046
930     U1(17,1)=19.1045
940     U1(4,5)=19.1960
950     U1(2,6)=19.5129
960     U1(0,6)=19.6159
970     U1(13,2)=19.8832
980     U1(7,4)=19.9419
990     U1(18,1)=20.1441
1000    U1(10,3)=20.2230
1010    U1(5,5)=20.5755
1020    U1(3,6)=20.9725
1030    U1(14,2)=21.0154
1040    U1(1,7)=21.1644
1050    U1(19,1)=21.1823
1060    U1(8,4)=21.2291
1070    U1(11,3)=21.4309
1080    U1(6,5)=21.9317
1090    U1(15,2)=22.1422
1100    ! *** SET Ymax(Mode,N,M) FOR dB SCALE 10*LOG(Y/Ymax) **********
1110    Ymax(1,0,1)=153866
1120    Ymax(1,0,2)=139582
1130    Ymax(2,0,2)=8.E+24
1140    Ymax(2,1,0)=1.85888E+23
1150    Ymax(2,1,2)=8.E+24
1160    Ymax(2,0,6)=8.E+24
1170    Ymax(2,1,3)=7.E+24
1180    Ymax(3,1,1)=.0755165
1190    Ymax(3,1,2)=.00116854
1200    Ymax(3,1,3)=.0001585062
```

```
1210      Ymax(3,1,4)=4.0124879E-5
1220      Ymax(3,3,1)=.0008514011
1230      Ymax(4,1,1)=.00266109
1240      Ymax(4,1,2)=.000338572
1250      Ymax(4,1,3)=8.32864E-5
1260      Ymax(4,1,4)=2.609801E-5
1270      Ymax(5,1,1)=.03573377
1280      Ymax(5,1,2)=.00282756
1290      Ymax(5,1,3)=.00088503
1300      Ymax(6,1,1)=.00568824
1310      Ymax(6,1,2)=.001804055
1320      Ymax(7,1,1)=10131.34
1330      Ymax(7,1,2)=826.0244
1340      GINIT
1350      GRAPHICS ON
1360      ! ********* DRAW GRAPH ACCORDING TO Gratype ********************************
1370      Graph(Gratype)
1380    SUBEND
1390    ! ************* FN. RETURNS Jn(X) N=ORDER,MUST BE INTEGER ******************
1400    DEF FNJn(N,X)
1410      REAL R
1420      J=0
1430      Jold=0
1440      R=0
1450      REPEAT
1460        Jold=J
1470        J=J+(-X*X/4)^R/(FNFact(R)*FNFact(R+N))
1480        R=R+1
1490      UNTIL ABS(J-Jold)<.00001
1500      RETURN (.5*X)^N*J
1510    FNEND
1520    ! ************ FN. RETURNS X! ***************************************************
1530    DEF FNFact(X)
1540      REAL Y,Z
1550      Z=1
1560      FOR Y=1 TO X
1570        Z=Z*Y
1580      NEXT Y
1590      RETURN Z
1600    FNEND
1610    ! ********** FN EVALUATES Enm(X,Y) ***************************************
1620    DEF FNMode(U(*),U1(*),N,M,Q,Mode,R,Thy,Coef,A,Ka,K,Gamma,Bnmk,W)
1630    ! *** Mode=1 TMnm,Mode=2 TEnm,Mode=3 HEnm,Mode=4 EHnm,Mode=5 HEnm ********
1640    ! ************** Mode=6 EHnm, Mode=7 HEnm ***********************************
1650      SELECT Mode
1660      CASE 1
1670        Fq=(U(N,M))/A*(Bnmk+COS(Q)+Gamma*(Bnmk-COS(Q)))*FNJn(N,Ka*SIN(Q))*FNJn
d(N,U(N,M))/(SIN(Q)*(1-(U(N,M)/(Ka*SIN(Q)))^2))
1680        Eq=(Ka*Fq*COS(N*Thy)*SIN(K*R)/(2*R))^2
1690        RETURN Eq
1700      CASE 2
1710        Fq=(1+Bnmk*COS(Q)+Gamma*(1-Bnmk*COS(Q)))*FNJn(N,U1(N,M))*FNJn(N,Ka*SIN
(Q))/SIN(Q)
1720        Sfq=(Bnmk+COS(Q)-Gamma*(Bnmk-COS(Q)))*FNJn(N,U1(N,M))*FNJnd(N,Ka*SIN(Q
))/(1-(Ka*SIN(Q)/U1(N,M))^2)
1730        Eq=N*W/(2*R)*Fq*SIN(N*Thy)*SIN(K*R)
1740        Ethy=Ka*W/(2*R)*Sfq*COS(N*Thy)*SIN(K*R)
1750        RETURN Eq^2+Ethy^2
1760      CASE 3
1770      ! ************************ METHOD 1 DIFF.*********************************
```

```
1780        Ui=Ka*SIN(Q)
1790        Lq=FNJn(N,Ui)*FNJn(N,U(N-1,M))/(Ui*U(N-1,M))
1800        Qq=(U(N-1,M)*FNJnd(N,Ui)*FNJn(N,U(N-1,M))-Ui*FNJn(N,Ui)*FNJnd(N,U(N-1,
M)))/(U(N-1,M)^2-Ui^2)
1810        E1=Ka^2*A/(2*U(N-1,M)*R)*SIN(K*R)*(1+COS(Q))*(Lq+Qq)
1820        RETURN E1^2
1830      CASE 4
1840        Ui=Ka*SIN(Q)
1850        Lq=FNJn(N,Ui)*FNJn(N,U(N+1,M))/(Ui*U(N+1,M))
1860        Qq=(U(N+1,M)*FNJnd(N,Ui)*FNJn(N,U(N+1,M))-Ui*FNJn(N,Ui)*FNJnd(N,U(N+1,
M)))/(U(N+1,M)^2-Ui^2)
1870        E1=Ka^2*A/(2*U(N+1,M)*R)*SIN(K*R)*(1+COS(Q))*(Qq-Lq)
1880        RETURN 2*E1^2
1890      CASE =5
1900      ! ************************** METHOD 2 DIFF ********************************
1910        Ui=Ka*SIN(Q)
1920        Wq=(Ui*FNJn(N-1,U(N-1,M))*FNJn(N,Ui)-U(N-1,M)*FNJn(N-1,Ui)*FNJn(N,U(N-
1,M)))/(Ui^2-U(N-1,M)^2)
1930        Ex=COS(Q)*SIN(K*R)*Wq
1940        RETURN Ex^2
1950      CASE 6
1960        Ui=Ka*SIN(Q)
1970        Wq=(Ui*FNJn(N+1,U(N+1,M))*FNJn(N,Ui)-U(N+1,M)*FNJn(N+1,Ui)*FNJn(N,U(N+
1,M)))/(Ui^2-U(N+1,M)^2)
1980        Ex=COS(Q)*SIN(K*R)*Wq
1990        RETURN 2*Ex^2
2000      CASE 7
2010      ! ************************** METHOD 3 F.T. ********************************
2020        Ui=Ka*SIN(Q)
2030        Lq=FNJn(N,Ui)*FNJn(N,U(N-1,M))/(Ui*U(N-1,M))
2040        Qq=(U(N-1,M)*FNJnd(N,Ui)*FNJn(N,U(N-1,M))-Ui*FNJn(N,Ui)*FNJnd(N,U(N-1,
M)))/(U(N-1,M)^2-Ui^2)
2050        Eq=SIN(K*R)*COS(N*Thy)*(Lq*(K+COS(Q))+Qq*(K*COS(Q)+1))
2060        RETURN 2*Eq^2
2070      END SELECT
2080    FNEND
2090    ! *************** SUB DRAWS AXES ***************************************
2100    SUB Graph(Gratype)
2110      GRAPHICS ON
2120      GINIT
2130      SELECT Gratype
2140      CASE 1
2150        WINDOW -90,90,0,150000
2160        AXES 10,10000
2170        FOR X=2 TO 10 STEP 2
2180          MOVE X/10-.1,-.15
2190          LABEL X/10
2200          MOVE -X/10-.08,-.15
2210          LABEL-X/10
2220        NEXT X
2230        FOR Y=2 TO 20 STEP 2
2240          MOVE -.3,Y/10-.1
2250          LABEL Y/10
2260        NEXT Y
2270        MOVE 1,-.26
2280          LABEL "R/Ro"
2290          MOVE -.5,1.9
2300          LABEL "E^2"
2310      CASE 2
2320        WINDOW -90,90,-47,0
```

```
2330        AXES 10,5,0,-40
2340        FOR X=10 TO 90 STEP 20
2350          MOVE X-12,-44
2360          LABEL X
2370          MOVE -X-4,-44
2380          LABEL-X
2390        NEXT X
2400        FOR Y=0 TO -35 STEP -5
2410          MOVE -15,Y-2
2420          LABEL Y
2430        NEXT Y
2440        MOVE 70,-46
2450        LABEL "O/DEG"
2460          MOVE -30,-2
2470          LABEL "dB"
2480      END SELECT
2490    SUBEND
2500    ! ************** FN RETURNS Jn'(X) N=ORDER,MUST BE INTEGER ******************
2510    DEF FNJnd(N,X)
2520      REAL R
2530      J=0
2540      Jold=0
2550      R=0.
2560      REPEAT
2570        Jold=J
2580        J=J+(-1)^R*(N+2*R)*X^(N+2*R-1)/(2^(N+2*R)*FNFact(R)*FNFact(N+R))
2590        R=R+1
2600      UNTIL ABS(J-Jold)<.00001 AND R>1
2610      RETURN J
2620    FNEND
2630    SUB Simpsons_rule(U(*),U1(*),N1,M,Mode,Q,Coef)
2640      RAD
2650      N=10
2660      A1=.0001
2670      B=1
2680      H=(B-A1)/N
2690      X=B
2700      Yn=FNSimpsons_rule2(U(*),U1(*),N1,M,X,Mode,Coef)
2710      X=A1
2720      Yo=FNSimpsons_rule2(U(*),U1(*),N1,M,X,Mode,Coef)
2730      Igl=0
2740      Cnt=1
2750      FOR T=0 TO N-2
2760        X=X+H
2770        PRINT X
2780        Y=FNSimpsons_rule2(U(*),U1(*),N1,M,X,Mode,Coef)
2790        IF Cnt=1 THEN
2800          Cnt=Cnt-1
2810          Igl=Igl+4*Y
2820        ELSE
2830          Cnt=Cnt+1
2840          Igl=Igl+2*Y
2850        END IF
2860      NEXT T
2870      Integral=H/3*(Igl+Yo+Yn)
2880      PRINT Integral
2890    SUBEND
2900    DEF FNSimpsons_rule2(U(*),U1(*),N1,M,X,Mode,Coef)
2910      RAD
2920      N=10
```

```
2930      A1=0
2940      B=PI/2
2950      H=(B-A1)/N
2960      Q=B
2970      Yn=FNMode(U(*),U1(*),N1,M,X,Mode,Q,Coef)*X
2980      Q=A1
2990      Yo=FNMode(U(*),U1(*),N1,M,X,Mode,Q,Coef)*X
3000      Igl=0
3010      Cnt=1
3020      FOR T=0 TO N-2
3030        Q=Q+H
3040        PRINT Q
3050        Y=FNMode(U(*),U1(*),N1,M,X,Mode,Q,Coef)*X
3060        PRINT N1,M,X,Q
3070        IF Cnt=1 THEN
3080          Cnt=Cnt-1
3090          Igl=Igl+4*Y
3100        ELSE
3110          Cnt=Cnt+1
3120          Igl=Igl+2*Y
3130        END IF
3140      NEXT T
3150      Integral=H/3*(Igl+Yo+Yn)
3160      RETURN Integral*4
3170    FNEND
3180    SUB Plot(X,Y,Oldx,Oldy,Gratype,Ymax(*),Mode,N,M)
3190      SELECT Gratype
3200      CASE 1
3210        DRAW X,Y
3220        PRINT X,Y
3230        MOVE -Oldx,Oldy
3240        DRAW -X,Y
3250        MOVE X,Y
3260        Oldx=X
3270        Oldy=Y
3280      CASE 2
3290        Y=10*LGT(Y/Ymax(Mode,N,M))
3300        IF Y<-40 THEN Y=-40
3310        DRAW X,Y
3320        MOVE -Oldx,Oldy
3330        DRAW -X,Y
3340        MOVE X,Y
3350        Oldx=X
3360        Oldy=Y
3370      END SELECT
3380    SUBEND
```

## APPENDIX 5.

The following experimental methods were tested in an attempt to measure, from a single pulse, the radiation intensity distribution across the output window

1) Liquid Crystal Sheet.

A heat sensitive liquid crystal sheet was calibrated for minimum energy required to detect a colour change in the crystal. The mode pattern of the maser will result in localised heating, producing a visible image of the mode pattern. This image will not be permanent; through heat dissipation, the temperature of the crystal will quickly reach a uniform distribution.

A sheet of liquid crystal approximately 10x30cm was tested using the B.W.O. The mm-wave output was shone on to the liquid crystal. An energy density of $\simeq 25 mJ/cm^2$ incident on the liquid crystal sheet was required before a colour change became evident.

2) Infra Red Camera.

In this instance the camera was focused on a film of mm-wave absorbing paint mounted on cling wrap polythene. Again a radiation pattern falling on the film will cause differential heating, corresponding to the radiation intensity distribution. The I/R camera will then produce a thermal image of this heat distribution on the monitor.

Again this system was calibrated using the B.W.O. and resulted in an image being visible on the monitor with an incident energy density of $\geq 25 mJ/cm^2$.

## REFERENCES.

1) J.L. Hirshfield, V.L. Granatstein. "The Electron Cyclotron Maser-An Historical Survey."
IEEE Trans. On Microwave Th. and Tech. Vol 25 No 6, June 1977.

2) J.L. Hirshfield. "Gyrotrons."
Infrared and Millimeter Waves. Vol 1, 1979.

3) R.S. Symons, H.R. Jory. "Cyclotron Resonance Devices."
Adv. in Electronics and Electron Phys. Vol 55, 1981.

4) R.Q. Twiss. "Radiation Transfer and the Possibility of Negative Absorption in Radio Astronomy."
Aust. J. Phys. Vol 11, 1958.

5) J. Schneider. "Stimulated Emission of Radiation by Relativistic Electrons in a Magnetic Field."
Physical Review Letters, Vol 2 No 12, June 1959.

6) A.V. Gaponov. "Addendum."
IZV. VUZ. Radiofizika, Vol 2, 1959.

7) R.H. Pantell. "Backward Wave Oscillations in an Unloaded Waveguide."
Proc. IRE. Vol 47, 1959.

8) K.K. Chow, R.H. Pantell. "The Cyclotron Resonance Backward Wave Oscillator."
Proc. IEEE, Vol 48, Nov 1960.

9) I.B. Bott. "Tuneable Source of Millimetre and Submillimetre Radiation."
Proc. IEEE, Vol 52, March 1964.

10) I.B. Bott. "A Powerful Source of Millimetre Radiation."
Phys. Letts. Vol 14 No 4. 1965.

11) J. Feinstein. "Research on Electronic Interaction with the Fields of Mirror Resonators."
Proc. Int. Cong. Microwave Tubes, 5™, 1964.

12) K.E. Kreischer, R.J. Temkin. "High Frequency Gyrotrons and their Application to Tokamak Plasma Heating."
Infrared and Millimeter Waves, Vol 7, 1983.

13) V.L. Granatstein, et al. "Gigawatt Microwave Emission from an Intense Electron Beam."
Plasma Physics. Vol 17, 1965.

14) N.S. Ginzburg, et al. "Experimental Investigation of a High Current Relativistic Cyclotron Maser."
Soviet Physics, Tech. Phys. Vol 24, 1979.

15) H.E. Frank, et al. "An Electron Cyclotron Maser for Nano-Second Megawatt Pulses.
Journal of Physics D: Applied Physics. Vol 15, 1982.

16) S.N. Voronkov, et al. "Stimulated Cyclotron Radiation of Millimetre Wavelengths from a High Power Relativistic Beam."
Soviet Physics: Tech. Phys. Vol 27, 1982.

17) S.H. Gold, et al. "High Voltage Ka-Band Gyrotron Experiment."
IEEE Trans. on Plasma Science, Vol 13 No 6, 1985.

18) H. Jory et al. "Gyrotron Oscillators for Fusion Heating."
Int. Symp. on Heating in Toroidal Plasmas (Grenoble 1982).

19) A.V. Gaponov, el al. "Powerful mm-Wave Gyrotrons."
Int. J. Electron. Vol 51, 1981.

20) A.A. Andronov, et al. "The Gyrotron High Power Source of Millimetre and Sub-Millimetre Waves."
Infrared Phys. Vol 18, 1978.

21) K.E. Kreischer and R.J. Temkin. "Single-Mode Operation of a High-Power, Step Tunable Gyrotron."
Physical Review Letters. Vol 59 No 5, 1987.

22) G.F. Brand. "Tunable Millimeter-Wave Gyrotrons."
Int. J. of Infrared and Millimeter Waves, vol 3 No 5, 1982.

23) A.C. England. "Electron Cyclotron Heating Experiments in Tokamaks and Stellarators."
IEEE Trans. on Plasma Science, Vol 12 No 2, 1984.

24) V.L. Granatstein, et al. "An Electron Cyclotron Maser Based on an Intense Relativistic Electron Beam."
J. Appl. Phys. Vol 46 No 5, 1975.

25) M.J. Smith. "The Gyrotron."
Electronics and Power, Vol 27 No 5, 1981.

26) Y.Y. Lau. "A Unified Theory of the Diocotron, Cyclotron Maser and Negative Mass Instabilities."
IEEE Trans. on Elect. Dev. Vol 31 No 3, 1984.

27) P.A. Lindsay. "Gyrotrons (Electron Cyclotron Masers): Different Mathematical models."
IEEE J. Quantum Electronics, Vol 17 No 8, 1981.

28) A.A. Sokolov, I.M. Ternov. "Radiation fron Relativistic Electrons."
New York: American Inst. of Phys. Translation Series, 1986.

29) E. Ott, W.M. Manheimer. "Theory of Microwave Emission by Velocity Space Instabilities of an Intense Relativistic Electron Beam."
IEEE Trans. on Plasma Sci. Vol PS-3 No 1, 1975.

30) Y.Y. Lau. "Simple Macroscopic Theory of Cyclotron Maser Instabilities."
IEEE Trans. on Elect. Dev. Vol 29 No 2, 1982.

31) P. Sprangle, A.T. Drobot. "The Linear and Self Consistent Nonlinear Theory of the Electron Cyclotron Maser Instability."
IEEE Trans. on Microwave Th. and Tech. Vol 25 No 6, 1977.

32) A.D.R. Phelps, T. Garvey, A.S. Hasaani. "Pulsed Electron Cyclotron Maser Experiments.
Int. J. of Electronics, Vol 57 No 6, 1984.

33) P.S. Bansal. Ph.D. Thesis Strathclyde University, 1986.

34) A.Z. Matuug. Ph.D. Thesis Strathclyde University, 1987.

35) A.D.R. Phelps, et al. "Cold Cathode 75-100GHz Gyrotron Experiments."
Int. J. Electronics. Vol 64, 1988.

36) F.W. Sears, M.W. Zemanski, H.D. Young. "University Physics."
6th Ed. Addison Wesley Publishing Co.

37) D.B. Montgomery. "The Generation of High Magnetic Fields."
Reports on Progress in physics, Vol XXV1, 1963.

38) S. Foner, H.H. Kolm. "Coils for the Production of High Magnetic Fields."
The Rev. of Scientific Instruments, Vol 28 No 10, 1957.

39) A.W. Fliflet. "Linear and Non-Linear Theory of a Doppler Shifted Cyclotron Resonance Maser, Based on TE and TM Waveguide Modes."
Int. J. Electronics, Vol 61 No 6, 1986.

40) R.A. Waldron. "Theory of Guided Electromagnetic Waves."
London:Van Nostrad Reinhold Co. 1969.

41) B. Arfin et al. "A High Power Gyrotron Operating in the $TE_{041}$ Mode."
IEEE Trans. on Elect. Dev. Vol 29 No 12, 1982.

42) R.A. Waldron. "The Theory of Reflections in a Tapered Waveguide."
Radio Electron Engineer, Vol 33, 1966.

43) A. Yariv. "Optical Electonics."
H.R.W. : New York, 1985.

44) H. Saito, et al. "Analytical Treatment of Linearised Self Consistent Theory of a Gyromonotron with Non-Fixed Structure."
Int. J. Electronics. Vol 61 No 6, 1986.

45) A.F. Harvey. "Microwave Engineering."
Academic Press : New York, 1963.

46) A.J. Toepfer. "Intense Particle Beams."
Proc. of the 20th Scottish Universities Summer School on "Laser Plasma Interactions."
Ed. R.A. Cairns, J.J. Sanderson, 1977.

47) F.B.A. Frungel. "High Speed Pulse Technology."
Vol 1, Academic Press.

48) T. Garvey. Ph.D. Thesis, Strathclyde University, 1982.

49) E. Kuffel, W.S.Zaengl. "High Voltage Engineering, Fundamentals."
Pergamon Press.

50) Ed. R.H. Huddlestone, S.L. Leonard. "Plasma Diagnostic Techniques."
Academic Press, 1965.

51) J.F. Ramsey. "Tubular beams from radiating apertures."
Advances in microwaves, Vol 3, 1968.

52) S.Y. Liao. "Microwave Circuit Analysis and amplifier Design."
Prentice Hall.

53) Z.X. Zhang, M. Thumm, R. Wilhelm. "Far Field Radiation Patterns from Oversized Circular Waveguides and Identification of Multi-Mode Outputs of Gyrotrons."
Institut Fur Plasmaforschung Der Universitat Stuttgart. IPF-83-5.

54) K. Felch, L. Vallier. "Calibration of a Millimetre Microwave Grating Spectrometer: 55-350 GHz."
Laboratoire P.M.I. Report #1052, August 1980.
Ecole Polytechnique, 91128 Palaiseau, Cedex, France.

55) M. Born, E. Wolf. "Principles of Optics."
3rd Ed. Pergamon press, 1964.

56) J. Strong "Consepts of Classical Optics."
W.H. Freeman and Co. 1958.

57) A.H. Hasaani. Ph.D. Thesis Strathclyde University, 1986.

58) H.S. Carslaw, J.C. Jaeger. "Conduction of Heat in Solids."
2nd Ed. Oxford University Press, 1959.

# PUBLICATIONS.

The Institute of Physics

PLASMA PHYSICS GROUP

THIRTEENTH ANNUAL CONFERENCE ON PLASMA PHYSICS

DEPARTMENT OF ENGINEERING SCIENCE
UNIVERSITY OF OXFORD

2–4 JULY 1986



# 100 GHz ELECTRON CYCLOTRON MASER

A.Z. Maatug, S.N. Spark and A.D.R. Phelps

Department of Physics, University of Strathclyde,
GLASGOW G4 ONG, Scotland.

Previously experiments were reported[1] which measured the output characteristics of a pulsed electron cyclotron maser operating in the 26.5-40 GHz band. For several applications including plasma heating and plasma diagnostics an efficient, tunable, high power source is needed in the range 60 GHz to 200 GHz. For an electron cyclotron maser operating at the fundamental electron cyclotron resonance this implies a magnetic field of magnitude 2T to 7T approximately.

By applying a magnetic field which can be varied up to 4T, to a mildly relativistic annular electron beam[2], which passes through a cylindrical cavity, an electron cyclotron maser has been constructed and observed to oscillate at frequencies up to approximately 100 GHz. A higher frequency grating has been inserted in the blazed grating spectrometer constructed and reported previously[1], which has enabled frequency measurements to be made in the 75-110 GHz band.

The remaining challenges to be overcome in progressing up to 200 GHz are discussed.

References

(1) P.S. Bansal, A.Z. Maatug and A.D.R. Phelps, XIIth Annual IOP Conf. on Plasma Physics, Glasgow 1985.

(2) A.D.R. Phelps, T. Garvey and A.S. Hasaani, Int. J. Electron, 57, 1141-1150, 1984.

FOURTEENTH ANNUAL CONFERENCE ON

# PLASMA PHYSICS

DEPARTMENT OF PHYSICS

UNIVERSITY OF ST ANDREWS

1 JULY-3 JULY 1987

CONFERENCE HANDBOOK

## PULSED 200GHz ELECTRON CYCLOTRON MASER EXPERIMENTS

S N Spark and A D R Phelps

Department of Physics and Applied Physics
University of Strathclyde,
Glasgow G4 ONG, Scotland

The capability of electron cyclotron masers of producing high-power millimetre waves, without the need for intra-cavity structures, becomes particularly advantageous as the frequency is increased. Conventional vacuum and solid state electronic devices appear to be incapable of producing many kilowatts of power at frequencies greater than 100GHz. To provide electron cyclotron resonance heating of magnetically confined plasmas, with an applied magnetic field in the 3T to 4T range, gyrotrons working at approximately 100GHz are needed for heating at the fundamental. For heating at twice the electron cyclotron frequency radiation at approximately 200GHz is needed. The present lack of available gyrotrons working above 140GHz stimulated the work in the 200GHz region reported here.

A series of electron cyclotron masers has been constructed and measurements of their outputs in the 8-12GHz, 26.5-40GHz and 75-110GHz frequency bands have been reported [1-3]. For the new experiment (Mk VI) reported here the interaction region has been designed for operation at frequencies near 200GHz. A stronger magnetic field coil has been designed and constructed. This coil has produced magnetic fields of up to 8T and the measured axial magnetic field profile agrees with the theoretical predictions.

To measure the millimetre wave radiation a new echellette grating has been designed and constructed. This grating is optimized for operation at frequencies near to 200GHz and uses the quasi-optical spectrometer system formerly used for the 100GHz electron cyclotron maser experiments.

References

(1) A D R Phelps, T Garvey and A S Hasaani Int. J. Electron., 57, 1141-1150, 1984

(2) A D R Phelps and T Garvey, J. Phys. D. :Appl. Phys.,19, 2051-2063, 1986.

(3) A Z Maatug, S N Spark and A D R Phelps, XIIIth. Annual IOP Conf. on Plasma Physics, Oxford, 1986.

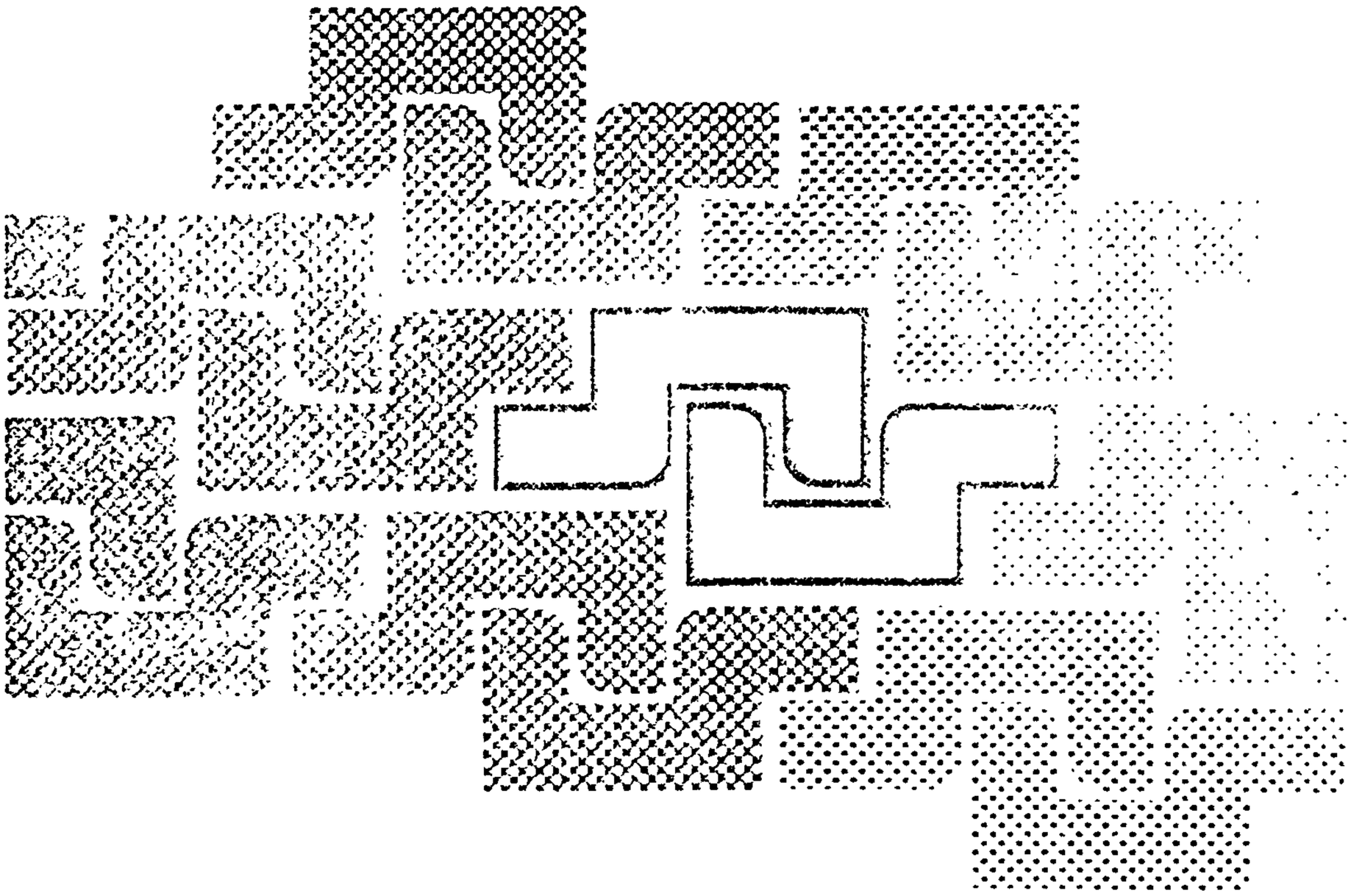

# High-Brightness Accelerators


Edited by

Anthony K. Hyder

M. Franklin Rose and

Arthur H. Guenter



PLENUM PUBLISHING CORPORATION

New York • London

Series B: Physics Vol. 178

ISBN 0-306-42938-1

# ELECTRON CYCLOTRON MASER USING A PULSED RELATIVISTIC ELECTRON BEAM

A. D. R. Phelps, A. Z. Maatug and S. N. Spark

Department of Physics and Applied Physics
University of Strathclyde
Glasgow G4 ONG, Scotland

## ABSTRACT

Measurements of high power millimetre-wave radiation from a pulsed electron cyclotron maser operating in the 75-110 GHz frequency range are reported. A mildly relativistic electron beam excites the electron cyclotron maser. The annular electron beam is extracted from a cylindrical cold cathode and propagates through a pulsed magnetic field of up to 4 T. The beam current in these experiments has been varied from 5 A to 1.25 kA. The pulse duration of the millimetre-wave emission is typically a few hundred ns and corresponds to the time for which energetic electrons are present. Gap closure within the accelerating diode limits the pulse duration.

The millimetre-wave radiation is produced within a highly overmoded cavity. An echelette grating spectrometer has been used to measure the frequency spectra. Far-field radiation patterns have also been measured. The ability to tune the emission frequency by varying the magnetic field has been successfully demonstrated.

The electron cyclotron maser in its performance at the longer wavelength end of the electromagnetic spectrum complements the short and medium wavelength free electron laser. It appears that the electron beam requirements for successful electron cyclotron maser operation are less stringent than those of the free electron laser.

## INTRODUCTION

The electron cyclotron maser instability can occur when a beam of relativistic electrons having a high transverse energy passes through a magnetic field region. In devices which exploit this instability it is usual for the electron beam/magnetic field interaction region to be

located within a resonant cavity of some kind. This can be either a microwave cavity resonator or a quasi-optical maser cavity. The operating frequency of the device lies near to the electron cyclotron frequency or one of its harmonics. The electron beam cyclotron mode (Allen and Phelps, 1977) has the characteristic equation

$$\omega - k_z v_{//} - s\Omega_c = 0 \tag{1}$$

where $v_{//}$ is the axial velocity of the electron beam, s is the cyclotron harmonic number and $\Omega_c$ is the relativistically correct cyclotron frequency

$$\Omega_c = \frac{eB}{\gamma m} \tag{2}$$

There is coupling between the fast wave represented by Eq. (1) and the waveguide electromagnetic mode, which is also fast and is represented by

$$\omega^2 - k_z^2 c^2 - \omega_{c0}^2 = 0 \tag{3}$$

where $\omega_{c0}$ is the cutoff frequency for the particular electromagnetic mode.

In the case of a single cavity

$$k_z = \frac{\pi q}{\ell} \tag{4}$$

where q is the axial eigenmode number and so Eqs. (1) and (3) become

$$\omega = \frac{q\pi v_{//}}{\ell} + \frac{seB}{\gamma m} \tag{5}$$

and

$$\omega = \left( \frac{q^2 \pi^2 c^2}{\ell^2} + \omega_{c0}^2 \right)^{1/2} \tag{6}$$

Equation (6) is the resonance frequency of the cavity for the particular electromagnetic mode and determines to first order the frequency at which interaction occurs.

With a given cavity, as the frequency of the electron cyclotron mode is varied, by varying the magnitude of the magnetic field B, as described by Eq. (5), it is possible to excite in turn each particular electromagnetic mode of the cavity. Each mode has its characteristics value of $\omega_{c0}$ determined by the transverse dimensions of the cavity and by the characteristic structure of that particular mode.

Cyclotron resonance devices have been reviewed by Symons and Jory (Symons and Jory, 1981) and an interesting comparison of the different models used to describe gyrotrons has been published by Lindsay (Lindsay, 1981).

This research at Strathclyde University started in 1978, the first emissions being measured in 1981. The results from these early experiments were concentrated in the 8-12 GHz range (Garvey, 1983; Phelps and Garvey, 1983). A magnetically-shielded diode was used to accelerate the electron beam in the first experiments, whereas in a second series of experiments a magnetic-field-immersed diode was used (Phelps et al., 1984; Phelps et al., 1984). Several configurations were constructed and operated (Hasaani, 1986). The MkV electron cyclotron maser used a higher magnetic field of up to 1.6 T and successfully operated in the 26.5-40 GHz range. In the experiments reported here the magnetic field has been further increased to a maximum of 4 T to provide emission in the 75-110 GHz range.

## EXPERIMENTS

A schematic diagram of the experiment is shown in Fig. 1. The Marx bank was designed and constructed as part of the experiment. It consists of ten 0.5 μF low inductance capacitors charged in positive and negative polarity pairs resulting in only five spark gaps being needed. The lowest two spark gaps are electrically triggered to enable the electron beam pulse to be precisely timed with respect to the peak of the much longer magnetic field pulse. In this way the electron beam interacts with a quasistatic magnetic field of known magnitude. In these experiments the capacitors are normally charged within the range 15-35 kV to obtain a mildly relativistic electron beam. The potential difference applied to the accelerator diode is monitored with a voltage divider and the beam current is measured using a Rogowski loop. The magnitude of the magnetic field has been calibrated using a standard magnetic coil probe.

The millimetre-wave cavity used in the these experiments is made using 23 mm internal diameter stainless steel tubing with a constriction which provides partial wave reflection at the cathode end. There is a small but calculable and measurable screening effect of the cavity on the relatively slowly varying magnetic field as it penetrates the wall of the cavity.

Three methods have been used to measure the millimetre-wave emission (i) direct reception of the emissions for power monitoring, (ii) spectral dispersion and measurement using a blazed echelette grating spectrometer,

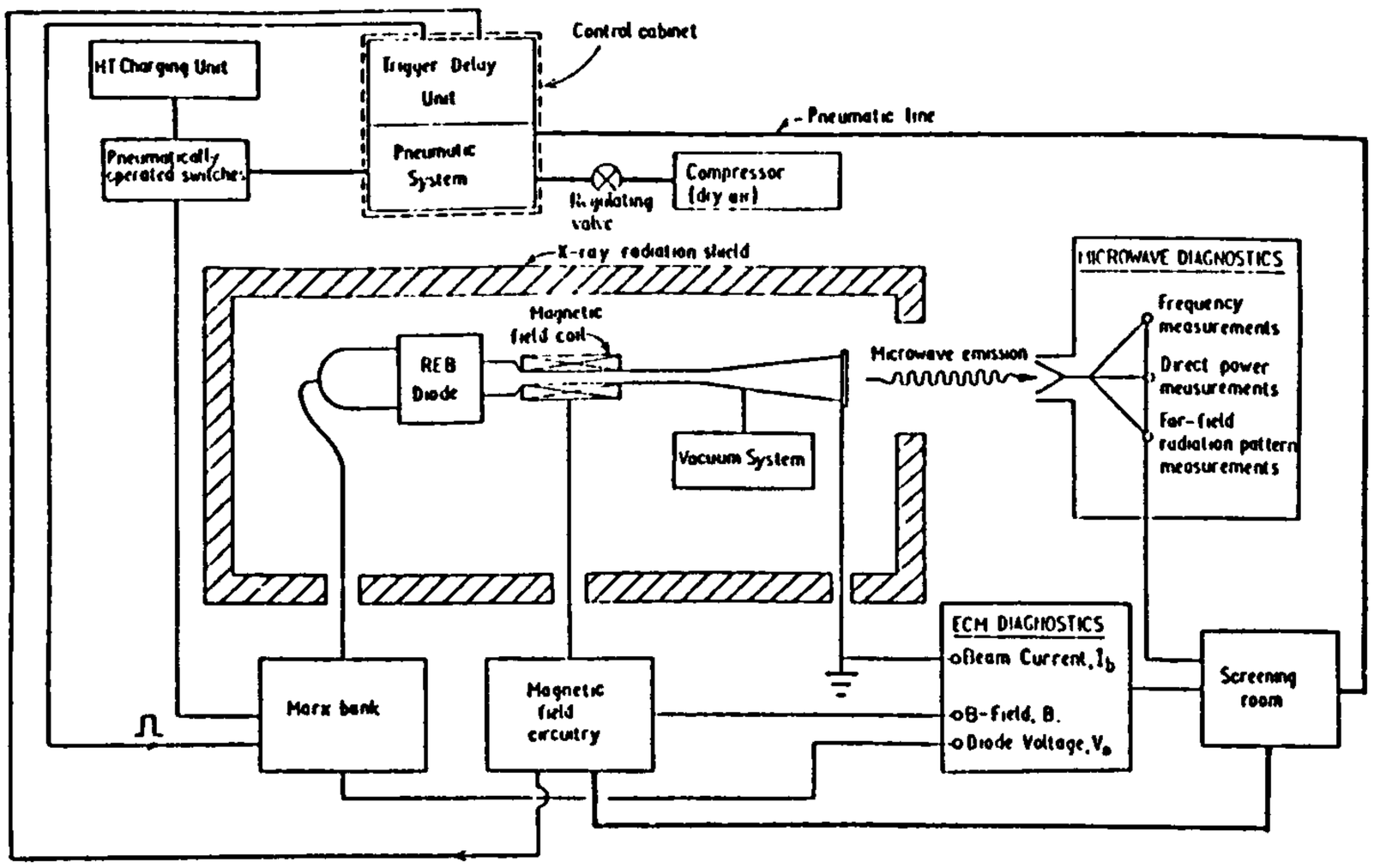


Fig. 1. Schematic diagram of the experiment.

(iii) far-field radiation pattern plots using a single scanned detector and relying on reproducibility to identify operating modes.

A pair of spectra are shown in Fig. 2, for a beam current of 1.25 kA. It is clearly demonstrated that as the magnetic field increases from 2.80 T to 3.33 T the emission spectrum shifts to higher frequencies. It is apparent from the mode scale at the top of these spectral plots that these are in high order modes and, as expected, the far-field pattern plots in these cases have a complicated appearance. The upshift in frequency is exactly what Eq. (5) predicts. Although the output levels shown in Fig. 2 are not yet absolutely calibrated, the known high insertion loss of the spectrometer and previous observations of megawatt power emissions in the MkV experiments indicate that these measurements correspond to quite high powers.

## CONCLUSIONS

Using an overmoded cavity implies possible mode competition, but an apparent compensation, demonstrated by these experiments, is that a spectrum of available modes allows the electron cyclotron maser to tune in frequency, albeit discretely, as the magnetic field is varied. This could have useful implications in any situation where it is desirable to change the operating frequency between one short pulse and the next. The powers available and the reasonable efficiencies of electron cyclotron

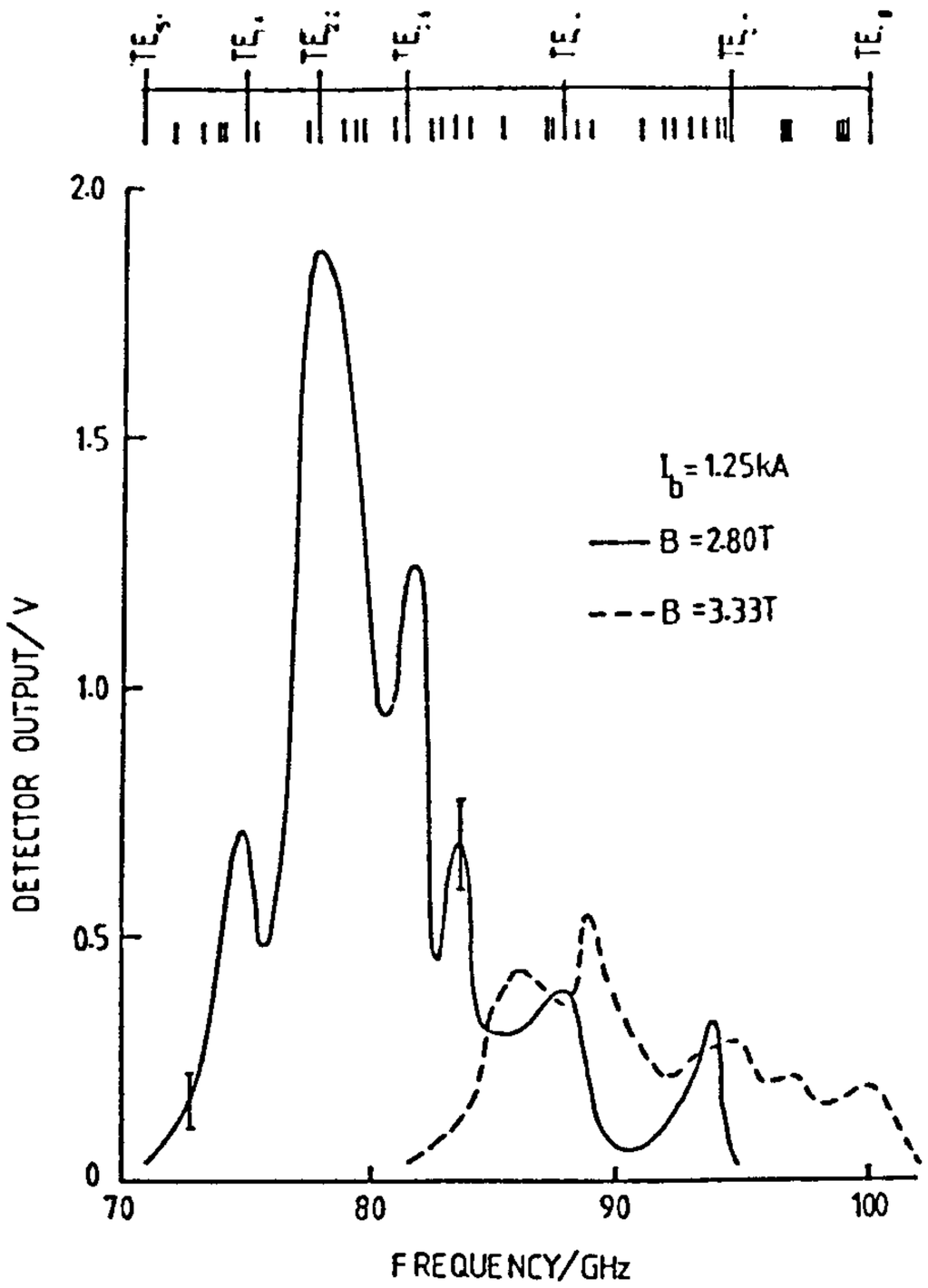


Fig. 2. Spectral analysis of the millimetre-wave emission.

masers tend to make them attractive alternatives to free electron lasers a the microwave and long millimetre-wave end of the spectrum.

It is anticipated that as the electron beam current increases there should be some spread in the particle velocities because of space charge. This lowering of the beam quality does not appear to prevent the electron cyclotron maser operating and leads to the suggestion that the electron cyclotron maser may operate with a lower electron beam quality than that required by a free electron laser. A quantitative investigation of the beam emittance and beam brightness is needed to confirm this.

ACKNOWLEDGMENTS

The support of the SERC and the earlier contributions of Dr. T. Garvey, Dr. A. S. Hasaani and Mr. P. S. Bansal are gratefully acknowledged.

REFERENCES


Allen, J. E. and Phelps, A. D. R., 1977, Waves and Microinstabilities in Plasmas - Linear Effects. Rep. Prog. Phys. 40:1305-68.

Garvey, T., 1983, Investigation of the Interaction of High-Current Relativistic Electron Beams with Electromagnetic Fields, Ph.D. Thesis, Strathclyde University.

Hasaani, A. S., 1986, Pulsed Electron Cyclotron Maser Experiments with Different Configurations, Ph.D. Thesis, Strathclyde University.

Lindsay, P. A., 1981, Gyrotrons (Electron Cyclotron Masers): Different Mathematical Models, IEEE J. Quant. Electron. 17:1327-33.

Phelps, A. D. R. and Garvey T., 1983, Gyroresonant Relativistic Electron Beam Emissions, Xth. Annual Conference on Plasma Physics, Institute of Physics, UCNW, Bangor, UK.

Phelps, A. D. R., Hasaani, A. S., and Bansal, P. S., 1984, Electron Cyclotron Maser Experiments, XIth Annual Conference on Plasma Physics, Institute of Physics, Cambridge, UK.

Phelps, A. D. R., Garvey T., and Hasaani, A. S., 1984, Pulsed Electron Cyclotron Maser Experiments. Int. J. Electron. 57:1141-50.

Symons, R. S., and Jory, H. R., 1981, Cyclotron Resonance Devices, Adv. Electronics and Electron Physics, Vol. 55, (New York: Academic Press), 1-75.

FIFTEENTH ANNUAL CONFERENCE ON
PLASMA PHYSICS
6-8 JULY 1988
University of Manchester Institute of Science and Technology

# HIGH FREQUENCY TUNABLE ELECTRON CYCLOTRON MASER EXPERIMENTS

S N Spark and A D R Phelps

Department of Physics and Applied Physics
University of Strathclyde
Glasgow G4 ONG, Scotland

Previous experiments were reported [1] describing the design and construction of an electron cyclotron maser (ECM) which could oscillate, under various operating regimes, from ~75GHz to ~220GHz. This required the successful generation of continuously varying magnetic fields up to ~8T. Preliminary results presented detected radiation up to a frequency of 183GHz. The Strathclyde ECM has been significantly improved and optimised, with similar improvements being made to the diagnostics. The results of these improvements will be presented in this paper.

An electron-beam-tuning coil was added in the cathode region. This increased the energy in the mm-wave output pulse by a factor of ~40. Via beam probing experiments, this was demonstrated to be entirely due to enhanced beam formation in the cavity. A novel .15mm thickness Mylar output window was developed, which increased the useful energy transmitted from the system by a factor of ~10.

A calorimeter was used to directly measure the output power of the device. A sensitive two detector system developed for the successful analysis of the near field radiation pattern, allowed the determination of the cavity mode of oscillation.

*References*

(1) S N Spark and A D R Phelps. "Pulsed 200GHz Electron Cyclotron Maser Experiments". XIVth Annual I.O.P. Conference on Plasma Physics, St Andrews, 1987.

INT. J. ELECTRONICS, 1988, VOL. 65, NO. 3, 369–376

# Cold cathode 75–110 GHz gyrotron experiments

A. D. R. PHELPS†, A. Z. MAATUG† and S. N. SPARK†

Measurements of the output characteristics of a pulsed cold-cathode, two-electrode, electron cyclotron maser are presented. Short pulses, ~0·2 μs, of W-band (75–110 GHz) millimetre radiation have been observed at power levels up to 0·3 MW. By varying the magnetic field over the range 2·2 T to 4·2 T the output frequency has been observed to be step-tunable in a manner consistent with the excitation of a series of cavity modes. The spatial pattern of the radiated output has been scanned to facilitate the identification of the modes of operation. Applications of this device to plasma diagnostics are discussed.

## 1. Introduction

Most gyrotron research has involved the thermionic MIG, three electrode, gyrotron, which has become a successful CW millimetre wave source. Another branch of research has used a cold-cathode, two-electrode configuration of the type used in the present paper. The capabilities and potential of high average power and high peak power gyrotrons have been reviewed by Granatstein (1984).

Earlier work such as that of Granatstein *et al.* (1975), Didenko *et al.* (1976), Ginzburg *et al.* (1979) and Frank *et al.* (1982) demonstrated that at conventional microwave frequencies very high peak power pulses of electron cyclotron maser radiation could be produced by intense relativistic electron beams. At frequencies which entered the millimetre wave region, Voronkov *et al.* (1982) reported the production of 23 MW at 40 GHz and Gold *et al.* (1985) in a cold-cathode high voltage $K_a$-band experiment successfully produced 20 MW at 35 GHz. A cold-cathode, two electrode design was used in a series of pulsed experiments, reported previously by Phelps *et al.* (1984, 1986), which produced radiation at several frequencies in the 8–40 GHz range.

The experiments reported in the present paper use a re-designed cathode, anode cavity and magnetic field coil to produce millimetre wave radiation in the W-band (75–110 GHz). This higher frequency millimetre wave band has been relatively unexplored previously by cold-cathode two-electrode gyrotrons. During our experiments peak powers of 0·3 MW have been achieved at wavelengths less than 4 mm using this simple light-weight tube and magnetic field coil. Associated with the progress to higher frequencies it has become possible to design, construct and use a diffraction grating spectrometer to measure the frequencies of emission. The spatial pattern of the radiated output has been measured to supplement the frequency measurements and thereby to identify the modes of operation.

The need to produce CW or long pulse MW output devices in the higher frequency millimetre wave bands, for applications in fusion research, has been pointed out by Riviere (1986). The present paper concerns an inherently pulsed device, although the reproducible operation using higher order cavity modes reported here

Received 21 December 1987; accepted 7 January 1988.

† Department of Physics and Applied Physics, University of Strathclyde, Glasgow, G4 0NG, Scotland, U.K.

is relevant to the use of similar modes in high average power millimetre wave gyrotrons. The use of these higher order modes is one of the proposed paths towards higher gyrotron powers at higher frequencies.

The pulsed device used in this paper is also relevant to the development of some types of plasma diagnostic. Certain plasma diagnostic sources do not require to be CW or long pulse. Whereas plasma scattering diagnostics usually require a very narrow emission line-width (Woskoboinikow 1986), which is best provided by a high $Q$ gyrotron cavity immersed in a stable superconducting magnet, low $Q$ cavities immersed in a pulsed magnetic field provide high peak power, which can be suitable for some plasma diagnostics. The high peak power enables plasma refractive index diagnostics, including interferometry, Faraday rotation and shadowgraph techniques to be applied at millimetre wave frequencies to large volumes of plasma using large area imaging. In the millimetre wave regions lower power sources have hitherto usually restricted these diagnostics to measurements along paths of individual beams or sets of beams. Diagnostic plasma electron cyclotron absorption (ECRA rather than ECRH) is also possible with a repetitively pulsed tunable gyrotron source.

## 2. Experiment

A schematic of the experimental layout is shown in Fig. 1. Both the electron beam and the magnetic field which is applied to the beam are pulsed. The magnetic field pulse is sufficiently long ($10^{-3}\,\mathrm{s} > \tau > 10^{-4}\,\mathrm{s}$) for the slowly varying peak of the magnetic field waveform to present a quasi-static magnetic field to the short pulse length ($\tau \leqslant 10^{-6}\,\mathrm{s}$) of the electron beam. Both the electron beam and the magnetic field are supplied from capacitor banks, the charging voltages of which are precisely monitored via fibre optic links to a microcomputer situated in the screened

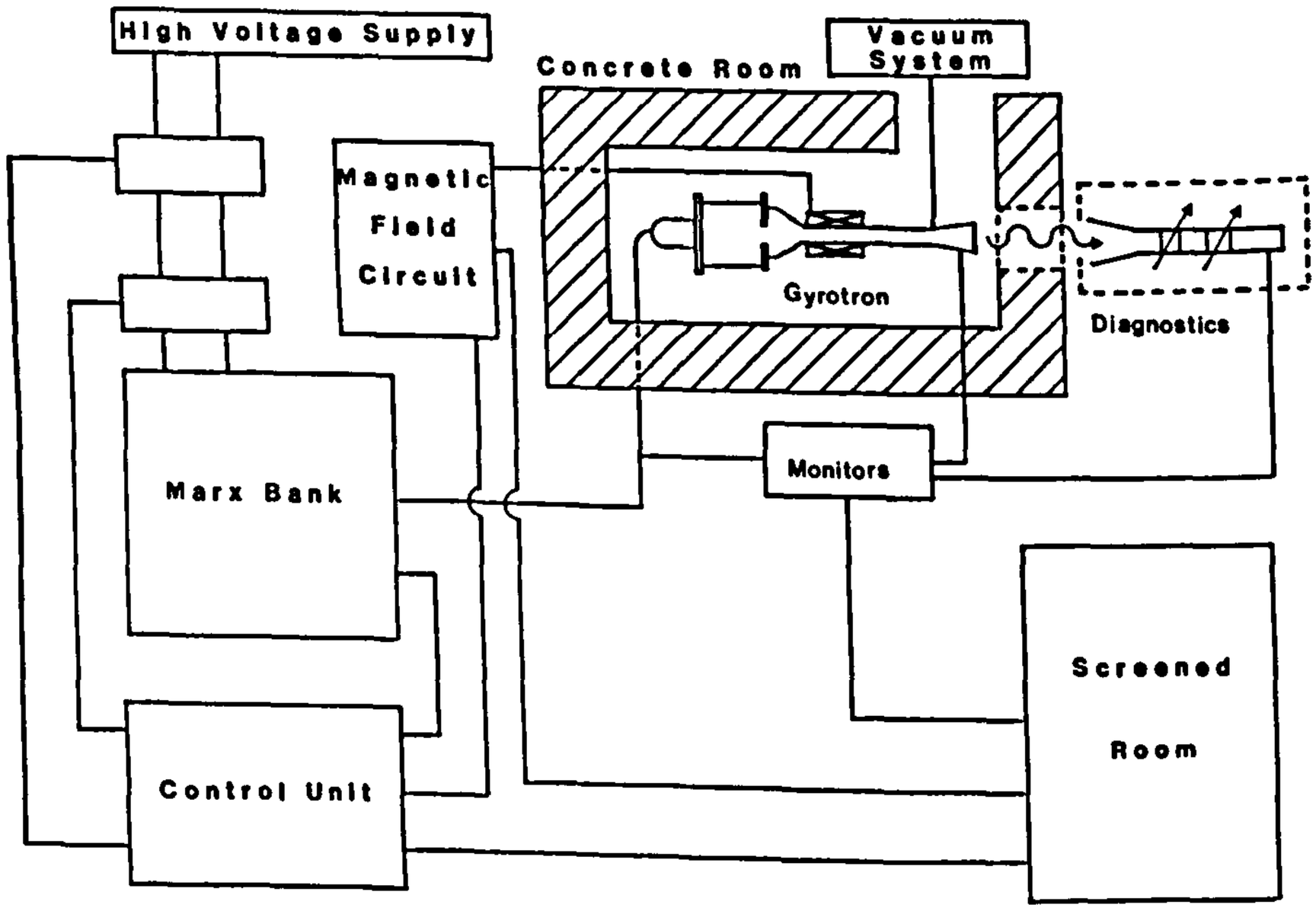


Figure 1. Schematic of experiment.

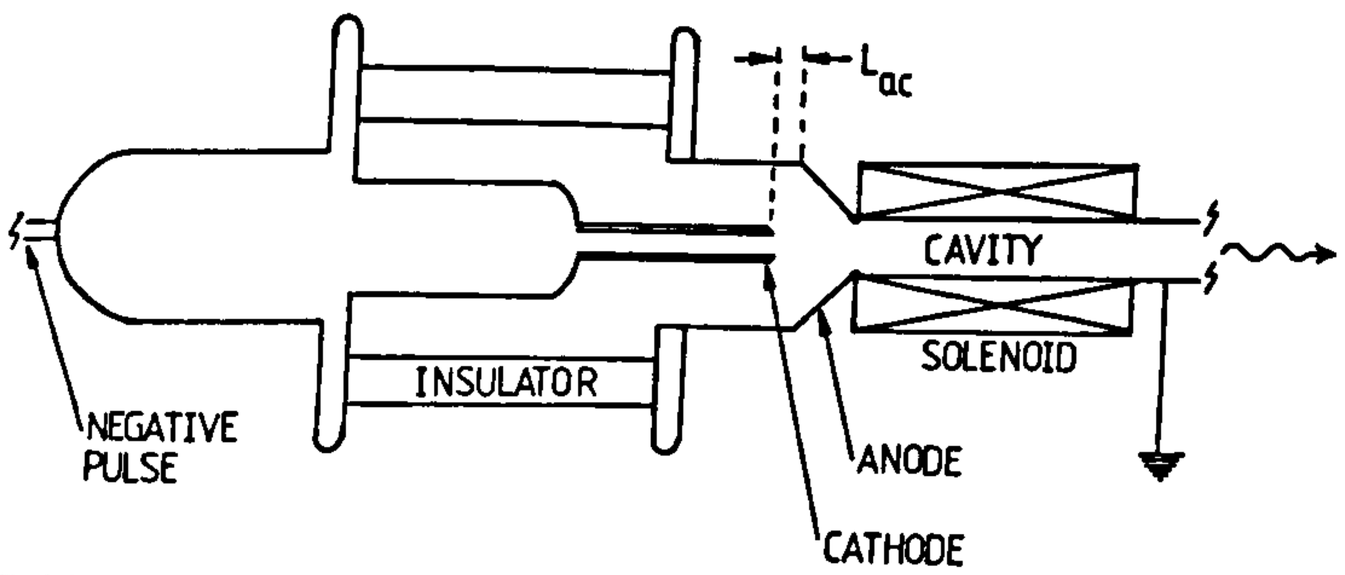


Figure 2. Cold-cathode, two-electrode gyrotron showing anode-cathode spacing $L_{ac}$ (not to scale).

room (Fig. 1). When the pre-arranged charging voltages on both capacitor banks have been reached the microcomputer can automatically trigger the magnetic field circuit. After a pre-determined delay, provided by a delay unit, the electron beam is then triggered. During the work described here the electron beam was normally synchronized with the peak of the magnetic field, and the magnetic field amplitude was varied by varying the charging voltage of the magnetic field circuit. An alternative method of varying the magnetic field, which has also been successfully used, is to keep the magnetic field charging voltage fixed, but to vary the time delay between the magnetic field and the electron beam pulses. The advantage of the former method is that the magnetic field more closely approximates to a quasi-static one. The magnitude of the magnetic field could be varied from effectively zero up to 4·2 T and in the present experiment the range 2·2–4.2 T was used.

The magnetic field solenoid was designed, constructed and tested in order to achieve a compact, light-weight, but mechanically strong coil. The magnetic field was measured to be uniform over a length of 100 mm. Continuous water cooling of the solenoid was used to extract the heat generated by each pulse, before the arrival of the succeeding pulse, so that the resistance of the solenoid remained constant for complete series of pulses. The solenoid was wound using a single layer of turns and was reinforced with resin impregnated glass fibre.

The cold-cathode two-electrode configuration is shown in Fig. 2. The anode cavity was held at earth potential while the cathode was pulsed negative. The cathode was constructed of a stainless steel tube, which had its emitting surface sharpened. The vacuum was produced by a standard oil vapour diffusion pump backed by a rotary pump. The typical operating pressure was $\sim 2 \times 10^{-6}$ mbar in the demountable vacuum tube. The main dimensions of the gyrotron are listed in Table 1. The radii of both the cathode and the anode cavity were smaller than those

| |
|---|
| Cathode radius = 6·35 mm |
| Cavity radius = 11·48 mm |
| Optimum $L_{ac}$ = 13 mm |
| Available $B$ = 2·2–4·2 T |
| mm wave pulse length ≈ 0·2 μs |
| mm wave peak power = 275 kW |
| Observed frequencies = 75–100 GHz |

Table 1. Gyrotron parameters.

used in our previously reported work (Phelps *et al.* 1984) in order that the number of modes did not become excessive in this higher frequency millimetre wave band.

The anode-cathode gap does not have an obvious or natural definition in this foil-less diode configuration, in which the electrons follow the magnetic field lines through the cavity to the collector at the output end of the cavity. Therefore to provide a quantitative parameter by which the position of the cathode could be measured the quantity $L_{ac}$ was defined with respect to a reference point on the anode as shown in Fig. 2. Beyond the output end of the cavity there was an electron collector region followed by a taper up to the radius of the output window.

Conventional pulsed relativistic electron beam diagnostics were used. A calibrated self-integrating Rogowski coil measured the electron beam current and a fast (risetime $\sim 10^{-8}$ s) potential divider measured the accelerating potential difference. Because of the radiated electromagnetic interference produced by the switches in the pulsed electron beam circuit the monitors and also the millimetre wave diagnostics were taken via double screened co-axial cables to transient recorders and oscilloscopes housed in the screened room (Fig. 1).

## 3. Measurements

Before making measurements of the output from the pulsed gyrotron a careful measurement of the pulsed magnetic field profile was made. Magnetic probe measurements were compared with theoretical predictions based on the coil geometry, the measured current flowing through the solenoid and the thickness of the cavity vacuum wall. Although the magnetic field pulse was relatively long and the cavity vacuum wall was made of thin, relatively resistive, metal, there was a predicted small reduction of the amplitude of the magnetic field by the requirement for the magnetic field to diffuse through the stainless steel wall. The measurements confirmed these predictions and all the values of the magnetic field reported in this paper correspond to the true magnetic field inside the cavity.

The first measurements of the gyrotron output were made using a W-band (75–110 GHz) broadband detector which samples part of the radiated output. The position of the cathode was then systematically varied, by varying $L_{ac}$. The output voltage of the detector was then averaged over several pulses for each value of $L_{ac}$. This was repeated for a series of measured electron beam current, $I_b$, values, and for a series of measured magnetic field values. The measurements for $I_b = 26$ A are shown in Fig. 3. The detector output although shown in units of volts is really a relative scale since absolute analysis depends upon several factors including the fraction of the wavefront sampled, the millimetre wave attenuator settings and pulse amplifier gains. All of these relative factors were maintained constant while the data for Fig. 3 was collected. Since the frequencies of emission are known to vary with variations in $B$ and the sensitivity of the broadband detector is not exactly constant throughout the frequency band, the variations of detector output shown in Fig. 3 may not accurately represent the variations in gyrotron output. Nevertheless, Fig. 3 indicates that the gyrotron produced measurable millimetre wave output over a large range of values of $L_{ac}$, typically $-2$ mm to $+23$ mm. For most values of magnetic field the highest detector output was observed at $L_{ac} = 13$ mm. For the remainder of the measurements reported in this paper $L_{ac}$ was set, therefore, at 13 mm.

The broadband detector was used to sample part of the gyrotron output as the magnetic field was varied over the range 2·2–4·2 T, with $L_{ac} = 13$ mm. The result

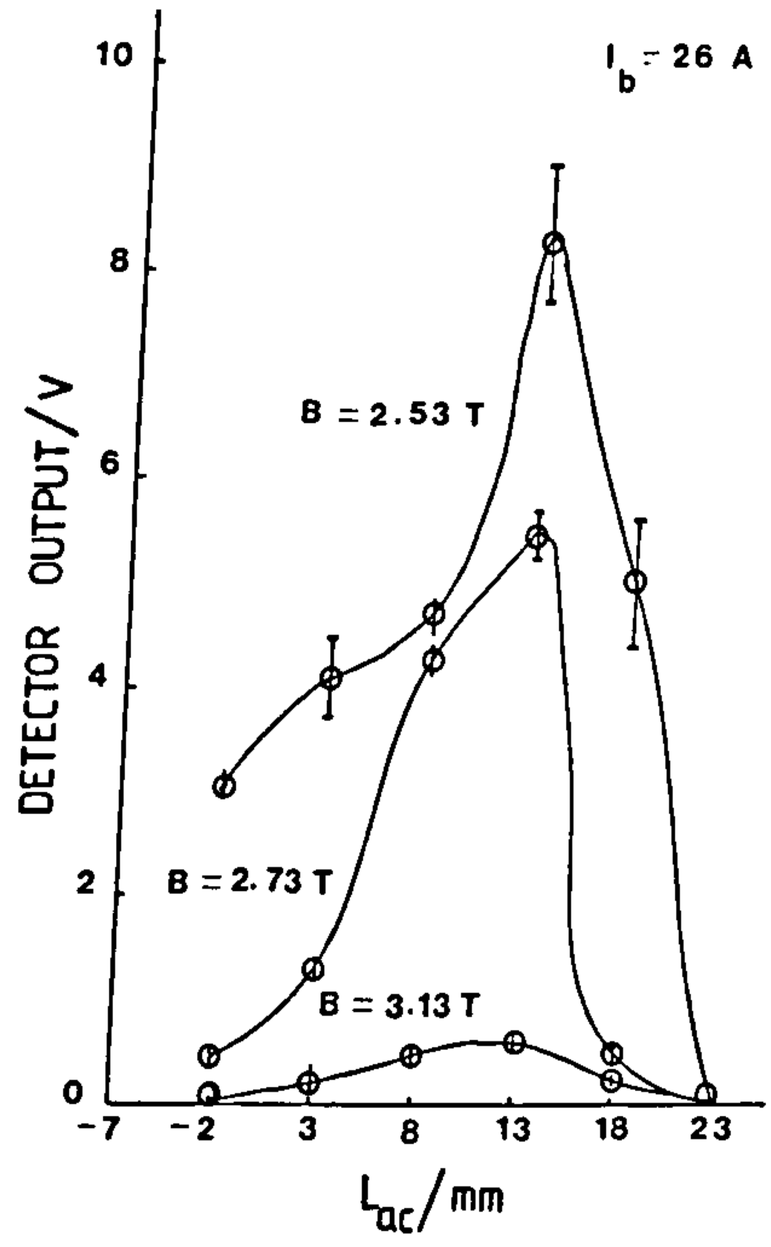


Figure 3. Variation of miilimetre wave detector output as a function of cathode position, for three values of magnetic field.

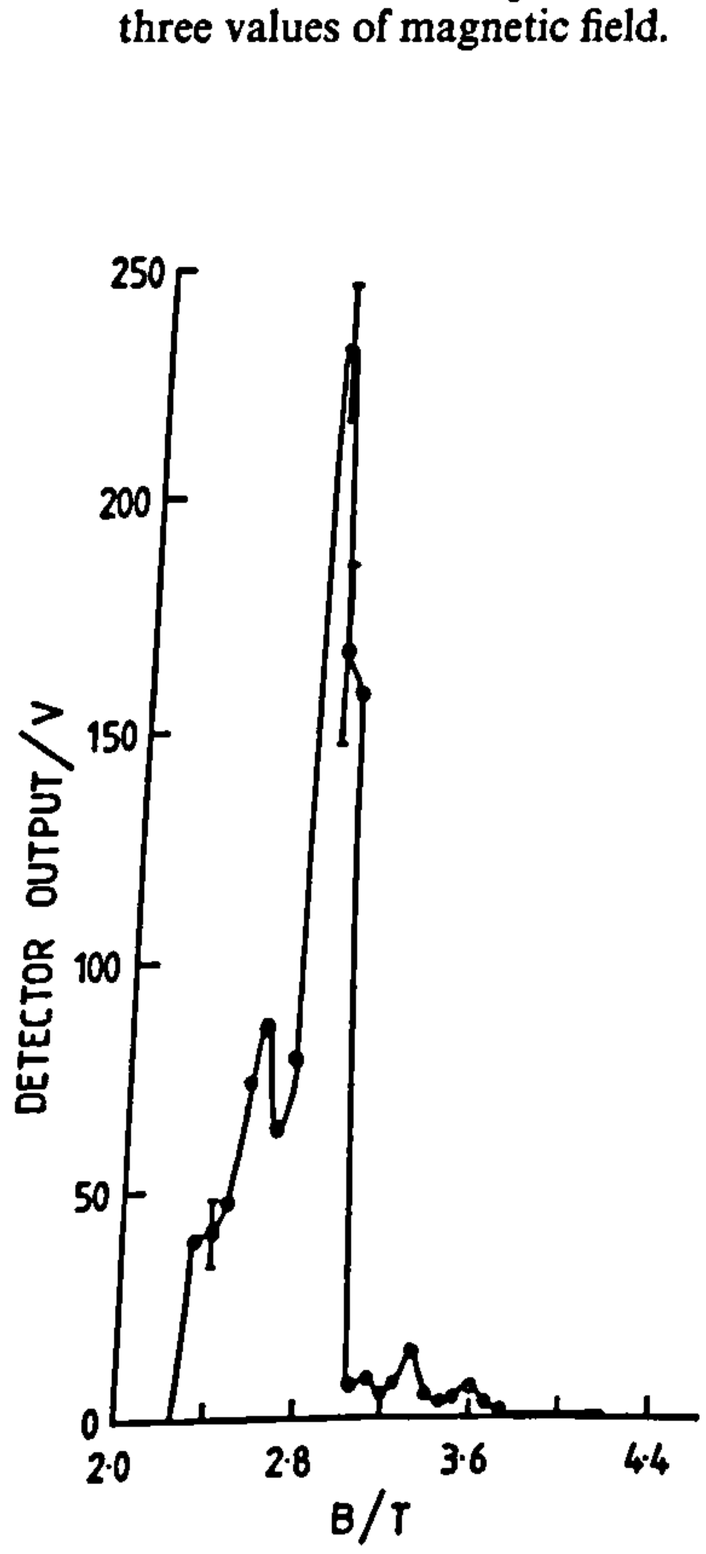


Figure 4. Millimetre wave detector output as a function of magnetic field.

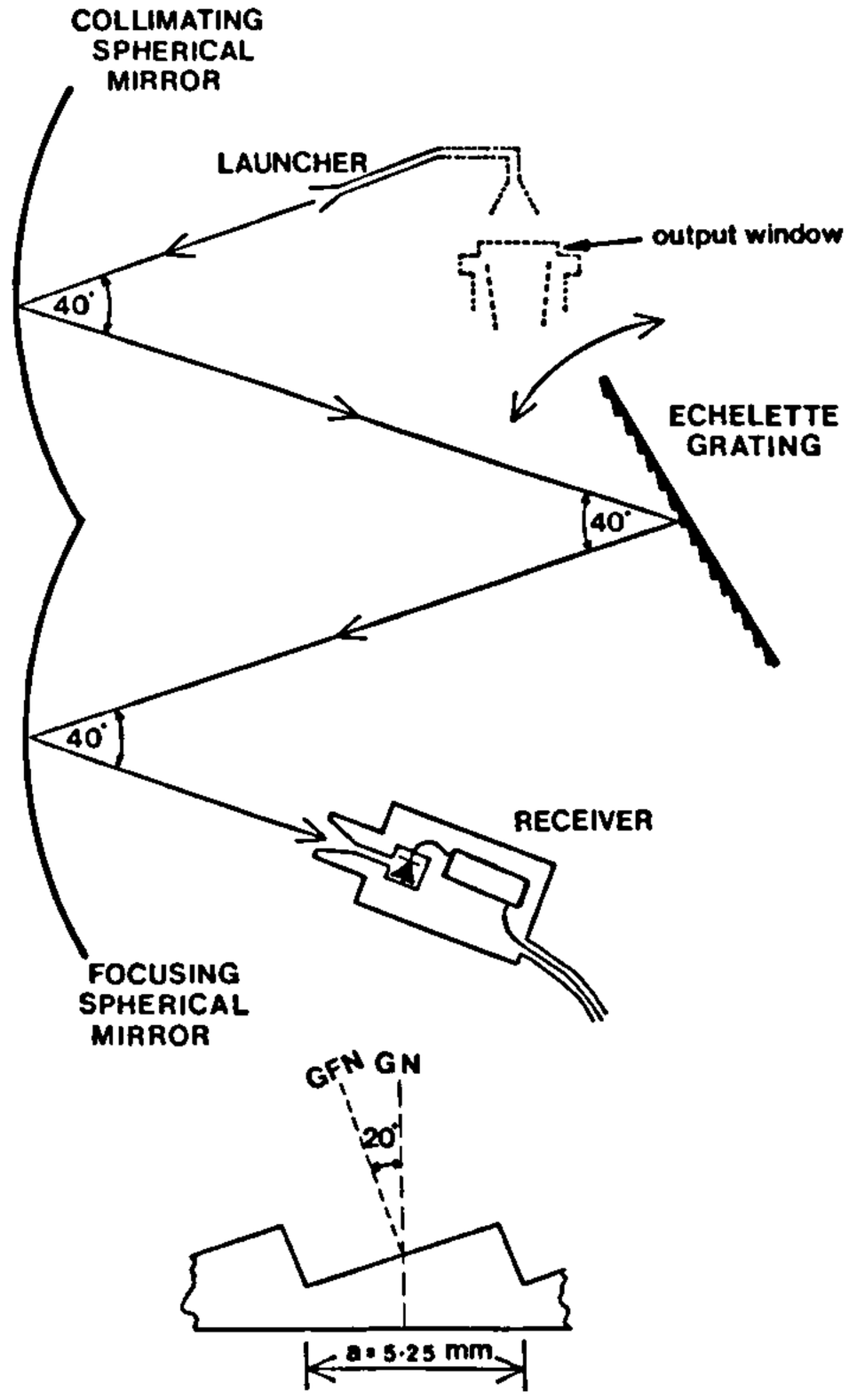


Figure 5. The layout of the diffraction grating spectrometer.

shown in Fig. 4 illustrates the dramatic dependence of the millimetre wave emission upon the magnetic field value. The main peak occurred at $B = 2{\cdot}80\,\mathrm{T}$, but there were smaller peaks at other magnetic field values.

To measure the frequencies of emission a diffraction grating spectrometer was used. The blazed echelette grating was designed and constructed so that it would operate optimally in first order for the frequency range 75–110 GHz (Fig. 5). The experimentally observed resolution of the grating spectrometer was in the range from 1·8–2·2 GHz. Using a calibrated power meter the detector in the receiver of the spectrometer was calibrated over the whole W-band. A BWO was used as the millmetre wave power source. This BWO was also used with a W-band calibrated attenuator to measure the transmission loss through the spectrometer at all frequencies in the W-band. With all gyrotron parameters fixed, the diffraction grating spectrometer was then scanned through its frequency range. Using the calibrated detector sensitivity and spectrometer transmission loss, the raw detector output voltage was then converted into spectral power density. An example of such a spectrum is shown in Fig. 6 for the case $B = 2{\cdot}80\,\mathrm{T}$. The total power emitted in this case was 275 kW, and the mode was a $TE_{16,1}$ mode. The peak power was emitted at 75·8 GHz for $B = 2{\cdot}80\,\mathrm{T}$. For higher magnetic fields the spectral peak moved to higher frequencies. The highest frequency peak in the emission was observed at approximately 100 GHz. The step tunability observed is consistent with the excitation of a series of cavity modes.

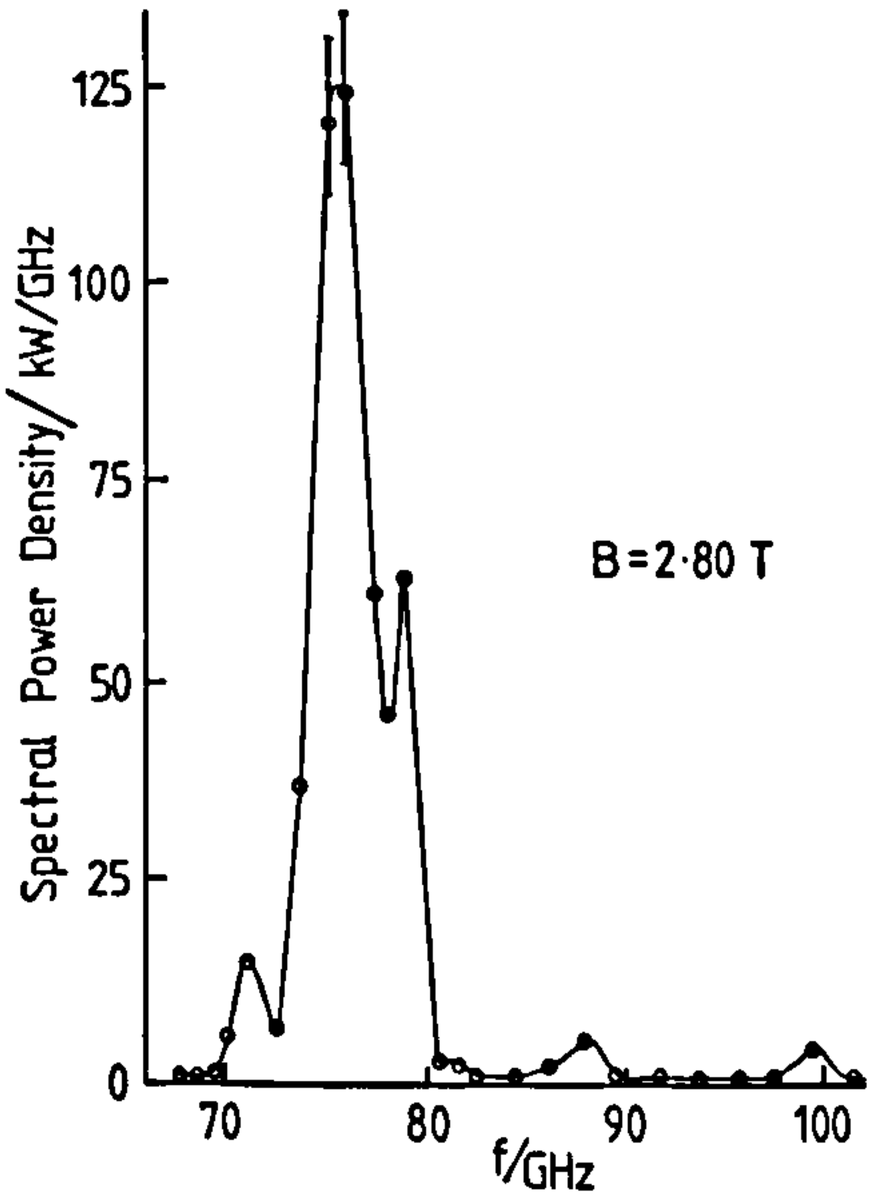


Figure 6. Spectral power density as a function of frequency, for magnetic field = 2·80 T.

By scanning a detector, pulse by pulse, across the emitted radiation pattern, while the gyrotron parameters were held fixed, the mode pattern of the radiation was measured. In some cases, such as $TE_{1,7}$ and $TE_{0,6}$ this mode pattern scan was a useful complementary diagnostic to the spectrometer, in determining the mode in which the gyrotron was oscillating.

The line-width of the gyrotron emission could not be measured in this experiment, because the spectrometer had a larger instrumental filter width. It is expected that the gyrotron emission line-width is much narrower than that shown in Fig. 6, which is simply dominated by the spectrometer filter width.

## 4. Conclusions

Cold-cathode, two-electrode gyrotrons although in principle possessing less capability for optimization of the electron trajectories than conventional three electrode gyrotrons, do permit some empirical optimization by means of variation of the relative cathode positions as demonstrated by Fig. 3. These results suggest that it is important to be able to adjust the axial position of the electron emitting surface in the inhomogeneous magnetic field, to provide the maximum power output for a given mode.

By progressively varying the magnetic field it has been possible to tune this gyrotron from one discrete mode to another, i.e. the emission is step-tunable. This behaviour is similar to that observed in thermionic MIG gyrotrons (Kreischer and Temkin 1987). In the present work it has been possible to achieve this discrete change in frequency between successive pulses, because the amplitude of the magnetic field is readily varied using the pulsed magnetic field coil.

The peak power measured in these experiments was approximately 0·3 MW for a $TE_{16,1}$ mode at 75·8 GHz. Amongst the other modes which could be excited, such diverse modes as $TE_{1,7}$ and $TE_{0,6}$ were identified.

The peak power of this gyrotron is sufficient for most plasma diagnostics. Until the line-width can be accurately measured it is not known whether it could be used as a source for plasma scattering diagnostics. Refractive index diagnostics could use this type of gyrotron provided pulsed measurements were required. Local ECRA and heat pulse propagation would also be appropriate as an application for this gyrotron. Nearly all applications however would depend upon mode conversion from higher order modes to a simpler gaussian (or similar) mode profile. There is clearly a need to develop such mode converters.

## Acknowledgments

This work has been supported by the SERC and EEV company. We have enjoyed helpful discussions with Prof. P. Lindsay, M. Esterson and H. E. R. Preston.

## References

Didenko, A. N., Zherlitsyn, A. G., Zelentsov, V. I., Sularshin, A. S., Fomenko, G. P., Shtein, Yu. G.,, and Yushkov, Yu. G., 1976, Generation of gigawatt microwave pulses in the nanosecond range. *Soviet Journal of Plasma Physics*, **2**, 283–285.

Frank, H. E., Müller, F., and Panzner, G., 1982, An electron cyclotron maser for nanosecond megawatt pulses, *Journal of Physics D: Applied Physics*, **15**, 41–49.

Ginzburg, N. S., Krementsov, V. I., Petelin, M. I., Strelkov, P. S., and Shkvarunets, A. K., 1979, Experimental investigation of a high-current relativistic cyclotron maser, *Soviet Physics: Tech Phys.*, **24**, 218–222.

Gold, S. H., Fliflet, A. W., Manheimer, W. M., Black, W. M., Granatstein, V. L., Kinkead, A. K., Hardesty, D. L., and Sucy, M., 1985, High-voltage $K_a$-band gyrotron experiment, *IEEE Trans. Plasma Science*, **13**, 374–382.

Granatstein, V. L., Herndon, M., Sprangle, P., Carmel, Y., and Nation, J. A., 1975, Gigawatt microwave emission from an intense relativistic electron beam, *Plasma Physics*, **17**, 23–28.

Granatstein, V. L., 1984, High average power and high peak power gyrotrons: present capabilities and future prospects, *International Journal of Electronics*, **57**, 787–799.

Kreischer, K. E., and Temkin, R. J., 1987, Single-mode operation of a high power, step-tunable gyrotron. *Physics Review Letters*, **59**, 547–550.

Phelps, A. D. R., and Garvey, T., 1986, Electron cyclotron maser emissions from pulsed electron beams. *Journal of Physics D: Applied Physics*, **19**, 2051–2063.

Phelps, A. D. R., Garvey, T., and Hasaani, A. S., 1984, Pulsed electron cyclotron maser experiments. *International Journal of Electronics*, **57**, 1141–1150.

Riviere, A. C., 1986, Applications for gyrotrons in fusion research. *International Journal of Electronics*, **61**, 693–695.

Voronkov, S. N., Krementsov, V. I., Strelkov, P. S., and Shkvarunets, A. K., 1982, Stimulated cyclotron radiation at millimetre wavelengths from a high-power relativistic electron beam. *Soviet Physics: Tech. Phys.*, **27**, 68–69.

Woskoboinikow, P., 1986, Development of gyrotrons for plasma diagnostics. *Rev. Sci. Instrum.*, **57**, 2113–2118.